Theory and numerical modeling of two phase flow: melt percolation process through porosity dependent viscous matrix inside the Earth

Suranita Kanjilal

aus Jhargram, West Bengal (Indien)

Theory and numerical modeling of two phase flow: melt percolation process through porosity dependent viscous matrix inside the Earth

vorgelegt beim Facheinheit Geowissenschaften/Geographie
der Johann Wolfgang Goethe-Universität
in Frankfurt am Main

von

Suranita Kanjilal

aus Jhargram, West Bengal (Indien)

Frankfurt 2016
(D30)

1. Gutachter: Prof. Dr. Harro Schmeling, Supervisor

2. Gutachter: Prof.Dr. Doris Breuer

Datum der Disputation:

To my family

Acknowledgement

There is a proverb in my native language that, when gratefulness surpasses a certain threshold, just a 'thanks' becomes inadequate to express the gratitude. So, this inadequacy is applicable for my PhD mentors Harro Schmeling and Guillaume Richard for their guidance during the entire scientific venture of converting my mathematical knowledge into an understanding of real world physical phenomena and making me capable of visualizing the mathematical equations beyond the symbols used in it.

My PhD journey have been enriched by the help I got from my colleagues Mélanie Forien, Herbert Wallner, Meysam Shahraki, Jan Philipp Kruse who helped me a lot scientifically or non- scientifically quite a number of times. I am truly thankful for all those discussions with them which helped me a lot to find my way out. I am specially thankful to Stephan Kettenbach and the entire HRZ unit who solved all those smaller to bigger hardware/software issues of my computer innumerable times. I am lucky to have Christine Ruhland who has always been there to successfully complete lot of administrative process and always has been super patient to help me to understand all those German letters in spite of having a hectic schedule. I want to express my heartfelt thanks to the DFG grant to support my doctoral studies without which nothing would have been possible.

Staying in a foreign country far away from home, would never have been possible without the immense support of my friends who have given me a feeling of second home here. I am grateful to each of them for their love, support and help.

I have faced many ups and downs during my journey of doctoral study one of which was a severe accident I met. I almost lost my motivation of writing my thesis after that. Therefore, it will be an injustice if I do not write about a Hibiscus plant grown in my balcony. Hibiscus plant usually loves warm weather and regular basis small amount of watering. During the time of heavy winter and snowfall in Germany, I thought the plant is not going to be alive anymore and stopped watering it for months. Then the summer came and I was going to throw that plant out one day. Right then I observed the tiny new green leaves all over its branches which surprised me to think how that small plant survived enduring all those odds of its environment.

Abstract

Melt segregation inside the earth consists of two different processes: 1) Generation of partially molten rock and 2) separation of melt, produced from partially molten rock, from the solid residual matrix. This thesis focuses on the later process. The two phase flow dynamics combines the study of flow dynamics of melt (i.e. the liquid phase) and matrix (i.e. the solid phase). Several studies have given the background theoretical frameworks for the flow dynamics of melt inside the earth [Ahern and Turcotte, 1979; Bercovici et al., 2001; Frank, 1968; McKenzie, 1984; Sleep, 1975]. [McKenzie, 1984] summarizes the studies of [Ahern and Turcotte, 1979; Frank, 1968; Sleep, 1975] and gives a complete set of governing equations for the two phase flow problem. The formulations proposed by [Bercovici et al., 2001] is more general in the sense that it gives the univariate system of equations related to matrix and melt flow and it includes the interfacial surface force. Also, the assumption of melt having negligible viscosity compare to the matrix has been abandoned in this formulations. Therefore, we have constructed our numerical model and thereafter a fortran code PERCOL2D to get an insight of melt percolation process through porous media, based on the governing equations proposed by [Bercovici et al., 2001] considering its generalized aspects. Additionally, we have used the Helmhotz decomposition for matrix and fluid viscosity in order to lower the number of linearly independent variables to minimize the computational complications.

This decomposition basically splits a smooth and rapidly decaying vector field into an irrotational vector field and an incompressible vector field [Šrámek, 2007].

The melt present in lithosphere resides at inter-granular areas and forms an interconnected network even at low porosity. Therefore, being less dense than the matrix, melt moves up through porous media due to its buoyancy. As soon as the melt separates from the matrix, compaction of matrix occurs in order to compensate the motion. The numerical modeling used in this thesis considers this matrix compaction where the effective bulk and shear viscosity of matrix are function of porosity or the melt fraction. We have effective bulk viscosity of matrix as inversely proportional to melt fraction.

Porosity dependence of effective bulk and shear viscosity leads to stronger melt focusing in highly porous region like mid ocean ridges [Katz, 2008] since the ratio of bulk and shear viscosity is smaller (< 10) than the constant viscosity case for the porous waves having non dimensional amplitude 0.05 or higher. Moreover, it is observed in [Richard et al., 2012] that the solitary wave formed in porosity dependent viscous matrix settings are steeper than the one formed in the constant matrix viscosity setting.

Under the assumptions of zero source term (i.e. no melting or no freezing) and negligible surface tension, first some 1D numerical experiments have been carried out using different boundary conditions (fixed and periodic) with the help of PERCOL2D.

Firstly a sensitivity analysis in 1D has been conducted varying the convergence parameter of the successive over relaxation method used in the solver of the code and varying the grid resolution of the model. Then the reason of choosing an optimized solver has been discussed.

Secondly, some 1D numerical experiments have been executed by choosing different gaussians as input porous waves. Then the characteristics of other variables like matrix velocity (V_{mz}), fluid velocity (V_{fz}), flux due to matrix compaction (ξ) and the porosity wave itself have been observed.

Three series of model setups with different initial conditions have been carried out varying the width, non dimensional amplitude and the background porosity value of the initial input of porous wave.

Then another experiment by changing the compaction length of the model has also been executed. This change was made by changing intrinsic viscosity of matrix i.e. η_m, the permeability constant i.e k_0 and the background porosity i.e. ϕ_0.

In all these experiments, the characteristics of segregation velocity, rate of compaction and phase velocity have thoroughly been investigated and a comparative observation with corresponding solitary wave has also been presented.

A solitary wave or soliton is a wave whose shape is undeformed during its time propagation. Also, a soliton's group and phase velocities are identical.

The numerical experiments under periodic boundary condition show almost solitary wave like characteristics when time propagation of porous wave, fluid velocity and matrix velocity are observed which indicates that the governing equations lead to a solitary wave solution for the porosity [Barcilon and Lovera, 1989; Barcilon and Richter, 1986; Scott and Stevenson, 1984; Spiegelman, 1993a,b]

A step by step algorithmic approach following the mathematical derivations is conducted in order to get a solitary wave solution for the two phase flow through porosity dependent compacting media in this thesis which is different than the study of [Barcilon and Lovera, 1989; Barcilon and Richter, 1986; Scott and Stevenson, 1984; Spiegelman, 1993a,b] as the effective viscosity of matrix is constant there. In all these studies, expressions for the dispersion relation i.e. speed of the wave as a function of its amplitude and the instability of 1D and 2D-solitary waves in higher

dimensions have been highlighted. Although [Simpson and Spiegelman, 2011] gives the solitary wave solutions in 1D, 2D and 3D considering the porosity dependent effective viscosity of the matrix, but using the small background porosity approximation, they neglect the background porosity (i.e ϕ_0). Since, variation of ϕ_0 causes the variation in compaction length and variation of compaction length causes variation in the shape as well as the dynamics of the solitary wave. Therefore, the study carried out in our thesis as well as in [Richard et al., 2012] can be used for more general purpose. It has been observed that the solitary waves which are observed in a medium whose effective bulk viscosity is porosity dependent, are steeper (cf fig.5.1) compared to that of constant effective bulk viscosity medium and their speed decreases as an inverse function of the background porosity. These phenomena may be a significant tool to interpret the geochemistry and morphology of melt-related processes. Additionally, this analytical solution is used in our code PERCOL2D and also in FDCON for numerical benchmarking (1D) of PERCOL2D.

This benchmarking has been done by comparing the phase velocity of resultant porous wave obtained both from PERCOL2D and FDCON.
A comparison of 2D results obtained from both FDCON and PERCOL2D has also been executed and this comparison has pointed out some computational flaws of PERCOL2D. Therefore, FDCON has been chosen to carry out the subsequent numerical experiments considering a differently formulated effective bulk and shear viscosities of matrix [Schmeling et al., 2012]. The melt grain contiguity plays an important role in determining the melt network geometry. But none of the formulations used in [Bercovici et al., 2001; Richard et al., 2012; Simpson and Spiegelman, 2011] and thereafter in PERCOL2D, incorporates this feature in the corresponding viscosity formulations. Therefore, these studies are not able to predict the disaggregation of the material at melt fractions below one due to the reason that effective shear and bulk modulus approach to zero then.

The bulk and shear viscosities predicted to become zero due to zero bulk and shear modulus of matrix when the melt fractions are 50 and 20 percent respectively for spherical melt fractions and tapered melt tubules. As a consequence, the partially molten rock starts to disaggregate.

The revised viscosity formulation which incorporates the phenomena of melt network geometry has been proposed in [Schmeling et al., 2012] based on elastic moduli theory of a fluid filled poroelastic medium.

A numerical experiment is conducted for different amplitude of input porous waves having 7 km maximum cross sectional diameter to compare their velocity and maximum amplitude variations with respect to time according to the viscosity formulations of [Bercovici et al., 2001] and [Schmeling et al., 2012].

A higher velocity for a certain amplitude of porous wave is observed while using [Schmeling et al., 2012] viscosity formulation compared to [Bercovici et al., 2001]. Also, the rate of increment of maximum value of porosity (ϕ_{max}) is higher according to [Schmeling et al., 2012] formulation compare to [Bercovici et al., 2001] formulation.

It is concluded from all these experiments that, the strong porosity dependence of bulk and shear viscosity according to [Schmeling et al., 2012] formulation leads to significantly narrower porosity waves compared to the time evolution of porous waves obtained using the [Bercovici et al., 2001] formulation.

A dispersion relationship between speed of the wave and the non dimensional amplitude of porous wave is presented based on both the viscosity formulations of [Bercovici et al., 2001] and [Schmeling et al., 2012] in fig. 6.20 from which we can see that the model based on [Bercovici et al., 2001] formulation, converges to the same dispersion relationship obtained from [Simpson and Spiegelman, 2011]. Whereas, the dispersion relationship using [Schmeling et al., 2012] formulations, shows time-dependent decrease of phase velocity with increasing amplitude and it

is not yet clear that whether these solutions converge to steady state porosity waves before the porosity becomes 1.

In a nutshell, this thesis gives an 1D solitary wave solution which fits in the governing equations of two phase flow system when the solid phase i.e. the matrix is compacting and has a porosity dependent bulk and shear viscosity without neglecting the background porosity term. Then it benchmarks the code PERCOL2D and FDCON using this solitary wave solution as an initial input for porous wave. Lastly it analyzes some numerical modeling incorporating the parameter of melt network geometry in the effective viscosity formulations of matrix as proposed by [Schmeling et al., 2012].

Zusammenfassung

Die Segregation von Schmelze im Inneren der Erde gliedert sich in zwei verschiedenen Prozesse: 1) die Bildung von partiell geschmolzenem Gestein und 2) die Separation von Schmelze, die aus teilgeschmolzenem Gestein der festen Restmatrix gebildet wurde. Schwerpunkt der Dissertation ist der letzere Prozess. Die Dynamik des Zweiphasenflusses kombiniert die Untersuchung der Strömungsdynamik der Schmelze, der fluiden Phase, und der Matrix, der festen Phase. Der Rahmen und theoretische Hintergrund zur Strömungsdynamik von Schmelze im Erdinneren wird in mehreren Studien dargestellt [Ahern and Turcotte, 1979; Bercovici et al., 2001; Frank, 1968; McKenzie, 1984; Sleep, 1975]. [McKenzie, 1984] fasst die Arbeiten von [Ahern and Turcotte, 1979; Frank, 1968; Sleep, 1975] zusammen und gibt einen vollständigen Satz von Erhaltungsgleichungen für das Zweiphasen-Strömungsproblem an. Die von [Bercovici et al., 2001] vorgeschlagenen Formulierungen sind allgemeiner in dem Sinne, dass sie das univariate Gleichungssystem von Matrix und Schmelze angeben, weiterhin umfasst es die Kräfte an den Grenzflächen. Auch die Annahme, dass die Schmelze eine vernachlässigbare Viskosität im Vergleich zur Matrix hat, konnte in dieser Formulierungen aufgegeben werden.

Wir haben daraufhin unser numerisches Modell aufgebaut und darauf basierend ein Fortran-Programm PERCOL2D entwickelt, um Einblick in den Prozess der Perkolation von Schmelze durch poröse Medien, dem die wesentlichen Gleichungen von [Bercovici et al., 2001] unter Berücksichtigung der verallgemeinerten Annahmen zu

Grunde liegen, zu bekommen. Darüber hinaus haben wir die Helmholtz-Zerlegung für die Matrix- und Fluidviskosität angewandt, um die Anzahl linear unabhängiger Variablen zu reduzieren und damit Schwierigkeiten bei deren Berechnung zu minimieren. Im Grunde teilt diese Separation ein glattes und schnell abklingendes Vektorfeld in ein wirbelfreies Vektorfeld und ein inkompressibles Vektorfeld [Šrámek, 2007].

Die lithosphärische Schmelze befindet sich zwischen den Korngrenzen der Minerale und bildet ein verbundenes Netzwerk, auch bei geringer Porosität. Aufgrund der geringeren Dichte relativ zur Matrix und des daraus resultierenden Auftriebs bewegt sich die Schmelze durch das poröse Medium nach oben. Sobald sich die Schmelze von der Matrix trennt, tritt eine Kompaktion der Matrix auf, um den Bewegungsfluss auszugleichen. Die in dieser Arbeit angewandte numerische Modellierung berücksichtigt diese Kompaktion der Matrix, hierbei sind die effektive Volumen- und Scherviskosität der Matrix Funktionen der Porosität beziehungsweise des Schmelzgrads. Die effektive Volumenviskosität der Matrix ist invers proportional zur Schmelzkonzentration.

Die Porositätsabhängigkeit der effektiven Volumen- und Scherviskosität führt zu einer stärkeren Fokussierung der Schmelze in hochporösen Gebieten, wie mittelozeanischen Rücken [Katz, 2008], da das Verhältnis von Volumen- zu Scherviskosität kleiner ist (< 10) als der Fall konstanter Viskosität für poröse Wellen mit dimensionslosen Amplituden von 0,05 oder höher. Außerdem wird beobachtet [Richard et al., 2012], dass solitäre Wellen, die sich in Matix mit porositätsabhängiger Viskosität bilden, steiler sind als die in Umgebungen mit konstanter Matrixviskosität. Unter den Annahmen eines verschwindenden Quellterms (d.h. kein Schmelzen oder kein Frieren) und vernachlässigbarer Oberflächenspannung wurden zunächst einige eindimensionale numerische Experimente mit Hilfe von PERCOL2D durchgeführt, wobei unterschiedliche Randbedingungen (feste und periodische) angewandt wurden.

Als erstes wurde eine Sensitivitätsanalyse in 1D durchgeführt. Die Konvergenzparameter der Methode der sukzessiven Überrelaxation, welche der Löser des Codes benötigt, und die Gitterauflösung wurden variiert. Danach wird die Begründung der Wahl eines optimierten Lösers diskutiert.

Als zweites wurden einige 1D numerische Experimente ausgeführt, bei denen verschiedene Gauß-Funktionen als Anfangsform der porösen Wellen dienten. Daraufhin wurde die Charakteristik von anderen Variablen, wie die Matrix-Geschwindigkeit (V_{mz}), die Fluid-Geschwindigkeit (V_{fz}), der Fluss aufgrund der Matrix-Kompaktion (ξ) und der Porositätswelle selbst untersucht. Drei Serien von Modellkonfigurationen mit verschiedenen Anfangsbedingungen wurden durchgeführt; die Breite, die dimensionslose Amplitude und der Wert der Hintergrundporosität der initialen porösen Welle wurden variiert.

Ein weiteres Experiment mit Änderungen der Kompaktionslänge des Modells wurde ebenfalls durchgeführt. Dazu wurden die intrinsische Viskosität der Matrix η_m, die Permeabilitätskonstante k_0 und die Hintergrundporosität ϕ_0 entspechend gewählt.

In all diesen Experimenten wurden die Eigenschaften der Segregationsgeschwindigkeit, der Kompaktiosrate und der Phasengeschwindigkeit gründlich untersucht. Auch eine vergleichende Betrachtung mit entsprechenden solitären Wellen wurde dargestellt. Eine solitäre Welle oder Soliton ist eine Welle, deren Form während der Ausbreitungszeit unverformt bleibt. Desweiteren sind die Gruppen und Phasengeschwindigkeiten des Solitons gleich. Unter periodischen Randbedingung zeigen die numerischen Experimente nahezu die Charakteristika von solitären Wellen bei Betrachtung der zeitlichen Ausbreitung der porösen Welle, der Fluid- und der Matrix-Geschwindigkeit. Dies indiziert, dass die Erhaltungsgleichungen zu einer Lösung der solitären Wellen für die Porosität führen [Barcilon and Lovera, 1989; Barcilon and Richter, 1986; Scott and Stevenson, 1984; Spiegelman, 1993a,b].

In dieser Arbeit wird ein schrittweiser algorithmischen Ansatz, der den mathematis-

chen Ableitungen folgt, durchgeführt, um eine Soliton-Lösung für den Zweiphasen-fluss durch porositätsabhängige kompaktierende Medien zu erhalten. Diese unterscheidet sich von den Untersuchungen von [Barcilon and Lovera, 1989; Barcilon and Richter, 1986; Scott and Stevenson, 1984; Spiegelman, 1993a,b], bei denen die effektive Viskosität der Matrix konstant ist. In all diesen Studien werden Ausdrücke für die Dispersionsrelation, d.h. der Geschwindigkeit der Welle in Abhängigkeit von ihrer Amplitude, und für die Instabilität von 1D- und 2D-solitären Wellen in höheren Dimensionen hervorgehoben. Obwohl [Simpson and Spiegelman, 2011] die Soliton-Lösungen in 1D, 2D und 3D unter Berücksichtigung einer porositätsabhängigen effektiven Viskosität der Matrix angeben, vernachlässigen sie die Hintergrundporosität ϕ_0 durch Nutzung der Näherung für eine kleine Hintergrundporosität.

Die Veränderung von ϕ_0 verursacht eine Veränderung der Kompaktionslänge und Änderung dieser wiederum eine Veränderung sowohl der Form als auch der Dynamik der solitären Welle. Daher kann die Untersuchung dieser Arbeit als auch die von [Richard et al., 2012] für eher allgemenere Zwecke verwendet werden. Es wurde beobachtet, dass solitäre Wellen in einem Medium mit Porositätsabhängigkeit der effektiven Volumenviskosität steiler sind (siehe Abbildung 5.1) im Vergleich zu Medien mit konstanter effektiver Volumenviskosität. Außerdem nimmt ihre Geschwindigkeit wie eine inverse Funktion der Hintergrundporosität ab. Diese Phänomene können ein wichtiges Werkzeug zur Interpretation der Geochemie und Morphologie von schmelzbezogenen Prozessen sein. Zusätzlich wird diese analytische Lösung für numerisches Benchmarking der Codes PERCOL2D und auch FDCON (1D) verwandt. Dieses Benchmarking wurde mittels eines Vergleichs der Phasengeschwindigkeit der resultierenden porösen Welle, die beide, PERCOL2D und FDCON, liefern, durchgeführt.

Ein Vergleich der 2D-Ergebnisse von FDCON und PERCOL2D wurde auch ausgeführt. Dieser wies auf einige Rechenfehler im PERCOL2D-Code hin.

Daher wurde FDCON gewählt, um die nachfolgenden numerischen Experimente

unter Berücksichtigung einer unterschiedlich formulierten effektiven Volumen- und Scherviskositäten der Matrix durchzuführen [Schmeling et al., 2012].

Die Schmelz-Korn Kontiguität spielt bei der Bestimmung der Netzwerk-Geometrie der Schmelze eine wichtige Rolle. Weder in den verwendeten Formulierungen von [Bercovici et al., 2001; Richard et al., 2012; Simpson and Spiegelman, 2011] und daraufhin in PERCOL2D, berücksichtigt diese Eigenschaft in der entsprechenden Viskositätsformulierung. Aufgrund der Näherung des effektiven Scher- und Kompressionsmoduls gegen Null sind daher diese Studien nicht in der Lage den Zerfall des Materials bei einem Schmelzanteil von eins vorherzusagen. Aufgrund der verschwindenden Kompressions- und Schermoduli der Matrix wird vorhergesagt, dass die Volumen- und Scherviskositäten Null werden, wenn der Schmelzgrad 50 bzw. 20 Prozent, entsprechend für kugelförmige Schmelze-Taschen und verjüngte Schmelz-Tubuli, erreicht. Als Folge beginnt das partiell geschmolzene Gestein zu zerfallen. Die überarbeitete Formulierung der Viskosität, welche die Eigenschaften der Netzwerkgeometrie der Schmelz beinhaltet, wurde von [Schmeling et al., 2012] vorgeschlagen; sie basiert auf der Theorie von Elastizitätsmoduli in einem fluidgesättigten poroelastischen Medium.

Entsprechend der Viskositätsformulierungen von [Bercovici et al., 2001] und [Schmeling et al., 2012] wurde ein numerisches Experiment für verschiedene Amplitude der Anfangsform der porösen Wellen durchgeführt. Der maximale Querschnittdurchmesser war 7 km, um deren Geschwindigkeit und maximale Amplitudenvariationen unter Berücksichtigung der Zeit zu vergleichen. Bei Verwendung der Viskositätsformulierung von [Schmeling et al., 2012] wird im Vergleich zu der von [Bercovici et al., 2001] eine höhere Geschwindigkeit für eine bestimmte Amplitude der porösen Welle beobachtet. Weiterhin ist die Zuwachsrate des Maximalwerts der Porosität ϕ_{max} höher mit der [Schmeling et al., 2012] - Formulierung im Vergleich zur [Bercovici et al., 2001] - Formulierung.

Aus all diesen Versuchen wird geschlossen, dass die starke Porositätsabhängkeit der Volumen- und Scherviskosität gemäß der Formulierung von [Schmeling et al., 2012] zu signifikant engeren Porositätswellen führt, vergleicht man sie mit der zeitliche Entwicklung von porösen Wellen, die man unter Verwendung der [Bercovici et al., 2001] - Formulierung erhält. Basierend auf den beiden Viskositätsformulierungen, [Bercovici et al., 2001] und [Schmeling et al., 2012], wird eine Dispersionsrelation zwischen der Geschwindigkeit der Welle und der dimensionslosen Amplitude der porösen Welle in Abb. 6.20 präsentiert. In Abb. 6.20 wird sichtbar, dass das Modell, welches der [Bercovici et al., 2001] - Formulierung folgt, gegen die gleiche Dispersionsrelation konvergiert, wie man sie von [Simpson and Spiegelman, 2011] erhält. Unter Verwendung der [Schmeling et al., 2012] - Formulierungen zeigt die Dispersionsrelation eine zeitabhängige Abnahme der Phasengeschwindigkeit mit zunehmender Amplitude. Es ist noch nicht klar, ob diese Lösungen gegen stationäre Porositätswellen konvergieren bevor die Porosität 1 wird.

Kurz zusammengefasst beschreibt diese Arbeit eine 1D Lösung der solitären Welle, die dem System der Erhaltungsgleichungen der Zweiphasenströmung genügt, wenn die feste Phase, d.h. die Matrix, kompaktiert und eine porositätsabhängige Volumen- und Scherviskosität hat und dies ohne den Term der Hintergrundporosität zu vernachlässigen. Unter Verwendung dieser Soliton - Lösung als Anfangsform der poröse Welle werden die Codes PERCOL2D und FDCON bewertet. Schließlich werden einige numerische Modellierungen, die die Parameter der Geometrie des Schmelz-Netzwerks in der Formulierungen der effektiven Viskosität der Matrix, wie von [Schmeling et al., 2012] vorgeschlagen, einbeziehen, analysiert.

List of Figures

List of Tables

Contents

Chapter 1

Introduction

The processes by which melt is extracted from partially molten source regions at depth and erupted at the earths surface are known collectively as melt segregation. It is convenient to think of melt segregation as a two-stage process in which magma is generated by partial melting at depth and then migrates upward toward the earths surface.

How the degrees of partial melt, necessary to generate the spectrum of magmas erupted at the Earths surface, can be achieved and what can be the reasons which link between the plate tectonic process and magma generation? These questions can be answered by the partial melting process.

1.1 Generation of melt

Partial melting occurs through three mechanisms:

1) Anomalous thermal perturbation of the geotherm.

2) Lowering the mantle solidus/liquidus by dehydration of hydrated minerals.

3) Adiabatic decompression of the mantle.

Hot crystalline rock ascending adiabatically from lower in the mantle finds itself above the pressure dependent melting temperature and begins to melt. As the rock continues to rise, it forms a two-phase mixture of solid and melt, which undergoes continual melting until, near the surface, the temperature drops and the rock solidifies.

There are three states of earths upper mantle: Solid, liquid or partially molten. The oceanic and shield geotherms differ at shallow depths but converge towards the adiabatic gradient at greater depths. For example, the oceanic and shield geotherms of Iherzolite converge towards the adiabatic gradient at depths greater than 150 km [Wyllie, 1981]. This denotes that under normal conditions the mantle beneath both continents and ocean must be totally solid when it is completely anhydrous as the geotherm never intersect the solidus. The addition of small amounts of H_2O and CO_2 have the effect of lowering the solidus such that for mantle with 0.4% H_2O, the geotherm intersects the solidus at depth approx 100-250 km. This could produce 0.1% partial melt within this depth range .

Deep mantle material ascends and partial melting occurs due to adiabatic decompression of the mantle rock. Decompressional melting of hot upwelling rock in the mantle creates a region of partial melt comprising a porous solid matrix through which magma rises buoyantly [Havlin and Parmentier, 2014; McKenzie, 1984, 1985; Raddick et al., 2002; Schmeling, 2000; Weinberg, 1997]. Magma transport and the compensating matrix deformation are commonly described by two-phase compaction models.

The major process which is responsible for the generation of magma at mid oceanic ridges, back arc spreading centers and at many intra-plate volcanic centers, is pressure released melting. But, in the subduction zone setting, partial melting might be triggered by lowering of the mantle solidus by addition of volatiles, derived from the subducted oceanic crust [Chapman and Pollack, 1977; Hirschmann, 2000; Ulmer, 2001; Wyllie and Ryabchikov, 2000].

1.1.1   Types of partial melting

There are two different kind of partial melting:

1) Equilibrium or batch melting: The partial melt formed continuously reacts and equilibrates with the residue crystalline till the moment of segregation upto which the bulk composition of the system remains constant.

2) Fractional or Rayleigh melting: The partial melt is removed from the system as soon as it is formed such that no reaction with crystalline residue can occur and for this type of partial melting the bulk composition of the system is changeable.

The critical parameter which controls the criteria that among these two kind which one should be the nature of a partial melting process, is the ability of the newly formed magma to segregate from the residual crystals [Maaløe, 1985]. The understanding of the nature of partial melting process helps to get an overview of the reason behind diversity of primary magma compositions erupted at the earth's surface.

However, in reality, actual partial melting process in the mantle is of a type intermediate between the batch and fractional melting models, known as 'critical melting' [Maaløe and Scheie, 1982]. This is the case when the mantle becomes permeable after certain degree of batch melting and then the melt is squeezed out continuously from the residuum and thus accumulated. This permeability threshold is variable according to different tectonic settings.

1.1.2   Zones of partial melting

Partial melting takes place both at divergent and convergent plate boundaries.

The temperature at mid-ocean ridges is elevated by upwelling mantle. Therefore, rising mantle (peridotite) crosses the solidus as pressure decreases which results

de-compressional partial melting. Due to partial melting, magma which is created from parent rock is always more felsic than the parent rock.

Sometimes upwelling of mantle causes the formation of divergent boundary within continental crust. Due to extensional faulting, the continental crust is stretched and thinned. Thus, a rift valley develops. Hence mafic magmas are produced by decompression melting of the peridotite of the asthenosphere. Sometimes, these mafic magmas erupt as they pass quickly through the thinned continental crust. Heating and hydration of the continental crust produces felsic magmas. These felsic magmas can rise and erupt forming rhyolite as the region is usually under tension. The mixture of mafic and felsic volcanism is called as 'bimodal volcanism.'

A localized source of basaltic magma that is stationary in the mantle, beneath the lithosphere, is known as 'hot spot'. Partial melting of mantle in a concentrated zone of the asthenosphere produces the basaltic magma.

During subduction, an oceanic plate dives beneath another plate and is recycled into the mantle. At a depth around 100 - 150km of subducting oceanic plate, large volumes of mostly basaltic magmas are formed. Two processes play a major role in this magma production:

1) Much of the subducted oceanic crust melts as it heats up which is referred to as the subduction component of the magma.

2) Water is released from the melting oceanic crust. The water reduces the melting temperature of surrounding asthenosphere which leads to the formation of basaltic magmas which is called as dewatering or as mantle component of the magma. The volcanic activity at the Earth's surface, caused by these magmas is called arc volcanism. The name derives from the many arc shaped island chains around the Pacific basin that result from this form of volcanic activity. When the overriding plate in a subduction zone is a continental plate, the magmas have to rise through continental crust to reach the surface. During this process, rising mafic magmas

often incorporate some continental crust through assimilation. These magmas may also reside for extended periods of time in crustal magma chambers and undergo fractional crystallization

Continental collisions thicken continental crust. Due to heating and compression, wet, felsic and intermediate rocks undergo partial melting within that thickened crust. Compressing wet felsic rock can cause melting due to the slope of the wet felsic solidus.

In reality, however, melt generation and migration probably occur simultaneously, and a theory which describes both stages of the process is therefore required. There are several mode of melt migration.

1.2 Ascent of melt

Partial melting depends on temperature, pressure, and chemical composition. On the one hand, melt migration is governed by the principles of conservation of mass and momentum. The model of porous flow was first proposed by Frank [1968], in which a partially molten region is regarded as a saturated porous medium. This model is supported by experimental evidences. [Waff and Bulau, 1979] shows that liquid formed by small degrees of partial melting will be distributed in an interconnected network along the grain edges of the residual crystals if the angle between two crystal faces in equilibrium with liquid (dihedral angle) is less than 60°. The average dihedral angle is observed to be about 45° in experiments on partially molten basalts Waff and Bulau [1982, 1979]; Watson [1982].

Three criteria determine the geometrical distribution and the connectivity of the melt in a partially molten polycrystalline rock. These are:

1) the melt fraction;

2) the location of melt; and

3) the minimum total free energy of the solid-solid and the solid-liquid interfaces.
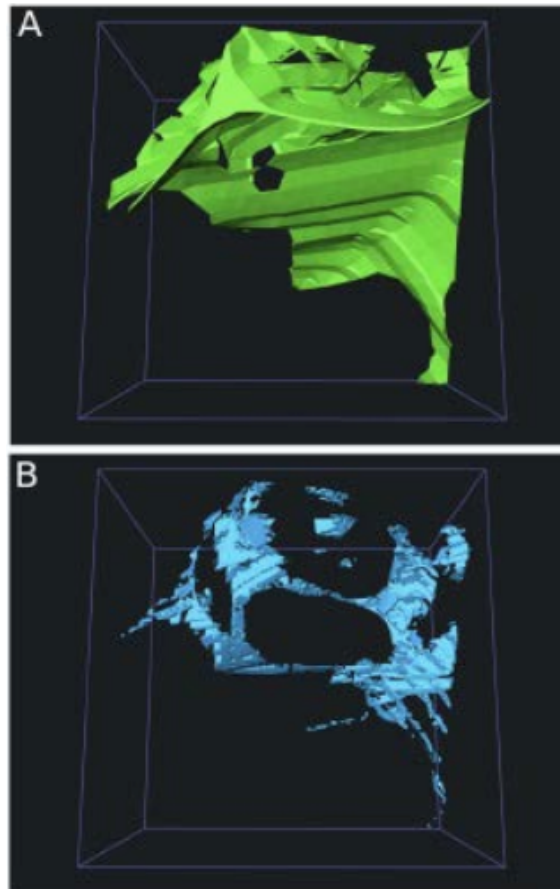
Fig. 1.1: Detail of the 3-D pore space of the sample: (a) At the full resolution of this study melt layers on grain boundaries and small triple-junctions are present. The voxel size is 0.025 μm. (b) The same volume as in (a) sampled with a voxel size of 0.7μm, the resolution of the X-ray tomographic study. The thin layers of melt are not captured at this resolution. Figure courtesy [Garapić et al., 2013]

The minimum interfacial energy is determined by the dihedral angle, ϕ which means that the curvature of the solid-liquid interface should have a constant minimum value. If $\phi = 0°$ the melt wets all grain faces, if $0° < \phi < 60°$, the melt situated at grain edges or corners will form an interconnected system of tubes, and if $\phi > 60°$ the melt will be concentrated in pockets at grain corners [Garapić et al., 2013; Schmeling, 1985]. The reconstructed 3-D melt distribution is shown in Fig.2.1 [Garapić et al., 2013], when the grain size is 33 μm and melt fraction is 3.6%

Crystalline material containing a small amount of melt can be regarded as a porous medium or "matrix" which is saturated with fluid ("melt"). Migration of melt through the matrix is driven by pressure gradients produced by the buoyancy of

the melt or the deformation of the matrix.

There are various forms of melt transports from the lower mantle to the surface of
the earth. Fig. 4.1 of [Gregg et al., 2012] represents a schematic diagram of those
various forms of melt transport.
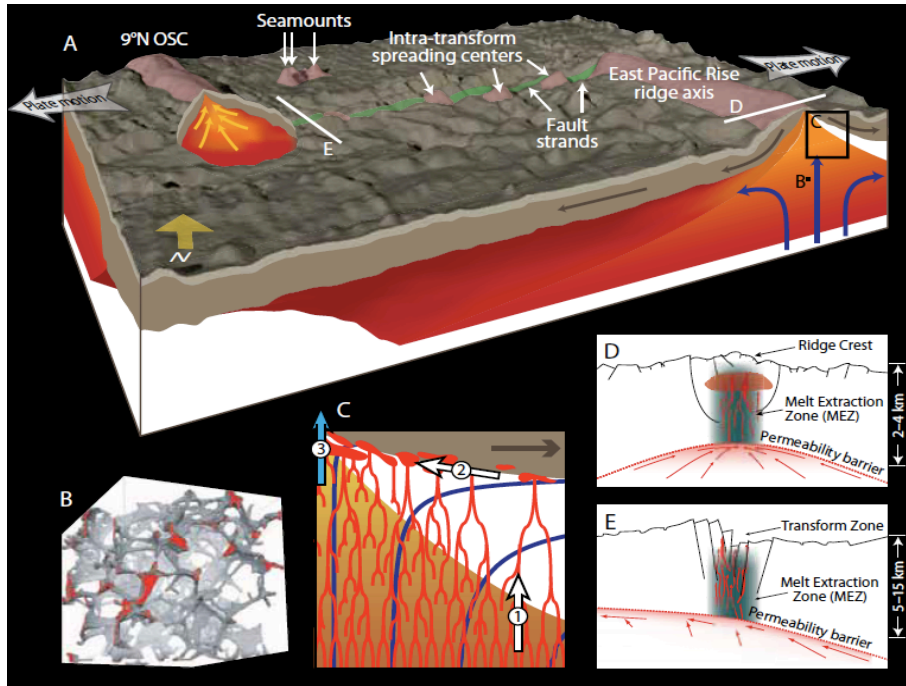
FIG. 1.2: Three-dimensional illustration of the melt region [Gregg et al., 2012] be-
neath the Siqueiros Transform Fault located at 8.5N on the East Pacific Rise (mantle
not to scale). Gray arrows show direction of plate motion, blue arrows stand for
mantle upwelling, and yellow arrows indicate melt focusing. (B) At depth beneath
the ridge, melt collects along grain boundaries and a porous flow through intercon-
nected network is initiated (three dimensional distribution of melt in a aggregate
of olivine and 5% basalt imaged using high-resolution synchrotron microtomogra-
phy; from Zhu et al., 2011). (C) Summary of the three steps of melt extraction:
(1) rapid, subvertical migration from the melting region, possibly in channels (red
lines), (2) accumulation and focusing along a permeability barrier along the base of
the lithospheric plate, and (3) extraction to the surface in a melt extraction zone
(MEZ, blue arrow) associated with faulting and the magma plumbing system of
the ridge axis and the transform domain. (D) and (E) represent schematically the
structures potentially present underneath the ridge (D) and the transform (E) with
black lines representing faults

1.2.1   Melt transport by channels

Flow through grain size scale melt networks is known as porous flow. A flow is called as channeled flow when the melt flows through a networks larger than the grain size. Melting of rock, developed by melt network along individual grains due to partial melting, is not the sole reason for melt localization. Brittle failure can be a reason for localization of melt into veins and dykes in the crust. But this mechanism is unlikely because of the pressure and temperature condition of upper mantle. There are three possible mechanisms behind the formation of channels: 1) Stress-driven melt segregation in the viscous regime 2) Reaction infiltration instability (RII) [Aharonov et al., 1995; Chadam et al., 1986; Ortoleva et al., 1987; Spiegelman et al., 2001] and 3) Freezing induced melt channels for compressible two phase flow [Spiegelman, 1993c].

Sleep [1988] shows how the melt is tapped in a pre existing vein and thus further veinlets occur. In the ductile regime, in a partially molten rock undergoing deformation, the reciprocal dependence of viscosity on melt fraction causes a dynamic instability which would localize melt to form melt veinlets [Richardson, 1998; Stevenson, 1989]. He shows that, the perturbations in shear stress translate into gradients in mean pressure which is responsible for driving melt from regions with lower melt fractions to regions with higher melt fractions. Thus a positive feedback system is set up such that the perturbations grow with continued deformation until melt is nearly completely extracted from the regions between melt-enriched layers. An analysis of two dimensional simple shear along with a linear stability analysis of band growth rate in a 2D shear flow is also proposed [Rabinowicz and Vigneresse, 2004; Spiegelman, 2003]. The porosity dependence of viscosity provides a nonlinearity to the problem which is required to initiate segregation in simple shear. Also, proportionality relation between deviatoric forces with the solid concentration is responsible for creating channels [Rabinowicz and Vigneresse, 2004].

Stress-dependence of the matrix viscosity, as introduced in Katz et al. [2006], leads to an additional feedback in the regions with elevated melt fraction.

In experimental studies of shear deformation of partially molten rocks [Holtzman et al., 2003; Holtzman and Kohlstedt, 2007], it is explained that how does melt segregate and self-organize into melt enriched bands driven by stress during deformation in the viscous regime. [Kohlstedt and Holtzman, 2009] focuses on melt transport in this viscous regime, giving emphasize on stress-driven alignment of melt at the grain scale and spontaneous segregation and organization of melt at a larger scale in deforming partially molten rocks.

Reaction infiltration instability(RII) is a mechanism due to which formation of finger-like structure takes place along an advancing reaction front when reactive flow occurs through a soluble porous matrix. This means, when unsaturated fluid flows through a soluble matrix, a region having porosity slightly higher than average will tend to have an increased influx of fluid. As a consequence, it will increase the rate of dissolution and and thus the porosity will be increased even further, in a positive feedback mechanism. Increased velocity in localized regions will cause lateral convergence of fluid upstream of the front into the high-porosity fingers [Ortoleva et al., 1987].

RII has been proposed as a mechanism for the localization of melt into channels in the upper mantle [Aharonov et al., 1995; Kelemen et al., 1995b]. To investigate the effect of melt/rock reaction on the mechanisms and kinetics of melt migration in mantle rocks and to test the hypothesis that reaction during melt migration could facilitate the transition from porous to channelized flow, a series of melt migration experiments was completed in which the melt was undersaturated in one of the mineral phases present in the infiltrated rock [Daines and Kohlstedt, 1994].

Geochemical and field evidence supports the fact that melt transport in some regions of the mantle is localized into mesoscale called 'chanels' which have widths of

0.1 - 100m or larger. One possible mechanism behind the formation of these chanels is the reaction infiltration instability (RII) [Aharonov et al., 1997]. It is proposed that dunites are originated as a result of dissolution channels [Daines and Kohlstedt, 1994; Kelemen et al., 1995b]. Since coupling of pyroxene dissolution and olivine precipitation increases liquid mass when temperature as well as enthalpy is constant [Daines and Kohlstedt, 1994; Kelemen et al., 1990], it follows that such reactions will increase magma mass and porosity under adiabatic conditions. Dissolution of pyroxene in olivine-saturated magma and porous flow of fluid through a partially soluble rock are analogous. Theoretical and experimental, both the studies show that the diffuse porous flow in these systems are unstable. Because initial perturbations in permeability lead to enhanced fluid flow, which in turn leads to more rapid dissolution. Thus, diffuse flow breaks is converted into focused porous flow through high porosity dissolution channels, elongate in the direction of fluid flow [Chadam et al., 1986; Daccord, 1987; Hoefner and Fogler, 1988] which is termed as the "reactive infiltration instability" (RII).

Orthopyroxene - free dunite dykes, veins, or irregularly shaped bodies often can be found in mantle sections of ophiolites . These dunites are residuals of those high porosity melt channels through which basaltic magmas generated in the deep mantle were extracted to the surface [Kelemen et al., 1997]. Therefore, due to dissolution of pyroxene and precipitation of olivine when olivine normative basalts percolate through a partially molten mantle, formation of dunite channels occurs [Aharonov et al., 1995; Daines and Kohlstedt, 1994; Hirschmann et al., 1999; Kelemen et al., 1995a,b; Morgan and Liang, 2003, 2005; Quick, 1981; Spiegelman et al., 2001]. Basaltic melts efficiently segregate through an interconnected coalescing network of high porosity orthopyroxene free dunite channels, from their source region preserving their geochemical signatures developed at depth [Braun and Kelemen, 2002; Kelemen et al., 1997; Korenaga and Kelemen, 2000]. The lower parts of a high porosity channel are made of harzburgite and lherzolite. Size and dimension of dunite channels, at the base of the melting column, depend on the amplitude of

lateral porosity variations and the depth where dunite channel initiates, depends on the melt flux entering the channel from below [Liang et al., 2010]. The dynamics and origin of melt conduits and pattern of these channels are discussed in detail in [Hart, 1993; Hesse et al., 2011; Hewitt, 2009].

Weatherley [2012] hypothesized in his thesis that Channelized reactive melt transport is a consequence of melting in compositionally heterogeneous mantle. In adiabatically upwelling mantle, heterogeneities enriched in recycled oceanic crust begin to melt at deeper depths than unaltered mantle peridotites. At slightly shallower depths, where the ambient mantle begins to melt, the enriched, partially molten heterogeneities will deliver an additional flux of magma to the background melting region. Chemical disequilibrium will exist between the partially melting peridotites and magma derived from the enriched heterogeneities. The disequilibrium will promote reactive melting and could lead to channel formation by a mechanism similar to the reaction infiltration instability. Furthermore, newly established and growing channels may coalesce with a pre-existing channel network, enabling magmas generated deep in the mantle to travel to the surface in chemical isolation.

For the compressible two phase flow, obstruction in melt flux causes solitary waves. At mid ocean ridge one of the major obstruction to the melt flow is a frozen and impermeable lid resulted by the spreading and cooling of plates. Melt percolates under gravity until it encounters the impermeable lid, develops some form of melt channel along the base of the sloping impermeable region and flows to the ridge axis through them [Sparks and Parmentier, 1991; Spiegelman, 1993c]. In this study matrix shear deformation is neglected because the matrix flow considered here, governs the thermal structure and therefore the shape of the freezing zone and as long as melt velocity is much greater than matrix velocity, approximation of a fixed freezing region without matrix shear is valid. When the freezing rate is large, the transition from high permeability background to impermeability occurs over a distance comparable to the compaction length. Then local influx of melt

becomes greater than the consumable amount of melt due to freezing. Therefore, the deformable matrix expands to accommodate the excess flux which leads to the growth of a high porosity channel near the freezing boundary at subsequent time. The compaction pressure induced by volume changes of viscous matrix, is significant when melt flux varies over the compaction length. But when freezing is distributed over many compaction lengths, it becomes negligible then. In that case, melt percolates vertically due to buoyancy alone and freezes into places without producing significant melt channels. When freezing zone is sufficiently narrow, high permeability melt channels which is able to transport time dependent melt flow along boundary are formed . These channels are not built in a single manner rather a rank ordered set of channels parallel to the boundary are formed and that gives an analogy with the dispersion of solitary wave. Therefore it is suggested that channeling may be an important mechanism for at least some of the lateral melt flow as well [Sparks and Parmentier, 1991; Spiegelman and Kenyon, 1992].

1.2.2   Melt transport through dykes

When molten rock is forced to flow or squeezed up to flow through vertical or near vertical crack in other rocks (viz. sedimentary rocks, folded metamorphic rocks or other igneous rocks) , the crack is forced to be separated. Then the molten rock cools in that space in such a way that a tabular igneous intrusion which cut across the surrounding rocks, is formed which is known as 'dyke'.

Veins are the places where the fluid pressure is low to obtain the amount of melt flowing into them and also as the space around which the pressure gradients can be expressed as a function of material properties. In other words, it can be said that deviatoric stress aids the growth of veins and due to having lower density the melt situated in large veins, can propagate upwards as dykes. A pressure gradient is necessary for melt to flow in relation to the solid and thus be able to segregate.

This pressure gradient may originate in three possible ways. One, the density contrast between melt and the average rock produces equivalent pressure gradient that causes melt to ascend vertically. Two, dynamic pressure gradients associated with broad-scale flow produced by the gradients of deviatoric stress drive porous flow. This mechanism is called as 'filter pressing' [Sleep, 1975]. When magma ascend towards the surface due to buoyancy, the segregation of the magma from solid mantle rock causes the matrix to compact under its own weight . Thus the third reason is, gradients in the amount of compaction can produce pressure gradients and drive porous flow. According to [Sleep, 1988], this occurs only when veins and dykes tap melt from the matrix. This process is also related to broad scale flow as veins grow when there are deviatoric stresses in the matrix. It has been considered a pre - existence of veins in a partially molten mush and obtained the criterion for lengthening the vein associated with broad scale deviatoric stress [Sleep, 1988]. Spacing of veins comparable to the compaction distance is needed to extract melt because each vein can tap melt only from within a compaction length [Ribe, 1987].

If the pressure in the vein is reduced below that of the surrounding pore space significantly, melt will flow into that vein. Large veins tap melt from small ones while they intersect as the fluid pressure is higher in small veins. The finite vertical extent of veins and the lower density of melt produce stresses which tend to cause them to propagate upward as dykes.

Field observations suggest that veins and dykes both are formed and grown in partially molten rock [Nicolas, 1986; Nicolas and Jackson, 1982]. Near the freezing boundary layers situated at the tops/within magma source region the initiation of dyke occurs as this is the place where excess magma pressures are supposed to be largest [Asimow et al., 1995; Kelemen et al., 1997; Kumarapeli et al., 1990]. Observational study on the chemistry of mid-ocean ridge basalts and associated residual peridotite insists that major portion of melt ascends without re-equilibrating with

the local host rock. Although rapid ascent in fractures could permit this dise-
quilibrium, a "reaction infiltration instability" occurs in which most of the melt
is captured by high-permeability dunite channels formed by pyroxene dissolution
[Kelemen et al., 1997]. This is an alternate mechanism for which direct field evidence
exists. It has been shown that if higher porosity leads to lower matrix viscosity,
the low melt pressure zones are the area where the tabular zones of high melt frac-
tion aligned perpendicular to the least compressive stress [Stevenson, 1989]. This
promotes the magma to flow through those regions where it has already been accu-
mulated and which can be an intermediate step prior to dyke initiation.
A schematic melt migration map has been shown in Fig.4.2. [Kohlstedt and Holtz-
man, 2009]. Melt migration mechanisms are dependent on driving forces which
causes the melt migration or melt segregation and deformation response of the rock
. Driving forces considered here are buoyancy force and shear stress and deformation
response indicates a rock to be brittle or viscous.
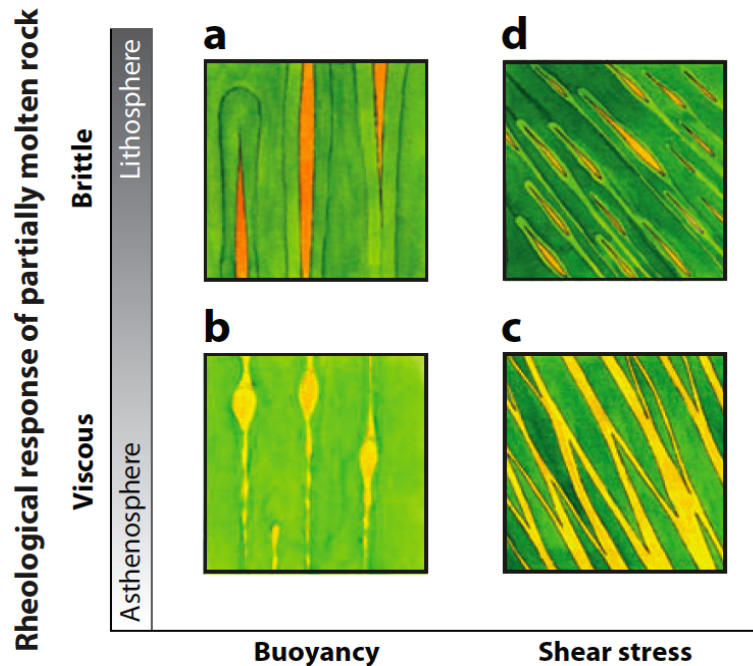
FIG. 1.3: a) Tensile dyke propagation in the brittle regime due to buoyancy driven
melt flow. b) Porous flow and porosity wave propagation in the viscous regime due
to buoyancy driven melt flow. c) Channel/vein formation in the viscous regime due
to stress driven melt migration. d) Sheared crack propagation in the brittle regime
due to stress driven melt flow.

Most of the melt flux in the asthenosphere occurs through dykes, based on observations of gabbro dykes in the mantle section of the Oman ophiolite [Nicolas, 1986]. Feasibility of fracture at high temperature and high confining pressure can be possible when a magma-filled dyke will attain a minimum volume in order to generate enough buoyancy force to penetrate the overlying rock and propagate upward [Sleep, 1988; Spence et al., 1987; Spence and Turcotte, 1985] which imposes a significant condition. Achieving the strength to make fracture in a rock mass is more easy at lower temperatures at which creep cannot relax tensile stresses at the tips of the crack. Therefore, dykes are more likely to form in the conductively cooling regions of the lithospheric mantle than in the hotter asthenosphere. Influence of a viscoelastic, porous matrix on propagation of hydro-fractures or magma-fractures through the middle ground between brittle and viscous end-member processes have also been discussed [Fowler Jr and Paterson, 1997; Rubin, 1993, 1998]

Time-dependent growth of buoyant dykes in partially molten poro - elastic source rock has been observed [Rubin, 1998]. When the ambient pore pressure exceed the least compressive stress, crack growth occurs in partial melt [Sleep, 1988; Stevenson, 1989]. Therefore, the melt pressure within the crack to be simultaneously less than the ambient pore pressures, so that melt flows into the crack. As a consequence, pressure inside the crack becomes greater than the least compressive stress which dilates the crack. Similarity solutions for laminar and turbulent fluid fracture have been proposed by [Emerman et al., 1986]. These solutions assume a constant rate of fluid flow into the crack. It shows that the flow resistance of the fluid is more significant than the fracture resistance of the solid for most geological problems. Ascent paths of magma-filled dykes under different stress conditions have been studied by [Kühn and Dahm, 2004] where effects of stress and pressure gradients, buoyancy and enclosed finite fluid mass have been considered.

1.2.3 Melt transport through porous media when the matrix is compacting: An introduction to two phase flow

The simultaneous flow of two immiscible fluids (phases) within common boundaries is known as two phase flow. Segregation of magma can be thought of consisting two processes. First, a partially molten rock will be generated and then the melt produced from the rock, must separate from the residual solid matrix. Such separation is only possible if there is a relative motion between the matrix and the melt which is the reason behind naming this melt segregation mechanism as two phase flow.

[Frank, 1968] first gave the idea that magma in partially molten region of earth could flow in a porous medium. This idea was further developed by [Sleep, 1975] who realized that the resulting problem was fundamentally one of two phase flow, involving the interacting motions of solid rock matrix and interstitial melt. [Ahern and Turcotte, 1979] provided simple but effective solution for the description of melting in upwelling regions. The basic dynamical phenomenon is that when melt is created, it will tend to rise through its own buoyancy.

These two phases namely matrix and melt both move with its own velocity . Mass of one phase can be transferred to another due to melting or freezing. We consider a continuum mechanics approach while setting up the mathematical formulations in order to build up the melt migration model, as size of the region of study is much larger than the characteristic grain/pore size in the two-phase mixture. The first geophysical models of two-phase flow was introduced in [Ahern and Turcotte, 1979; Sleep, 1975; Turcotte and Ahern, 1978]. [McKenzie, 1984] gave mathematical formulation for a general model of a partially molten rock which has later been used widely in modeling of partially molten zones and magma migration.

Although the mantle is said to be solid, the temperatures and pressures condition makes a large parts of it to deform by creeping in a viscous manner. This plastic portion of the mantle is known as asthenosphere which begins at around 100 km depth from the surface. The shallower parts of the mantle which is more rigid, together with the crust, is called as lithosphere. The melt present at the inter-granular areas, are expected to form an interconnected network, even at low porosity [McKenzie, 1984]. The melt is therefore able to move through the porous solid matrix. Being less dense, melt will rise buoyantly. Hence, the separation of melt from matrix causes matrix to compact in order to compensate the motion. Ascending melt may solidify when it reaches the base of the relatively cold lithosphere or it may continue its rise through out the lithosphere by flowing into conduits to reach a magma chamber or to erupt directly at the surface.

In this thesis, we have focussed on the region of melt migration where melt percolates through a viscously compacting porous matrix due to its buoyancy. Therefore, we have set up a melt migration model using two phase flow and porous flow through viscously compacting media framework using the formulation proposed by [Bercovici et al., 2001].

There are few differences between the formulations proposed by [McKenzie, 1984] and [Bercovici et al., 2001]. In other words, the later one is more generalized than the former according to some physical point of view namely, ratio of viscosities of the two phases is kept arbitrary so that one of the phases needs not to be much less viscous than the other all the time. This choice of viscosity values makes the set of equations invariant to the permutation of phases which is exploited in our model development. But, till now, our model assumes zero surface tension which leads to the fact that the viscosity of melt phase is much smaller than the viscosity of solid matrix. Surface tension is assumed to be negligible in [McKenzie, 1984] which is not in the formulations made by [Bercovici and Ricard, 2003; Bercovici et al., 2001]. According to rheology, in [McKenzie, 1984] the solid matrix is considered as

compressible fluid. The rheological relation of two phase flow system contains two constant viscosities (effective bulk viscosity and shear viscosity of the two phase flow system) which are functions of porosity in the later case. In [McKenzie, 1984], the liquid phase is considered as an incompressible fluid with negligible viscosity. In our model, we assume that both the phases i.e. melt and the matrix are incompressible. The presence of the interfacial area between these two phases and thus the surface energy or interfacial surface force is considered in [Bercovici et al., 2001] but was not considered in [McKenzie, 1984]. Due to inclusion of interfacial surface force, pressure difference (between two phase) term is non-zero even if surface tension is negligible (in our model) as long as the two-phase medium is deforming. Moreover, melting rate is a prescribed term in [McKenzie, 1984] whereas the similar is presented as a coupling term with the deformation process of the two-phase mixture. Although, melting or freezing is neglected in our model. In this way, it is possible for us to study the effect of the dynamical deformation on the phase change but we need to restrict our focus to a univariant phase change which is not the case in [McKenzie, 1984].

In this thesis, we show how a solitary wave profile has been obtained for a variable effective bulk and shear viscosity of the two phase medium considering the matrix as a compacting media [Richard et al., 2012]. Thus we benchmark our code and FD-CON (which is a finite difference code developed by Schmeling H.) in 1D by showing the shape preserving propagation of porosity wave with respect to time assuming the initial porosity wave profile as solitary wave. The justification of our work for future research in melt propagation theory are discussed subsequently.

1.2.3.1 Why compaction of matrix is considered?

Earlier [Goldschmidt, 1954] realized that fluid expulsion could only occur if the rock compacts and squeezes the pore fluid out. The compaction process of matrix is a form of deformation which is driven by the weight of the overlying rock. The

downward flow of the solid rock matrix due to gravity drives the flow of the less dense pore fluid upward. Compaction driven fluid flow is complex because it is inseparable from rock deformation and because the hydraulic properties which limit fluid flow through the rock matrix, such as permeability and porosity, are dynamic.

Magma can not penetrate the cold lithosphere via dyke propagation always. Sometimes the upwelling magma solidifies once it reaches the base of the lithosphere. When the source term is either zero or prescribed then the energy equation is neglected and hence these studies become as kinematic where the temperature has no role. Although, melting as a result of adiabatic decompression of matrix is included in [Scott and Stevenson, 1989], due to negligible compaction and heat conduction, temperature disappears from their model too. [Fowler, 1990a,b] consider two thermodynamic relations to set up the boundary condition. [Fowler, 1990b] assumes that partially molten medium responds to a heat imbalance almost instantaneously in such a way that the temperature is locally constant but the momentum flux is not i.e. the interfacial temperature is at local equilibrium when the stress field is not. This assumption underlies the inclusion of compaction in a large-scale model. A number of simple solutions to the equations show that, if the porosity is initially constant, matrix compaction only occurs within a distance $\sim \delta_c$ of an impermeable boundary [McKenzie, 1984]. It is shown that [Fowler, 1990a] due to imposition of thermal boundary layer, compaction occurs through whole partially molten region beyond the compaction length within which compaction is supposed to occur [McKenzie, 1984; Schmeling, 2000].

[Sparks and Parmentier, 1991] show that porous flow models which neglect compaction of the matrix result in vertical melt flow. This flow can not account for melt focussing at mid ocean ridge. Dilation, or decompactiom of the porous matrix creates a high-porosity boundary layer, beneath an impermeable cap of cooler, solid mantle. The thickness of the boundary layer (200-300 m) is determined by a balance between the buoyancy of the melt and the viscous stresses resisting decom-

paction. Layer thickness controlling parameters are respectively upwelling velocity, mantle viscosity and density difference between the melt and solid. This layer exists near the solidus where melt starts to freeze, and therefore deepens with distance from the ridge axis. The component of gravity along this boundary layer drives melt in this highly permeable layer toward the ridge axis.

1.2.3.2 Why inclusion of variable bulk and shear viscosities of two phase medium is important?

Scott and Stevenson [1986a]s study of 2D compaction waves has been extended to the case of a mush with a viscosity strongly dependent on melt concentration [Khodakovskii et al., 1998]. They find that the solitary-wave behavior of porosity wave is similar to the one obtained in constant viscosity cases, where the 2D-cylindrical waves always form due to occurrence of instability in well developed 1D solitary waves. From their study it can be concluded that the growth rate of both 1D- and 2Dwaves is roughly one order of magnitude faster than the growth rate in a similar case with a constant viscosity [Richard et al., 2012]. Also, it is observed that the length of the waves decreases strongly at the time of viscosity drop occurs because of a narrower melt increment [Richard et al., 2012].

1.2.3.3 Geophysical importance of solitary wave

2D numerical calculations show that solitary wave disturbances can propagate along thermal plumes in a homogeneous, viscous fluid with a thermally activated rheology similar to the mantle [Bercovici et al., 1989]. Two-phase or two - fluid model can be applied to solitary waves in the thermally activated plume. Therefore, a two-fluid model of solitary waves on cylindrical conduits is applied to mantle plumes in order to estimate the propagation speeds, time durations, and pulse lengths of solitary waves as a function of background mantle viscosity, plume flux, plume density deficit, plume viscosity, and the volume of material transported by the

solitary wave. It can be concluded that mantle plumes may be episodic via solitary waves and these disturbances might be helpful to explain the observed variations in the durations of episodes of enhanced hotspot volcanic activity (10 m.a) . Solitary waves in mantle plumes could be generated due to various reasons like interactions among plumes or between plumes or due to the large-scale, time-dependent mantle circulation.

Also, the ability of the two-dimensional solitary waves to drive matrix convection has been discussed in [Richter and Daly, 1989; Scott and Stevenson, 1989].

Fluid, having lower density and viscosity, can rise buoyantly through a viscous fluid through conduits that support simple pipe flow. The conduits also support solitary waves which shows near soliton behavior. Results obtained from laboratory experiments on the characteristics of solitary waves and their interactions have been compared with theory and it shows good agreement with theoretical predictions [Whitehead and Helfrich, 1991]. Large amplitude waves travels slightly faster than their theoretical prediction because of higher order effects associated with wave slope and it was not considered in theory. It is also confirmed both theoretically and practically that the solitary waves have closed streamlines in a frame moving with the wave. Thus transport of isolated packets of fluid over large distances is possible. i.e. the solitary waves convey isolated pockets of conduit material with them as they propagate.

A steady state source of an intrusive buoyant and low viscosity fluid at the bottom of a more viscous external fluid results in the formation of a uniform conduit supporting simple pipe flow when the Reynolds number is small [Whitehead and Luther, 1975]. The buoyancy of the intrusive fluid is balanced by shear stress. If the source is unsteady it has been shown that these conduits then support solitary waves [Olson and Christensen, 1986; Scott and Stevenson, 1986a].

A model for channels of magma flow within mantle undergoing decompression melt-

ing is studied [Hewitt, 2009]. Existence of cylindrical conduits in a viscous, porous, compacting matrix are considered. The dynamics of the conduit walls are governed by the competition between melting (caused by decompression) and viscous closure (caused by the reduced pressure in the conduit).

It is not known that whether such open melt channels exist in the mantle or not. Mechanisms which can produce such open conduits are like fracturing of the partially molten matrix [Nicolas, 1986], and mechanical or reactive instabilities to the flow [Aharonov et al., 1995; Spiegelman et al., 2001; Stevenson, 1989]. Therefore, the existence of such open conduits is possible as the mechanisms to produce them are there in the ascending mantle. Ascent velocities of melt through the conduit are predicted to be on the order of 100 meter per year. Flow from the surrounding porous partially molten matrix into the low-pressure channel is considered as a continual source of melt. The accumulation region is on the order of the compaction length and the porosity of residual matrix is reduced to be very low, typically $< 0.5\%$. Channels can also form naturally from porous flow in the matrix because of the enhanced melting rate in regions of higher porosity, having a larger heat flux from below. The vast majority of melt is expected to flow eventually into one of these channels, which therefore offer a possible physical explanation of near-fractional melting models used in field observations.

From several papers by [Michaut et al., 2009, 2013] another aspect of solitary wave in geophysics is found but it is in the field of two phase flow of magma which consists of the phase liquid melt and the gas incorporated in it. Gas segregation from magma is similar to the process of melt segregation through porous and viscously compacting matrix. In general, compaction expels lighter fluid from a mixture in the form of buoyant pulses or solitary waves with higher fluid content; It is shown that the rapid decompression of the magma column below a pre-existing plug are caused by, for example, dome collapse [Michaut et al., 2009]. This leads to volatile exsolution which induces a gas pulse [Lensky et al., 2008] and that potentially rises through the

degassed magma as a solitary wave [Michaut et al., 2009]. Similar results have been shown for the propagation of melt through solid matrix in [Barcilon and Lovera, 1989; Scott and Stevenson, 1986b; Spiegelman, 1993a,b].

In the subsequent chapters the theoretical background for setting up our code, detail about obtaining the solitary wave profile and using the profile to benchmark our code and results obtained by using a new viscosity formulation [Schmeling et al., 2012] in FDCON will be discussed.

Chapter 2

Mathematical Background and Set Up of Code PERCOL2D

The dynamics of multicomponent flow is a well studied field [Bear, 2013; Birchwood and Turcotte, 1994; Dake, 1983; Drew, 1983; Drew and Passman, 1999; Dullien, 1991]. In order to develop our model we follow a theoretical framework on two phase flow mixture where each phase (solid matrix phase and melt phase) is distinguishable from each other having nonzero interfacial areas, whereas, their mixture represents a single flow model having a variable phasic composition [Drew, 1983; Wang and Beckermann, 1993].

2.1 Governing Equations

The basic framework of governing equations are based on [McKenzie, 1984]. In order to use our code in future for investigating the general phenomena like the process of microcracking and damage of matrix due to compaction with or without considering the effect of surface tension, we use the modified and generalized formulations of two phase flow as proposed by [Bercovici et al., 2001].

We set up our code (PERCOL2D) using these formulations to get porosity (i.e. melt fraction) profile, velocity profile of fluid and matrix. The set of governing equations, which we use to describe the two phase system of matrix and melt are listed below:

1) Matrix mass conservation

$$\frac{\partial(1-\phi)}{\partial t} = -\nabla.(1-\phi)V_m - \frac{\dot{\Gamma}}{\rho_m} \tag{2.1.1}$$

2) Fluid mass conservation

$$\frac{\partial \phi}{\partial t} = -\nabla.\phi V_f + \frac{\dot{\Gamma}}{\rho_f} \tag{2.1.2}$$

3) Fluid momentum conservation equation

$$\frac{\eta_f \phi}{k(\phi)}\delta v + \rho_f \mathbf{g} - \nabla P_f = 0 \tag{2.1.3}$$

4) Matrix momentum conservation equation

$$(1-\phi)\rho_m \mathbf{g} - (1-\phi)\nabla P_m + \nabla.[(1-\phi)\bar{\bar{\tau}}_m] - \eta_f \frac{\phi^2}{k(\phi)}\delta v + \delta P \nabla \phi = 0 \tag{2.1.4}$$

and

5) The rheological equation

$$\frac{\partial \phi}{\partial t} + V_m \cdot \nabla \phi = -\phi(1-\phi)K\frac{\delta P}{\eta_m + \eta_f} \tag{2.1.5}$$

where Γ is the source term, $\bar{\bar{\tau}}_m = \eta_m(\nabla V_m + \nabla V_m{}^t - \frac{2}{3}\nabla V_m \bar{\bar{I}})$ is deviatoric stress tensor and $\bar{\bar{I}}$ is identity matrix . ϕ is the porosity of the matrix, t denotes the time and $\delta x = x_m - x_f$, where x_m and x_f are the properties of matrix and fluid respectively. V_i, P_i, ρ_i and η_i are velocity, pressure, density and viscosity of phase i and i = m or f denoting the matrix and fluid phase respectively. K is the geometric factor and is assumed to be equal to 1. The definition $\bar{x} = \phi x_f + (1-\phi)x_m$, where x_m and x_f are the properties of matrix and fluid respectively.

2.1.1   Assumptions

To begin with we have made the following assumptions and we plan to remove the assumptions step by step in future

- At present we assume that, source term or the term, which denotes rate of dehydration (melting) equals to zero. i.e. $\Gamma = 0$

- Viscosity of fluid is negligibly smaller than viscosity of matrix. i.e. $\eta_f << \eta_m$

- The permeability is $k(\phi) = k_0\phi^2$ where the permeability constant is k_0(i.e. in the definition $k(\phi) = k_0\phi^n$, we assume n=2). i.e. we assume that the model contains an ideal melt network in which grains are of uniform size and the melt resides at the triple junction point.

- We also consider preliminarily that the surface tension is zero (the momentum conservation equations of matrix and melt are written assuming this simplification). So, the formulations are same as of [McKenzie, 1984] with the assumption that porosity dependent shear viscosity of the matrix is identical to intrinsic matrix shear viscosity and the same for the case of porosity dependent bulk viscosity.

2.2   Mathematical Formulation of Two Phase Flow Problem

2.2.1   Darcy Law

Darcy's law (named after Henry Darcy, a French hydraulic engineer who conducted an experiment to determine water flow rate through a sand filter), is a generalized relationship between volumetric flow rate and pressure for flow in porous media. Since, in our model we concentrate on the dynamics of two phase flow through a porous medium, this law helps us to understand the fundamental concept behind the fluid mass conservation equation. In this section we show that how the mass conservation equation for fluid can be derived with the help of Darcy's law. This

law says that, u which is the volumetric flow rate per unit area , is proportional to the gradient of Hydraulic head H.

i.e. $u \propto \nabla H$

$\Rightarrow$

$$u = -K\nabla H \tag{2.2.1}$$

where $K \equiv \frac{k(\phi)\rho g}{\mu}$.

Here $k(\phi)$ is the permeability function of the medium, ϕ is the volume fraction, ρ is density of the fluid , μ is the dynamic viscosity of the fluid and g is the constant of gravitational acceleration.

It can be proved that [Hubbert, 1940], $H.g$ is the total energy of a fluid packet of unit mass.

According to cf. Fig. 2.1, the total energy of a fluid packet

= Kinetic energy required to accelerate the velocity say from v_2 to v_1 + Energy required to raise fluid packet from elevation z_2 to z_1 + Energy required to raise fluid pressure from P_2 to P_1.
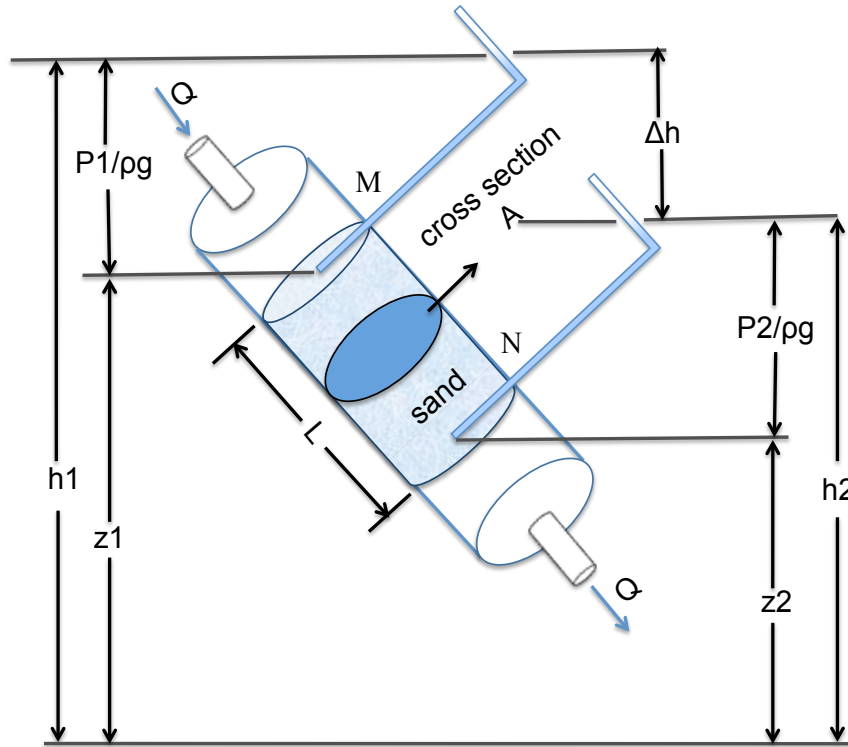
FIG. 2.1: This figure summarizes the experiment conducted by Henry Darcy in order to determine the volumetric flow rate of water through the sand filter where Q represents the flux of the water

Now kinetic energy $= m \int_{v_2}^{v_1} v \, dv = \frac{1}{2} m v^2$, where m is the mass of the fluid packet.

Energy required to elevate height of the fluid level $= mg \int_{z_2}^{z_1} dz = mgz$

At point M, volume per unit area in the outlet $= \frac{P_1}{\rho g}$

At point N, volume per unit area in the outlet $= \frac{P_2}{\rho g}$. Now at point M, work done to elevate the fluid level to h_1 in the outlet $= -P_1 \times \frac{P_1}{\rho g}$

The work done for the fluid to come at point N and to raise its height in the outlet at $h_2 = \int_{P_2/\rho g}^{P_1/\rho g} P.dV + P_2 \times \frac{P_2}{\rho g}$

$\therefore$ Total energy required for the fluid to come from the outlet connected to the cylindrical tube at point M to the outlet connected at the point N

$= \int_{P_2/\rho g}^{P_1/\rho g} P dV + P_2 \times \frac{P_2}{\rho g} - P_1 \times \frac{P_1}{\rho g}$, where V is the volume of the fluid per unit mass.

Now, $d(PV) = PdV + VdP$

$\therefore \int_{P_2^2/\rho g}^{P_1^2/\rho g} d(PV) = \int_{P_2/\rho g}^{P_1/\rho g} P dV + \int_{P_2}^{P_1} V dP$

Hence, $\int_{P_2/\rho g}^{P_1/\rho g} P dV = \frac{P_1^2}{\rho g} - \frac{P_2^2}{\rho g} - \int_{P_2}^{P_1} V dP$

Therefore, the total energy required for the fluid to come from the outlet connected to the cylindrical tube at point M to the outlet connected at the point N

$= \frac{P_1^2}{\rho g} - \frac{P_2^2}{\rho g} - \int_{P_2}^{P_1} V dP + P_2 \times \frac{P_2}{\rho g} - P_1 \times \frac{P_1}{\rho g}$

$= \int_{P_1}^{P_2} V dP$

$= m \int_{P_2}^{P_1} \frac{V}{m} dP$,

$= m \int_{P_2}^{P_1} \frac{1}{\rho} dP$, where ρ is the density of the fluid.

$= \frac{mP}{\rho}$

Therefore, the total energy of a fluid packet per unit mass $= \frac{v^2}{2} + gz + \frac{P}{\rho}$

i.e. $H.g = \frac{v^2}{2} + gz + \frac{P}{\rho}$

Since for flow in porous media, v is too small,

$\therefore H.g = gz + \frac{P}{\rho}$

$\Rightarrow$

$$H = z + \frac{P}{\rho g} \tag{2.2.2}$$

$\therefore$ for horizontal flow, from eq. 2.2.1 and eq. 2.2.2 we get,

$$u = -\frac{k(\phi)}{\mu} \frac{\partial P}{\partial x}$$

Also, for vertical flow, from eq. 2.2.1 and eq. 2.2.2 we get,

$$u = -\frac{k(\phi)}{\mu} \left[\frac{\partial P}{\partial z} + \rho g\right]$$

Now, if ϕ is the volume fraction, η_f is the fluid viscosity, ρ_f is the fluid's density, P_f is the pressure of the fluid and V_m, V_f are the velocities of matrix and fluid respectively then $u \equiv -\phi \delta v$ and therefore,

$\phi \delta v = \frac{k(\phi)}{\eta_f} \left[\frac{\partial P}{\partial z} + \rho_f g\right]$, where $\delta v = V_m - V_f$

Taking the r.h.s into l.h.s we get,

$$\frac{\eta_f \phi}{k(\phi)} \delta v + \rho_f \mathbf{g} - \nabla P_f = 0$$

where $\mathbf{g} = -gz$ and thus we get eq. 2.1.3

2.2.2   Potential Formulation

In order to make future simplification of the governing equations, we use the potential formulation. The gravity is a potential field and so,

$$\mathbf{g} = -g\mathbf{z} = -\nabla U \tag{2.2.3}$$

Therefore, if we define $\theta = \frac{k_0}{\eta_f}(P_f + \rho_f U)$, $\frac{\delta v}{\phi}$ is also a potential field as

$$\frac{\delta v}{\phi} = \nabla\theta \tag{2.2.4}$$

by eq.(2.1.3). Therefore, clearly, $\nabla\theta$ can be regarded as the differential flux between matrix and fluid velocity.

2.2.3 Helmholtz Decomposition

According to Helmholtz Decomposition Theorem, every smooth vector field u can be decomposed into a rotational part and an irrotational part when u and its derivative are well defined in space and vanish at infinity [Joseph, 2006].

Since, $\bar{v}$ and its derivative are well defined in space and vanish at infinity, we can use Helmholtz decomposition theorem for a vector field in order to decompose $\bar{v}$ and can write it as,

$$\bar{v} = \phi V_f + (1 - \phi)V_m = \nabla \times \mathbf{\Psi} + \phi^2 \nabla(\xi - \theta) \tag{2.2.5}$$

Where $\mathbf{\Psi} = \psi(x, z)\mathbf{y}$, denotes the stream function in 2D and $\nabla\xi$ is the flux related to the matrix compaction

2.3 Derivations of equations to solve the key variables

It is possible to directly solve the set of governing equations in order to get the desired outcome. But, we use potential formulation, Helmholtz formulations and make the following derivations so that we can use comparatively simpler solvers in

our code.

Solving eq. 2.2.4 and eq. 2.2.5 we obtain,

$$V_m = \nabla \times \boldsymbol{\Psi} + \phi^2 \nabla \xi \qquad (2.3.1)$$

and

$$V_f = V_m - \phi \nabla \theta \qquad (2.3.2)$$

With the help of some algebras (involving eq.(2.2.3), eq.(2.2.4) and eq.(2.2.5), the matrix momentum conservation equation (2.1.4), can be recast as :

$$\nabla[(k_0 - \frac{2}{3}\phi)\frac{(1-\phi)\eta_m}{\phi}\nabla \cdot \phi^2\nabla\xi] - (1-\phi)\delta\rho\nabla U$$
$$+ \nabla \cdot (1-\phi)\eta_m[\nabla(\nabla \times \boldsymbol{\Psi} + \phi^2\nabla\xi) + \nabla(\nabla \times \boldsymbol{\Psi} + \phi^2\nabla\xi)^t] - \frac{\eta_f}{k_0}\nabla\theta = 0 \quad (2.3.3)$$

For the sake of simplicity[1], we take the curl of this expression and a weighted divergence, $\nabla \cdot [\phi^2(2.3.3)]$. So in 2D geometry ($\boldsymbol{\Psi} = \psi(x,z)\mathbf{y}$) the momentum conservation yields to a couple of scalar equations:

$$G[(1-\phi)G\psi] + 4\frac{\partial^2}{\partial x \partial z}[(1-\phi)\frac{\partial^2\psi}{\partial x \partial z}] = \frac{\delta\rho g}{\eta_m}\frac{\partial\phi}{\partial x}$$
$$+ G[(1-\phi)(\frac{\partial(\phi^2\frac{\partial\xi}{\partial z})}{\partial x} + \frac{\partial(\phi^2\frac{\partial\xi}{\partial x})}{\partial z})] - 2\frac{\partial^2}{\partial x \partial z}[(1-\phi)(\frac{\partial(\phi^2\frac{\partial\xi}{\partial x})}{\partial x} - \frac{\partial(\phi^2\frac{\partial\xi}{\partial z})}{\partial z})] \quad (2.3.4)$$

---

[1] $\nabla \times \nabla \cdot \mathbf{X} = 0$

$$
(\frac{\partial \phi^2 \frac{\partial}{\partial z}}{\partial x} + \frac{\partial \phi^2 \frac{\partial}{\partial x}}{\partial z})[(1 - \phi)(\frac{\partial \phi^2 \frac{\partial \xi}{\partial z}}{\partial x} + \frac{\partial \phi^2 \frac{\partial \xi}{\partial x}}{\partial z})]
$$

$$
+ 2\left(\frac{\partial}{\partial x}[\phi^2 \frac{\partial}{\partial x}((1 - \phi)\frac{\partial \phi^2 \frac{\partial \xi}{\partial x}}{\partial x})] + \frac{\partial}{\partial z}[\phi^2 \frac{\partial}{\partial z}((1 - \phi)\frac{\partial \phi^2 \frac{\partial \xi}{\partial z}}{\partial z})] \right)
$$

$$
+ \frac{\partial}{\partial x}[\phi^2 \frac{\partial}{\partial x}(C(\frac{\partial \phi^2 \frac{\partial \xi}{\partial x}}{\partial x} + \frac{\partial \phi^2 \frac{\partial \xi}{\partial z}}{\partial z}) - \frac{\eta_f}{\eta_m k_0}\xi)]
$$

$$
+ \frac{\partial}{\partial z}[\phi^2 \frac{\partial}{\partial z}(C(\frac{\partial \phi^2 \frac{\partial \xi}{\partial z}}{\partial z} + \frac{\partial \phi^2 \frac{\partial \xi}{\partial x}}{\partial x}) - \frac{\eta_f}{\eta_m k_0}\xi)]
$$

$$
= \frac{\delta \rho g}{\eta_m} \frac{\partial \phi^2 (1 - \phi)}{\partial z} - \frac{\eta_f}{\eta_m k_0} \frac{\delta \rho}{\rho_m \rho_f} \dot{\Gamma}
$$

$$
- \left(\frac{\partial \phi^2 \frac{\partial}{\partial x}}{\partial z} + \frac{\partial \phi^2 \frac{\partial}{\partial z}}{\partial x} \right) [(1 - \phi)G\psi]
$$

$$
- 2(\frac{\partial \phi^2 \frac{\partial}{\partial z}}{\partial z} - \frac{\partial \phi^2 \frac{\partial}{\partial x}}{\partial x})[(1 - \phi)\frac{\partial^2 \psi}{\partial x \partial z}] \quad (2.3.5)
$$

where $G = \frac{\partial^2}{\partial x^2} - \frac{\partial^2}{\partial z^2}$ and $C = (\frac{K}{\phi} - \frac{2}{3})(1 - \phi)$

We also can derive a mixture mass conservation equation from eq.(2.1.1) and eq.(2.1.2), which is :

$$
\nabla \cdot \bar{\mathbf{v}} = \frac{\delta \rho}{\rho_m \rho_f} \dot{\Gamma} \tag{2.3.6}
$$

Using equation (2.2.5) we have,

$$
\nabla \cdot \phi^2 \nabla(\xi - \theta) = \frac{\delta \rho}{\rho_m \rho_f} \dot{\Gamma} \tag{2.3.7}
$$

Now we solve V_m and V_f using equations (2.2.4) and (2.2.5) and then replace V_m in matrix mass conservation equation (2.1.1). Thus we get,

$$
\frac{\partial \phi}{\partial t} = \nabla \cdot (1 - \phi)(\nabla \times \psi \mathbf{y} + \phi^2 \nabla \xi) + \frac{\dot{\Gamma}}{\rho_m} \tag{2.3.8}
$$

Therefore, we solve the four unknowns of this system of equations ϕ the porosity, ψ the magnitude of stream function, $\nabla \xi$ the flux related to the matrix compaction and $\nabla \theta$ the differential flux between the matrix and fluid from equations (2.3.8),

(2.3.4), (2.3.5) and (2.3.7) respectively.

2.3.1   Set up of PERCOL2D

We follow several algorithms in the code and to do that we take help of different numerical schemes:

MPDATA (Multidimensional Positive Definite Advection Transport Algorithm) [Smolarkiewicz and Margolin, 1998] is an advection algorithm and which merges the flux corrected transport methodology with its iterative formalism. We solve the advective equation of porosity (2.3.8) by this method. This corresponds to box 4 into the flowchart (cf. Figure 2.1).

First we implemented SOR (successive over Relaxation) which is an algorithm to solve linear system of equation in a more efficient way than Gauss-Seidel iterative method. We use it to solve for the parameters θ, ψ and ξ from (2.3.7), (2.3.4) and (2.3.5) by this method. This corresponds to the diamond shaped box between box 2 and 3 into the flowchart (cf. Figure 2.1). Later we have changed this scheme into a direct solver method in order to improve the runtime of our program.

We use Finite Difference scheme to solve velocity of fluid and matrix and the source term i.e. V_m , V_f (correspond to box between box number 3 and 4 in Figure 2.1) and Γ respectively.

It must be noted that, this code is fully dimensional. i.e. all the velocity variables have unit ms^{-1}. The stream function have unit m^2s^{-1}. The variables ξ and θ have unit m^2s^{-1}. Pressure term has unit Pa and the source term has the unit $kgm^{-3}s^{-1}$. Units of k_0 and viscosities are m^2 and $Pa.s$ respectively.

Flow chart (cf. Fig 2.2) of our model is given as a further reference.
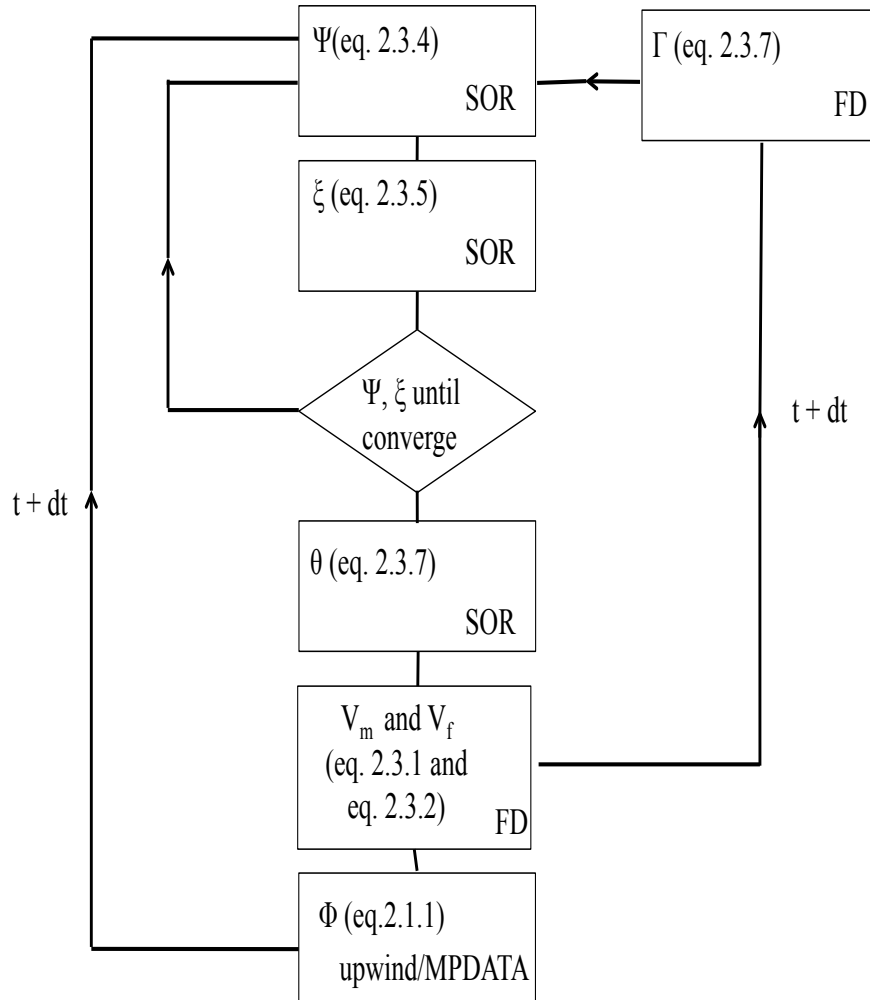
Fig. 2.2: Flow chart (1D) of our model

We use a staggered grid settings (cf. Fig. 2.3) in our code in order to get the solution. The detail description of the numerical solver and the numerical experiments with the code in 1D will be discussed in the next chapter.
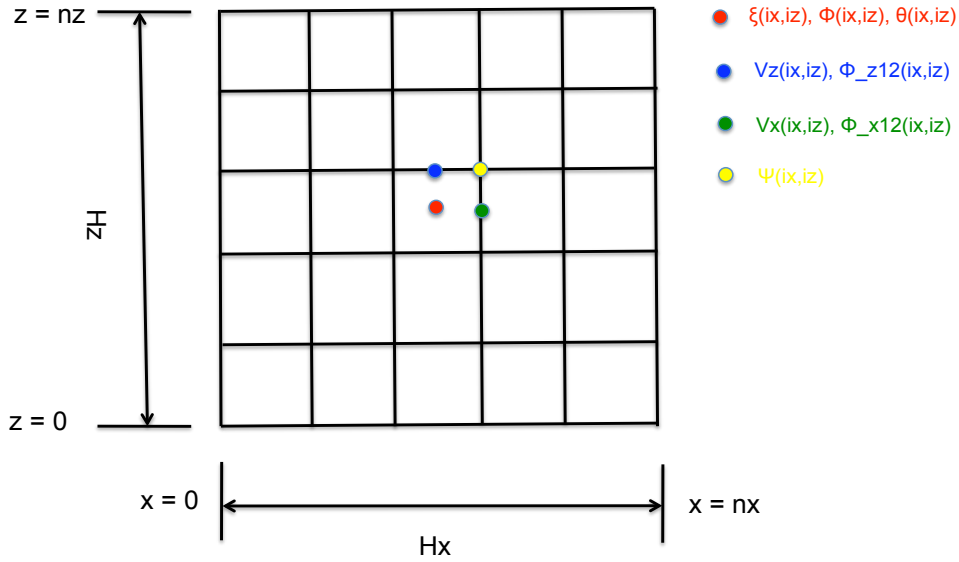
FIG. 2.3: The variables' (ix,iz) position on the grid corresponds to the color. Here $\phi\_z12(ix, iz)$ and $\phi\_x12(ix, iz)$ denote the arithmetic mean of ϕ along x and z direction respectively, Hz is the hight of the model box, Hx is the width of the model box and nx, nz are the number of grid points along x and z direction respectively.

Chapter 3

Numerical Approach

3.1 Implication of Block Successive Over Relaxation Method (BSOR) for a Biharmonic Equation

The governing equations and the derived equations from the governing equations which we are using to determine the variables like porosity, fluid and solid viscosity etc. at each time step are already stated in chapter 2. Now, the numerical detail of those calculations will be presented in this chapter.

Initially during 1D experiments of the code, the numerical scheme called block successive over relaxation (BSOR) [Ehrlich, 1971] method was used to determine several variables like stream function ψ, the variable ξ which measures the flux due to matrix compaction and the differential flux between matrix and fluid i.e. θ, using the equations 2.3.4, 2.3.5 and 2.3.3 respectively. The advantage of using the iterative scheme BSOR is that it is faster than any other iterative method like Chebyshev accelerated Jacobi iteration method, Gauss-Seidel method, cyclic Chebyshev semi-iteration method and the unsymmetric modified SOR method [Ehrlich, 1972].

3.1.1 Formation of matrix

We apply BSOR to the foresaid equations in 3 steps:

1) We first discretize the equations maintaining the variables' position at (i, j)th grid of our model (Fig.2.3) where i can take any value from 1 to nx (i.e. total number of grid points in horizontal or x direction) and j can take any value from 1 to nz (i.e. total number of grid points in vertical or z direction)

2) Then we re-write the discretized equation in the form $\Sigma p_{ij} y_{ij} = q_{ij}$.

3) Since, the equations 2.3.4, 2.3.5 and 2.3.3 have a bi-harmonic or fourth order elliptic form, for a particular i and j, the equation should contain the variables at {i-2, j}, {i-1, j-1}, {i-1, j}, {i-1, j+1}, {i, j-2}, {i, j-1}, {i, j}, {i, j+1}, {i, j+2}, {i+1, j-1}, {i+1, j}, {i+1, j+1} and {i+2, j} th position of the grid respectively. In this step we rename the coefficients (i.e. p_{ij}) of y_{ij} as described in step 2, according to these positions as $a_{ij}, b_{ij}, c_{ij}, d_{ij}, e_{ij}, f_{ij}, g_{ij}, h_{ij}, i_{ij}, j_{ij}, k_{ij}, l_{ij}, m_{ij}$ respectively. The stencil diagram which demonstrates this step, is shown in Fig.3.1.
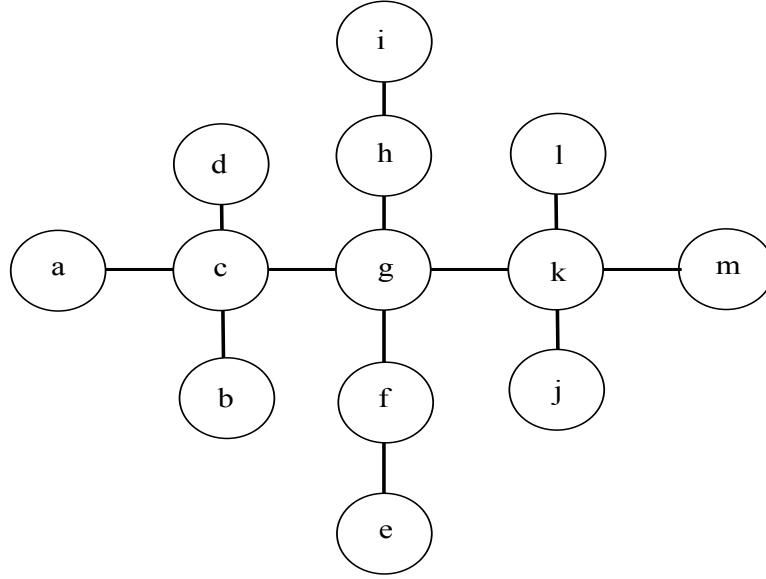
FIG. 3.1: The coefficients position according to the variables' position on the grid for a given i and j value.

For example, if we take the first term of equation 2.3.5, then the term is $\{\frac{\partial}{\partial x}(\phi^2\frac{\partial}{\partial z})\}\frac{\partial}{\partial x}(\phi^2\frac{\partial \xi}{\partial z})$. We discretize this term by finite difference method assuming the variable's position at (i, j) which means the variable is positioning at the intersection point of i-th x grid and j-th z grid. Then,

$$
\begin{aligned}
\{\frac{\partial}{\partial x}&(\phi^2\frac{\partial}{\partial z})\}\frac{\partial}{\partial x}(\phi^2\frac{\partial \xi}{\partial z}) \\
= [\phi^2{\_}x12_{i,j}&\{\phi^2{\_}z12_{i+1,j}(\xi_{i+1,j+1} - \xi_{i+1,j}) - \phi^2{\_}z12_{i,j}(\xi_{i,j+1} - \xi_{i,j}) - \phi^2{\_}z12_{i+1,j-1} \\
(\xi_{i+1,j} - \xi_{i+1,j-1})& + \phi^2{\_}z12_{i,j-1}(\xi_{i,j} - \xi_{i,j-1})\} - \phi^2{\_}x12_{i-1,j}\{\phi^2{\_}z12_{i,j}(\xi_{i,j+1} - \xi_{i,j}) \\
&- \phi^2{\_}z12_{i-1,j}(\xi_{i-1,j+1} - \xi_{i-1,j}) - \phi^2{\_}z12_{i,j-1}(\xi_{i,j} - \xi_{i,j-1}) \\
&\qquad + \phi^2{\_}z12_{i-1,j-1}(\xi_{i-1,j} - \xi_{i-1,j-1})\}]dx^{-2}dz^{-2} \quad (3.1.1)
\end{aligned}
$$

According to fig.2.3 the variables $\phi{\_}x12_{i,j}$ and $\phi{\_}z12_{i,j}$ in eq.3.1.1 are arithmetic mean of ϕ along horizontal and vertical direction respectively. The variables' position is maintained in a fashion that the whole term on which the differentiation is operated, is taken at the same position. i.e. for this example, $\frac{\partial}{\partial x}$ is operated on

$\{\phi^2\frac{\partial}{\partial z}\}\frac{\partial}{\partial x}(\phi^2\frac{\partial\xi}{\partial z})\}$. Therefore, $\{\phi^2\frac{\partial}{\partial z}\}\frac{\partial}{\partial x}(\phi^2\frac{\partial\xi}{\partial z})\}$ should be positioned at the same position on x, z grid system of our model. Again this term can be split into ϕ^2 and $\frac{\partial}{\partial z}\frac{\partial}{\partial x}(\phi^2\frac{\partial\xi}{\partial z})$. Therefore, both ϕ^2 and $\frac{\partial}{\partial z}\frac{\partial}{\partial x}(\phi^2\frac{\partial\xi}{\partial z})$ should be discretized in such a way that they both maintain the same position and for this reason, while discretizing these terms, instead of taking ϕ in the discretized formulation, we consider the variable ϕ_x12 or ϕ_z12 in the formulation.

After writing the discretized form we follow step 2 as described before and re write r.h.s of equation 3.1.1 as $\Sigma p_{ij}y_{ij}$, where y_{ij} is $\xi_{i,j}$:

$$[\xi_{i+1,j+1}\phi^2\_z12_{i+1,j}\phi^2\_x12_{i,j} - \xi_{i+1,j}\phi^2\_x12_{i,j}(\phi^2\_z12_{i+1,j} + \phi^2\_z12_{i+1,j-1})$$
$$-\xi_{i,j+1}\phi^2\_z12_{i,j}(\phi^2\_x12_{i,j}+\phi^2\_x12_{i-1,j})+\xi_{i,j}(\phi^2\_x12_{i,j}+\phi^2\_x12_{i-1,j})(\phi^2\_z12_{i,j}+\phi^2\_z12_{i,j-1})$$
$$+ \xi_{i+1,j-1}\phi^2\_z12_{i+1,j-1}\phi^2\_x12_{i,j} - \xi_{i,j-1}\phi^2\_z12_{i,j-1}(\phi^2\_x12_{i,j} + \phi^2\_x12_{i-1,j})$$
$$+ \xi_{i-1,j+1}\phi^2\_z12_{i-1,j}\phi^2\_x12_{i-1,j} - \xi_{i-1,j}\phi^2\_x12_{i-1,j}(\phi^2\_z12_{i-1,j} + \phi^2\_z12_{i-1,j-1})$$
$$+ \xi_{i-1,j-1}\phi^2\_z12_{i-1,j-1}\phi^2\_x12_{i-1,j}]dx^{-2}dz^{-2} \quad (3.1.2)$$

Therefore, according to step 3, we rewrite the r.h.s of equation 3.1.1 over bracing the terms which have partial contribution in constructing the coefficients as described in Fig. 3.1.

$$[\overbrace{\phi^2\_z12_{i+1,j}\phi^2\_x12_{i,j}}^{l}\,\xi_{i+1,j+1} \overbrace{-\phi^2\_x12_{i,j}(\phi^2\_z12_{i+1,j} + \phi^2\_z12_{i+1,j-1})}^{k}\,\xi_{i+1,j}$$
$$\overbrace{-\phi^2\_z12_{i,j}(\phi^2\_x12_{i,j} + \phi^2\_x12_{i-1,j})}^{h}\,\xi_{i,j+1} \overbrace{+\phi^2\_z12_{i+1,j-1}\phi^2\_x12_{i,j}}^{j}\,\xi_{i+1,j-1}$$
$$\overbrace{+(\phi^2\_x12_{i,j} + \phi^2\_x12_{i-1,j})(\phi^2\_z12_{i,j} + \phi^2\_z12_{i,j-1})}^{g}\,\xi_{i,j} \overbrace{+\phi^2\_z12_{i-1,j}\phi^2\_x12_{i-1,j}}^{d}\,\xi_{i-1,j+1}$$
$$\overbrace{-\phi^2\_z12_{i,j-1}(\phi^2\_x12_{i,j} + \phi^2\_x12_{i-1,j})}^{f}\,\xi_{i,j-1} \overbrace{-\phi^2\_x12_{i-1,j}(\phi^2\_z12_{i-1,j} + \phi^2\_z12_{i-1,j-1})}^{c}\,\xi_{i-1,j}$$
$$\overbrace{+\phi^2\_z12_{i-1,j-1}\phi^2\_x12_{i-1,j}}^{b}\,\xi_{i-1,j-1}]dx^{-2}dz^{-2} \quad (3.1.3)$$

Therefore, after discretization at the (i, j) th position of the gird, equation 2.3.5

can be written as:

$$a(i,j)\xi_{i-2,j} + b(i,j)\xi_{i-1,j-1} + c(i,j)\xi_{i-1,j} + d(i,j)\xi_{i-1,j+1} + e(i,j)\xi_{i,j-2} + f(i,j)\xi_{i,j-1}$$
$$+ g(i,j)\xi_{i,j} + h(i,j)\xi_{i,j+1} + i(i,j)\xi_{i,j+2} + j(i,j)\xi_{i+1,j-1} + k(i,j)\xi_{i+1,j} + l(i,j)\xi_{i+1,j+1}$$
$$+ m(i,j)\xi_{i+2,j} = sm(i,j) \quad (3.1.4)$$

where $sm(i,j)$ denotes the right hand member of equation 2.3.5, discretized in the same way at (i, j) th position of the gird.

3.1.2   Boundary Conditions:

For 1D experiments with PERCOL we use two boundary conditions: 1) Fixed Boundary Condition and 2) Periodic Boundary Condition. Both boundary conditions will be discussed in detail in subsequent paragraphs.

3.1.2.1   Fixed Boundary Condition

The model box has a $Hx \times Hz$ dimension with vertical grid spacing dz and horizontal grid spacing dx. The model box has nz numbers of vertical grid points and nx numbers of horizontal grid points i.e. $Hx = nx \times dx$ and $Hz = nz \times dz$. By the heading 'Fixed Boundary Condition' it is meant that the vertical solid and fluid velocities are set/fixed to zero at both the vertical boundaries. Similarly, horizontal solid and fluid velocities are set/fixed to zero at both the horizontal boundaries i.e. $V_z = 0$ (z direction velocities of both solid and fluid) at $z = 0$ and $z = Hz$ and $V_x = 0$ (horizontal solid and fluid velocities) at $x = 0$ and $x = Hx$. Therefore, $V_{z_{i,nz+1}} = -V_{z_{i,nz-1}}$. Also, the stream function is set to zero at both vertical and horizontal boundaries. i.e. $\Psi = 0$ at $z = 0$, $z = Hz$; at $x = 0$, $x = Hx$. Hence, $\Psi_{i,nz+1} = -\Psi_{i,nz-1}$, $\Psi_{i,nz+2} = -\Psi_{i,nz-2}$, $\Psi_{i,-1} = -\Psi_{i,1}$, $\Psi_{i,-2} = -\Psi_{i,2}$ and similar boundary condition holds for horizontal direction. Also, we assume Hz = 20km. For the 1D model, dx is much larger compared to dz. We assume dx = 5000 m whereas $dz \leq 100$ m. Boundary conditions of Ψ and V_z at $z = 0$ and $z = Hz$ leads

to the conclusion that (From eq. 2.2.4) $\theta_{i,nz+1} = \theta_{i,nz}$, $\theta_{i,nz+2} = \theta_{i,nz-1}$, $\theta_{i,0} = \theta_{i,1}$, $\theta_{i,-1} = \theta_{i,2}$ (cf. Fig.2.3). From eq. 2.2.4 and eq. 2.2.5 using boundary conditions of vertical fluid and solid velocities, θ and Ψ, we obtain similar boundary conditions for ξ as it is for θ. Boundary conditions of solid and fluid velocities on vertical boundaries leads to the fact that ϕ has symmetric boundary condition along z direction i.e. $\phi_{i,0} = \phi_{i,1}$, $\phi_{i,nz+1} = \phi_{i,nz}$ according to eq. 2.1.4.

V_z has symmetric boundary condition along x direction and V_x (x direction velocities of both solid and fluid) has symmetric boundary condition along z direction. i.e. $V_{mz_{nx+1,iz}} = V_{mz_{nx,iz}}$, $V_{mz_{0,iz}} = V_{mz_{1,iz}}$ and similar boundary condition holds for vertical fluid velocity V_{fz}. Similarly, $V_{mx_{ix,nz+1}} = V_{mx_{ix,nz}}$, $V_{mx_{ix,0}} = V_{mx_{ix,1}}$ and the same holds for horizontal fluid velocity V_{fx}.

Using the same set of equations (i.e. eq. 2.1.4, 2.2.4 and 2.2.5), boundary conditions of Ψ, V_x, similar set of boundary conditions can be derived for θ, ξ and ϕ along horizontal direction as it was derived for vertical direction.

1D numerical experiments using this boundary conditions will be discussed in subsequent sections later onwards.

3.1.2.2   Periodic Boundary Condition

Like the fixed boundary condition the way fixed velocity condition was imposed on the boundary for both the solid and fluid velocity, periodicity is applied as a boundary condition for both solid and fluid velocity. Under this boundary condition we assume that $V_{z_{i,0}} = V_{z_{i,nz}}$, $V_{z_{i,nz+1}} = V_{z_{i,1}}$. Also, periodicity is applied on boundary condition for ϕ. i.e. $\phi_{i,nz+1} = \phi_{i,1}$ and $\phi_{i,0} = \phi_{i,nz}$

It must be noted that deriving periodic boundary condition for all the other variables is possible only for 1D case. So, the numerical experiments with periodic boundary condition are executed only for 1D case. For 1D case, stream function $\Psi = 0$ everywhere in the model box.

Also, for 1D case we assume that $\theta = \xi$ everywhere in the model box. Because, in 1D $\bar{v} = 0$ and $\Psi = 0$. Therefore, from eq. 2.2.5, we have $\xi - \theta = constant$ and this constant can be chosen according to arbitrary constant background pressure and we assume the background pressure is zero in order to make a preliminary

simplification of our code.

Symmetric boundary conditions are applied along x direction for all the variables. Determining periodic boundary condition along z direction for ξ is a bit tricky whose derivations are shown in the next paragraph .

Derivation of periodic boundary condition for ξ:

Let's take eq.2.1.4 which is: $-\nabla[(1-\phi)\delta P]+(1-\phi)\delta\rho\mathbf{g}+\nabla\cdot[(1-\phi)\bar{\bar{\tau}}_m]-\frac{\eta_f}{k_0}\frac{\delta\mathbf{v}}{\phi}=0$, where $\bar{\bar{\tau}}_m=\eta_m(\nabla\mathbf{v_m}+\nabla\mathbf{v_m}^t-\frac{2}{3}\nabla\cdot\mathbf{v_m}\bar{\bar{I}})$ is the deviatoric viscous stress tensor

For 1D case, replacing deviatoric stress tensor by $\frac{4}{3}(1-\phi)\frac{\delta}{\delta z}(V_{mz})$ we have ,
$-\nabla[(1-\phi)\delta P)]+(1-\phi)\delta\rho g+\nabla.[\frac{4}{3}(1-\phi)\frac{\delta}{\delta z}(V_{mz})]-\frac{\eta_f\delta v}{k_0\phi}=0$

i.e. $-\nabla[(1-\phi)\delta P)]+(1-\phi)\nabla(\delta\rho gz)+\nabla[\frac{4}{3}(1-\phi)\frac{\delta}{\delta z}(V_{mz})]-\frac{\eta_f\delta v}{k_0\phi}=0$

Now since, $\frac{\delta v}{\phi}=\nabla\theta=\nabla\xi$ (when $\Gamma=0$) and $\mathbf{g}=-g\mathbf{k}$, where $\mathbf{k}$ is the unit vector along z direction, so replacing this term in previous equation we have,

$$-\nabla[(1-\phi)\delta P)]-(1-\phi)\nabla(\delta\rho gz)+\nabla[\frac{4}{3}(1-\phi)\frac{\delta}{\delta z}(V_{mz})]-\nabla(\frac{\eta_f\xi}{k_0})=0 \qquad (*)$$

Now if we want to write l.h.s of the above equation in the form

$$-\nabla[(1-\phi)\delta P)]-\nabla[(1-\phi)(\delta\rho gz)]+\nabla[\frac{4}{3}(1-\phi)\frac{\delta}{\delta z}(V_{mz})]-\nabla(\frac{\eta_f\xi}{k_0})$$

then we have to add the term $\delta\rho gz\frac{\delta}{\delta z}(\phi)$ to both sides of equation (*) as,

$$-\nabla[(1-\phi)(\delta\rho gz)]=\delta\rho gz\frac{\delta}{\delta z}(\phi)-(1-\phi)\nabla(\delta\rho gz)$$

Then we have,

$$-\nabla[(1-\phi)\delta P)]-\nabla[(1-\phi)(\delta\rho gz)]+\nabla[\frac{4}{3}(1-\phi)\frac{\delta}{\delta z}(V_{mz})]-\nabla(\frac{\eta_f\xi}{k_0})=\delta\rho gz\frac{\delta}{\delta z}(\phi)$$

Integrating both sides from 0 to Hz (length of the box of our model) we have,

$$[-\{(1-\phi)\delta P)\}-\{(1-\phi)(\delta\rho gz)\}+\{\frac{4}{3}(1-\phi)\frac{\delta}{\delta z}(V_{mz})\}-(\frac{\eta_f\xi}{k_0})]_0^{Hz}=\int_0^{Hz}[\delta\rho gz\frac{\delta}{\delta z}(\phi)]\delta z$$

Integrating by parts the integrand of r.h.s and putting the limit in l.h.s we have,

$-[(1 - \phi_{Hz})(\delta\rho gHz)] - \frac{\eta_f}{k_0}(\xi_{Hz} - \xi_0) = \delta\rho gHz\phi_{Hz} - \delta\rho g \int_0^{Hz} \phi dz$ (**)

Since, ϕ and V_{mz} satisfy periodic bc, from equation 2.1.1 i.e.

$\frac{\partial\phi}{\partial t} = \nabla \cdot (1 - \phi)\mathbf{v_m} + \frac{\dot{\Gamma}}{\rho_m}$

and the rheological equation 2.1.5 i.e

$\frac{\partial\phi}{\partial t} + v_m \cdot \nabla\phi = -\phi(1 - \phi)K\frac{\delta P}{\eta_m + \eta_f}$

we can note that,

$\delta P = -\frac{K\eta_m}{\phi}\nabla.V_m$, where K=1 . Therefore, δP also satisfies periodic bc

Hence, we can write from equation(**) that,

$- \delta\rho gHz - \frac{\eta_f}{k_0}(\xi_{Hz} - \xi_0) = -\delta\rho g \int_0^{Hz} \phi dz$

Since, ϕ satisfies mass conservation equation so

$\delta\rho g \int_0^{Hz} \phi dz$ should be a constant say C_1

Therefore, now we have,

$(\xi_{Hz} - \xi_0) = -\frac{k_0}{\eta_f}(\delta\rho gHz - C_1)$

i.e. we can write $\xi_{i,0} = \xi_{i,nz} + \frac{k_0}{\eta_f}(\delta\rho gHz - C_1)$, $\xi_{i,-1} = \xi_{i,nz-1} + \frac{k_0}{\eta_f}(\delta\rho gHz - C_1)$, $\xi_{i,nz+1} = \xi_{i,1} - \frac{k_0}{\eta_f}(\delta\rho gHz - C_1)$, $\xi_{i,nz+2} = \xi_{i,2} - \frac{k_0}{\eta_f}(\delta\rho gHz - C_1)$ which are the required bc for ξ. We calculate C_1 by Simpson's 1/3 rd formula by the information of ϕ values at each grid point available at each time step according to the algorithm flow chart (cf. Fig.2.2) to get a proper bc of ξ

3.1.3   BSOR algorithm in brief

For solving a system of linear equations,

$$Ax = b \tag{3.1.5}$$

where A is a matrix of $n \times n$ order and x and b are column vectors of $n \times 1$ order. Firstly, the matrix A is decomposed in to a strictly triangular matrix L, a strictly upper triangular matrix U and a diagonal matrix D. i.e. $A = L + D + U$. Hence, equation 3.1.5 can be rewritten as,

$$x = -(D + L)^{-1}Ux + (D + L)^{-1}b \tag{3.1.6}$$

Therefore, in iterative format, one can write equation 3.1.5 as,

$$x^{(k+1)} = Gx^{(k)} + c \tag{3.1.7}$$

where $G = -(D+L)^{-1}U$ and $c = (D+L)^{-1}b$ and $x^{(k)}$ denotes the value of x obtained at k-th iteration. However, equation 3.1.6 represents the formula of Gauss-Seidel method which upon forward substitution, takes the form as,

$$x_i^{(k+1)} = \frac{b_i - \Sigma_{j<i}a_{ij}x_j^{(k+1)} - \Sigma_{j>i}a_{ij}x_j^{(k)}}{a_{ii}} \tag{3.1.8}$$

where i =1, 2, ... , n.

Now for relaxation method a parameter ω is introduced $(0 < \omega < 2)$ such that, equation 3.1.5 can be written as,

$(D + \omega L)x = \omega b - [\omega U + (\omega - 1)D]x$, i.e.

$x = (D + \omega L)^{-1}[b - \{\omega U + (\omega - 1)D\}x]$ which upon forward substitution, can be

written as:

$$x_i^{(k+1)} = (1 - \omega)x_i^{(k)} + \frac{\omega(b_i - \Sigma_{j<i}a_{ij}x_j^{(k+1)} - \Sigma_{j>i}a_{ij}x_j^{(k)})}{a_{ii}} \qquad (3.1.9)$$

combining equation 3.1.8 and 3.1.9 one can write equation 3.1.9 as,

$$x_i^{(k+1)} = (1 - \omega)x_i^{(k)} + \omega x_i^{GS} \qquad (3.1.10)$$

where x_i^{GS} denotes the value of the i-th component of vector x obtained from Gauss - Seidel method as described in equation 3.1.8. If, $0 < \omega < 1$, then the method is known as under relaxation method and if $1 < \omega < 2$, then the method is known as over relaxation method. ω takes higher values (i.e. close to 2) with increasing number of grid points. In our code, with 100-200 vertical grid points and 4 horizontal grid points, $\omega = 1.6$ gives the optimal solution.

If $r(x_i^{(k)}) = b_i - \Sigma_{j<i}a_{ij}x_j^{(k+1)} - \Sigma_{j\geq i}a_{ij}x_j^{(k)}$, where $r(x_i^{(k)})$ is known as the residual term, then one can write equation 3.1.9 as:

$$x_i^{(k+1)} = x_i^{(k)} + \frac{\omega r(x_i^{(k)})}{a_{ii}} \qquad (3.1.11)$$

i.e.

$$x_i^{new} - x_i^{old} = \frac{\omega r(x_i^{(k)})}{a_{ii}} \qquad (3.1.12)$$

So, when the residual term is close to zero, it can be said that $x_i^{new} \to x_i^{old}$ or in other words, the solution has converged. Therefore, we prescribe an infinitesimal parameter ϵ and as soon as the residual term $r(x^{(k)}) < \epsilon$, we stop our computation. How the solution is well converged according to the choice of ϵ, that will be discussed later in section 3.3.

We write the BSOR solver routines for solving equation 3.1.4 or equation 2.3.5, equation 2.3.4 and equation 2.3.7.

3.2   Implication of Direct Solver

Solving ψ and ξ by iterative method was time consuming and therefore a direct solver was required to get the values of these two variables. In order to do that, same finite discretization as described in equation 3.1.1-3.1.4 were followed. We can then write the matrices both for ξ and ψ. Therefore, it is possible to solve directly by inverting these matrices by LU decomposition method in order to get the values of ψ and ξ. From fig. 3.1, it is clear that both the matrices for ξ and ψ will be of band diagonal block matrix's form with each block (corresponding to a fixed i and a varying j as described in equation 3.1.4) having 2 subdiagonals i.e. positioned to left or below of diagonal , 2 superdiagonals i.e. positioned to right or above of diagonal and a diagonal. So, to be specific and to form a quicker direct solver we follow the simplified LU decomposition which is appropriate for band diagonal matrices. The solution of the linear system by LU decomposition for the band diagonal matrix is much effective according to time consumption and storage required by the solver than the LU decomposition for the general matrices.

3.2.1   LU decomposition

Let's assume A be a matrix of $n \times n$ order.

i.e.

$$A = \begin{pmatrix} a_{11} & a_{12} & \dots & a_{1n} \\ a_{21} & a_{22} & \dots & a_{2n} \\ \dots\dots\dots\dots\dots\dots \\ a_{n1} & a_{n2} & \dots & a_{nn} \end{pmatrix}$$

Then A is decomposed into lower triagular matrix L and upper triangular matrix U such that $A = LU$

where

$$L = \begin{pmatrix} l_{11} & 0 & 0 & \ldots & 0 & 0 \\ l_{21} & l_{22} & 0 & \ldots & 0 & 0 \\ l_{31} & l_{32} & l_{33} & 0 & \ldots & 0 \\ \multicolumn{6}{c}{\ldots\ldots\ldots\ldots\ldots\ldots\ldots\ldots\ldots\ldots} \\ l_{n1} & l_{n2} & l_{n3} & \ldots & l_{nn-1} & l_{nn} \end{pmatrix}$$

and

$$U = \begin{pmatrix} u_{11} & u_{12} & u_{13} & \ldots & u_{1n-1} & u_{1n} \\ 0 & u_{22} & u_{23} & \ldots & u_{2n-1} & u_{2n} \\ 0 & 0 & u_{33} & u_{34} & \ldots & u_{3n} \\ \multicolumn{6}{c}{\ldots\ldots\ldots\ldots\ldots\ldots\ldots\ldots\ldots\ldots} \\ 0 & 0 & 0 & \ldots & u_{nn-1} & u_{nn} \end{pmatrix}$$

Hence, it can be said that $\sum_{k=1}^{min(i,j)} l_{ik}u_{kj} = a_{ij}$, where i and j both take the values from 1 to n.

Therefore, in order to solve the equation 3.1.5 we need to solve two equations namely,

$$Ux = y \tag{3.2.1}$$

where $x = \begin{pmatrix} x_1 \\ x_2 \\ \vdots \\ x_n \end{pmatrix}$, $y = \begin{pmatrix} y_1 \\ y_2 \\ \vdots \\ y_n \end{pmatrix}$ and

$$Ly = b \tag{3.2.2}$$

where $b = \begin{pmatrix} b_1 \\ b_2 \\ \vdots \\ b_n \end{pmatrix}$. Then by forward substitution from equation 3.2.2 we have,

$$y_1 = \frac{b_1}{l_{11}}$$

$$y_i = \frac{1}{l_{ii}}[b_i - \sum_{j=1}^{i-1} l_{ij}y_j], \quad i = 2, 3, \dots, n$$

Hence, by backward substitution we have,

$$x_n = \frac{y_n}{u_{nn}}$$

$$x_i = \frac{1}{u_{ii}}[y_i - \sum_{j=i+1}^{n} u_{ij}x_j], \quad i = n-1, n-2, \dots, 1$$

The algorithm of LU decomposition is similar for band diagonal matrices. For quicker computation, we use a compact storage system for the band diagonal matrices so that the use of storage space is less. We use the routines given in [Press et al., 1992] to solve 2.3.4 and 2.3.5. Let A be a $N \times N$ matrix having m_1 subdiagonals and m_2 superdiagonals where both $m_1 > 0$, $m_2 > 0$ and $m_1 + m_2 + 1 < N$. i.e. a matrix A is said to be band diagonal if its elements a_{ij} are such that $a_{ij} = 0$ when $j > i + m_2$ or $i > j + m_1$ and i, j both take the values from 1 to N.

The algorithmic flowchart of obtaining the solution is given in Fig.3.2. In order to keep a particular element in the diagonal position from which the pivot is about to be selected, some permutations of rows and columns can be executed. Execution of interchanging rows is called partial pivoting and execution of permutations between rows and columns is called full pivoting. This pivoting helps to prevent non stability of matrix equations.
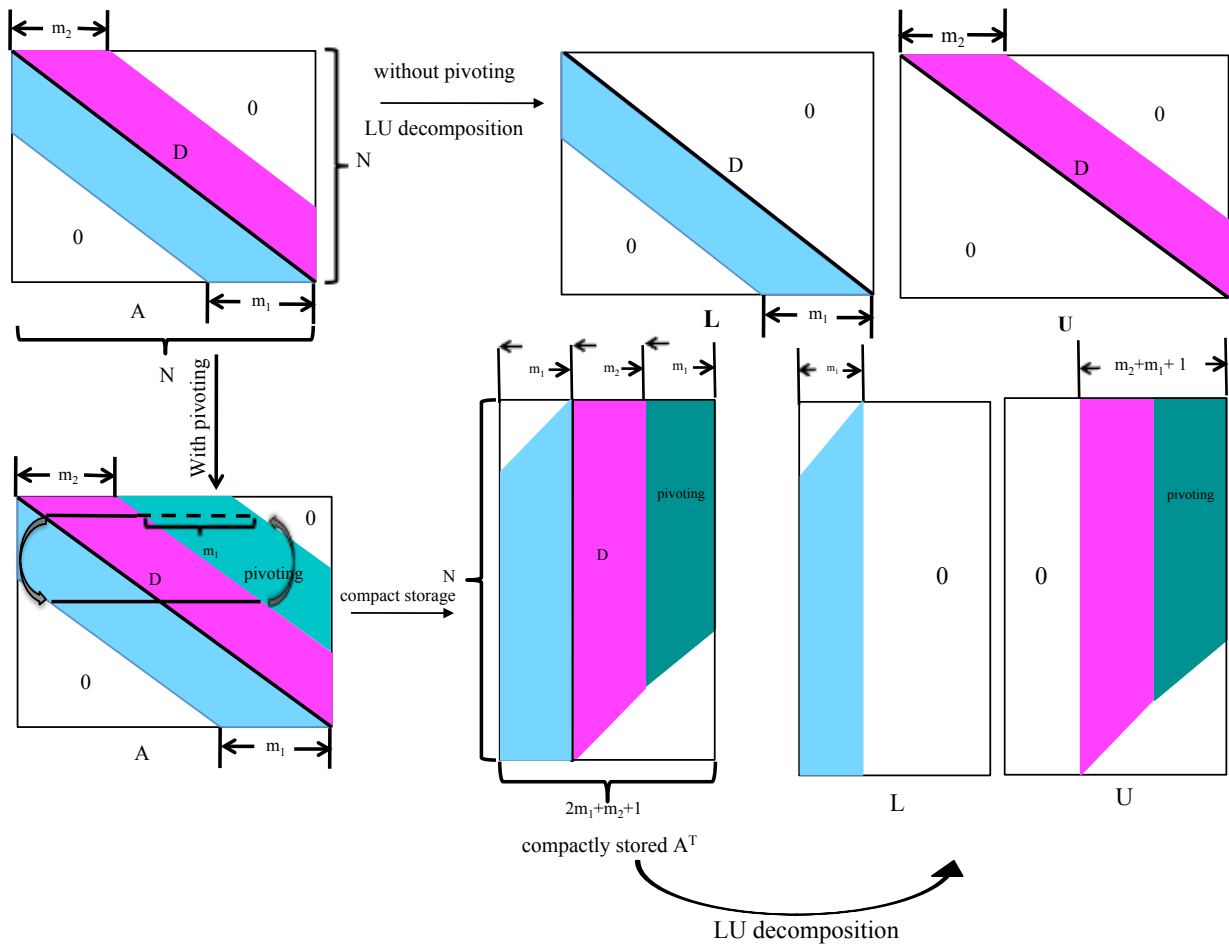
Fig. 3.2: Graphical representation of LU decomposition algorithm for a banded matrix where D represents the diagonal of the matrix.

After the decomposition, the equation 3.1.5 is solved using forward and backward substitution as discussed earlier. Before discussing further about the choice of numerical scheme table4.1 is given to get an idea about the set of parameters which are used in the code PERCOL2D most of the time.

3.2.2   A comparison between 1D solutions obtained by BSOR and direct solver.

It is needed to decide which solver to use. The direct solver or the BSOR? To decide it a comparative plot is presented in fig.3.3. 1D profiles of Porosity, fluid velocity, matrix velocity and ξ at the first time step obtained from BSOR and the direct solver method, are presented in 3.3 with the assumption $\epsilon = 10^{-23}$ (as discussed in section 3.1) used in BSOR. As the a_{ii} term in eq.3.1.12 has order of magnitude approximately 10^{-14}, choice of ϵ is much smaller in the convergence routine for ξ and in Ψ (the stream function). An assumption of background porosity $\phi_0 = 0.01$ and a Gaussian of amplitude 0.1 having 7 km width is used as an initial input of porosity in this comparison figures. Vertical length of the model box is assumed as Hz=20 km with 200 vertical grid points and 4 horizontal grid points in order to obtain 1D profiles. Also, a fixed or Dirichlet's boundary condition is used while obtaining the solution using both the methods.
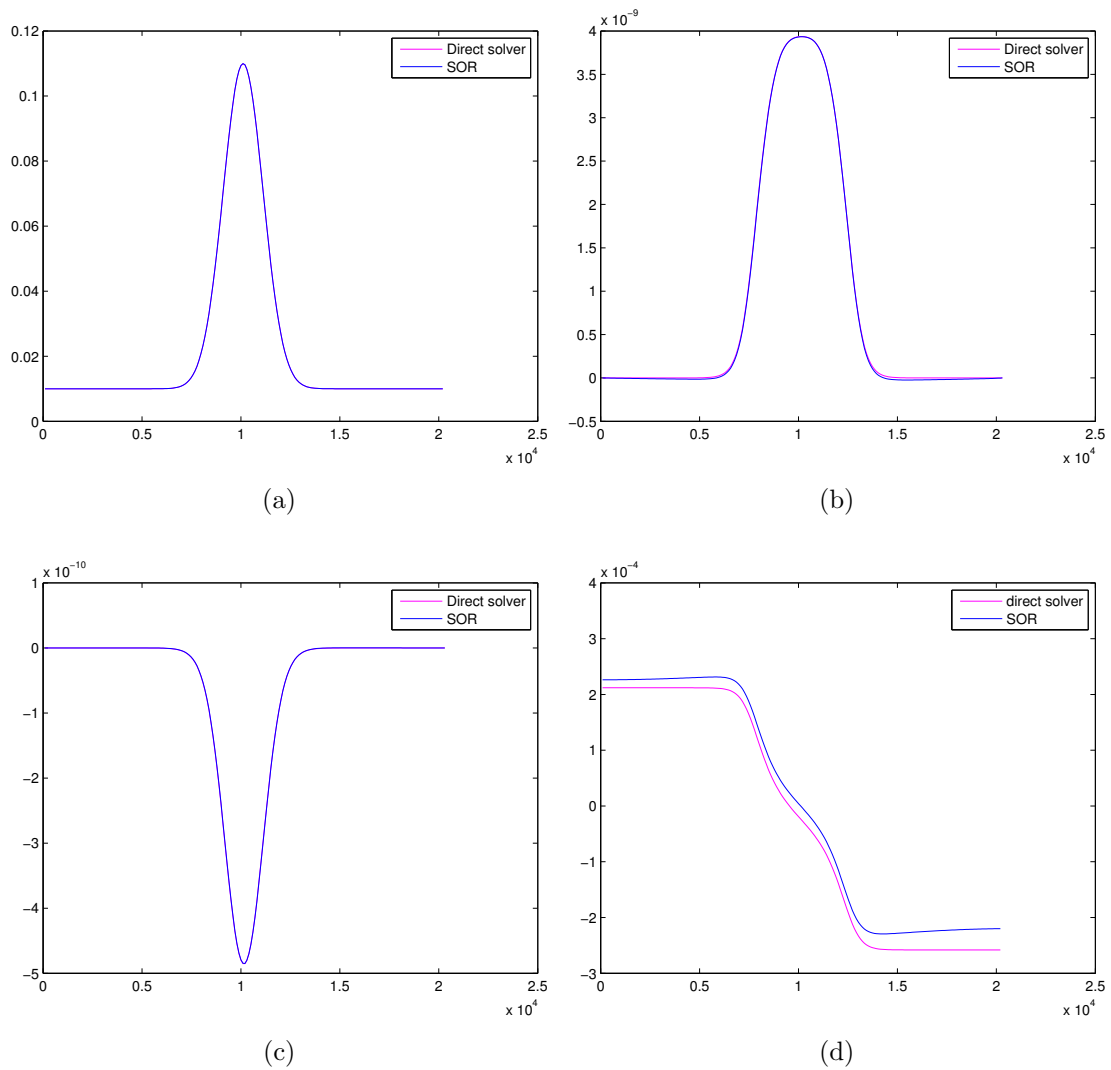
FIG. 3.3: Comparison between BSOR and direct solver: comparative initial profiles of (a) Porosity, (b) Fluid velocity (ms^{-1}), (c) Matrix velocity (ms^{-1}) and (d) ξ (m^2s^{-1}) at time = 10^{-6} Myr along the vertical direction of model box having the length of 20 km

Remark: Direct solver method is much more efficient than BSOR method according to the runtime of the program (8 times faster than BSOR) as well as accuracy of the solution. The direct solver takes care of the fact that the matrix associated

with the solution of ξ is non singular and hence gives a unique solution for ξ. One can notice that the profiles of initial porosity, fluid and matrix velocities are not visibly different (0.4-1.2% in terms of maximum norm) while using BSOR and direct solver in spite of having much different ξ values ($\sim 15\%$ in terms of maximum norm). If we observe the ξ profiles, we can find out that there is almost a constant shift between the profiles obtained using two solvers. Therefore, one can say $\nabla(\xi + constant) = \nabla\xi$. As, throughout the code only gradient of ξ is used in order to calculate porosity and the other variables, this difference does not contribute significant difference in the solutions of other variables.

3.3 Accuracy factor for the solution while using BSOR solver

To investigate about accuracy factor of the 1D solution we have chosen initial porosity profile as a Gaussian curve of width 7 km having background porosity $\phi_0 = 0.01$ and amplitude 0.1.

ϵ is chosen in such a way that it controls the convergence process of SOR. i.e. when norm (which is average of absolute value of the residual term of the linear system of equations for ξ over $nx \times nz$ grid points) is less than ϵ then the SOR for ξ converges towards a solution. Now, we see how the solution varies according to the choice of number of vertical grid points (cf. Fig.3.4). and according to the choice of ϵ (cf. Fig.3.6).

Keeping $\epsilon = 10^{-20}$ we get fig.3.4 varying grid resolution as 4×100 and 4×500 respectively.
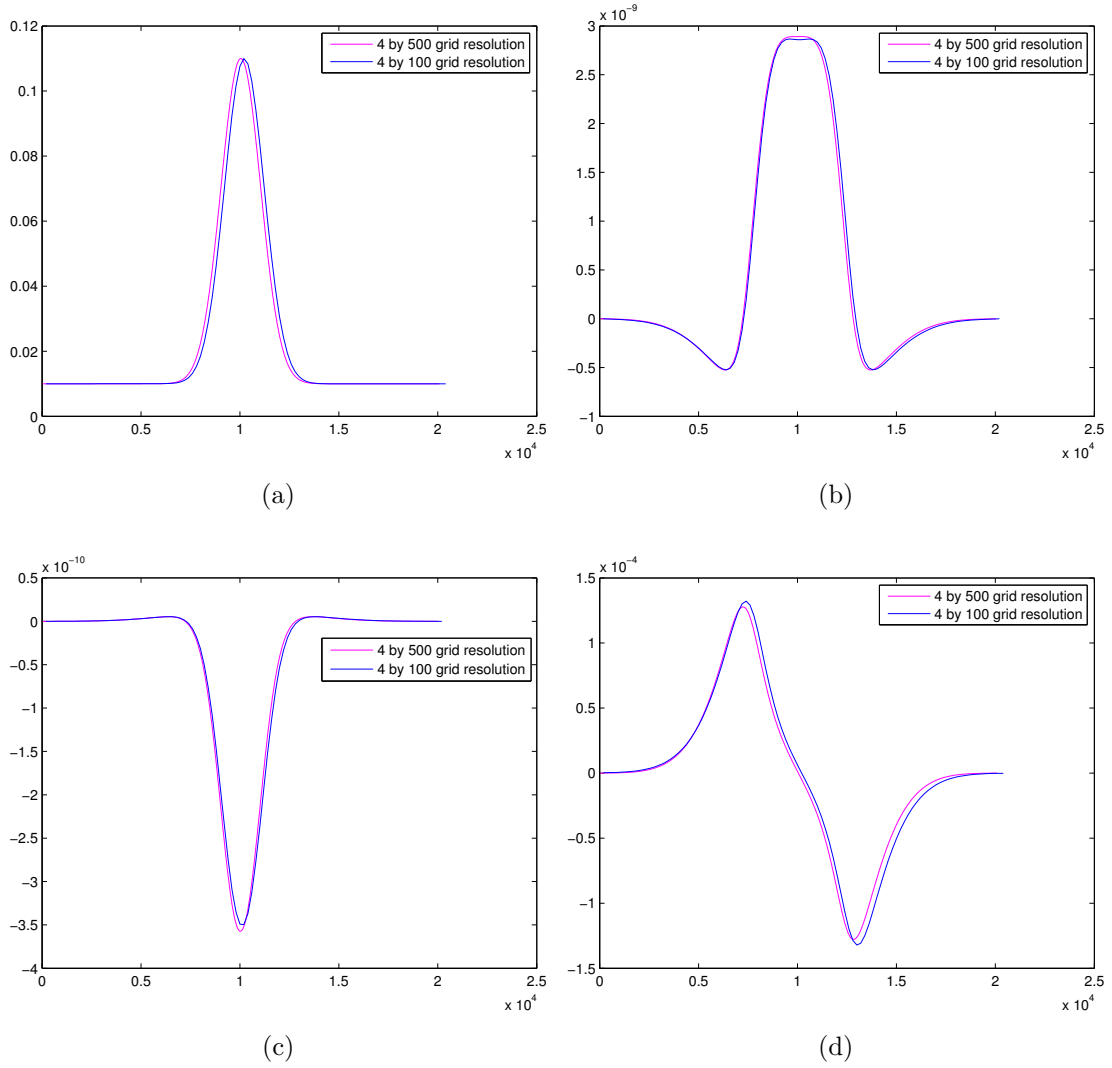
FIG. 3.4: Resolution test for initial profiles of (a) Porosity, (b) Fluid velocity (m/s), (c) Matrix velocity (m/s) and (d) ξ (m^2/s) at time $= 10^{-6}$ Myr along the vertical direction of model box having the length of 20 km.

Remarks: The solution is less sensitive to the choice of number of grid points. i.e. the 1D profiles are not much different for 100 vertical grid points and 500 vertical grid points. The solution of all the profiles improve by the range of $2 - 6\%$ in terms of maximum norm by the increment of number of grid points.

The phase velocity of porous wave increases with decreasing number of grid points. It increases by 10.8% while number of grid points decreased from 500 to 300 and it increases by 4.8% when the decrement is from 300 to 100 grid points (cf. fig 3.5). According to the choice of different ϵ ($= 10^{-20}$, 10^{-23}, 10^{-26} respectively) the fig.3.6 is obtained.
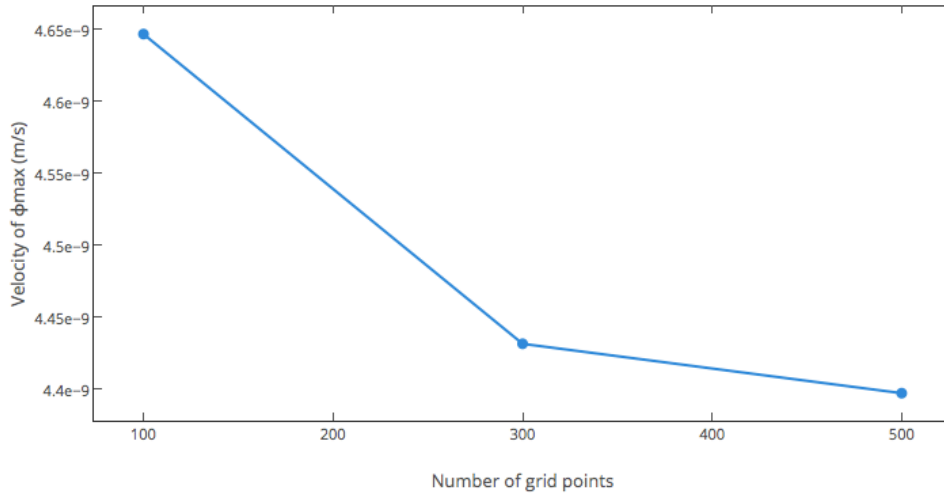
FIG. 3.5: comparison of phase velocity i.e. the velocity of maxima of porosity wave with varying number of grid points
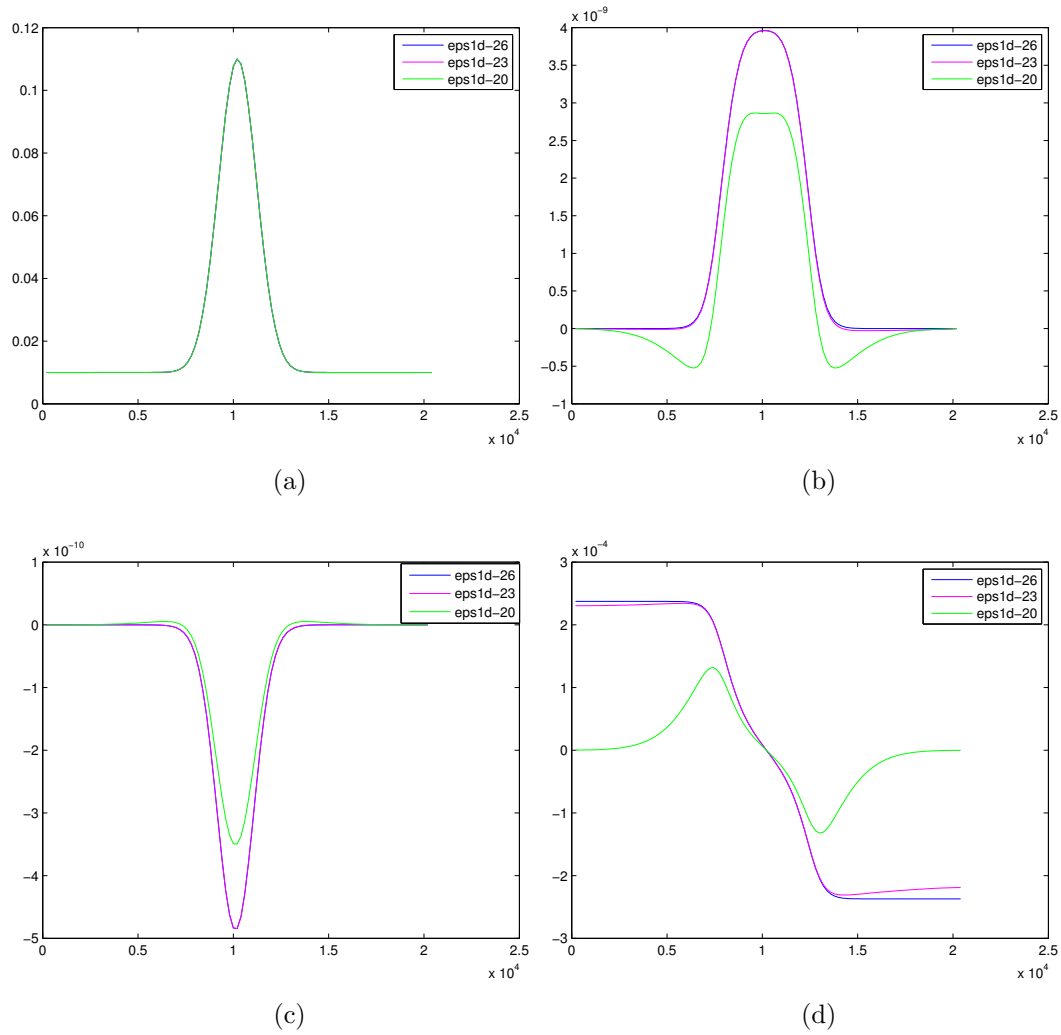
Fig. 3.6: Epsilon(ϵ) test for initial profiles of initial profiles of (a) Porosity, (b) Fluid velocity (m/s), (c) Matrix velocity (m/s) and (d) ξ (m^2/s) at time $= 10^{-6}$ Myr along the vertical direction of model box having the length of 20 km.

Conclusion: Therefore, choice of epsilon (ϵ) is more important than choice of grid resolution in order to get the expected accuracy of the solution. In fact $\epsilon = 10^{-23}$ leads the solution to converge to the expected one.

Also, reason behind a bigger shift between the ξ profiles obtained by BSOR and

direct solver in the lower part (cf. Fig. 3.3) can be clarified by the ξ profile given in fig. 3.6. A smaller epsilon gives rise of the lower part of ξ profile. But fig. 3.3 was obtained using 200 grid points for which choosing $\epsilon = 10^{-26}$ was not possible as this choice of ϵ leaded to oscillation in the convergence process of BSOR.

Therefore, it is evident that use of direct solver gives better solution than BSOR according to time consumption and to avoid oscillation problem during process of convergence in BSOR while using higher number of grid points. So, it can be concluded that BSOR convergence process is slower for longer wavelength profiles. In the next chapter 1D numerical experiments taking different gaussian curves as input for porous wave will be discussed.

Chapter 4

1D numerical experiments

4.1 Fixed boundary condition

According to boundary condition discussed in 3.1.2.1 we execute the following numerical experiments in 1D. In short, vertical matrix and fluid velocities are zero at vertical boundaries. Horizontal matrix and fluid velocities are zero at horizontal boundaries. Gradient of ξ, θ is zero at both the horizontal and vertical boundaries. The stream function ψ is set to 0 at both the boundaries. The porosity ϕ has symmetric boundary condition along both horizontal and vertical boundaries. Table 4.1 should be consulted before going through the description of numerical experiments.

parameters symbol	description of parameters	value of parameters
k_0^*	Permeability constant	$10^{-10} m^2$
η_m^*	Matrix viscosity	10^{18} Pa.S
η_f	Fluid viscosity	10 Pa.S
ρ_m	Matrix density	3300 kg/m^3
ρ_f	Fluid density	2300 kg/m^3
Lx	Aspect ratio of model box	1
Hz	Vertical length of model box	20 km
nx	Number of grid points in horizontal direction	4
nz*	Number of grid points in vertical direction	300

*Different values of k_0 and η_m are used in 4.1.3.
For the periodic boundary condition cases nz
value is 100

Table 4.1: List of parameter values

4.1.1 Effect of variation of width and amplitude of initial input of porosity wave

We use a Gaussian as an initial input for the porosity profile and vary its width in order to investigate the characteristics of the velocity profiles of solid and fluid as well as of ξ whose gradient contributes to matrix compaction. For a background porosity $\phi_0 = 0.01$, table 4.2 describes the characteristics of porosity, velocities of matrix and fluid, ξ profiles. Fig.4.1 and fig.4.2 show the porosity, fluid velocity, matrix velocity and ξ profiles after 1st time step. The first and 2nd column of fig.4.1 and fig.4.2correspond to the porosity, fluid velocity, matrix velocity and ξ profiles respectively obtained at initial time step for the input of porous wave as a gaussian having different amplitudes (0.1, 0.08 and 0.06 respectively)and a width of 3.5 km. Fig.4.3-fig4.4 and fig.4.5-fig.4.6 give the same profiles corresponding to different width of Gaussian curve (7 km and 14 km respectively) which are used as the initial input for the porous wave in the PERCOL2D code. In this model, the other parameters like viscosity of the matrix and fluid, permeability constant are set in such a way that the compaction length $\delta(=\sqrt{\frac{k_0 \phi_0 \eta_m}{\eta_f}})$ value is approximately

300 meter. For each model as described in fig.4.1-fig.4.6, there are 5 grid points per compaction length. Increasing number of grid points per compaction lengths doesn't make any significant changes in the plots of fig.4.1-fig.4.6

ϕ_0	width of wave (km)	amplitude of wave	observations
0.01	3.5 (cf. Fig.4.1 and Fig.4.2)	0.1	The porous wave and matrix velocity profiles have sharp peaks and the fluid velocity profile has a double maxima for all the different amplitudes. But this double maxima has a tendency to converge to a single maxima with decreasing amplitude of the wave. Overall, the slope of ξ profile is lesser with decreasing amplitudes of the wave.
		0.08	
		0.06	
0.01	7 (cf. Fig.4.3 and Fig.4.4)	0.1	The porosity and matrix velocity profiles have blunter peak than as it is observed in fig.4.1 and fig.4.2. Decreasing overall slope feature of the ξ profile with decreasing amplitude of porous wave is similar to fig.4.2. No double maxima for fluid velocity profile is observed. Height of ξ profile (i.e. max. value of ξ - min. value of ξ) is larger than the 3.5 km wide porous wave input case.
		0.08	
		0.06	
0.01	14 (cf. Fig.4.5 and Fig.4.6)	0.1	The porosity and matrix velocity profiles have the most blunt peak among fig.4.1 - fig.4.6. Decreasing slope feature of the ξ profile with decreasing amplitude of the porous wave remains the same like fig.4.2 and fig.4.4. No double maxima for fluid velocity profile is observed. Height of ξ profile (i.e. max. value of ξ - min. value of ξ) is more than the 7 km wide porous wave input case. Fig.4.8 giving a profile of gradient of ξ, is produced for input of 14 km wide porous wave and therefore is recommended for exact information about slope of ξ with decreasing amplitude of input porous wave. This gradient, scaled by ϕ^2, is the irrotational component of matrix velocity. The characteristics of this profile is similar for other porous wave input of varying width accordingly.
		0.08	
		0.06	

TABLE 4.2: observations based on varying height and width of initial input for porosity
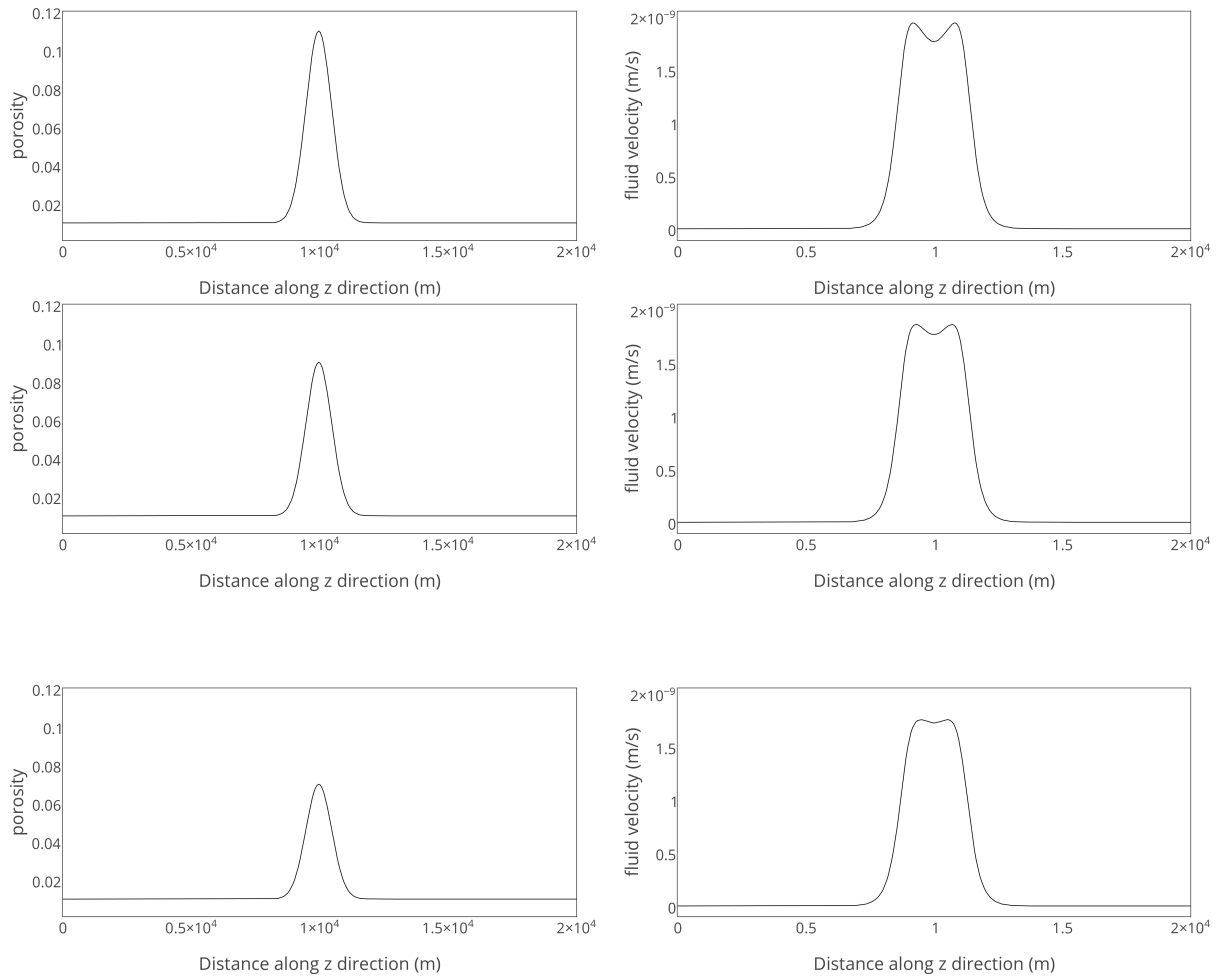
FIG. 4.1: left column is for the input of porous wave which is a gaussian of varying amplitude (viz. 0.1, 0.08, 0.06 respectively) having width as 3.5 km and background porosity value as 0.01 and the right column gives three different profiles of fluid velocity obtained at initial time step corresponding to the three different amplitudes of the porous wave plotted at left.

Fig. 4.2: left and right column present the matrix velocity and the ξ profiles respectively obtained at initial time step corresponding to the input of porous wave which is a gaussian of varying amplitude (viz. 0.1, 0.08, 0.06 respectively) having width as 3.5 km and background porosity value as 0.01.
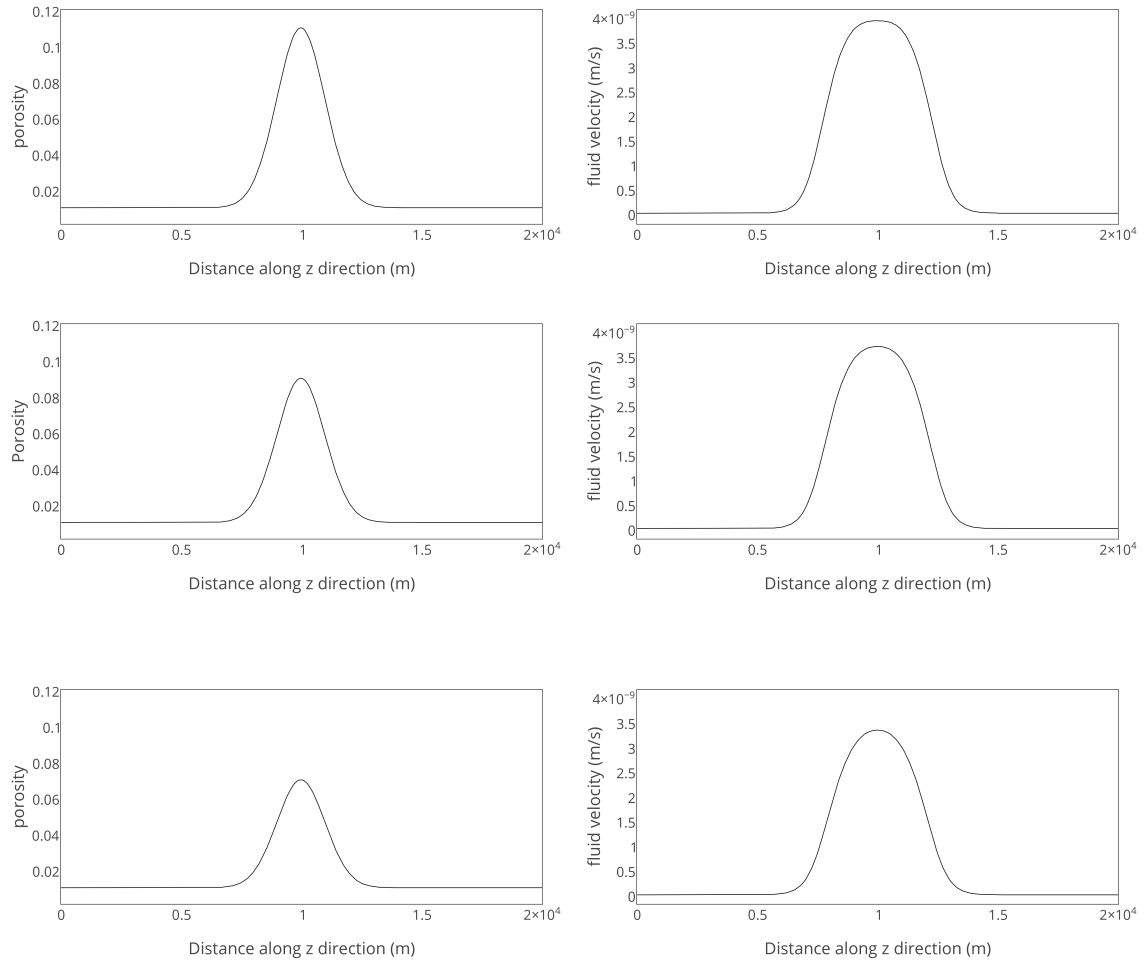
FIG. 4.3: left column is for the input of porous wave which is a gaussian of varying amplitude (viz. 0.1, 0.08, 0.06 respectively) having width as 7 km and background porosity value as 0.01 and the right column gives three different profiles of fluid velocity obtained at initial time step corresponding to the three different amplitudes of the porous wave plotted at left.

Fig. 4.4: left and right column present the matrix velocity and the ξ profiles respectively obtained at initial time step corresponding to the input of porous wave which is a gaussian of varying amplitude (viz. 0.1, 0.08, 0.06 respectively) having width as 7 km and background porosity value as 0.01.
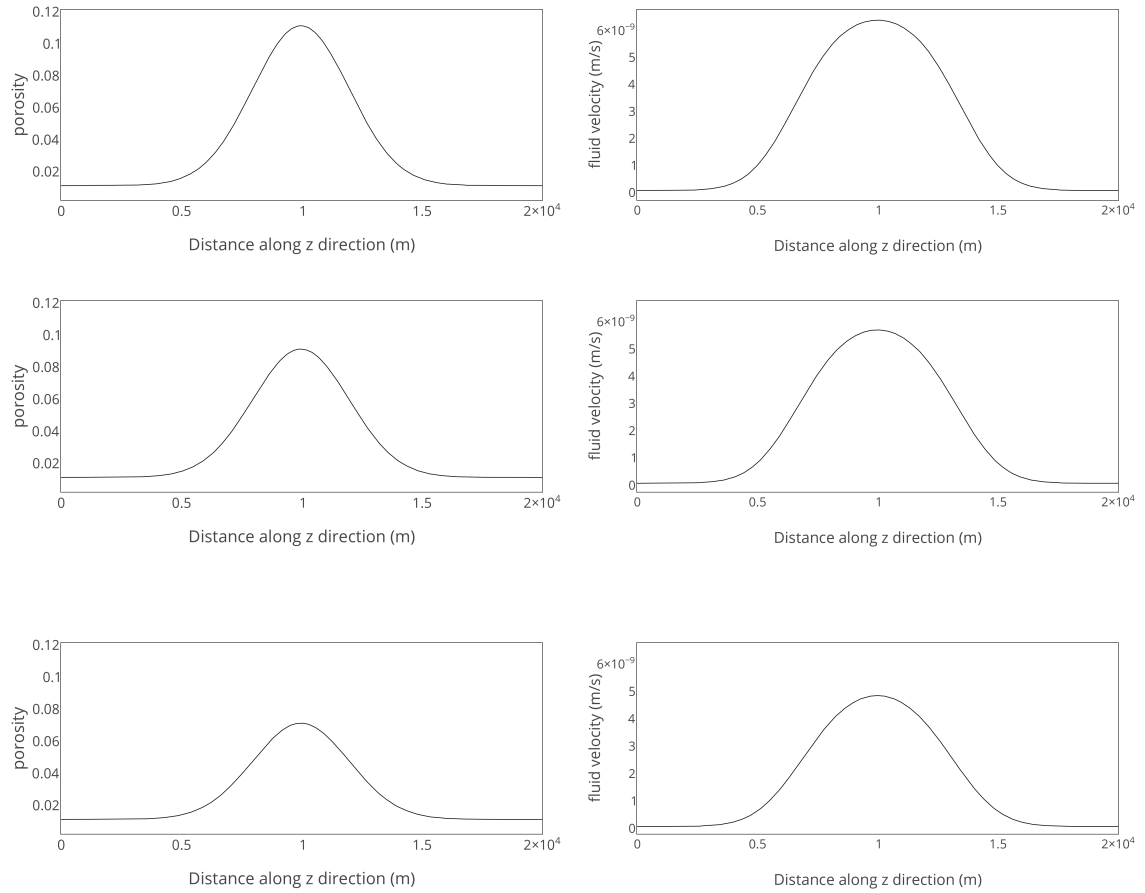
FIG. 4.5: left column is for the input of porous wave which is a gaussian of varying amplitude (viz. 0.1, 0.08, 0.06 respectively) having width as 14 km and background porosity value as 0.01 and the right column gives three different profiles of fluid velocity obtained at initial time step corresponding to the three different amplitudes of the porous wave plotted at left.
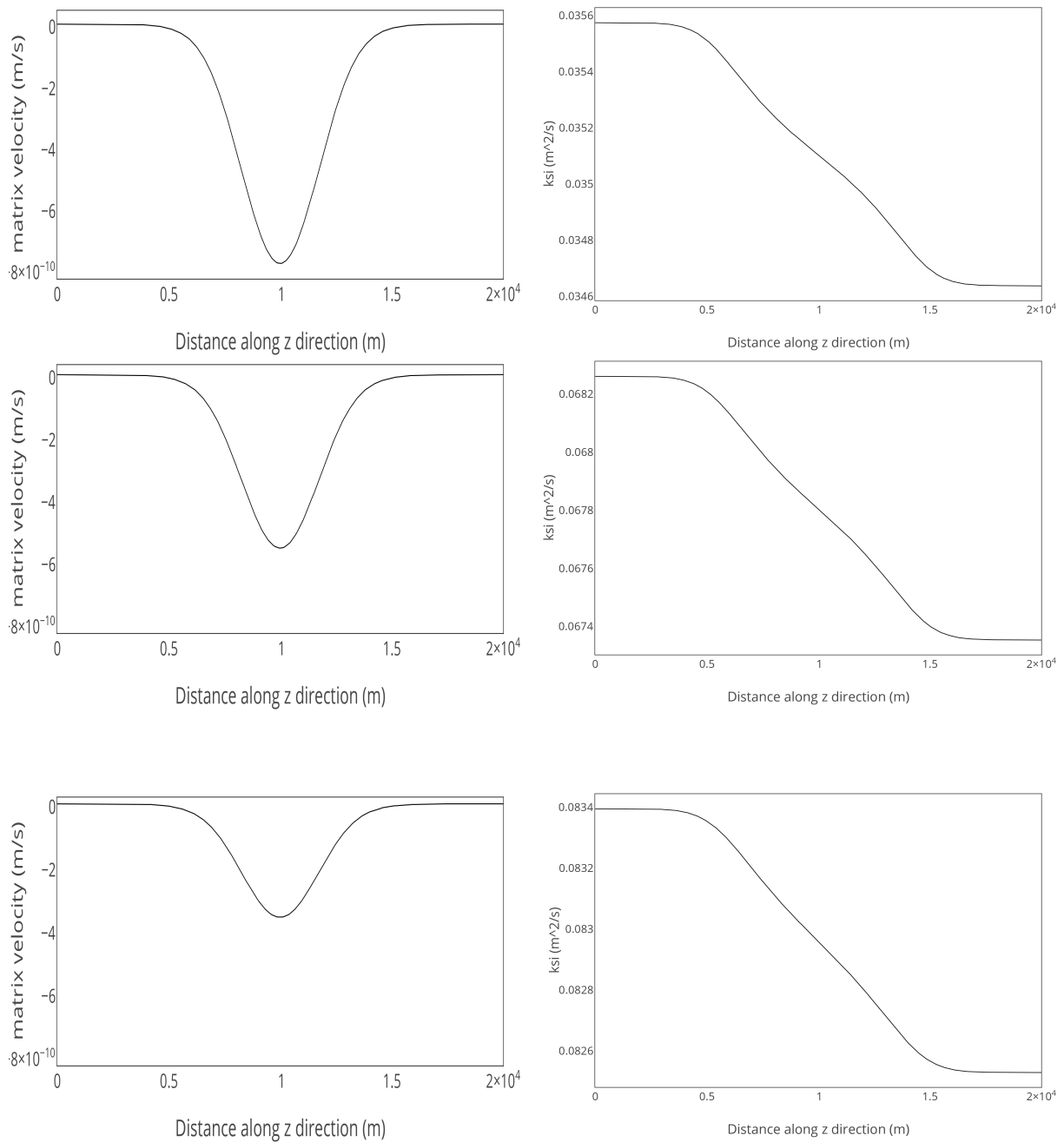
Fig. 4.6: left and right column present the matrix velocity and the ξ profiles respectively obtained at initial time step corresponding to the input of porous wave which is a gaussian of varying amplitude (viz. 0.1, 0.08, 0.06 respectively) having width as 14 km and background porosity value as 0.01.

Remarks:

1) Due to fixed boundary condition, both the matrix and fluid velocity profiles have the value zero in 4.1 - 4.6 near the boundary although the porosity has a finite background value near the boundary.

2) Based on observations derived from fig.4.1 - 4.6 and 4.8, it is clear that with wider gaussian wave, used as an input for porosity, $\nabla \xi$ profile is wider. Also, from 4.7 we see that, segregation velocity profile is wider and has a higher amplitude with wider porous wave (cf. fig. 4.7).

3) Similarly for a particular width, since ξ has lesser slope with decreasing amplitude of the porous wave, segragation velocity also has a smaller amplitude with decreasing amplitude of the porous wave following the assumption $\xi = \theta$ in 1D and the eq.2.2.4 (cf. fig. 4.7).

4) Velocity of the point of maxima of porous wave is smaller with decreasing amplitude of input Gaussian and the velocity increases (for a particular amplitude and background porosity) when the input wave is wider.

5) The decompaction rate (i.e. $\nabla . V_m$) profile has also lesser amplitude with decreasing amplitude of the porous wave having a particular width and the profile is wider as the input porous wave is wider (cf. fig. 4.9).

6) The possible physical explanation to justify fig. 4.9 is, a narrow porosity wave does not produce large overpressure to decompact the matrix on the upper flank. A wide porosity wave needs a wide decompaction region associated with larger distance of porous fluid flow to fill the decompacting porosity region since the fluid can not immediately fill this region. Hence decompaction rate is reduced . Thus there exists a porosity wave with associated with a maximum decompaction rate. In this case, 7 km wide Gaussian input having amplitude 0.11 and background porosity $\phi_0 = 0.01$ for porous wave gives the maximum decompaction rate. It must be noted that for this particular amplitude, background porosity value and associated compaction length the solitary wave (a wave which preserves its shape while propagating until and unless it confronts with any other wave) is 34 compaction length i.e. 10.2 km wide. So, it seems as soon as the width of the initial porous wave is comparable/ nearer to its equivalent solitary wave, the decompaction rate is higher.
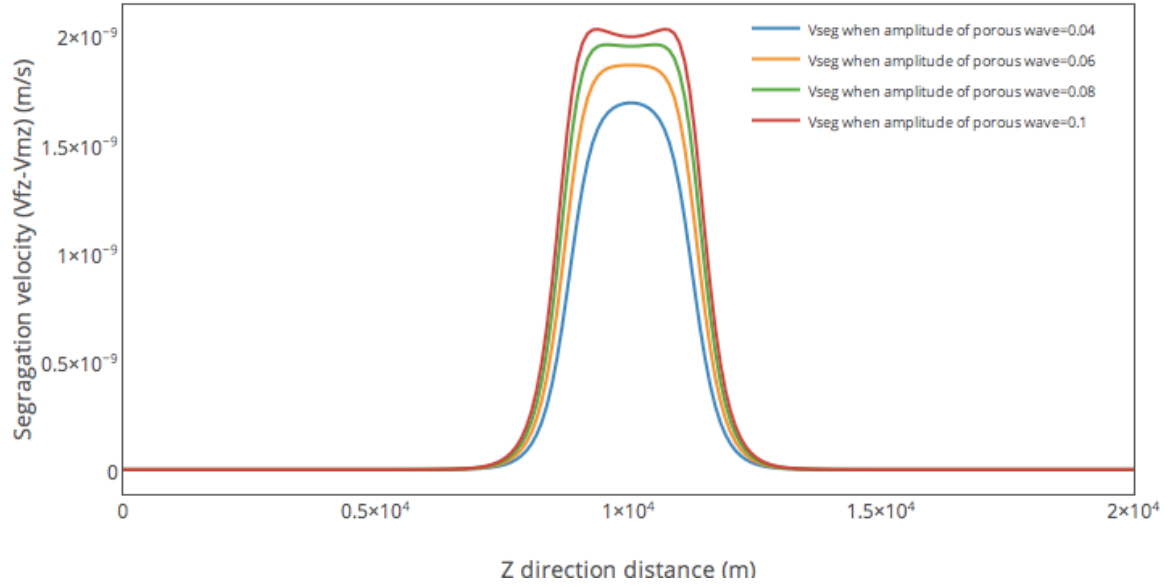
(a)
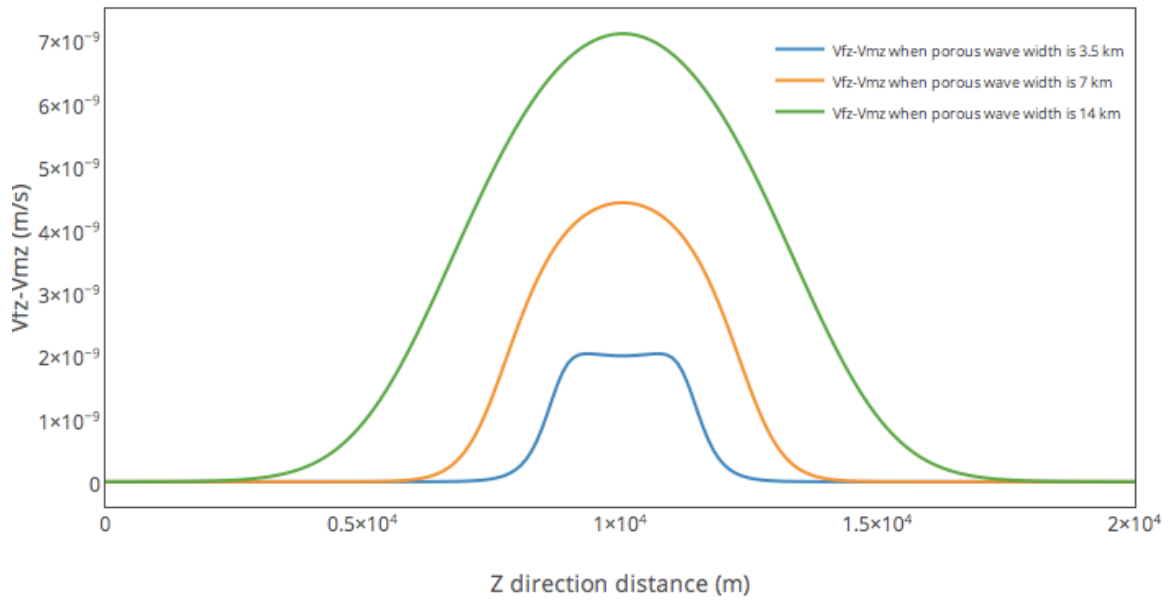
(b)

FIG. 4.7: Initial profiles of segregation velocity ($V_{fz} - V_{mz}$): (a) the segregation velocity profile at initial time step for different amplitude (0.1, 0.08, 0.06 and 0.04 respectively) of input porous wave which is 3.5 km wide (b) the segregation velocity profile at initial time step for input porous wave of amplitude 0.1, having different widths (i.e. 3.5 km, 7 km, 14 km respectively).
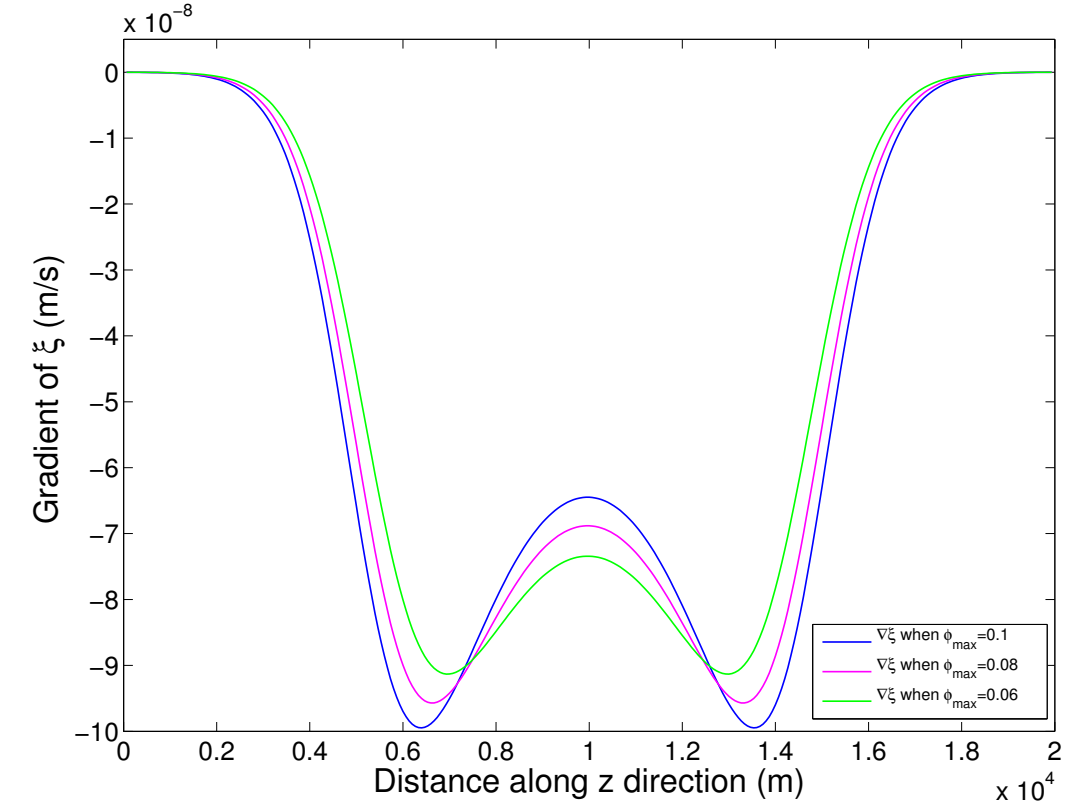
(a)
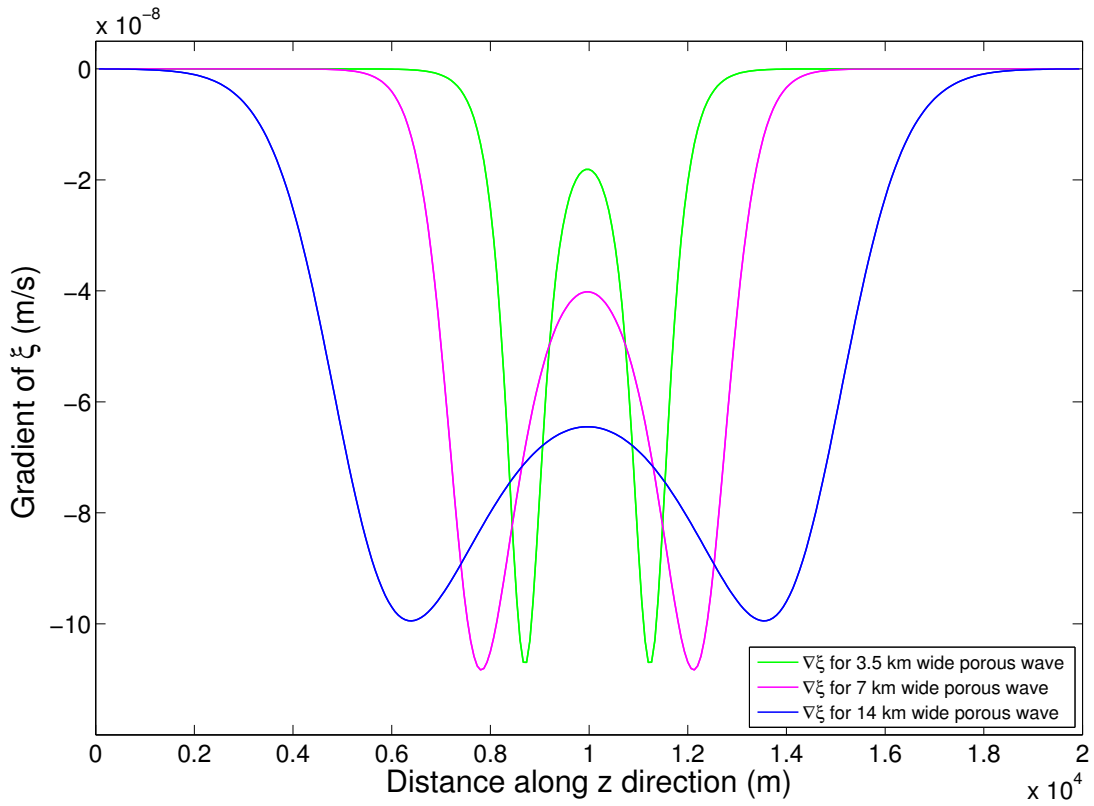
(b)

FIG. 4.8: Initial profiles of $\nabla\xi$: (a) $\nabla\xi$ profile at initial time step for different amplitude (i.e. 0.07, 0.09 and 0.11 respectively) of input porous wave having width 14 km and $\phi_0 = 0.01$ (b) $\nabla\xi$ profile at initial time step for varying width of porous wave (i.e. 3.5 km, 7 km and 14 km respectively) having amplitude 0.11 and $\phi_0 = 0.01$
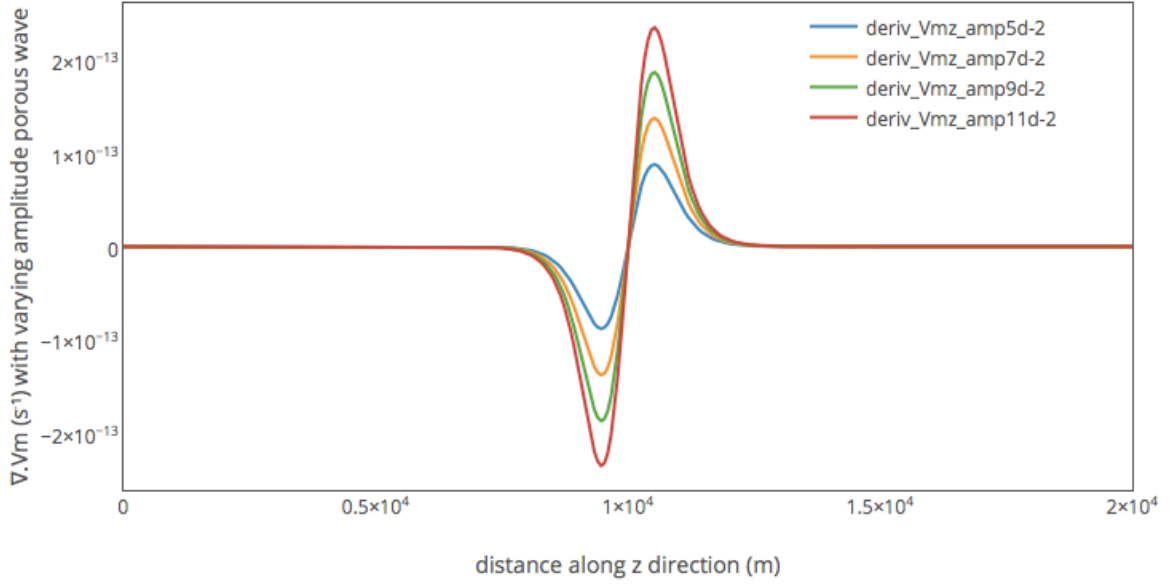
(a)
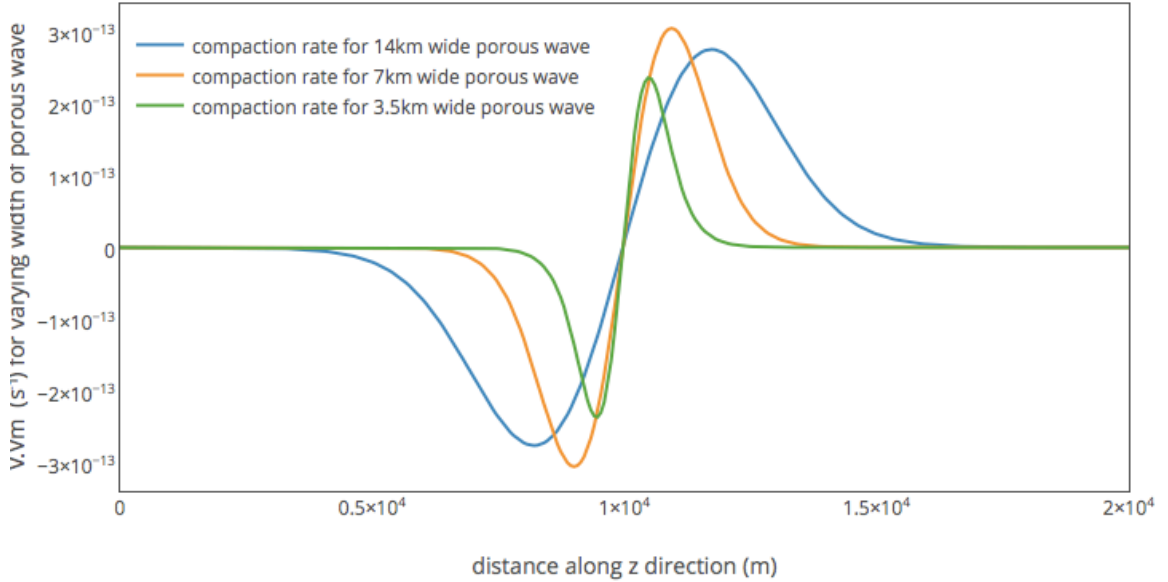
(b)

Fig. 4.9: Initial profiles of matrix compaction rate $(\nabla.V_m)$: (a) matrix compaction rate profile at initial time step for different amplitude (i.e. 0.05, 0.07, 0.09 and 0.11 respectively) of input porous wave having width 3.5 km (b) matrix compaction rate profile at initial time step for varying width of porous wave (i.e. 3.5 km, 7km and 14 km respectively) having amplitude 0.1 and $\phi_0 = 0.01$

4.1.2   Effect of variation of background porosity

In the previous paragraph, effect of varying width and varying amplitude of input porous wave have been discussed. A correlation among matrix compaction rate, segregation velocity and phase velocity of porous wave with decreasing amplitude

or increasing width of input porous wave have been highlighted. Now the input porous wave is modified in such a way that its background porosity is increased keeping fixed its amplitude. i.e. Effective height of input porous wave ($=$ amplitude - ϕ_0) is decreased from the bottom unlike the previous case where effective height of input porous wave was decreased from the top by decreasing its amplitude. This way, we change the compaction length of the model too since compaction length $\delta = \sqrt{\frac{k_0 \phi_0 \eta_m}{\eta_f}}$. Initial profiles of ϕ, ξ, V_{fz} and V_{mz} are illustrated in fig.4.10-4.11 for various background porosity i.e. for $\phi_0 = 0.01$, 0.03 and 0.05 respectively.

ϕ_0	width of wave (km)	amplitude of wave	observations
0.01	14 (cf. Fig.4.10-4.11)	0.11	The magnitude of amplitude of both V_{mz} and V_{fz} profile is decreasing with increasing background porosity of the wave. No double maxima for fluid velocity profile is observed.
0.03	14 (cf. Fig.4.10-4.11)	0.11	
0.05	14 (cf. Fig.4.10-4.11)	0.11	

TABLE 4.3: observations based on varying background porosity when a Gaussian wave having a fixed amplitude and a width is used as an initial input for porosity
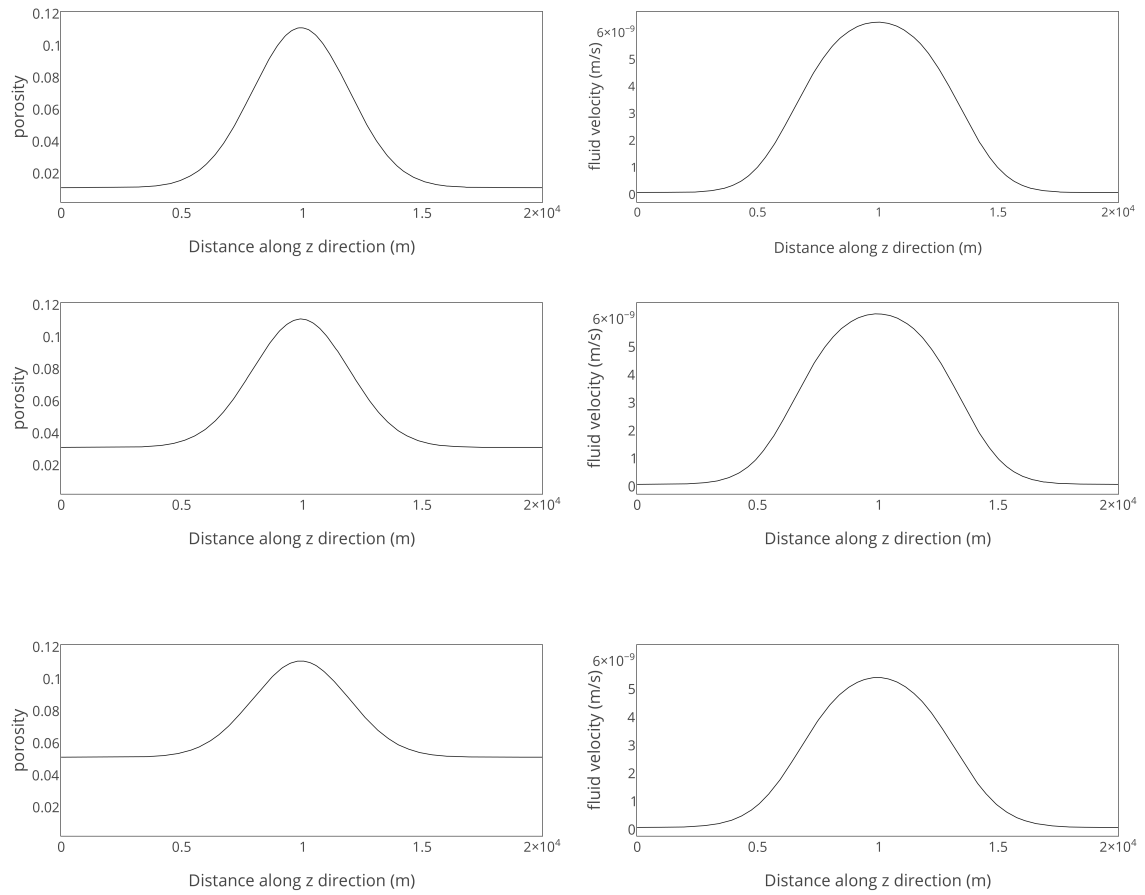
FIG. 4.10: left and right column present the porosity and matrix velocity profiles respectively obtained at initial time step corresponding to the input of porous wave which is a 14 km wide gaussian of varying background porosity values (viz. 0.01, 0.03 and 0.05 respectively) and having amplitude as 0.11.
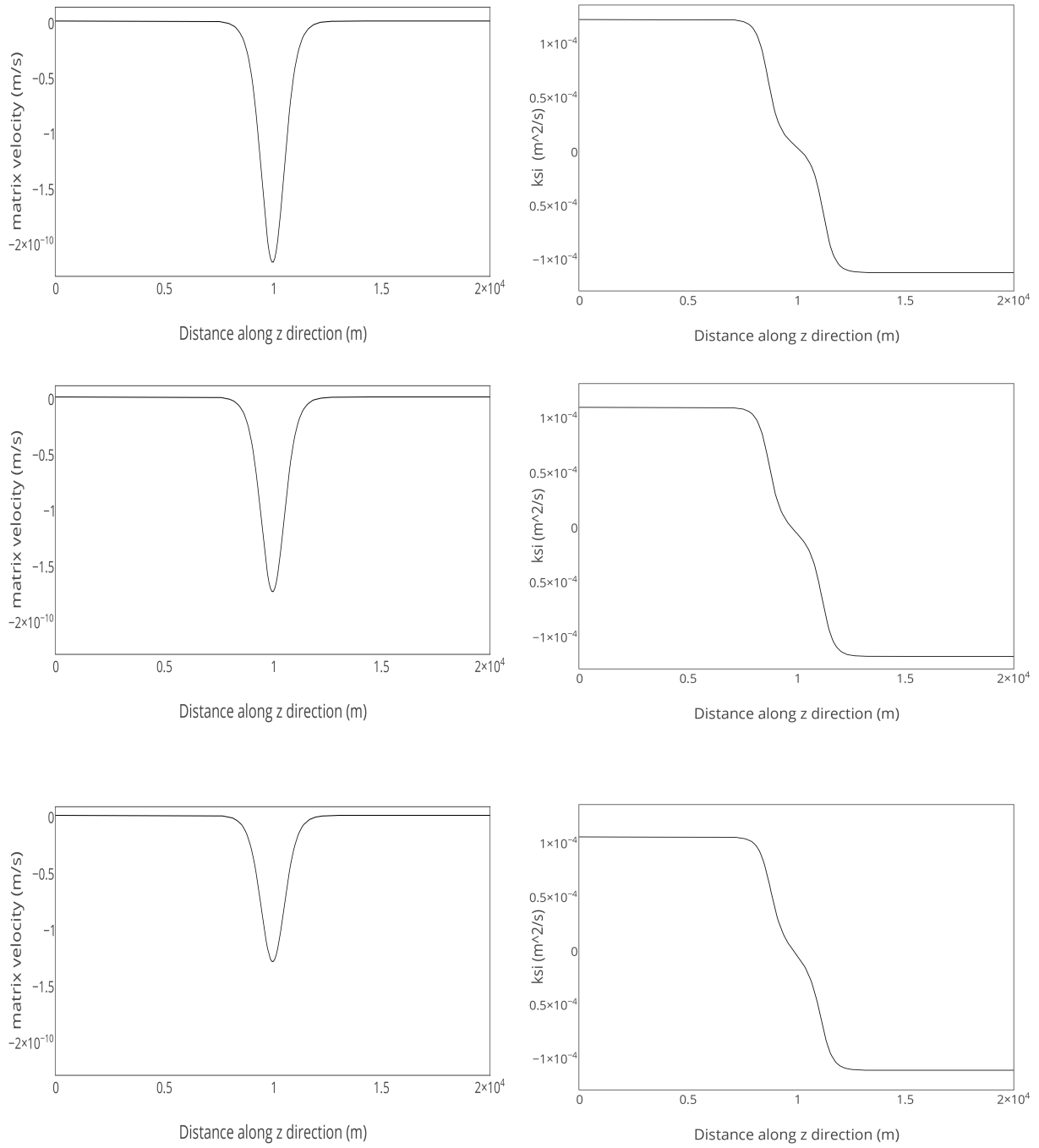
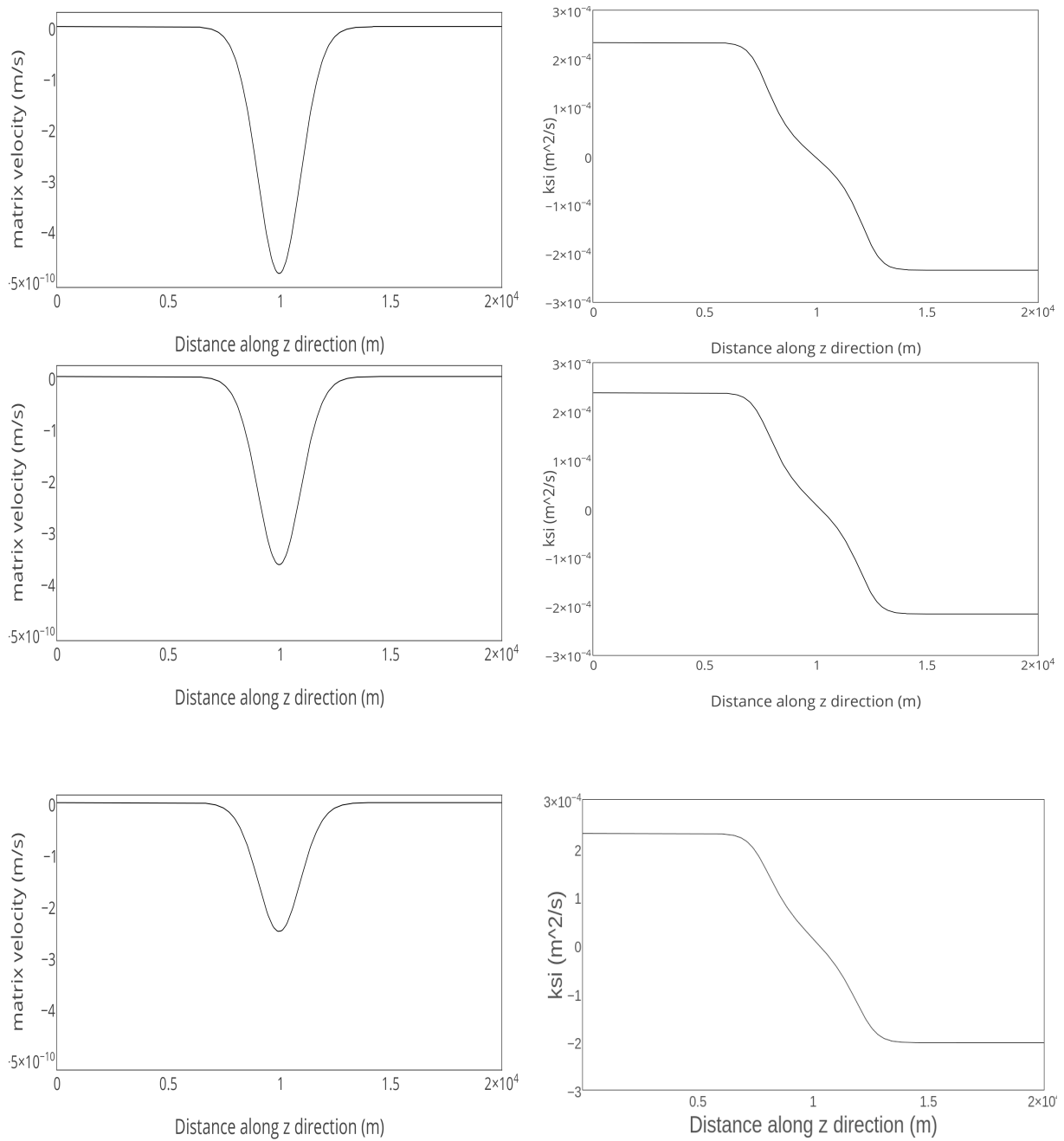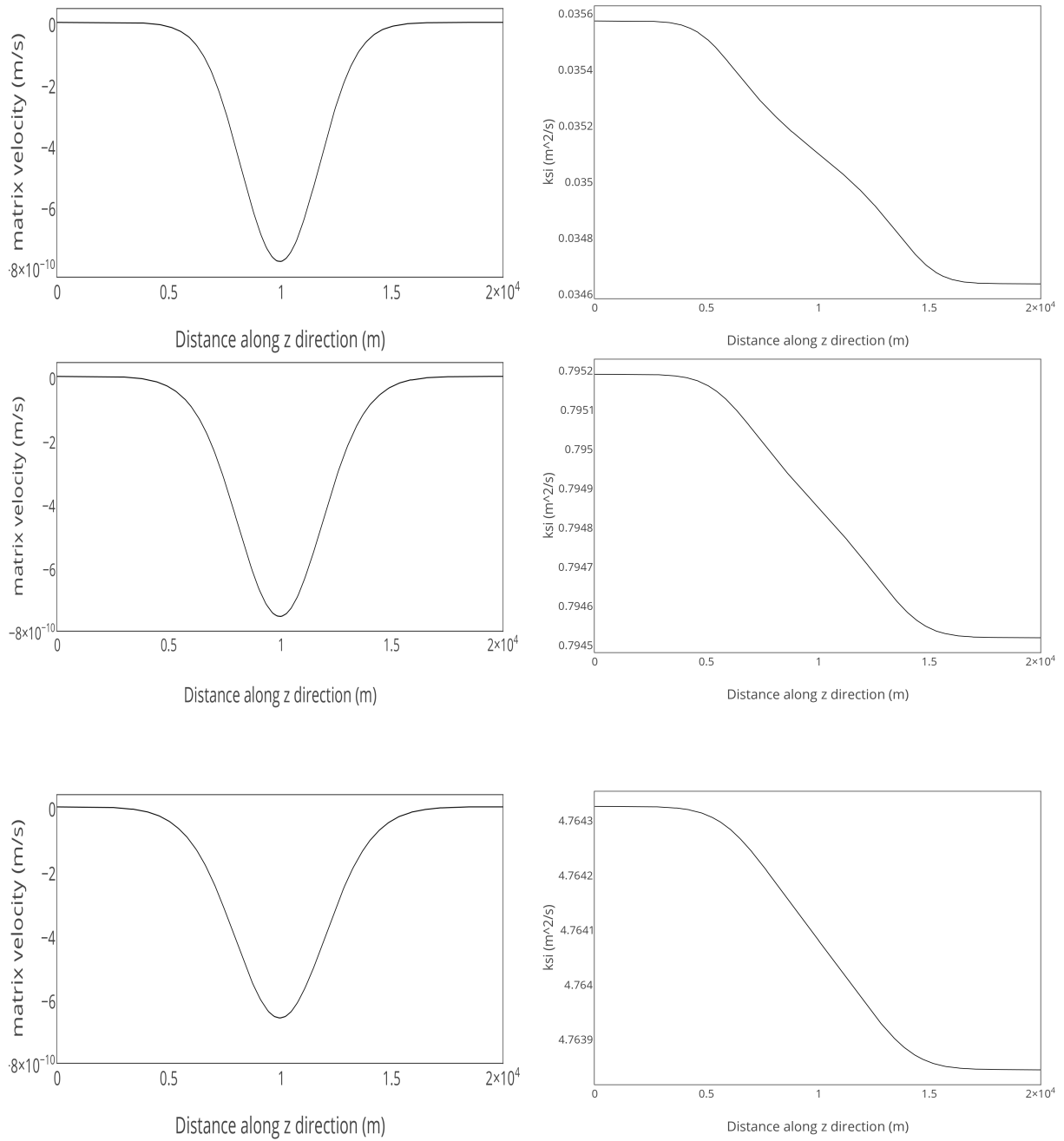FIG. 4.11: left and right column present the matrix velocity and the ξ profiles respectively obtained at initial time step corresponding to the input of porous wave which is a 14 km wide gaussian of varying background porosity values (viz. 0.01, 0.03 and 0.05 respectively) and having amplitude as 0.11.
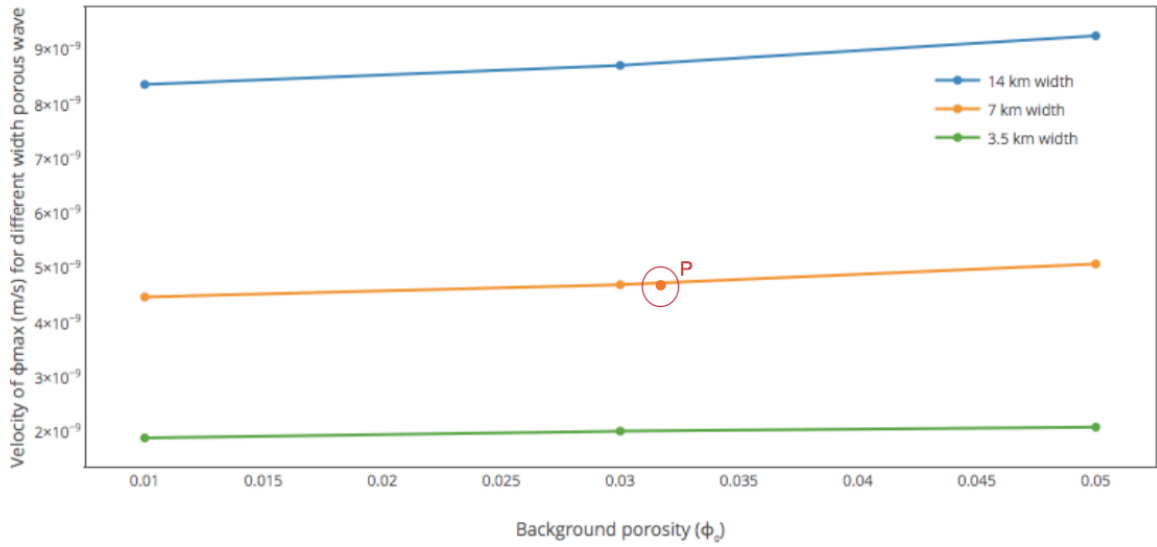
(a)
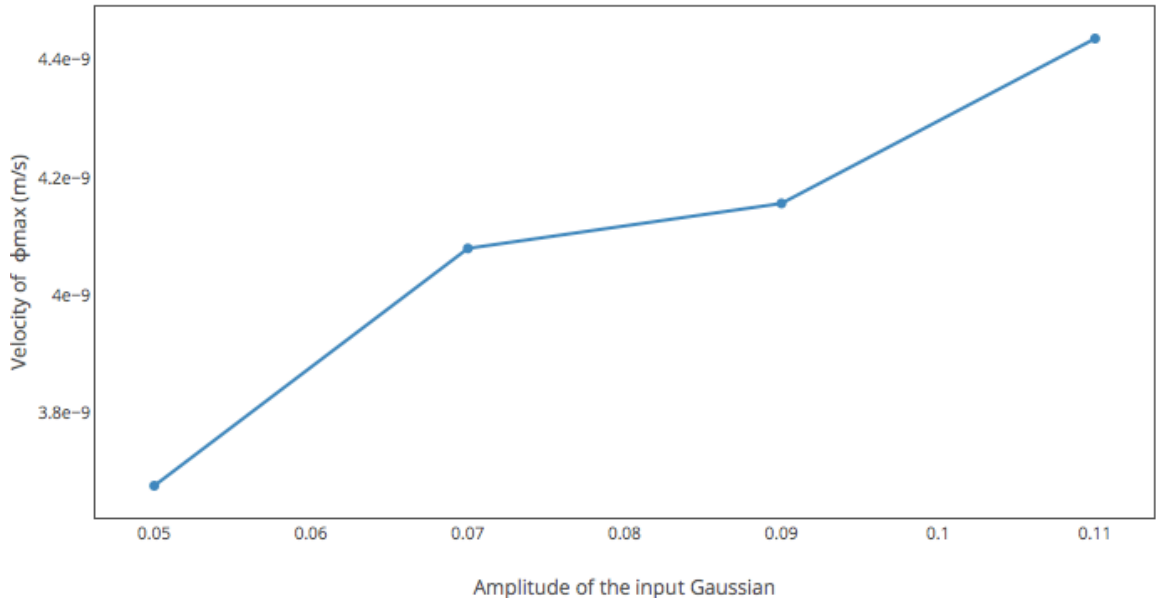
(b)

Fig. 4.12: (a) phase velocity of porous wave w.r.t varying ϕ_0 (0.01, 0.03 and 0.05 respectively) when input Gaussian has a width of 3.5 km, 7 km and 14 km and amplitude as 0.11. The point P marked with a red circle represents velocity of the same Gaussian i.e. of 7km width, 0.11 amplitude but $\phi_0 = 0.01$ under periodic boundary condition. (b) phase velocity of porous wave w.r.t varying amplitude when width of the input Gaussian is 7 km and $\phi_0 = 0.01$

Remarks: For 14 km wide input Gaussian wave having amplitude = 0.11, segregation velocity profile is narrower and shorter (cf. fig. 4.13) with increasing background porosity whereas phase velocity of porous wave increases with increment of background porosity ϕ_0 (fig. 4.12)

FIG. 4.13: Initial segregation velocity $(V_{fz} - V_{mz})$ profile when input Gaussian has a width of 14 km and amplitude = 0.11.
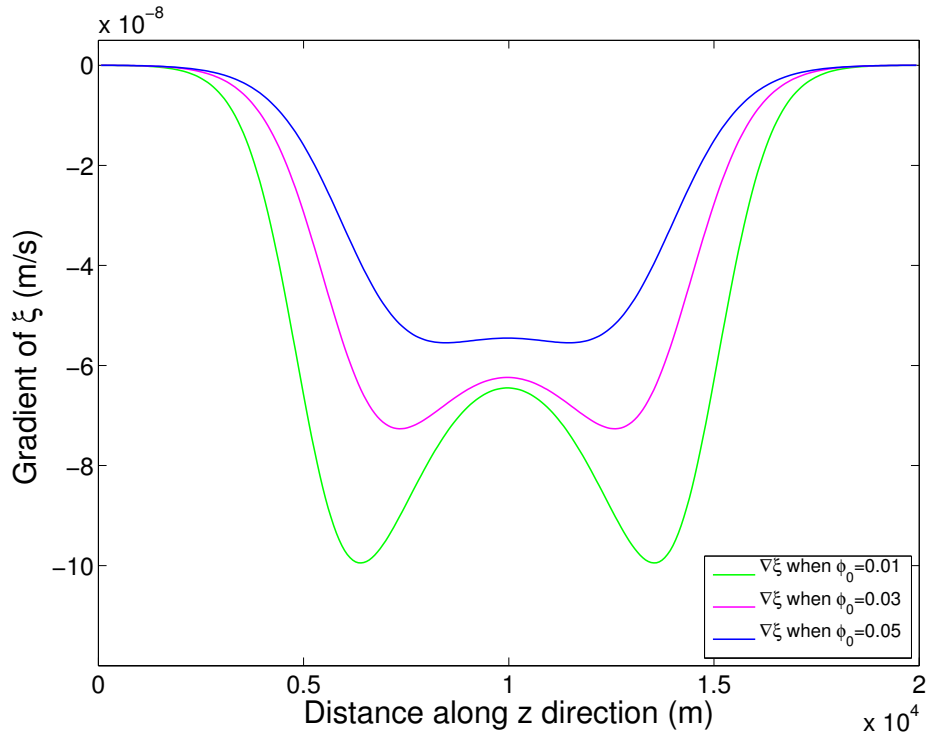
(a) $\nabla\xi$ at 10^{-6} Ma for varying ϕ_0
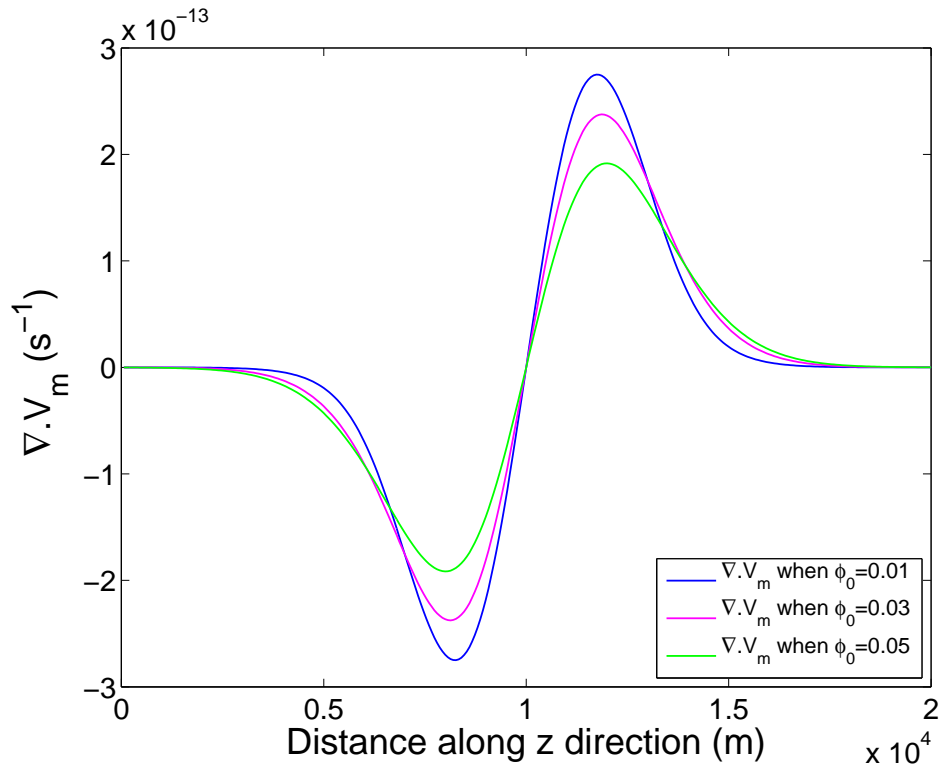
(b) compaction rate ($\nabla.V_m$) profile at 10^{-6} Ma for varying ϕ_0

Fig. 4.14: (a) $\nabla\xi$ profile for different ϕ_0 (i.e. 0.01, 0.03 and 0.05 respectively) of input porous wave having width 14 km and amplitude 0.11 at initial time step (b) $\nabla.V_m$ profile for varying ϕ_0 (i.e. 0.01, 0.03 and 0.05 respectively) of input porous wave having width 14 km and amplitude 0.11 at initial time step

Conclusion: From the discussion in 3.4.1, 3.4.2 and observations derived from fig. 4.13, fig.4.14 it can be concluded that

1) when effective height of input porous wave (i.e. amplitude of the wave - ϕ_0) is decreased the amplitudes of segregation velocity profile, compaction rate profile and $\nabla \xi$ profile also decrease irrespective of the fact that whether amplitude of the input gaussian wave is reduced or the value of ϕ_0 is increased.

2) When amplitude of input porous profile is reduced i.e. when effective height is reduced from the top, the phase velocity of porous profile decreases (fig.4.12) but when background porosity increases i.e. when effective height of input porous profile is reduced from bottom, velocity of porous wave increases (fig. 4.12). In the first case of reducing amplitude of input porous wave doesn't change the compaction length but in the later case the compaction length is changed due to change of value of ϕ_0. Therefore, its the parameter compaction length δ which is responsible for dual characteristics of porous wave velocity whereas in both the cases, effective height of input porous profiles are reduced.

3) Although the porosity has a finite background value at the boundary, the matrix and fluid velocities or the segregation velocity is zero near the boundary and the reason for that is the boundary condition imposed here which says that the velocities are zero at the boundary.

4) Phase velocity of porous wave increases with its increased width (fig.4.12). One must notice that similar correlation between increment of phase velocity and increment of background porosity, increment of width, increment of amplitude for the case of solitary wave but the ratio of increment of phase velocity and increment of other parameters are not necessarily same with that of a normal Gaussian. For example, in fig. 4.12 we see that phase velocity of porous wave almost doubles when its width is doubled keeping its amplitude fixed. But for two solitary waves whose amplitudes are same but one of them has double width compare to other has a velocity almost 3.5 times higher than the other [Richard et al., 2012].

5) The right hand side figure of fig. 4.12 is also comparable with the solitary wave behavior regarding the relation between its speed and its amplitude as discussed in[Richard et al., 2012]. Because, as soon as dimensional wave's amplitude increases, from 0.05 to 0.11, its corresponding non dimensional solitary wave has an amplitude of 11 and 5 respectively and according to equations given in [Richard et al., 2012] one can calculate that the speed of the solitary wave having amplitude 11 is almost 1.2 times its speed when its amplitude is 5 and the similar behavior we observe for the Gaussian in figure (b) of fig. 4.12. The step like shape instead of a linear one as seen in figure (b) of fig. 4.12, is mainly due to numerical which can be justified by comparing this figure with fig.3.5.

4.1.3   Effect of variation of compaction length

Solitary wave's wavelength has been observed as 30-40 compaction length wide [Barcilon and Lovera, 1989; Barcilon and Richter, 1986; Scott and Stevenson, 1984, 1986a; Simpson and Spiegelman, 2011]. Therefore the motivation of this test by changing the compaction length is to observe the wave propagation characteristics when their wavelength are narrower, broader or closer compare to that of an equivalent solitary wave. A change of compaction length is made in such a way that changing the value of 3 parameters i.e. the permeability constant k_0, matrix viscosity η_m, background porosity ϕ_0 result in a same compaction length which is approximately 100 m. This is executed by 1) changing matrix viscosity η_m, 2) by changing value of permeability constant k_0 and 3) by changing background porosity ϕ_0. The numerical tests which are discussed in 4.4.1 and 4.4.2, matrix viscosity $\eta_m = 10^{18} Pa.S$, $\phi_0 = 0.01$ (in 3.4.1) and $k_0 = 10^{-10} m^2$ were used. Therefore, 1) in first step, we make $\eta_m = 10^{17} Pa.S$, 2) in second step changing permeability constant k_0 value from $10^{-10} m^2$ to $10^{-11} m^2$ keeping old values of ϕ_0, η_m same and 3) in third step changing the background porosity ϕ_0 to 0.001 keeping the old η_m, k_0 same. Hence, in all the three cases, compaction length δ is equal to 100 m. By doing so, for the first test discussed in 3.4.1, i.e. for 3.5 km wide gaussian as an input of porous wave, we now have around 35 compaction lengths through out the Gaussian's wavelength. Then we observe that in any of these three cases, the fluid velocity profile at initial time step doesn't produce any double maxima (cf. fig.4.14) unlike fig.4.1.
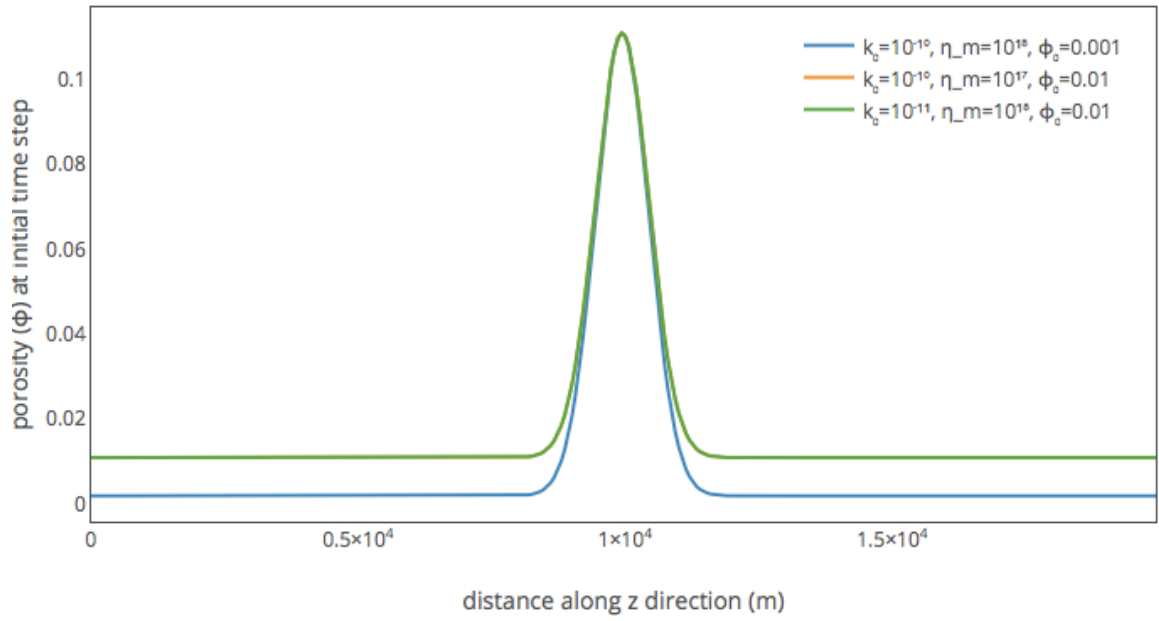
(a) Porosity (ϕ) at 10^{-6} Ma
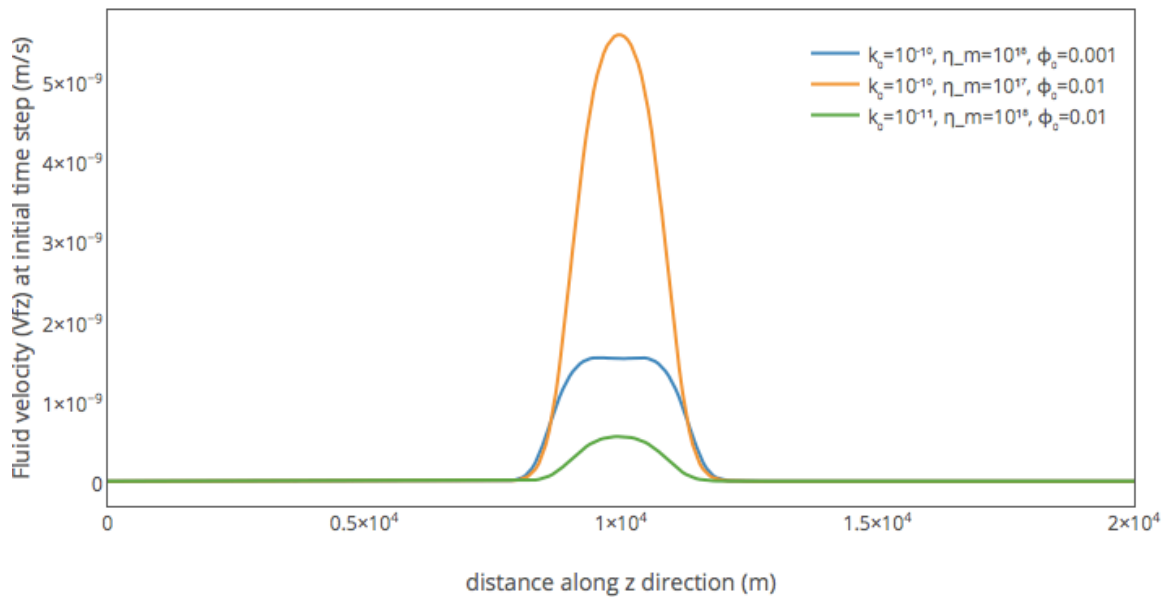
(b) Fluid velocity (V_{fz}) profile at 10^{-6} Ma
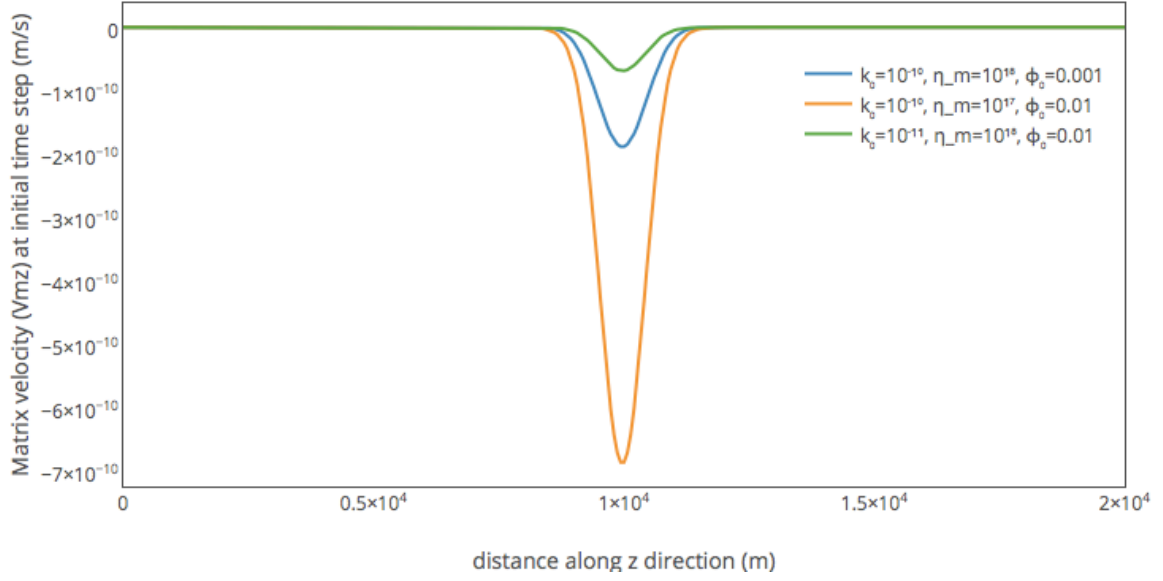
(c) Matrix velocity (V_{mz}) profile at 10^{-6} Ma
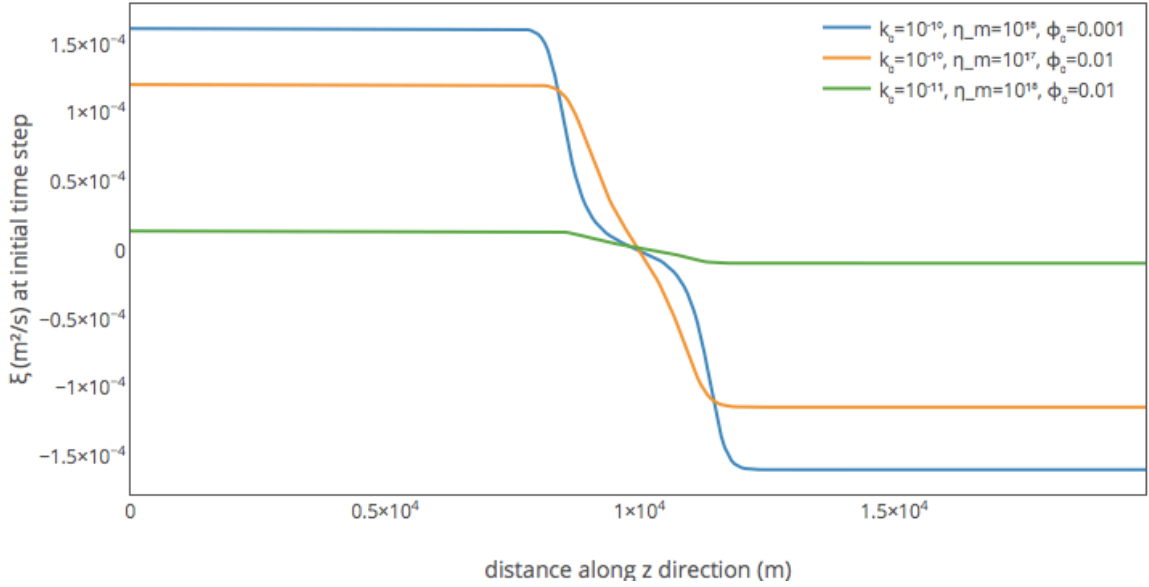
(d) ξ profile at 10^-6 Ma

FIG. 4.14: (a) ϕ profile for different ϕ_0, k_0, η_m respectively when input porous wave having width 3.5 km and amplitude 0.11 at initial time step (b) V_{fz} profile for different ϕ_0, k_0, η_m respectively when input porous wave having width 3.5 km and amplitude 0.11 at initial time step (c) V_{mz} profile for different ϕ_0, k_0, η_m respectively when input porous wave having width 3.5 km and amplitude 0.11 at initial time step (d) ξ profile for different ϕ_0, k_0, η_m respectively when input porous wave having width 3.5 km and amplitude 0.11 at initial time step

Observations: In the first two cases, the dimensionless numbers controlling the physics are the same when $\phi_0 = 0.01$ were used and together they constructed same melt retention number scaled with k0. But the 3rd case where $\phi_0 = 0.001$ is used, is physically different. The curve shapes are not similar as can be seen be

the flat maximum on the V_f profile or the segregation profile (cf fig.4.14, fig.4.16). Magnitude of amplitude of both fluid and matrix velocity profiles are highest when matrix viscosity η_m is lowest i.e. 10^{17} Pa s and these amplitudes are lowest when permeability constant k_0 is lowest i.e. $10^{-10} m^2$.
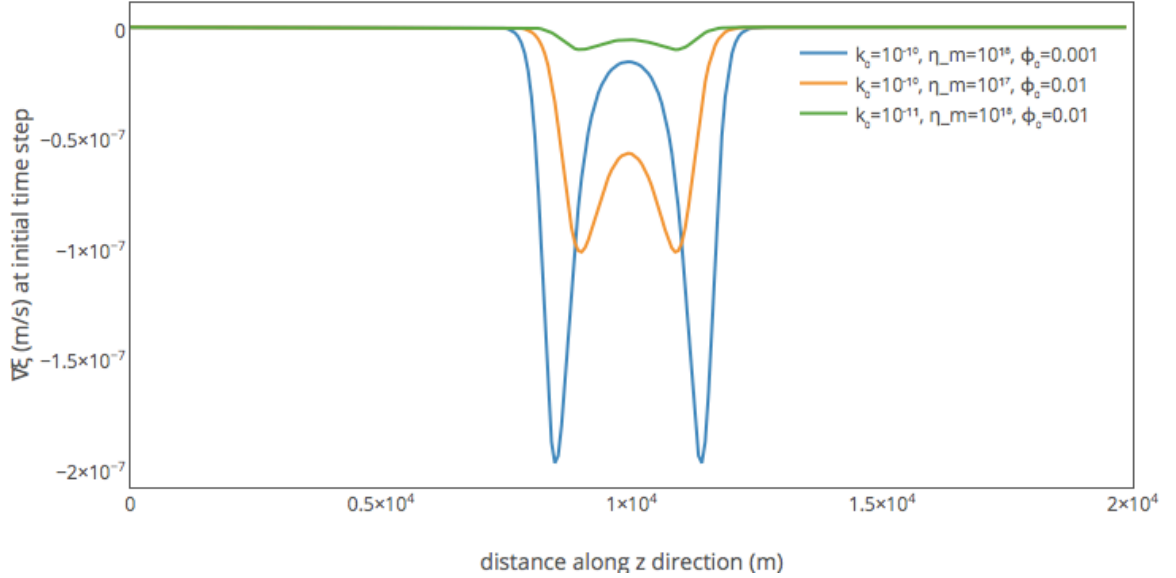
(e) $\nabla\xi$ at 10^{-6} Ma
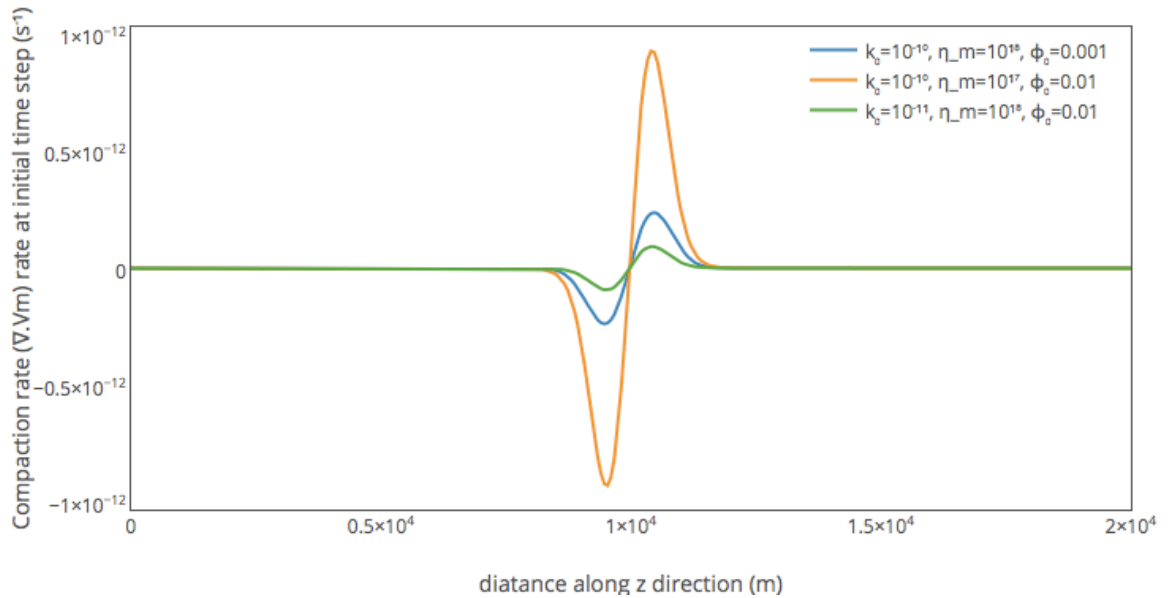
(f) $\nabla.V_m$ profile at 10^{-6} Ma

FIG. 4.15: (a) Flux due to matrix compaction ($\nabla\xi$) profile for different ϕ_0, k_0, η_m respectively when input porous wave having width 3.5 km and amplitude 0.11 at initial time step (b) Compaction rate ($\nabla.V_m$) profile for different ϕ_0, k_0, η_m respectively when input porous wave having width 3.5 km and amplitude 0.11 at initial time step
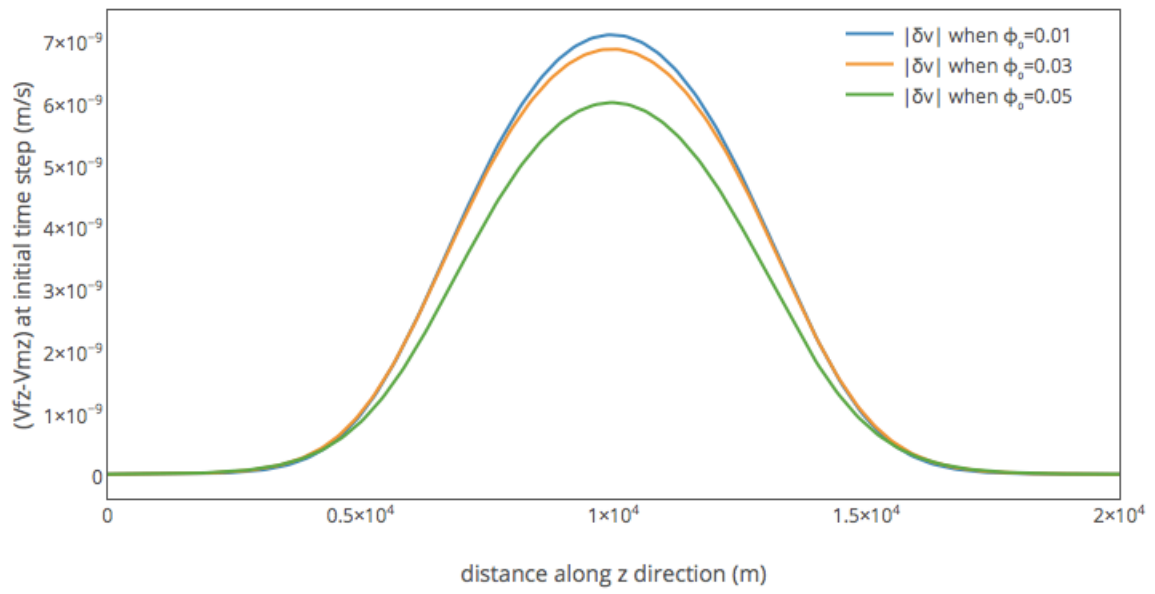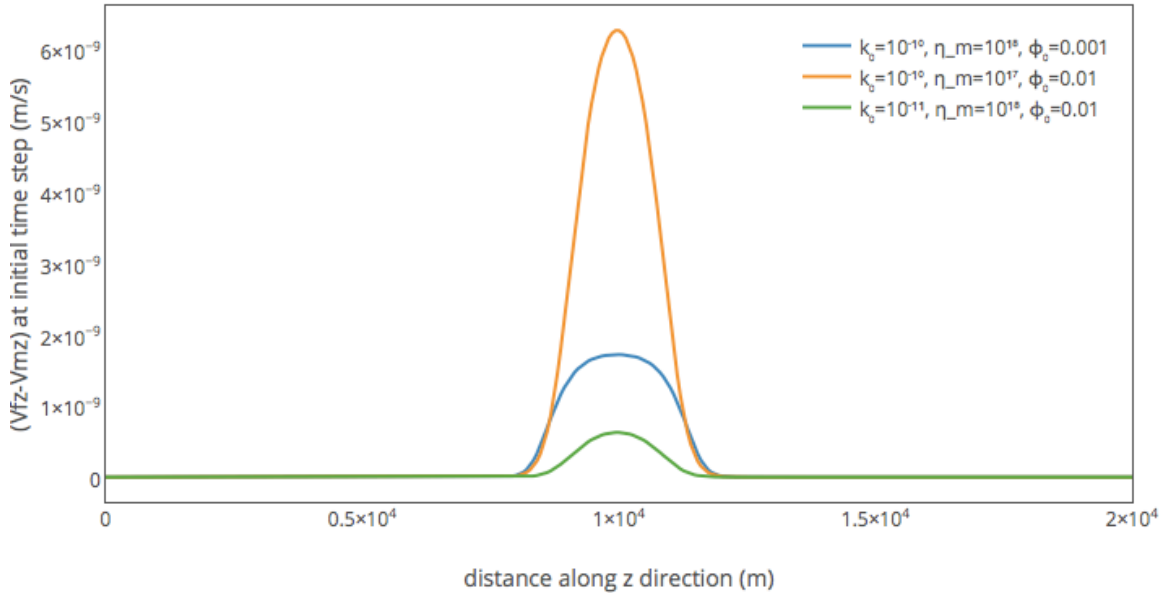
FIG. 4.16: Initial segregation velocity $(V_{fz} - V_{mz})$ profile when input Gaussian has a width of 3.5 km and amplitude $= 0.11$.

The porosity wave propagation nature is different for compaction lengths 300 m and 100 m. (cf. fig 4.17). For larger compaction length, the Gaussian wave of wavelength 7 km or 10 km, increases its amplitude creating a solitary wave train and at the same time it becomes narrower compare to its original shape after a certain time interval. Both the 7 km and 14 km wide Gaussian never drops down its background porosity during their time propagation. But the Gaussian having wavelength 3.5 km becomes wider , decreases its amplitude and also it goes below the background porosity after a certain time interval. For the smaller compaction length i.e. when the compaction length is 100 m the 3.5 km wide wave behaves in the same way like the 7 km and 14 km wide Gaussians for the case when compaction length $\delta = 300$ m was used.
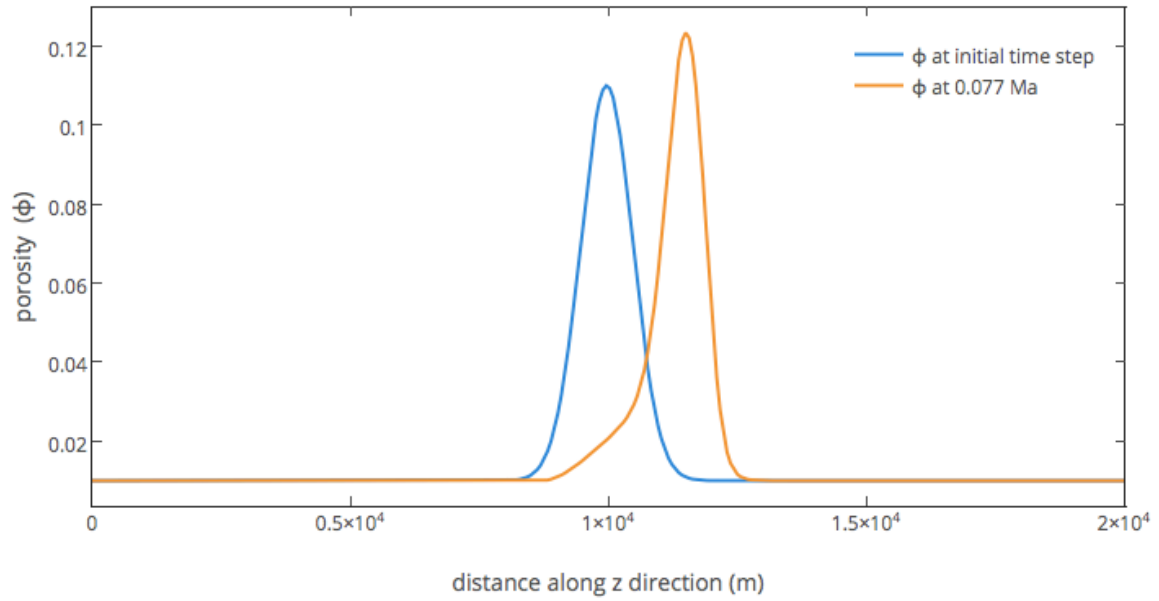
(a)
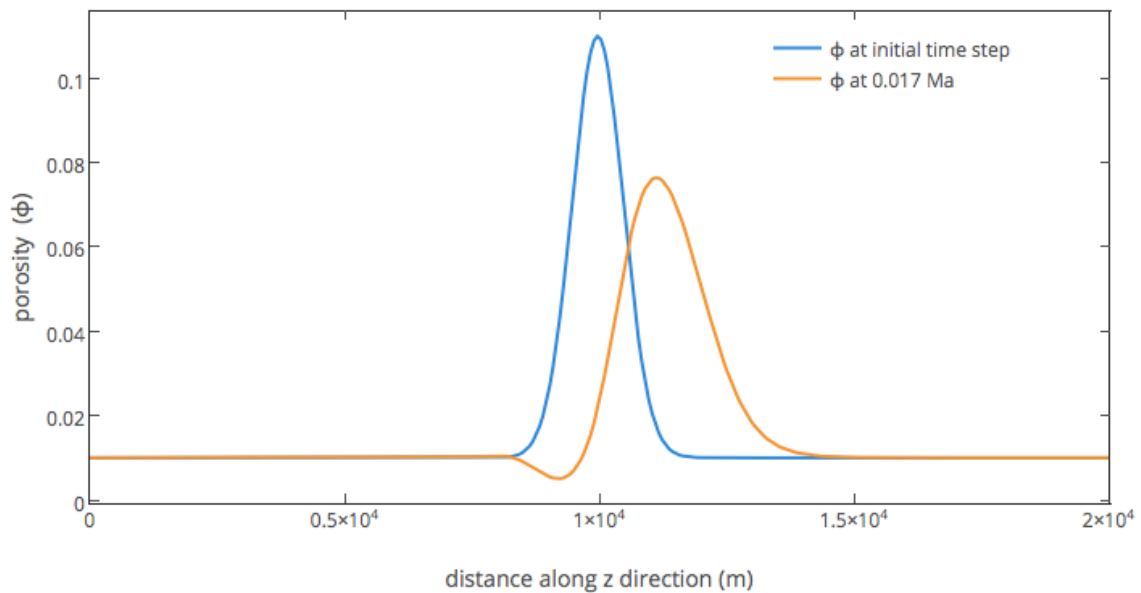
(b)

FIG. 4.17: (a) time propagation of porosity wave when $\delta = 100$m (b) time propagation of porosity wave when $\delta = 300$m

The possible physical explanation for this different characteristics of different width waves is, when the wave is too narrow compare to its equivalent solitary wave the compaction pressure distribution is asymmetric. Therefore, it is not synchronized with buoyancy of the two phase flow and so the fluid has a tendency to flow downwards whereas part of that fluid moves upward with higher amplitude and this way the depression occurs in fluid velocity profile cf fig. 4.1. In $\delta = 300$m case, the equivalent solitary wave i.e. the solitary wave which has the same dimensional

amplitude and ϕ_0 as it is for the Gaussian input , has wavelength of 34 compaction length which is approximately 10.2 km. As the 3.5 km Gaussian is too narrow compare to its equivalent solitary wave the fluid velocity's depression phenomenon as discussed earlier, occurs. In this case, at the same time due to the asymmetric pressure distribution, two regions of pressure are created in the porous wave profile. The region of overpressure widens the wave and the region of underpressure wants to suck melt inside but due to fixed boundary condition background melt velocity is forced to be zero and hence porosity accumulates the required melt from its surrounding which is the reason why after a certain time interval at some part of the profile porosity goes below the background porosity. This phenomena doesn't occur with 7km or 10 km wide wave because they were closer in wavelengths compare to their equivalent solitary wave. Same situation appears for 3.5 km wide Gaussian in the later case i.e. when $\delta = 100$m. In this case its equivalent solitary wave has a width of 37 compaction lengths i.e. the wave is 3.7 km wide and 3.5 km wide Gaussian is very close to that which is why neither the depression phenomena of fluid velocity profile nor the tendency of porous wave going below its background porosity at some part of the profile after certain time interval is observed.

Remarks: For segregation velocity and compaction rate, magnitude of their respective amplitude is highest when matrix viscosity η_m is lowest i.e. 10^{17} Pa.S and the same are lowest when permeability constant k_0 is lowest i.e. $10^{-11}m^2$. But $\nabla\xi$ is more controlled by effective height of input porous wave (i.e. actual amplitude-ϕ_0) it seems as magnitude of its amplitude is highest when ϕ_0 is lowest i.e. the effective height of input porous wave is highest.

4.2 1D numerical experiments with periodic boundary condition

According to the boundary conditions discussed in 3.1.2.2. we execute the following numerical experiments in 1D. For this experiment we use gaussian curve of width 7 km as an initial input for porosity and the background porosity $\phi_0 = 0.01$ and $\phi_0 = 0.03$ respectively in order to get an insight of effect of variation of background porosity on porosity, fluid and matrix velocity and ξ profiles since changing ϕ_0 causes change in compaction length as discussed in 3.4.3. The observations of this experiment are given in the table 4.4.

ϕ_0	width of wave (km)	amplitude of wave	observations
0.01	7 (cf. Fig.4.18)	0.11	It is observed that increase of value of ϕ_0 leads to the uplift of magnitude of boundary values of ϕ, V_{fz} , V_{mz} and ξ profiles. It must be noted that the boundary values of velocity profiles are non zero because of having different boundary conditions. A double maxima is observed for fluid velocity profile when $\phi_0 = 0.03$
0.03	7 (cf. Fig.4.18)	0.11	

TABLE 4.4: observations under periodic boundary conditions when the background porosity ϕ_0 of input porous wave having width 7 km and an amplitude 0.11, is varied

Discussion: The initial parameters which are used to produce left column of fig.4.18 make the compaction length $\delta \sim 300$ m. Changing ϕ_0 from 0.01 to 0.03 increases the compaction length. For $\phi_0 = 0.03$ with remaining parameters same, doesn't produce any double maxima for fluid velocity profile under fixed boundary condition when the same gaussian was used as an input. Therefore, from the discussion in 3.4.3, it seems that under periodic boundary conditions, more number of compaction lengths are required throughout the width of the input wave in case of periodic boundary conditions compare to fixed boundary condition. That's why no double maxima is observed for $\phi_0 = 0.03$ in fig.4.19 when width of initial input is doubled i.e. 14 km so that there are enough number of compaction lengths throughout the width of initial porous wave. If we compare fig.4.14 and fig. 4.20, we will see that all the profiles have similar characteristics with increment of ϕ_0 except the boundary values due to having different boundary conditions. Effective height of segregation velocity (i.e. actual amplitude-background value) decreases in both the figures with the decrease of effective height (amplitude - ϕ_0) of input porous wave.
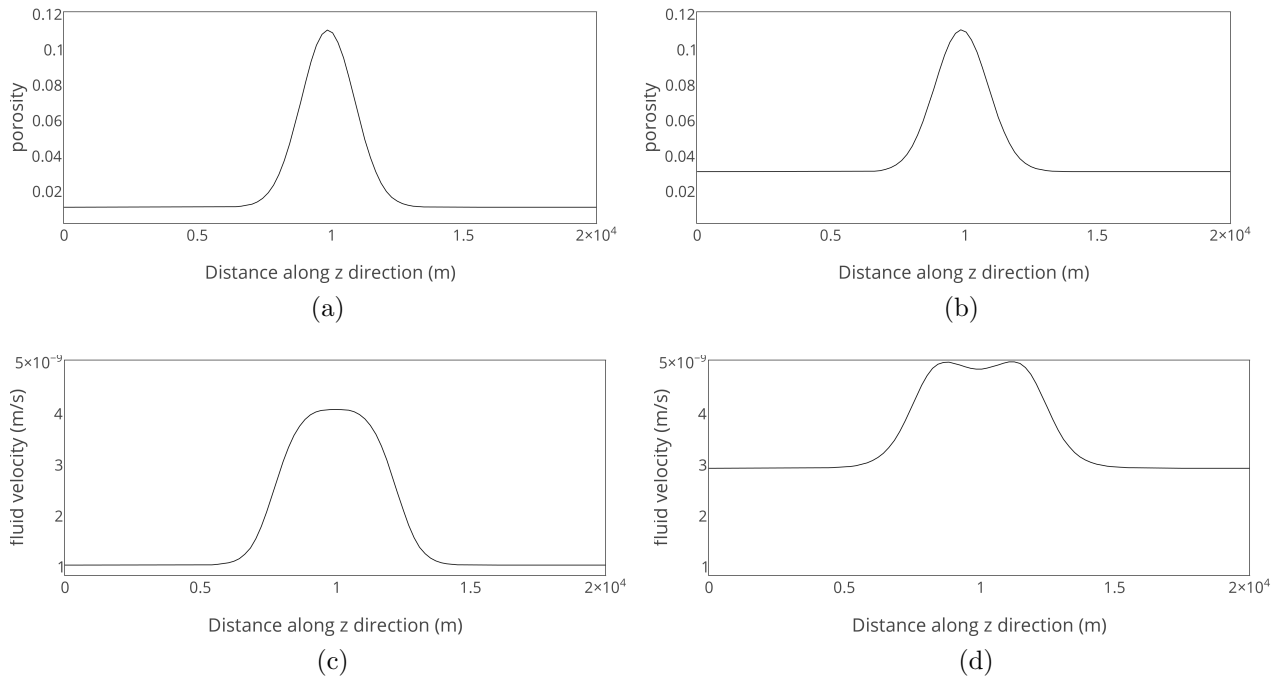
FIG. 4.18: Initial profiles of (a) Porosity for $\phi_0 = 0.01$, (b) Porosity for $\phi_0 = 0.03$, (c) Fluid velocity for $\phi_0 = 0.01$ and (d) Fluid velocity for $\phi_0 = 0.03$ under periodic boundary condition.

(e)

(f)

(g)

(h)
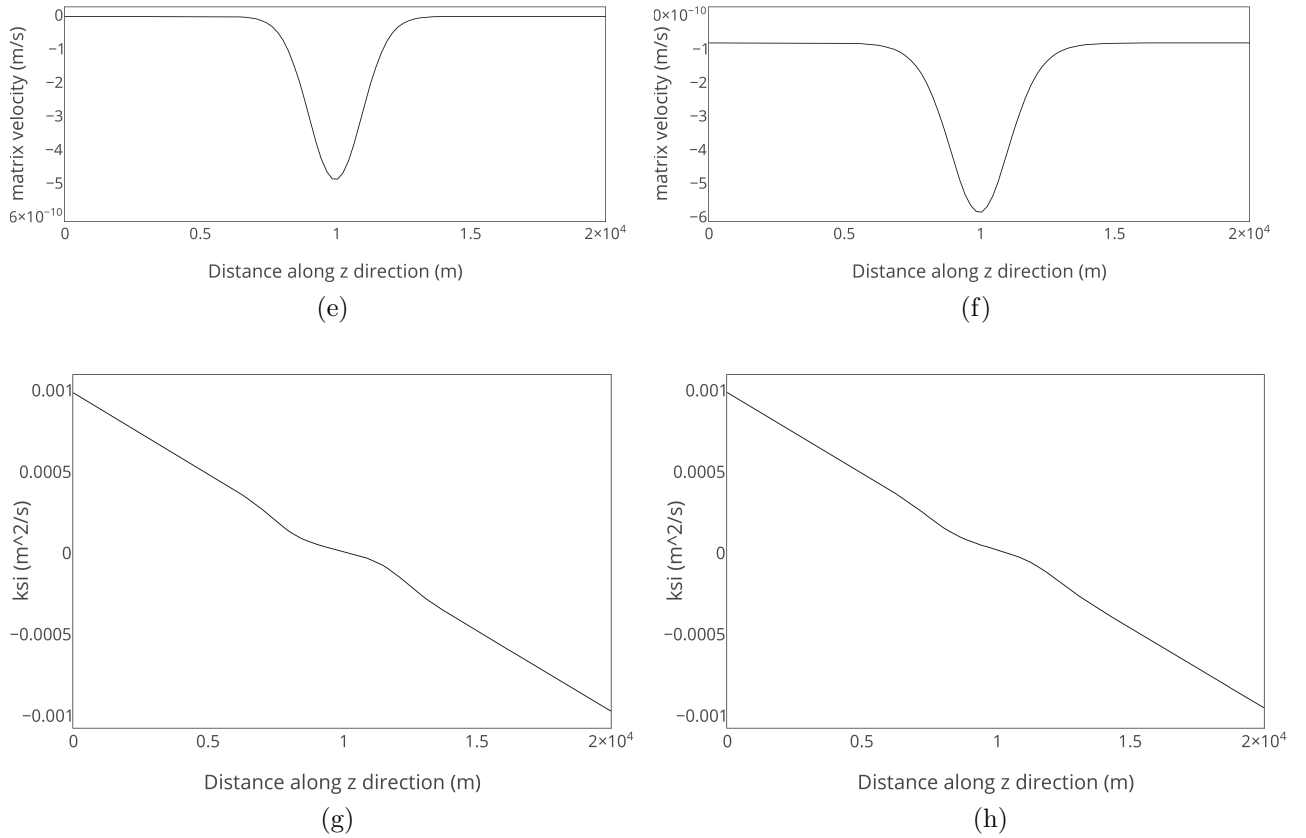
FIG. 4.18: Initial profiles of (a) Matrix velocity for $\phi_0 = 0.01$, (b) Matrix velocity for $\phi_0 = 0.03$, (c) ξ for $\phi_0 = 0.01$ and (d) ξ for $\phi_0 = 0.03$ under periodic boundary condition.
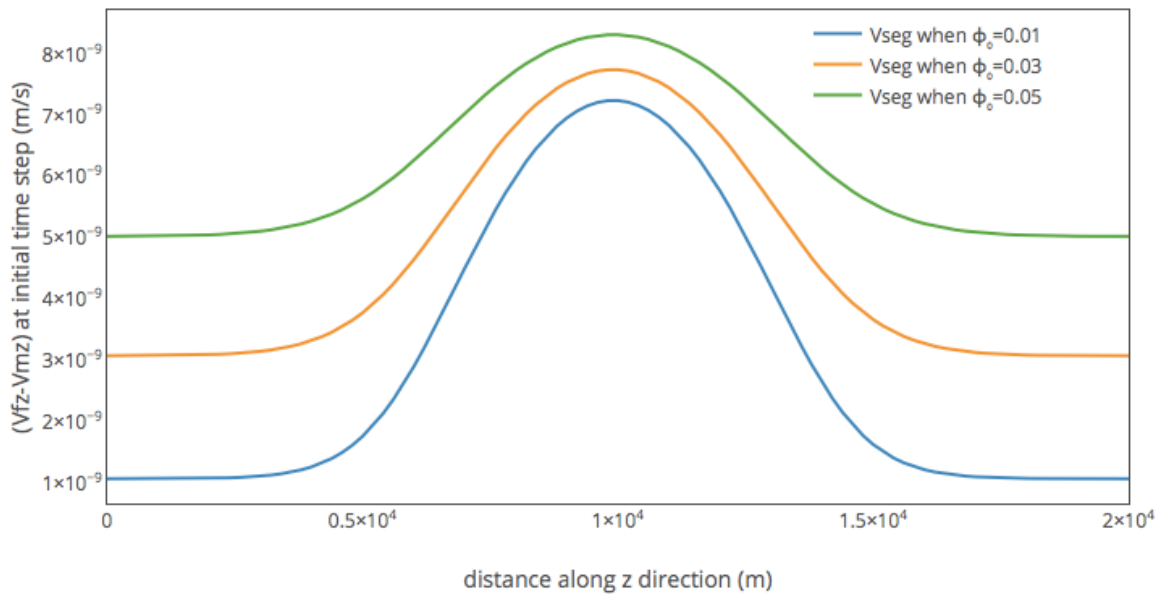
FIG. 4.19: Initial segregation velocity $(V_{fz} - V_{mz})$ profile at initial time step under periodic boundary condition when input Gaussian has a width of 14 km and amplitude $= 0.11$.
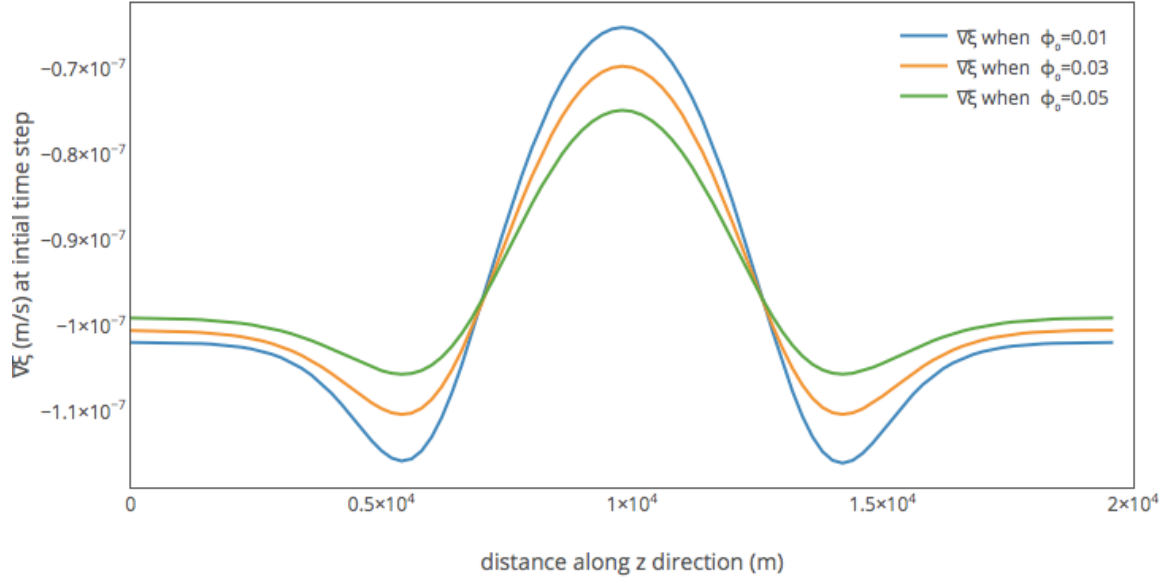
(a) $\nabla \xi$ at 10^{-6} for varying ϕ_0
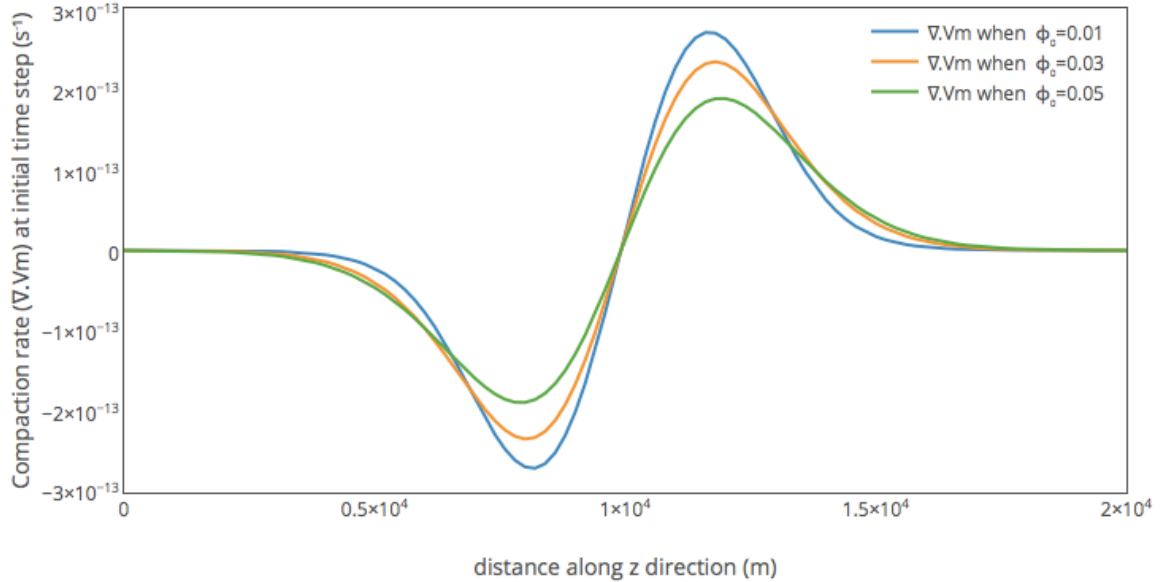
(b) compaction rate ($\nabla.V_m$) profile at 10^{-6} Ma for varying ϕ_0

FIG. 4.20: (a) $\nabla \xi$ profile for different ϕ_0 (i.e. 0.01, 0.03 and 0.05 respectively) of input porous wave having width 14 km and amplitude 0.11 at initial time step (b) $\nabla.V_m$ profile for varying ϕ_0 (i.e. 0.01, 0.03 and 0.05 respectively) of input porous wave having width 14 km and amplitude 0.11 at initial time step under periodic boundary conditions

Remarks: We do not imply direct solver method while solving for periodic boundary condition as change of boundary condition needs a change in the matrix for ξ which is a bit cumbersome.

In order to show how under periodic boundary condition porosity, matrix velocity and fluid velocity profiles propagate with time leaving the right side boundary of

the model box and re-entering from the left side boundary of the model box fig. 4.20 is presented.
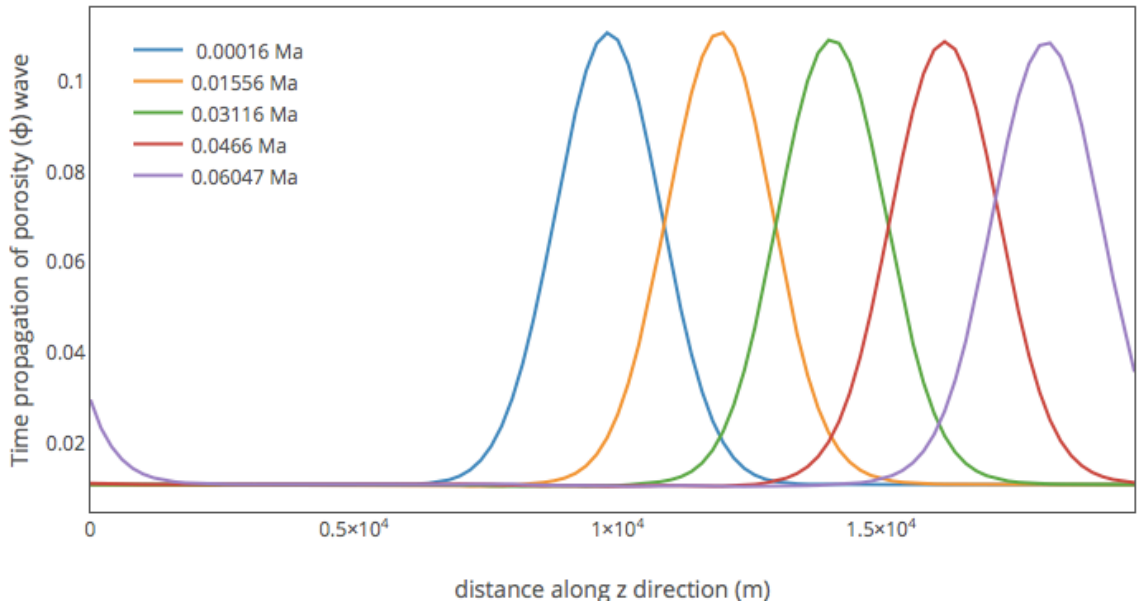
(a) Time propagations of porous wave

(b) Time propagation of velocity of fluid
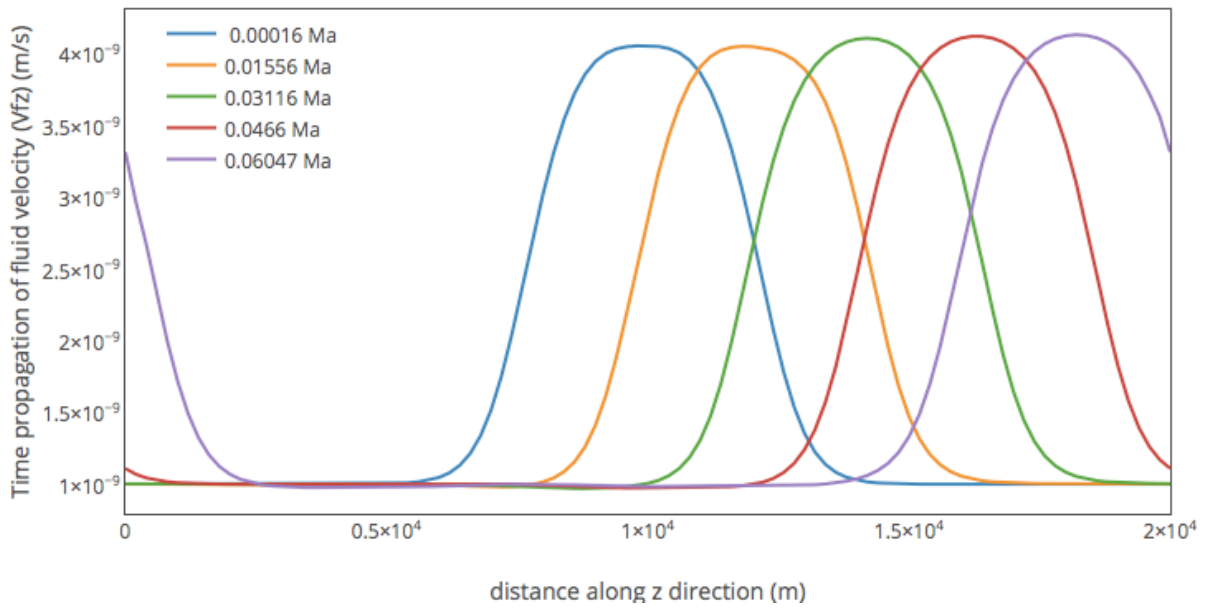
(c) Time propagation of velocity of matrix
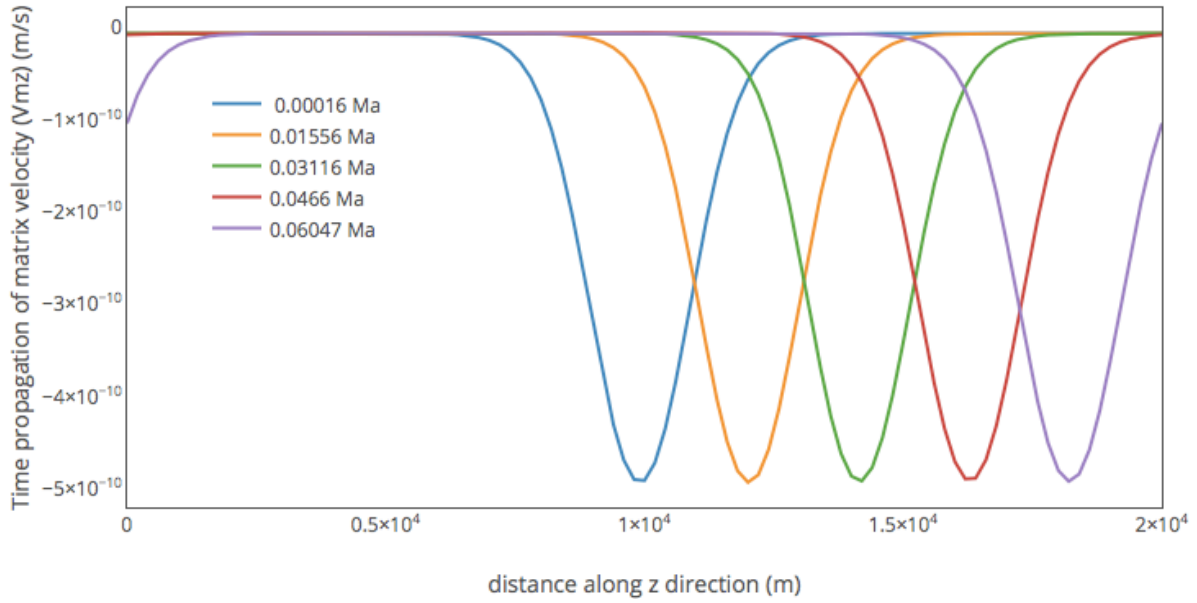
FIG. 4.20: (a) Propagations of Porosity, (b) Velocity of Matrix and (c) Velocity of Fluid under periodic boundary condition along z direction. Here the input porous wave having background porosity as 0.01, is a gaussian of amplitude 0.11 and width 7 km.

In this figure we see that the porous wave almost travels like a solitary wave which preserves its shape while propagates with time until and unless confronting with another wave. We also observe that, time propagation of porous wave under a certain range of compaction length (100-300 m) , creates a wave train each of which travels like a solitary wave at a later time step indicating that the governing equations have a solution which is a solitary wave [Barcilon and Lovera, 1989; Barcilon and Richter, 1986; Scott and Stevenson, 1984; Spiegelman, 1993a,b]. The solution of this solitary wave (1D) when the two phase mixture effective bulk and shear viscosity are functions of porosity, will be discussed in the next chapter.

Chapter 5

Solitary Wave and More

5.1 Introduction

The mathematical formulation of the two-phase theory for compaction, which implicitly accounts for a porosity dependent effective (bulk) viscosity of the two-phase mixture is investigated to better understand the process of geofluid (melt, water) migration in the earths mantle. Following previous studies [Barcilon and Lovera, 1989; Barcilon and Richter, 1986; Scott and Stevenson, 1984; Simpson and Spiegelman, 2011; Spiegelman, 1993a,b], a solitary wave's semi-analytical 1D solution is presented in our paper [Richard et al., 2012]. To understand differences of characteristics, a comparison of the properties of these waves with the waves produced in a two-phase mixture with constant effective (bulk) viscosity is presented. It has been observed that the solitary waves which are observed in a medium whose effective bulk viscosity is porosity dependent, are steeper (cf fig.5.1) compare to that of constant effective bulk viscosity medium and their speed decreases as an inverse function of the background porosity. These phenomena may be a significant tool to interpret the geochemistry and morphology of melt-related processes. Additionally, this analytical solution is used in our code PERCOL2D and also in FDCON for numerical benchmarking (1D) of PERCOL2D.

In McKenzies mathematical model [McKenzie, 1984], a concept of the effective matrix shear and bulk viscosity i.e. viscosities that physically depend of the shape and volume fraction of pores[McKenzie, 1984; Richter and McKenzie, 1984; Simpson and Spiegelman, 2011; Simpson et al., 2010a,b], have been introduced. Previously for the sake of simplicity,assuming a constant background porosity and a bulk viscosity independent of porosity, an analytical solution of solitary wave have been

found in [Nakayama and Mason, 1999; Scott and Stevenson, 1984; Takahashi et al., 1990; Takahashi and Satsuma, 1988]. Also under this assumption, the shape of solitary-waves and their properties have been computed numerically in different geometrical settings viz in 1D [Barcilon and Richter, 1986], in 2D and 3D [Barcilon and Lovera, 1989; Spiegelman, 1993a; Wiggins and Spiegelman, 1995]. In all these studies, expressions for the dispersion relation i.e. speed of the wave as a function of its amplitude and the instability of 1D and 2D-solitary waves in higher dimensions have been highlighted. In [Simpson and Spiegelman, 2011] the solitary wave solution (in 1D, 2D and 3D) is given with an approximation of small background porosity in a porosity dependent bulk viscosity settings but the 1D solitary wave solution which is going to be discussed in subsequent sections, is not having the approximation of small background porosity and the effect of higher background porosity is visible in the wave shape (cf. fig.5.1). Since the background porosity changes the compaction length (as discussed in 4.1.3), the original dynamics of porous wave obtained from two phase flow settings, changes accordingly (read 4.1.3 for more detail). So, in other words, the small background porosity approximation doesn't explain fully the porous wave dynamics.

5.2   Mathematical Formulations

The governing equations we use, are taken from section 2.1. From 2.1, one can see that, in this formulation effective matrix bulk viscosity is not introduced explicitly. Therefore, If $\eta_m(1-\phi)$ is replaced by η and $\frac{\eta_m(1-\phi)}{\phi}$ is replaced by ξ then under the assumption of negligible surface tension, large dirrefence of viscosity between two phases (i.e. $\eta_f << \eta_m$), small porosity approximation (i.e $\phi << 1$), this formulation (proposed by [Bercovici et al., 2001]) is equivalent to that of [McKenzie, 1984]. Multiplying eq. 2.1.3 by $\phi(\phi - 1)$ and eq. 2.1.4 by $(1 - \phi)$, we sum them up. Then using eq. 2.1.1 under the assumption of $\Gamma = 0$, one can obtain the equation

5.2.1.

$$-\frac{\eta_f \phi \delta v}{k(\phi)} + (1-\phi)\delta\rho\mathbf{g} - (1-\phi)\nabla P_m + \nabla.[(1-\phi)\eta_m\{\nabla V_m + \nabla V_m^t\}$$

$$+ \nabla[(\frac{1}{\phi} - \frac{2}{3})(1-\phi)\eta_m\nabla.V_m] = 0 \quad (5.2.1)$$

Since in 1D, in Lagrangian co-ordinate system velocity of center of mass is zero, i.e. $\phi\delta v = V_m$, eq. 5.2.1 reduces to:

$$-\eta_f V_{mz} - k(\phi)(1-\phi)\delta\rho g + k(\phi)\frac{\partial}{\partial z}[(\frac{1}{\phi} + \frac{4}{3})(1-\phi)\eta_m\frac{\partial V_{mz}}{\partial z}] = 0 \quad (5.2.2)$$

A non dimensionalisation of porosity, permeability, velocities of fluid and solid phase, length-scale and time is introduced using the background values of the porosity, the permeability, the Darcy velocity, the compaction length and the compaction time respectively.

$\phi = \phi_0\phi'$

$k(\phi) = k(\phi_0)\phi'^n$

$(V_{mz}, V_{fz}) = \frac{k(\phi_0)}{\eta_f}(1-\phi_0)\delta\rho g(V'_{mz}, V'_{fz})$

$z = \sqrt{\frac{k(\phi_0)\eta_m}{\phi_0\eta_f}}z'$

$t = \frac{1}{(1-\phi_0)\delta\rho g}\sqrt{\frac{\eta_m\eta_f}{k(\phi_0)\phi_0}}t'$

Lastly, dropping the primes, the 1D eq.5.2.3 can be derived from eq.5.2.2.

$$-\frac{V_m}{\phi^n} - \frac{1-\phi_0\phi}{1-\phi_0} + \frac{\partial}{\partial z}[(\frac{1}{\phi} + \frac{4\phi_0}{3})(1-\phi\phi_0)\frac{\partial V_m}{\partial z}] = 0 \quad (5.2.3)$$

Also eq. 2.1.1 under the assumption of $\Gamma = 0$, now can be written as,

$$-\phi_0\frac{\partial\phi}{\partial t} = \frac{\partial}{\partial z}(1-\phi\phi_0)V_m \quad (5.2.4)$$

eq.5.2.3 and eq.5.2.4 are similar to [Barcilon and Richter, 1986] except the fact that η and ξ are constant.

In order to find out the 1D solitary wave solution, we use the ansatz $y = z - ct$ for 1D forward propagating wave where c is the speed of solitary wave and t is the

variable denoting time. Then we search for solution for $\phi(z,t)$ and $V_m(z,t)$ of the form f(y) and g(y) respectively (i.e. $\phi(z,t) = f(y)$ and $V_m(z,t) = g(y)$). Hence the eq.5.2.3 and eq.5.2.4 are reduced to the form

$$-\frac{g}{f^n} - \frac{1 - \phi_0 f}{1 - \phi_0} + \frac{d}{dy}[(\frac{1}{f} + \frac{4\phi_0}{3})(1 - \phi_0 f)g'] = 0 \tag{5.2.5}$$

and

$$-\phi_0 c f' = [(1 - \phi_0 f)g]' \tag{5.2.6}$$

respectively. Here $'$ denotes the derivative w.r.t 'y'. Now $f \to 1$ and $g \to -1$ when $y \to \infty$. Therefore integrating eq. 5.2.6 within the range ∞ to y, it can be derived that,

$$g = -\frac{\phi_0 c(f-1) + (1-\phi_0)}{(1 - \phi_0 f)} \tag{5.2.7}$$

Similarly, from eq.5.2.5 and 5.2.7 it can be derived that,

$$\frac{\phi_0 c(f-1) + (1-\phi_0)}{(1 - \phi_0 f)f^n} - \frac{1 - \phi_0 f}{1 - \phi_0} - \phi_0(c+1)(1-\phi_0)\frac{d}{dy}[(\frac{1}{f} + \frac{4\phi_0}{3})\frac{f'}{1 - \phi_0 f}] = 0 \tag{5.2.8}$$

We know that, for any variable X which is a function of f and y, $\frac{dX}{dy} = f'\frac{dX}{df}$. We assume $X = (\frac{1}{f} + \frac{4\phi_0}{3})\frac{f'}{1-\phi_0 f}$. Also, keeping in mind that $2X\frac{dX}{df} = \frac{dX^2}{df}$, eq.5.2.9 can be derived from eq.5.2.8.

$$\frac{\phi_0 c(f-1) + (1-\phi_0)}{(1 - \phi_0 f)f^n} - \frac{1 - \phi_0 f}{1 - \phi_0} - \frac{\phi_0(c+1)(1-\phi_0)(1-\phi_0 f)}{2(\frac{1}{f} + \frac{4\phi_0}{3})}\frac{d}{df}[\frac{(\frac{1}{f} + \frac{4\phi_0}{3})^2 p^2}{(1 - \phi_0 f)^2}] = 0 \tag{5.2.9}$$

where $p = f'$. Integrating eq.5.2.9 we have,

$$\frac{(\frac{1}{f} + \frac{4\phi_0}{3})^2 p^2}{(1 - \phi_0 f)^2} = \frac{2\phi_0(c - C(f, \phi_0, n))}{(c+1)(1-\phi_0)}\int_1^f \frac{(\frac{1}{\phi_0 x} + \frac{4}{3})(x-1)}{(1 - \phi_0 x)^2 x^n} dx \tag{5.2.10}$$

where

$$C(f, \phi_0, n) = \frac{\frac{ln(f)}{\phi_0(1-\phi_0)} + \frac{4(f-1)}{3(1-\phi_0)} - (1-\phi_0)\int_1^f \frac{\frac{1}{\phi_0 x} + \frac{4}{3}}{(1-\phi_0 x)^2 x^n} dx}{\phi_0 \int_1^f \frac{(\frac{1}{\phi_0 x} + \frac{4}{3})(x-1)}{(1-\phi_0 x)^2 x^n} dx} \tag{5.2.11}$$

At the point of maxima i.e. when $f = A_{max}$, $p = f' = 0$. Hence, from eq.5.2.10, one can follow that the wave speed c has to satisfy the eq.5.2.12

$$c = C(A_{max}, \phi_0, n) \tag{5.2.12}$$

Since, $f' = \frac{df}{dy} = p(f, A_{max}, \phi_0, n)$, the shape of the solitary wave centered at $y = 0$ can be obtained by the eq.5.2.13 which is derived using eq.5.2.10

$$y = -\int_f^{A_{max}} \frac{1}{p(x, A_{max}, \phi_0, n)} dx \tag{5.2.13}$$

where

$$p(f, A_{max}, \phi_0, n) = \sqrt{\frac{2\phi_0(C(A_{max}, \phi_0, n) - C(f, \phi_0, n))}{(C(A_{max}, \phi_0, n) + 1)(1 - \phi_0)}}$$

$$\frac{1 - \phi_0 f}{\frac{1}{f} + \frac{4\phi_0}{3}} \times \sqrt{\int_1^f \frac{(\frac{1}{f} + \frac{4\phi_0}{3})(x - 1)}{(1 - \phi_0 x)^2 x^n} dx} \tag{5.2.14}$$

Since p vanishes when $x = A_{max}$, to deal with the point of singularity in eq.5.2.13, the integral is split up around the point $x = A_{max}$. The integration is executed through the ranges $x = f$ to $x = Amax - \epsilon$ and $x = A_{max} - \epsilon$ to $x = A_{max}$ respectively where ϵ chosen to be a very small number approaches to 0. Hence, we have,

$$y = -[\int_f^{A_{max} - \epsilon} \frac{1}{p(x, A_{max}, \phi_0, n)} dx + \int_{A_{max} - \epsilon}^{A_{max}} \frac{1}{p(x, A_{max}, \phi_0, n)} dx] \tag{5.2.15}$$

Using Taylor's series expansion for p^2 around the point $x = A_{max}$, we have, $p^2(x, A_{max}, \phi_0, n) = 2\kappa(x - A_{max})$, where

$$\kappa = \frac{1}{2} \frac{\partial p^2}{\partial f}\bigg|_{f=A_{max}} = -\frac{\phi_0(1 - \phi_0 A_{max})^2}{(C(A_{max}, \phi_0, n) + 1)(1 - \phi_0)(\frac{1}{A_{max}} + \frac{4\phi_0}{3})^2} \tag{5.2.16}$$

$$\frac{d}{df} C(f, \phi_0, n)|_{f=A_{max}} \times \int_1^f \frac{(\frac{1}{f} + \frac{4\phi_0}{3})(x - 1)}{(1 - \phi_0 x)^2 x^n} dx$$

Here κ denotes the curvature of the wave profile at its point of maxima.
Therefore, eq.5.2.15 yields:

$$y = -[\int_{f}^{A_{max}-\epsilon} \frac{1}{p(x, A_{max}, \phi_0, n)} dx + \sqrt{\frac{2\epsilon}{|\kappa|}}] \qquad (5.2.17)$$

5.2.1   A step by step algorithm for obtaining the solitary wave solution

A fortran code (SWG) is constructed to generate the solitary following the algorithm
given below:

1. Values of ϕ_0 and n need to be selected.

2. Tabulate $C(f, \phi_0, n)$ for $f \in [1, \frac{1}{\phi_0}]$

3. Values of f and C should be recorded as f_{max} and C_{max} respectively where
$\frac{dC}{df} = 0$.

4. Now A_{max} should be chosen from $[1, f_{max}]$.

5. Read $C(A_{max}, \phi_0, n)$.

6. Compute $p(x, A_{max}, \phi_0, n)$ for $x \in [1, A_{max}]$.

7. To find f i.e. the shape of the wave, the equation $f' = \frac{df}{dy} = p(f, A_{max}, \phi_0, n)$
needs to be solved. In order to do that a 4th order Runge-Kutta method is then to
be used with the value of f at distance $\epsilon(= 10^3)$ away from the point of maxima
as initial value $(f(y_{max} + \epsilon) = f(y_{max} + \frac{\epsilon^2}{2!}f''(y_{max}) + o(\epsilon^3) \sim A_{max} + \frac{\epsilon^2}{2!}\kappa)$. In our
model 8000 grid points are used to discretize each profile displayed in fig.5.1.

Assuming n=3, for $\phi_0 = 0.01$ and $\phi_0 = 0.05$, following the previous algorithm
fig. 5.1 is obtained. In this figure the similar results obtained from [Barcilon and
Richter, 1986] assuming constant viscosity also presented in order to compare results
between [Barcilon and Richter, 1986] and the one from our code.
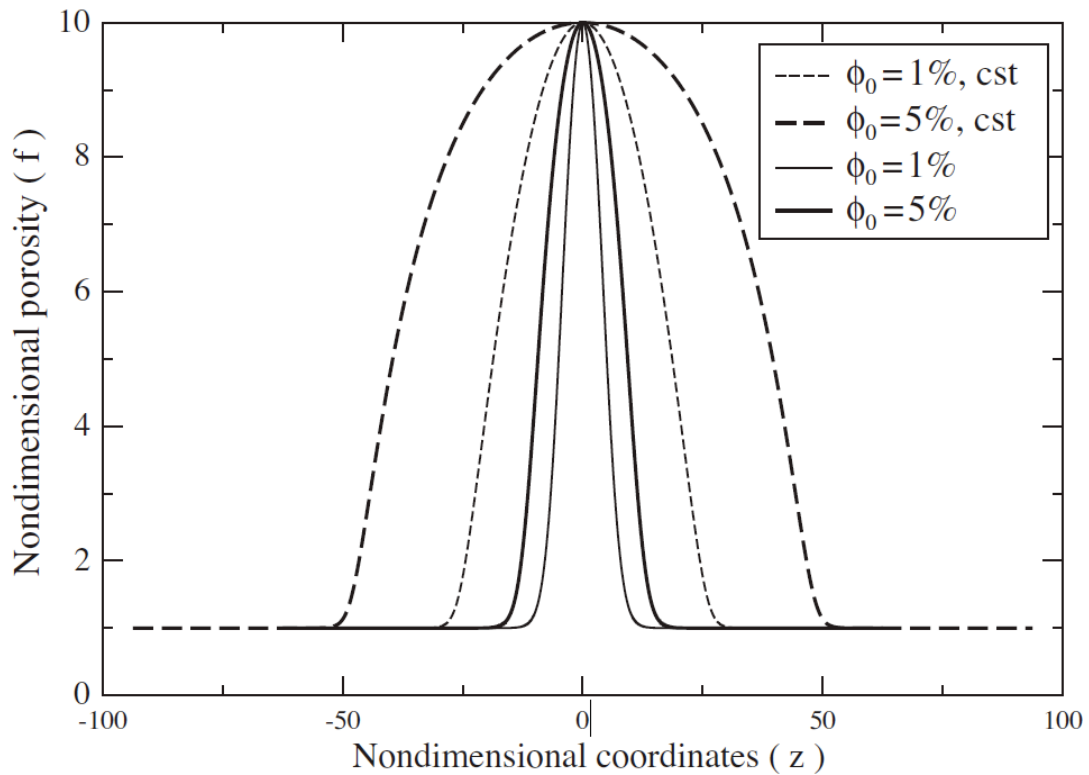
FIG. 5.1: Solitary wave profile having amplitude 10 (n=3) and background porosity $\phi_0 = 0.01$ (thin line) and $\phi_0 = 0.05$ (bold line) respectively. The corresponding figures assuming constant viscosity also presented from [Barcilon and Richter, 1986] in thin dashed line and bold dashed line respectively for $\phi_0 = 0.01$ and $\phi_0 = 0.05$ respectively.

Remarks: From the fig.5.1 it is observed that,

1) The solitary wave is wider for constant viscosity case.

2) The solitary wave is wider for higher background porosity.

5.2.2   Low background porosity approximation

We consider the case when $\phi_0 << 1$ i.e. $(1 - \phi_0 f) \simeq 1$. In this case ananalogue of eq.5.2.11 would be

$$\phi_0 C(A_{max}, \phi_0 << 1, n) = n(n-1)\frac{ln(A_{max}) + \frac{1}{nA_{max}^n} - \frac{1}{n}}{1 - \frac{n}{A_{max}^{n-1}} + \frac{n-1}{A_{max}^n}} \qquad (5.2.18)$$

Upon re - dimensionalization of the variables, eq.5.2.18 is identical to the one given in [Nakayama and Mason, 1992; Scott and Stevenson, 1984] for an effective viscosity which is inversely proportional to ϕ.

While comparing this result with the relation $\phi_0 c = 2A_{max} + 1$ derived by [Barcilon and Richter, 1986] assuming constant effective bulk and shear viscosities, for n=3, significant deviation due to ϕ dependency of viscosities is observed. The wave speed scaled by the background porosity has not only a non linear characteristics while plotted against A_{max} but also is much smaller than that of [Barcilon and Richter, 1986] when the amplitude of the wave is more than two times the background porosity. The wave speed scaled by ϕ_0 is almost two times smaller than that of constant viscosity case when the amplitude of the wave is of a magnitude higher than its background porosity (cf. fig. 5.2).

This variance of wave speed is mainly due to the non linearity of the wave speed with the increment of A_{max} which also causes wave steepening (cf. fig.5.1). As a consequence, it can be concluded that solitary wave formed in a ϕ dependent viscous system, transports less fluid and also has a smaller velocity than the wave formed in constant viscous system.
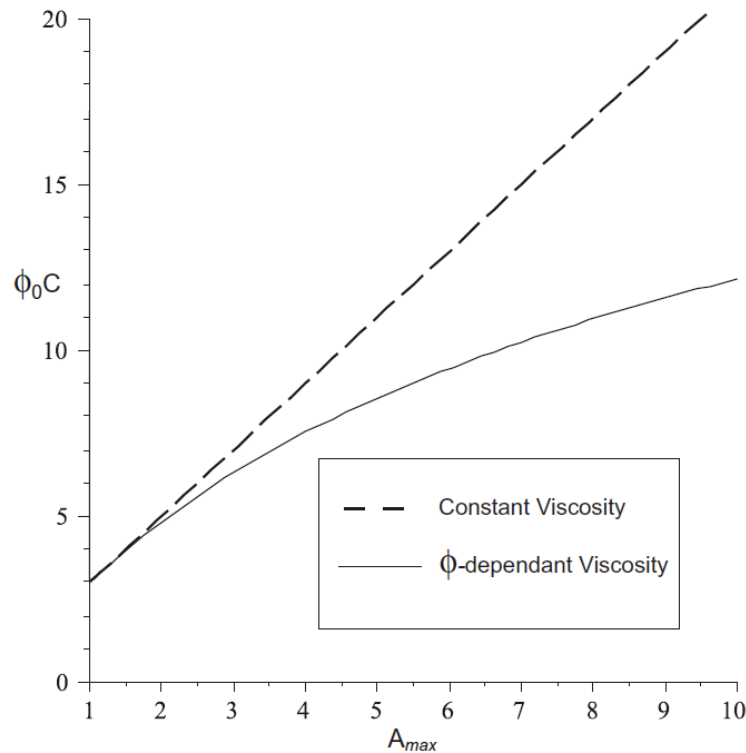
FIG. 5.2: Solitary wave speed scaled by the background porosity ϕ_0 profile against varying amplitude and n=3 where background porosity $\phi_0 << 1$ (solid line). The corresponding figure assuming constant viscosity also presented from [Barcilon and Richter, 1986] which is in dashed line. Figure courtesy [Richard et al., 2012]

The parameter value of n is set to 2 or 3 as a good approximation for permeabilities. n = 2 represents a melt network of tubular (i.e. long cylinders) shape along the three adjacent grain edges and n = 3 represents a connected disk-shaped inclusion. For small porosity, disk-shaped inclusions are more likely and so n = 3 was chosen for the comparisons (cf. fig.5.2).

The similar comparison can be studied for n=2, by comparing the results obtained from [Michaut et al., 2009] and our code[Richard et al., 2012] respectively.

5.3   1D solitary wave characteristics

In 4.1.1 and 4.1.2 it has been discussed that how the change of effective height of the input gaussian (amplitude of the wave-the background value of the wave) influences the wave's phase velocity. Here we execute the similar experiment for Solitary wave's velocity i.e. the behavior of the solitary wave is observed in two steps: 1) by changing the amplitude of the wave and 2) by changing the background porosity.

5.3.1   Effect of variation of background porosity

The characteristics of solitary wave speed with the change of background porosity ϕ_0 is illustrated in fig.5.3. It is observed that increment of ϕ_0 causes a slower propagation of wave. i.e. solitary wave speed c decreases as soon as the background porosity ϕ_0 increases.

For a given amplitude, the decrease of wave speed is approximately of order $\frac{1}{\phi_0}$ (cf. fig.5.3) . As soon as the dimensional amplitude of the wave i.e. $\phi_0 A_{max} = 1$, the wave speed drops down to zero (cf. fig.5.3) since in this case only one phase exists which causes the wave to stop propagating. The effective viscosity of the background (i.e. the region of solid matrix phase) controls the speed of the wave. When ϕ_0 increases this viscosity decrease which causes the faster propagation of wave.

It may seem that this result is different than the case of Gaussian as discussed in chapter 4. Keeping in mind the difference of dimensional and non dimensional setting in chapter 4 and in the present one, following the discussion in [Richard et al., 2012], it can be understood that how upon re-dimensionalisation of variables changes the relationship between phase velocity of Gaussian with increasing porosity.
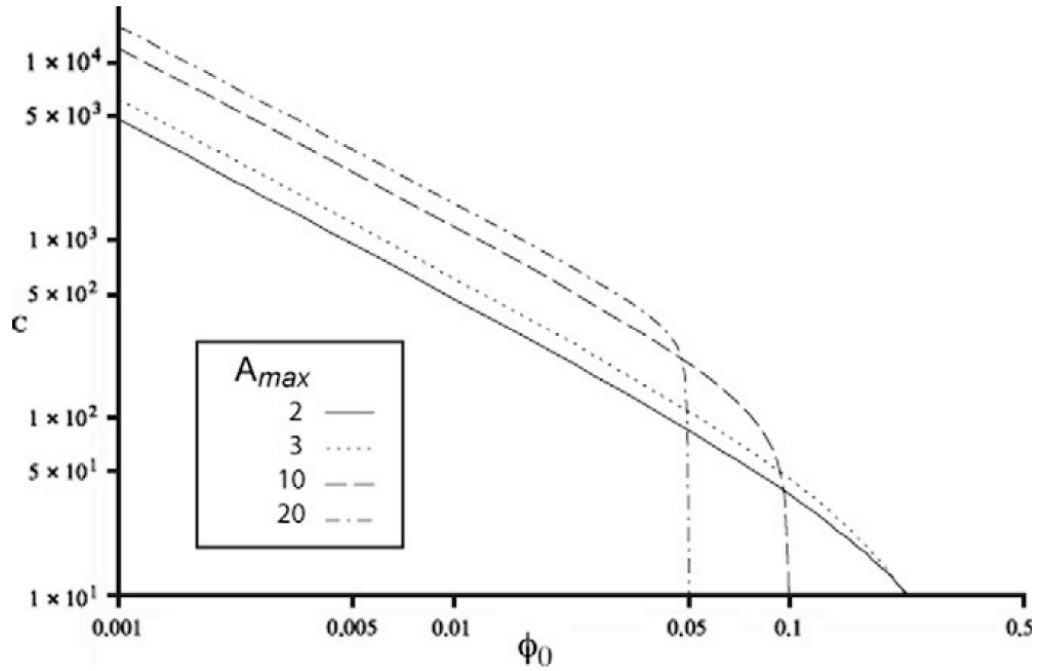
FIG. 5.3: Non-dimensional speed (c) of solitary wave as a function of its background porosity for different maximum non-dimensional amplitudes (A_{max}) using logarithmic scales. The permeability exponent n = 3. The speed c is decreasing with increasing background porosity ϕ_0 approximately as an inverse function of ϕ_0. When the dimensional amplitude i.e $\phi_0 A_{max} = 1$, the speed goes to zero. Figure courtesy [Richard et al., 2012]

According to eq.5.2.12 the phase velocity c is also a function of the maximum amplitude of the wave i.e. A_{max}. The larger the amplitude is, the larger is the solitary wave speed c (cf. fig.5.4). Since, effective viscosity of the two-phase mixture is inversely proportional to the porosity, the wave speed c has an upper bound. The solitary wave speed c profile is non linear w.r.t the wave's maximum amplitude A_{max}. When the dimensional amplitude of the wave i.e. $\phi_0 A_{max}$ approaches to 1 i.e. when there is almost no existence of solid matrix phase, the speed c drops down to zero. This threshold value of $A_m ax$ depends on the value of background porosity ϕ_0. For small background porosity viz $\phi_0 = 0.01$, such value of A_{max} is controlled by $\phi_0 A_{max} = 0.95$ and for large background porosity viz. $\phi_0 = 0.1$ the controlling equation for maximum limit of A_{max} is $\phi_0 A_{max} = 0.075$.
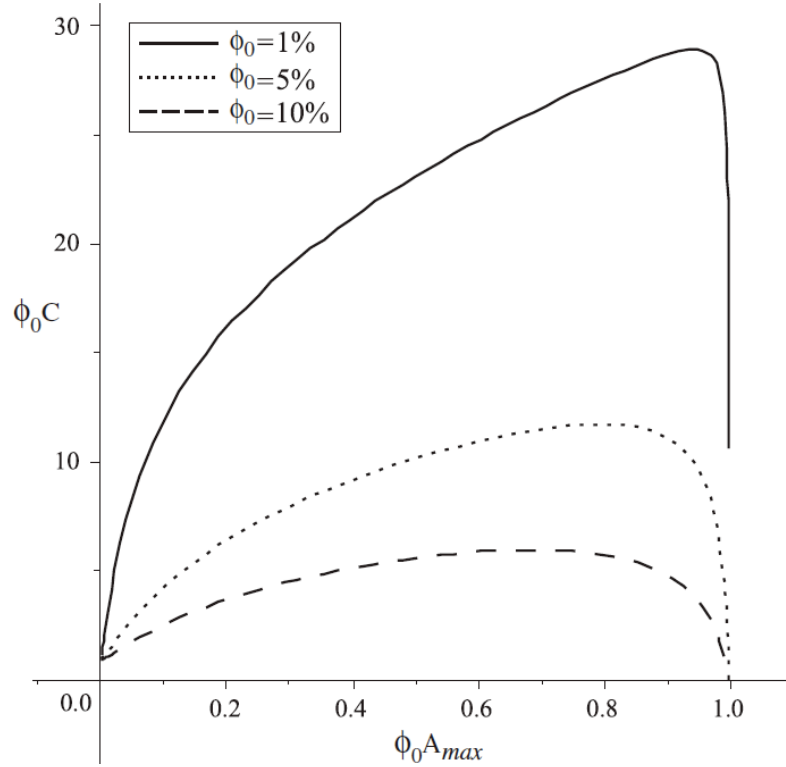
FIG. 5.4: Solitary wave speed c, scaled by ϕ_0 vs. the wave's maximum dimensional amplitude $\phi_0 A_{max}$ for different background porosities (i.e. for $\phi_0 = 0.01$, $\phi_0 = 0.05$ and $\phi_0 = 0.1$ when n=3. Figure courtesy [Richard et al., 2012]

Remarks:

To find the semi analytical solution which resembles with solitary wave solution, of the system of equations proposed by [Bercovici et al., 2001], the same methodology has been followed as that of [Barcilon and Richter, 1986]. The difference between the results presented by [Rabinowicz et al., 2002; Scott and Stevenson, 1984; Simpson and Spiegelman, 2011] and [Richard et al., 2012] is that, no prior approximations are made about background porosity ϕ_0. The effect of porosity dependent effective viscosity of solid phase on the shape and speed of a solitary wave has been distinguished this study from [Barcilon and Richter, 1986; Scott and Stevenson, 1984]. There are two significant points to be summarized in this study.

1) The solitary wave traveling in a medium whose effective viscosity is inversely

proportional with porosity, is sharper and slower than the one traveling in a constant viscous medium.

2) For a given amplitude over background porosity ratio, the non-dimensional speed of a wave traveling in a medium having large background porosity, is smaller than the one traveling in a medium having small background porosity. The sharpening of the wave propagating through a porosity dependent viscous medium, relative to the one traveling in a medium having constant effective viscosity is proportionally smaller.

5.4   Benchmarking of 1D solution

The solitary wave solution obtained from the code SWG, is used as an initial input in PERCOL2D and in FDCON. Then the propagation of the wave in both the codes PERCOL2D and FDCON are observed. In both the figures the wave propagates preserving its shape almost at the same time steps (cf. fig.5.4).

(a)

(b)
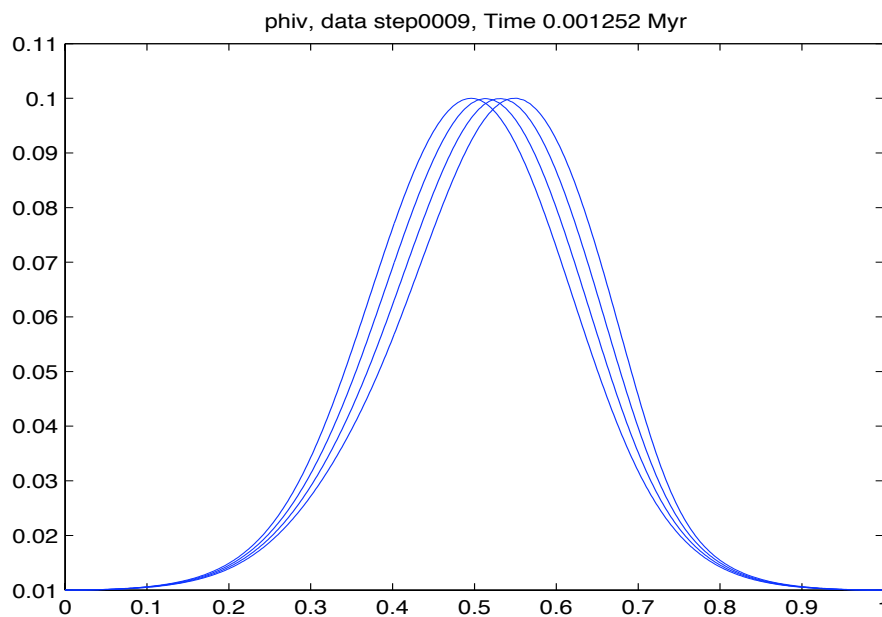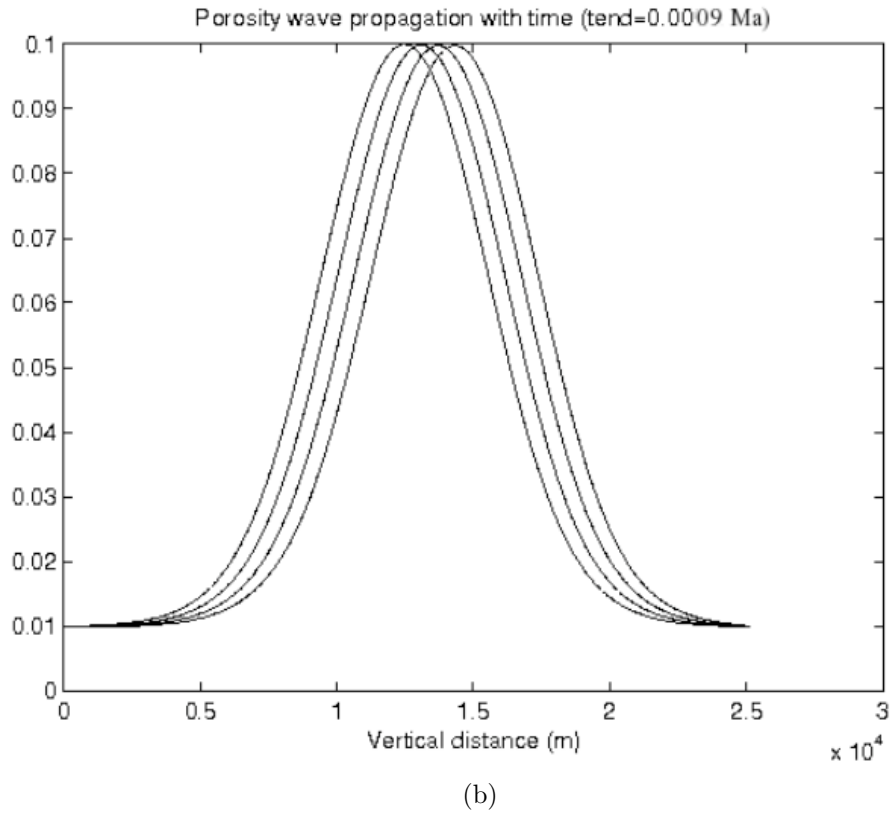
Fig. 5.4: (a) propagation of ϕ profile using FDCON with initial input of solitary wave solution obtained from SWG having $\phi_0 = 0.01$ and amplitude 0.1 at initial time step. (b) propagation of ϕ profile using PERCOL2D with initial input of solitary wave solution obtained from SWG having $\phi_0 = 0.01$ and amplitude 0.1 at initial time step under fixed boundary conditions

The difference of propagation of solitary wave as obtained from SWG, FDCON and PERCOL2D is within 1% relative error (cf. fig. 5.5)
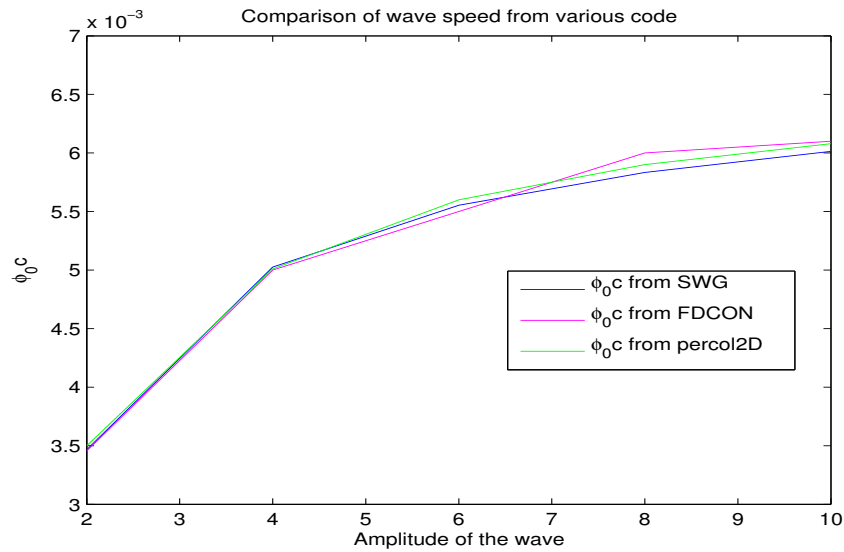
FIG. 5.5: Solitary wave speed multiplied by background porosity (n=2) as a function of non dimensional amplitude of the wave

Remarks: 1) The error shown in fig.5.5 is probably a numerical error due to the resolution of the model. Numerous experiments show that number of grid points per compaction length strongly influences the accuracy and convergence of the solution (not shown here). Hence, a test with the improvement of resolution is needed in order to check whether the accuracy is better than the present case.

2) The propagation and phase velocity comparison tests thus benchmarks PER-COL2D together with FDCON using the solitary wave solution obtained from SWG.

In the next chapter a detail study on the dynamics of porous wave, melt and solid velocities and the subsequent comparisons with FDCON in order to benchmark the code in 2D will be discussed.

Chapter 6

Comparison of 2D two phase flow results obtained from two different codes (PERCOL2D and FDCON) and implementation of a different viscosity formulations

6.1 Introduction

At low background viscosities, the melt extraction method is governed by either melt transport in a compacting host rock or by the advective transport of melt through a convective host rock. Therefore, the shear and compaction viscosity ratio controls the fact that whether melt transport will be executed via compaction waves (i.e. symmetrical or channel flow) [Aharonov et al., 1995; Hesse et al., 2011; Hewitt, 2009; Kelemen et al., 1995a,b; Rabinowicz and Vigneresse, 2004; Spiegelman et al., 2001; Weatherley, 2012] or via convective diapirism which is nothing but upwelling driven by the buoyancy of the locally accumulated melt [Bercovici and

Ricard, 2003; Bercovici et al., 2001; Berkowitz and Ewing, 1998; Keller et al., 2013; McKenzie, 1984; Scott and Stevenson, 1984, 1986a, 1989; Spiegelman, 1993a,b,c; Šrámek et al., 2007].

The melt present at the inter-granular areas, are expected to form an interconnected network, even at low porosity [McKenzie, 1984; Zhu et al., 2011]. Therefore the melt is able to traverse through the porous solid matrix. Since melt has relatively lower density than solid matrix, it will rise buoyantly. Hence, the separation of melt from matrix causes matrix to compact in order to compensate the motion. To get an insight of the melt migration process when melt percolates through a viscously compacting porous matrix due to its buoyancy, we have set up a FORTRAN code called PERCOL2D. This work establishes a melt migration model which requires the theoretical knowledge of two phase flow through porous and viscously compacting media using the governing equations proposed by [Bercovici et al., 2001]. The mathematical formulations prescribed by [Bercovici et al., 2001] is different than the formulation proposed by [McKenzie, 1984] in the sense that the presence of the interfacial area between the two phases and thus the surface energy or interfacial surface force is considered in [Bercovici et al., 2001] formulation which has not been so in [McKenzie, 1984]. Due to inclusion of interfacial surface force, pressure difference (between two phase) term is non-zero even if surface tension is negligible (in our model) as long as the two-phase medium is deforming. Also, the theory proposed in [Bercovici et al., 2001], is more generalized than [McKenzie, 1984] according to some physical point of view namely, ratio of viscosities of the two phases is kept arbitrary so that one of the phases needs not to be much less viscous than the other all the time. This choice of viscosity values makes the set of equations invariant to the permutation of phases which is exploited in our model development. Moreover, melting rate is a prescribed term in [McKenzie, 1984] whereas it is presented as a coupling term with the deformation process of the two-phase mixture. Although, melting or freezing is neglected in our model, in this way, it is possible for us to study the effect of the dynamical deformation on the phase change. But we need to restrict our focus to a univariant phase change which is not the case in [McKenzie, 1984]. As a matter of simplicity to start with the numerical experiments with PERCOL2D, source term and surface tension terms are assumed to be zero. Hence, at present state our model is somewhat equivalent or similar to

that of [McKenzie, 1984] which will be discussed later in this chapter by comparing our results with the results obtained from FDCON which uses the Mckenzie formulations [Schmeling, 2000]. Now when the source term is either zero or prescribed then the energy equation is neglected and hence these studies become as kinematic where the temperature has no role which is the reason that we do not deal with any temperature issue and the energy equation itself at the moment.

6.2 Comparison of 2D two phase flow results obtained from PERCOL2D and FDCON

6.2.1 equivalence of mathematical framework used by PERCOL2D and FDCON

We consider in our model that both the matrix and fluid phases to be incompressible. But In [McKenzie, 1984], matrix was considered as compressible macroscopically (i.e. the intrinsic matrix material is incompressible) and the liquid phase was considered as an incompressible fluid with negligible viscosity compare to the matrix viscosity.

It can be shown from [Šrámek, 2007] that mathematical framework of our model and physical background can be comparable to [Schmeling, 2000]version although [Schmeling, 2000] uses formulations proposed by [McKenzie, 1984]. In this 2D version of benchmarking we keep all other parameters same as described in tab.4.1 excluding the number of grid points along horizontal and vertical direction i.e. nx and nz which are now each 100.

All the other physical assumptions of 1D simulations as mentioned in chapter 3, viz. negligible surface tension, zero source term etc. are same in 2D too. Also, the notations of all other variables are kept same. Here only fixed boundary condition can be used unlike the case in 1D where application of periodicity on boundary condition is possible (ref. 3.1.2.2). It is because due to having more number of grid

points together in vertical and horizontal directions, using BSOR solver is impossible as it slows down the solution beyond the limitation and starts to oscillate as well. The matrix required for using direct solver method in PERCOL2D was written only considering the fixed boundary conditions. Writing another matrix for periodic boundary condition was time consuming and therefore, here we will discuss about the comparative results only under fixed boundary conditions.

Since the mathematical framework for PERCOL2D has already been discussed in chapter 3, here the mathematical framework used for FDCON are given in brief and thereafter they have been shown equivalent to the mathematical framework used by PERCOL2D. For this comparison, we keep the assumptions of negligible surface tension, zero source term everything same in FDCON formulations. The governing equations used for FDCON are as follows:

1) Matrix mass conservation

$$\frac{\partial(1-\phi)}{\partial t} = -\nabla.(1-\phi)V_m - \frac{\dot{\Gamma}}{\rho_m} \tag{6.2.1}$$

2) Fluid mass conservation

$$\frac{\partial \phi}{\partial t} = -\nabla.\phi V_f + \frac{\dot{\Gamma}}{\rho_f} \tag{6.2.2}$$

3) Fluid momentum conservation equation

$$\frac{\eta_f \phi}{k(\phi)}\delta v + \rho_f \mathbf{g} - \nabla P_f = 0 \tag{6.2.3}$$

4) Matrix momentum conservation equation

$$\bar{\rho}\mathbf{g} - \nabla \mathcal{P} + \nabla.\bar{\bar{\tau}} = 0 \tag{6.2.4}$$

where $\bar{\bar{\tau}}$ is the viscous stress tensor and $\bar{\bar{\tau}} = \eta_s(\nabla V_m + \nabla V_m^t) + (\eta_b - \frac{2}{3}\eta_s)\bar{\bar{I}}\nabla.V_m$ and

$\mathcal{P}$ is the dynamic pressure of fluid or matrix (i.e. $\mathcal{P} = P_f$ or P_m) as they are equal because of the zero surface tension approximation at the interface of solid matrix and fluid melt. Here η_s and η_b are effective shear and bulk viscosity of the matrix which are of the form

$$\eta_s = \eta_m(1 - \phi)$$
$$\eta_b = \frac{\eta_m(1 - \phi)}{\phi}$$

(6.2.5)

respectively in PERCOL2D formulations.

Now eq. 2.1.1, 2.1.2, 2.1.3 and eq. 6.2.1, 6.2.2, 6.2.3 respectively are directly comparable as they are exactly same in PERCOL2D and FDCON.

But eq. 2.1.4 and eq. 6.2.4 are not directly comparable in that way. Therefore a brief derivation is required to prove the equivalence of eq. 2.1.4 and 6.2.4. In order to do it first eq. 2.1.3 and eq. 2.1.4 are multiplied by ϕ and $\frac{\phi}{1-\phi}$ respectively and then added. The resultant equation is then

$$\phi(1 - \phi)\delta\rho\mathbf{g} - \phi(1 - \phi)\nabla(\delta P) + \phi\nabla.[(1 - \phi)\bar{\bar{\tau}}_m] - \eta_f \frac{\phi^2}{k(\phi)}\delta v + \phi\delta P\nabla\phi = 0 \quad (6.2.6)$$

Then dividing eq. 6.2.6 by ϕ and doing some simple arithmetic calculations one can get

$$(1 - \phi)\delta\rho\mathbf{g} - \nabla[(1 - \phi)\delta P] + \nabla.[(1 - \phi)\bar{\bar{\tau}}_m] - \eta_f \frac{\phi}{k(\phi)}\delta v = 0 \qquad (6.2.7)$$

Since $\eta_f \ll \eta_m$, from eq. 2.1.5, eq. 2.1.1 and 6.2.5, it is possible to derive that $(1 - \phi)\delta P = -\eta_b\nabla.V_m$. Putting this value of $(1 - \phi)\delta P$ in eq. 6.2.7 and then adding the equation with eq. 2.1.3 or with eq. 6.2.3 the equation $\bar{\rho}\mathbf{g} + \nabla.\bar{\bar{\tau}} - \nabla P_f = 0$, can be obtained which is exactly the same as eq. 6.2.4 since in FDCON formulations it has been assumed that $P_f = \mathcal{P}$.

It must be noted that despite of the difference of assumptions about δP in FDCON and PERCOL2D (i.e. $\delta P = 0$ in FDCON and its non zero quantity in PERCOL2D), use of different stress tensors in eq. 2.1.4 and 6.2.4 makes these formulations equivalent to each other at the final level.

The Helmhotz decomposition used in FDCON is of the form $V_m = v_1 + v_2$ where $v_1 = \nabla \times \boldsymbol{\Psi}$ and $v_2 = \nabla \chi$. Here $\boldsymbol{\Psi}$ is the stream function defined in the similar way as it was defined for PERCOL2D in chapter 3 and χ is the velocity potential for the irrotational part of the flow. If this decomposition is compared with the decomposition used in PERCOL2D, it can be seen that $\nabla \chi = \phi^2 \nabla \xi$.

Therefore, $\frac{\partial \chi}{\partial x} = \phi^2 \frac{\partial \xi}{\partial x}$ and $\frac{\partial \chi}{\partial z} = \phi^2 \frac{\partial \xi}{\partial z}$

Since at the present scenario, the temperature and energy equations are not under consideration of PERCOL2D, the resulting dimensional 2D flow equation neglecting energy and temperature equations and considering full compaction as used in FDCON is:

$$G[\eta_s G\psi] + 4\frac{\partial^2}{\partial x \partial z}[\eta_s(\frac{\partial^2 \psi}{\partial x \partial z})] = \delta\rho\mathbf{g}\frac{\partial \phi}{\partial x} - 2\frac{\partial^2}{\partial x \partial z}[\eta_s G\chi] + 2G[\eta_s \frac{\partial^2}{\partial x \partial z}(\chi)] \quad (6.2.8)$$

, where $G \equiv \frac{\partial^2}{\partial x^2} - \frac{\partial^2}{\partial z^2}$

Now using the fact $\frac{\partial \chi}{\partial x} = \phi^2 \frac{\partial \xi}{\partial x}$, $\frac{\partial \chi}{\partial z} = \phi^2 \frac{\partial \xi}{\partial z}$ and substituting the value of η_s with $\eta_m(1 - \phi)$, eq. 2.3.4 can be obtained from eq.6.2.8. Hence the decomposition used in FDCON [Schmeling, 2000; Šrámek, 2007] and the decomposition used in PERCOL2D are proved to be equivalent formulations.

To start with the benchmarking process, the assumption of $\theta = \xi$ kept unchanged while changing the code settings from 1D to 2D for the code PERCOL2D. The idea is to increase the computational complications while converting the code from 1D to 2D step by step. Although its not physical since $\bar{v}$ no more has the value zero in 2D unlike the case in 1D. The intention of keeping this simplification is to test that how this over simplification effects the physical results of PERCOL2D from that of FDCON in 2D as FDCON doesn't use this oversimplification. If the deviation is within the range of $15 - 20\%$, then the complications of calculating θ can be avoided in some cases. But if its not, then we come to the conclusion that the idea of keeping this over simplification in 2D is neither physical nor computationally effective.

6.2.2   Comparison of 2D results obtained from FDCON and PERCOL2D

A Gaussian of amplitude 0.05 whose maximum cross sectional radius is 7 km and having a background value of 0.01 has been chosen for the initial input of porous wave in PERCOL2D and FDCON for the required comparison. Solitary wave's wavelength has been observed as a summation of 30-40 compaction lengths [Barcilon and Lovera, 1989; Barcilon and Richter, 1986; Richard et al., 2012; Scott and Stevenson, 1984, 1986a; Simpson and Spiegelman, 2011]. This observation is based on 1D results although. As discussed in chapter 4, we have compaction length $\delta = 300$ m which means the possible range of width of an equivalent solitary wave is supposed to be from 9 - 12 km. Also from fig.4.20(a) we have seen that the Gaussian of width 7 km propagates almost like a soliton though its amplitude is different i.e. 0.11. So, as a possible approximation to a solitary wave like profile, we have chosen the Gaussian of amplitude 0.05 and of width 7 km as an initial input of porosity in PERCOL2D and FDCON. The profiles of porosity ϕ, stream function ψ, the horizontal vertical segregation velocity $(V_{fx} - V_{mx})$ and the vertical segregation velocity $(V_{mz} - V_{fz})$ are presented hereafter, obtained from PERCOL2D and FDCON at the initial time step, at the time step when they travel halfway the model box and at the time step when they reach near the boundary. The time step is calculated using the Courant number as 0.1 in both the code PERCOL2D and in FDCON. This courant number is a necessary condition which is required to guarantee convergence process of time iterative scheme for solving certain partial differential equation [Courant et al., 1928]. The results from PERCOL2D are presented in non dimensional scaling although the code is a dimensional one, so that the results can be easy to compare with those of FDCON. In order to do that the non dimensionalisation of the variables are executed following the non dimensionalisation formulations provided in [Schmeling, 2000] which are as follows:

spatial variable x=hx',

velocity $u = \frac{\kappa}{h}u'$,

time $t = \frac{h^2}{\kappa}t'$,

matrix viscosity $\eta = \eta_m \eta'$ and

matrix density $\rho = \rho_m \rho'$, where h denotes the height of the model box, value of thermal diffusivity κ is taken as $10^{-6} m^2/s$, η_m and ρ_m are taken from table 4.1

An observation is made on the displacement of porous profile along the vertical direction of non dimensional model box from fig.6.1(a), (c), (e). Thus speed of the porous wave, obtained from FDCON is 3.9×10^{-9} m/s (which is in quite good agreement with fig.4.12 (b)) and the speed of the porous wave obtained from PER-COL2D (by similar observation from fig. .6.1(b), (d), (f)) is 3.5×10^{-9} m/s.

In the fig. 6.1 it can be observed that amplitude of porous wave obtained from PERCOL2D increases 5% more than the porosity profile obtained from FDCON while propagating. Moreover, the porous wave obtained from PERCOL2D travels slower (9.43%) than the porous wave obtained from FDCON.

The magnitude and span of the stream function profiles obtained from FDCON and PERCOL2D are significantly different which can be seen in fig.6.2. The stream function obtained from FDCON almost fills the model box but the stream function profile obtained from PERCOL2D is occupying much smaller region compare to FDCON.

Also, the magnitude of stream function profile obtained from FDCON is approximately 50% more than the one obtained from PERCOL2D. At time $t = 0.038668$ Myr (cf. fig. 6.2(c),(d)), the magnitude of the stream function obtained from PER-COL2D deviates approximately 16% compare to the highest magnitude of stream function obtained from FDCON. The difference of highest magnitudes of stream functions obtained from PERCOL2D and FDCON becomes approximately 50% when the stream function almost reaches the boundary for both the programs FD-CON and PERCOL2D. The maximum amplitude of stream function obtained from FDCON decreases with due course of time while propagating but its the opposite i.e. the magnitude of maximum amplitude increases during the time propagation of stream function profiles obtained from PERCOL2D

It can be observed from fig.6.3 that both the horizontal and vertically segregation velocity profiles obtained from PERCOL2D and FDCON are significantly different than each other . The horizontal segregation velocity profile obtained from FDCON is of a pattern of 4 petals while the one obtained from PERCOL2D has an 8 petals pattern. Although the core 4 petals pattern of the horizontal segregation velocity profile obtained from PERCOL2D has some resemblances with the one obtained

from FDCON. But this core part is occupying much smaller area of the model box when compared to the one obtained from FDCON. The increment of maximum amplitude of the profile obtained from PERCOL2D is within 10-15% compare to the one obtained from FDCON. From fig. 6.3(a) horizontal divergence of melt in top of porous wave and convegence at the bottom part of porous wave can be observed which is consistent with the moving porous wave. Since, over pressure in the top of the wave pushes the melt to the sides and upper direction. But in fig. 6.3(b), outer lobes are not physical as background melt in front of anomaly converges to the central line and percolates back towards the wave.

One can observe that the profile obtained from FDCON (cf. fig. 6.4(a)) is vertically elongated whereas the profile obtained from PERCOL2D (fig. 6.4(b)) is horizontally elongated. The reason behind the deviation of pattern of vertical segregation velocity profiles obtained from PERCOL2D and FDCON is probably due to minimal effect of stream function on the vertical segregation velocity profile obtained from PERCOL2D compare to the effect of stream function on the vertical segregation profile obtained from FDCON. Although the tendency of vertical elongation of the core part of vertical segregation velocity profile with course of time is present in both the figures. Also, while propagating towards the upper boundary of model box, the vertical segregation velocity profile obtained from FDCON shows approximately 16% increment of its maximum amplitude compare to the one obtained from PERCOL2D. Comparing the absolute amplitudes of vertical and horizontal segregation profiles, one can see that amplitude of vertical segregation profile is almost of one order magnitude higher on average than the amplitude of horizontal segregation profile with course of time. Since vertical segregation profile has more significant contribution for melt upwelling than stream function, the relative differences between porosity profiles obtained from FDCON and PERCOL2D (5%) are small.
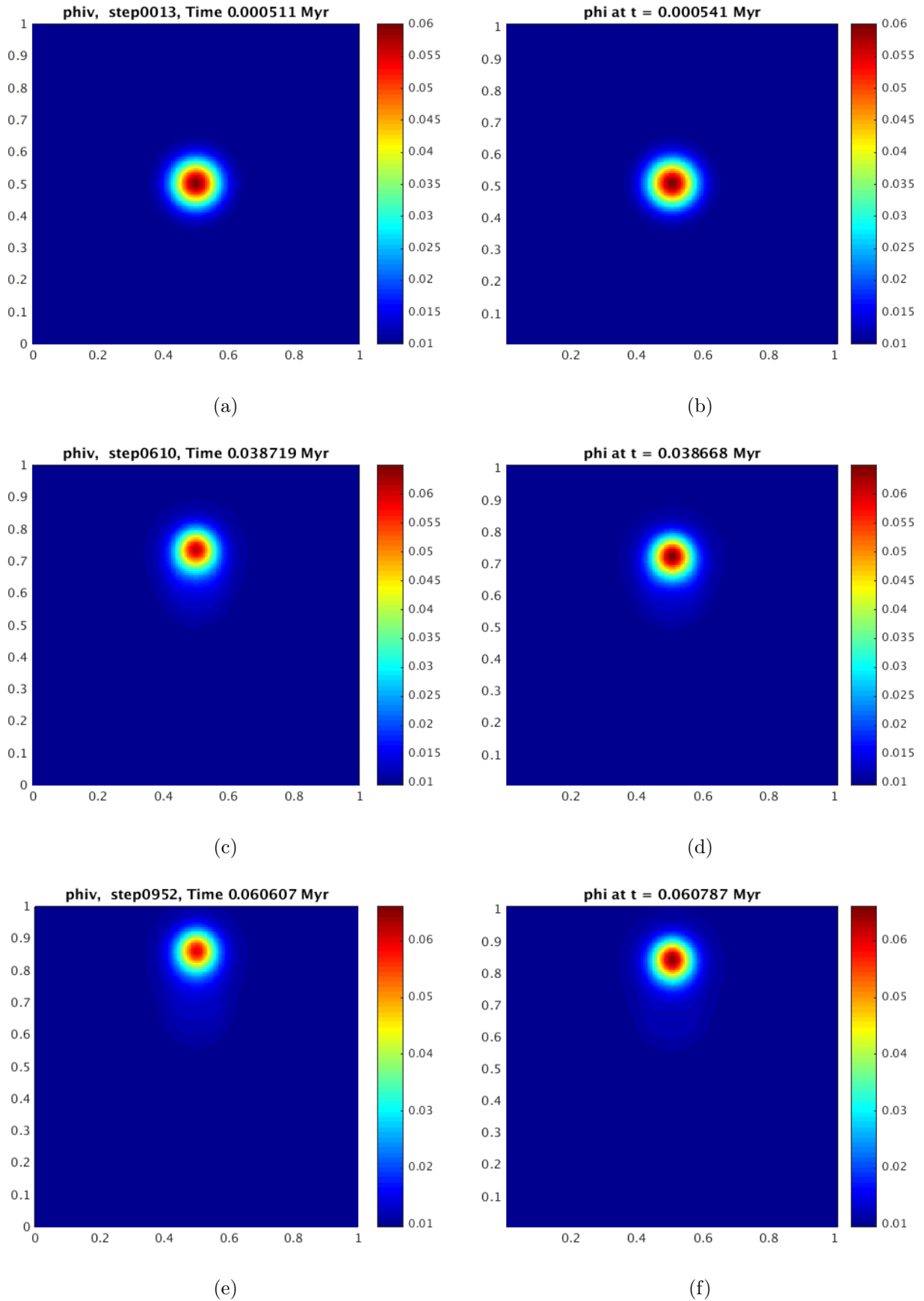
FIG. 6.1: Comparison of porosity profiles obtained FDCON (left column) and PER-COL2D (right column) at various time steps. The initial input for porous wave is a Gaussian wave of amplitude 0.05 and having the maximum cross sectional diameter of 7 km and the background porosity value of 0.01
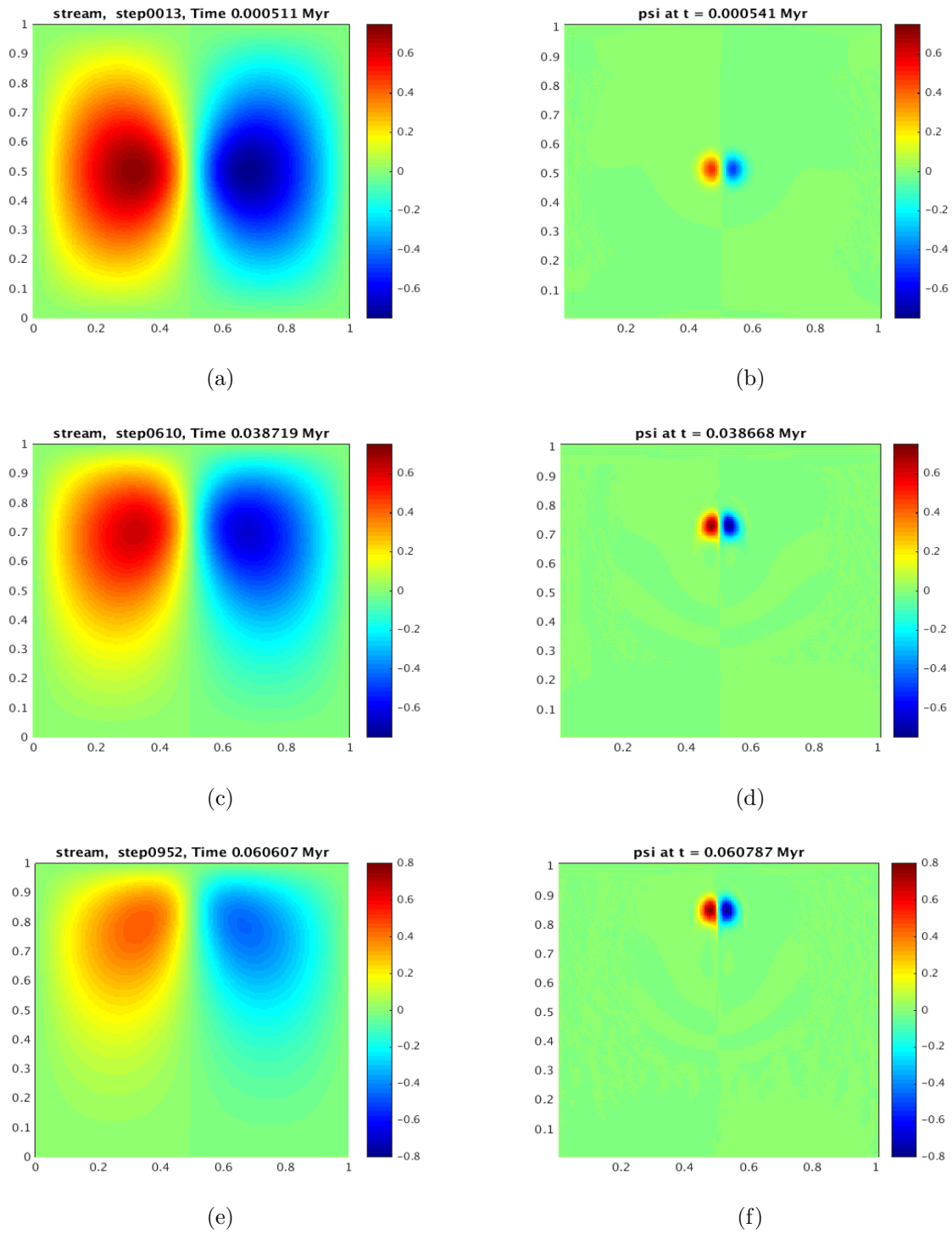
FIG. 6.2: Comparison of stream functions obtained FDCON (left column) and PER-COL2D (right column) at various time steps.
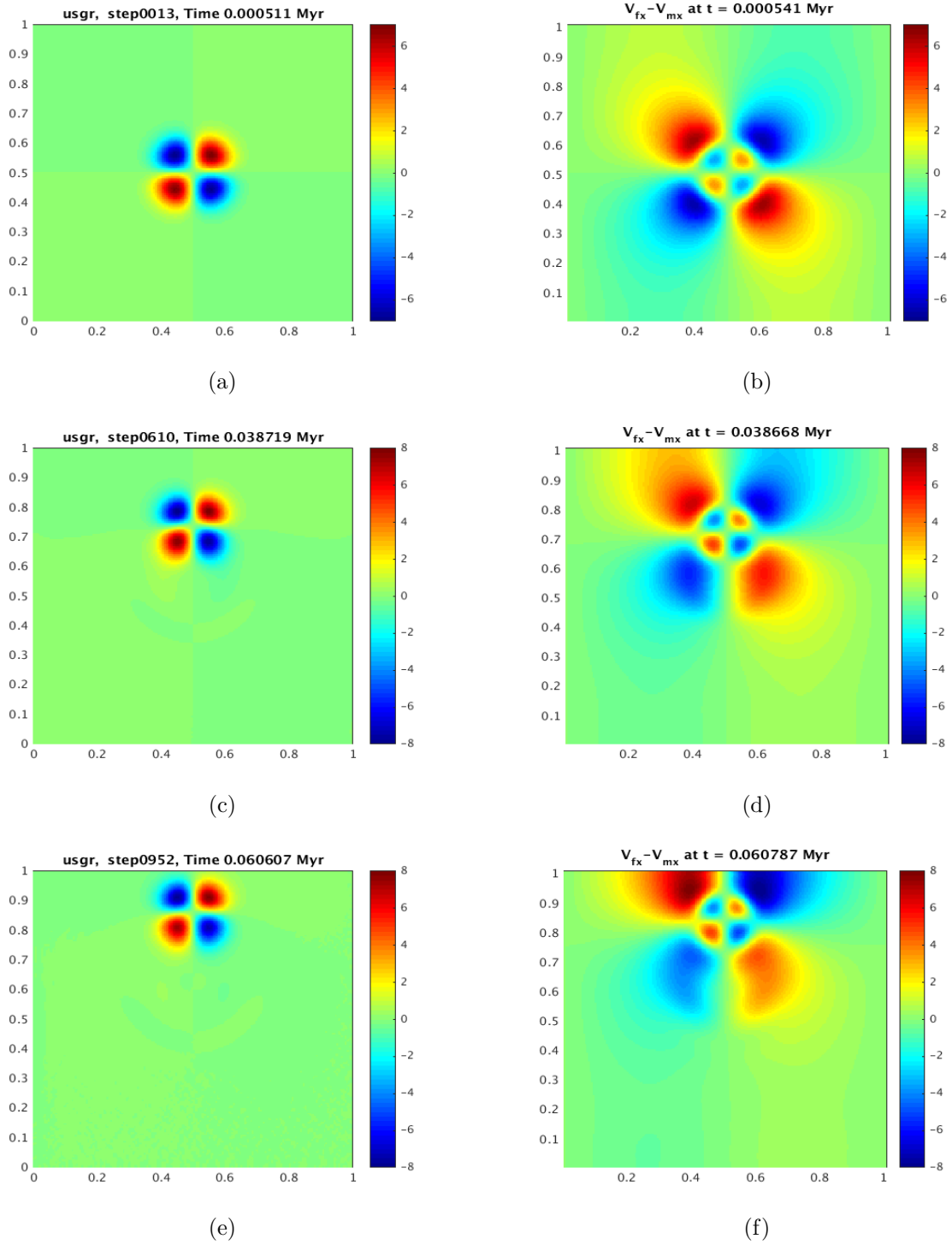
FIG. 6.3: Comparison of horizontal segregation velocity profiles obtained from FD-CON (left column) and PERCOL2D (right column) at various time steps.
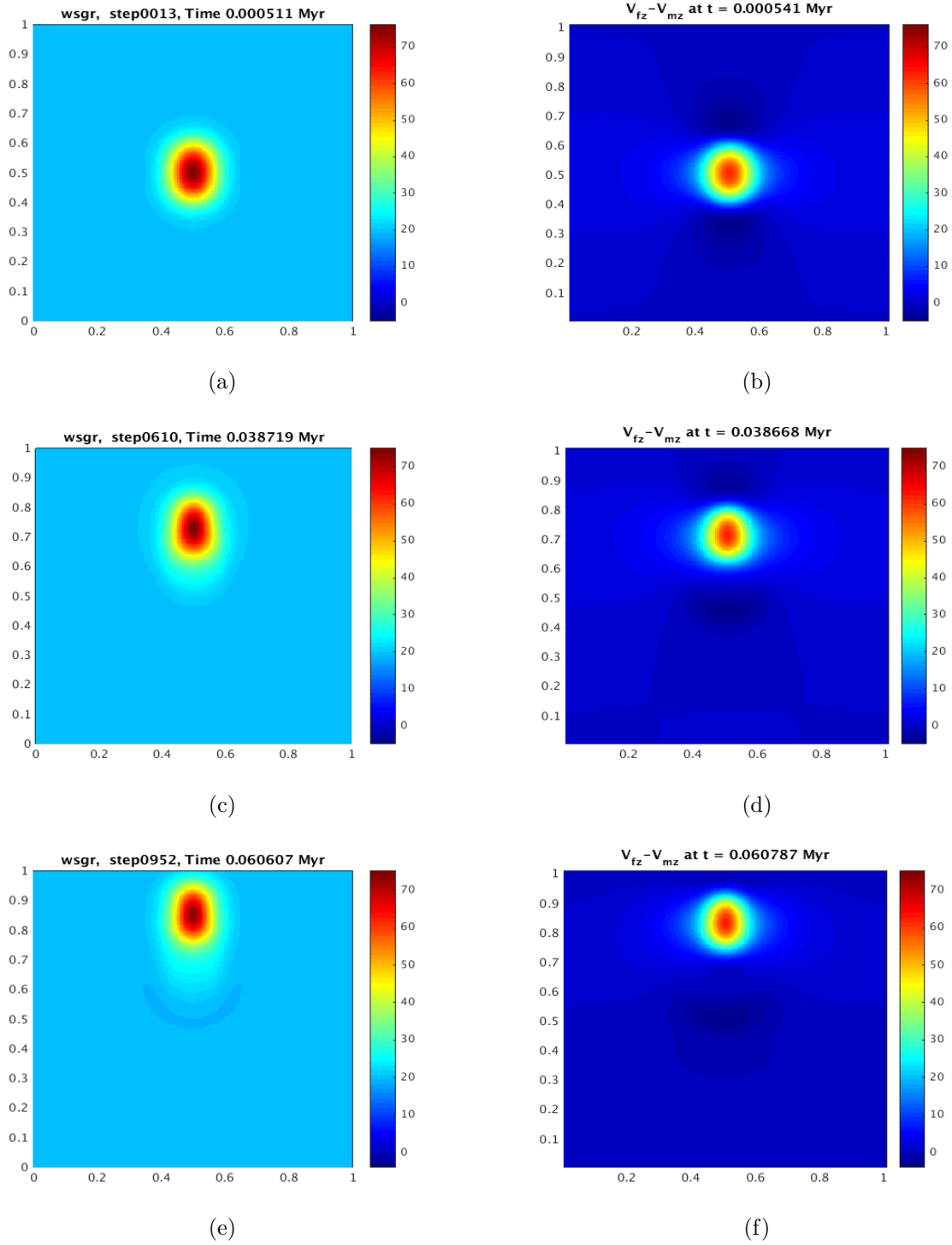
FIG. 6.4: Comparison of vertical segregation velocities obtained from FDCON (left column) and PERCOL2D (right column) at various time steps.

Conclusion : The 1D oversimplification which doesn't allow the relative vertical movement of two phase flow (i.e. $\bar{v} = 0$), simply neglects the large scale buoyancy force and so the buoyancy effect on stream function ψ is not visible. Therefore, this 1D approximation doesn't allow large scale downwelling. On the contrary, in FDCON due to this large scale buoyancy effect, the porous wave moves towards the upper boundary faster than PERCOL2D.

In spite of the disagreement in stream function and horizontal segregation velocity profile, the porous wave profile and the vertical segregation velocity profiles are within 15% of deviation. Since in PERCOL2D due to the oversimplification, the effect of buoyancy force on stream function becomes negligible and therefore its not capable of upwelling the matrix due to buoyancy, its not a wise idea to use this over simplification for PERCOL2D anymore when the 2D profiles are investigated. Therefore, PERCOL2D is left for future work upon excluding the oversimplification. Therefore, the logical conclusion is to continue the 2D experiments with FDCON implementing the new viscosity formulations [Schmeling et al., 2012], are carried out with the code FDCON

6.3   2D results obtained using different viscosity formulation

6.3.1   Motivation and theoretical background

Effective bulk and shear viscosity of matrix play an important role to drive the melt percolation in two phase flow setting and also for the mechanism of matrix compaction process. Although a number of experiments have been executed to determine shear viscosity [Faul and Jackson, 2007; Hirth and Kohlstedt, 1995a], the effective bulk viscosity of partially molten rock has not been much investigated both experimentally and theoretically. The effective bulk viscosity and effective shear viscosity of matrix obtained from the effective viscosity formulations used in PERCOL2D (eq. 6.2.5), are respectively slightly below and above the upper Hashin Shtrikman bound [Hashin and Shtrikman, 1963], which represents the upper bound for all possible isotropically distributed pore geometries.

In the effective shear and bulk viscosity formulations which does not incorporate melt fraction, for solid-liquid composites based on grain-boundary contiguity proposed by [Takei, 1998; Takei and Holtzman, 2009a,b], it has been shown that the bulk viscosity drops from infinity (when melt fraction is zero) to the order of the intrinsic shear viscosity η_{s0} at a grain contiguity of ~ 0.1. Later, both the effective bulk and shear viscosity of matrix reach the value zero when the contiguity value approaches to zero for increasing melt fraction. The either formulations proposed and used in [Simpson et al., 2010b], [Richard et al., 2012] are not able to predict the disaggregation of the material at melt fractions below one due to the reason that effective shear and bulk modulus approach to zero then.

The melt grain contiguity is associated with the geometrical feature of melt network. The bulk and shear viscosities predicted to become zero due to zero bulk and shear modulus of matrix when the melt fractions are 50 and 20 percent respectively for spherical melt fractions and tapered melt tubules. As a consequence, the partially molten rock starts to disaggregate.

Therefore, incorporation of melt network geometry is necessary to predict the effective bulk and shear viscosity of matrix. The revised viscosity formulation which incorporates the phenomena of melt network geometry has been proposed in [Schmeling et al., 2012] based on elastic moduli theory of a fluid filled poroelastic medium according to which the effective bulk and shear viscosity of matrix are :

$$
\begin{aligned}
\eta_s &= \eta_m (1 - \frac{\phi}{c_1})^{k_1} \\
\eta_b &= \eta_m c_2 \frac{(c_1 - \phi)^{k_2}}{\phi}
\end{aligned}
\tag{6.3.1}
$$

, when $c_1 \leq \phi \leq 1$ otherwise $\eta_s = 0 = \eta_b$. Here $k_1 = a_1[a_2 + \alpha(1 - a_2)]$, $c_1 = \frac{b_1 \alpha}{1 + b_2 \alpha^{k_3}}$, $c_2 = \frac{4}{3} \alpha c_1^{-k_2}[c_3(1 - \alpha) + \alpha]$, $a_1 = 0.97$, $a_2 = 0.8$, $b_1 = 2.2455$, $b_2 = 3.45$, $k_2 = 1.25$, $k_3 = 1.29$ and $c_3 = 2.4$. In this formulation, $\alpha = 0.1$ stands for the aspect ratio of oblate ellipsoidal inclusions whose net effect is equivalent to that of tapered tubules which is the geometry of melt network we use in our model. Throughout our model, n=2 has been chosen in the permeability law. How this viscosity formulation varies from the Bercovici's formulations, have been shown in fig.6.5 and in fig.6.6 respectively. These two figures indicate that the deviations of the effective bulk viscosities are more than the deviation of effective shear viscosities proposed by [Schmeling et al., 2012] and [Bercovici et al., 2001]. These deviations are more or less conservative according to the theoretical study but according to the experimental study ([Hirth and Kohlstedt, 1995a,b]), these deviations are even stronger with increasing value of melt fraction. Comparing fig. 6.5 and fig. 6.6 it can be concluded that both the effective bulk viscosity and effective shear viscosity of matrix deviate in the same manner with increasing porosity in 1D and 2D. Also, one can notice from fig. 6.5 and fig. 6.6 that both the effective bulk and shear viscosities are much weaker according to [Schmeling et al., 2012] formulation compare to [Bercovici et al., 2001] formulation with increasing porosity. In [Bercovici et al., 2001] formulation, effective shear viscosity reduces by maximum 10% whereas it reduces by 50 % according to [Schmeling et al., 2012] formulation with increasing melt fraction (cf. fig. 6.5(b)).
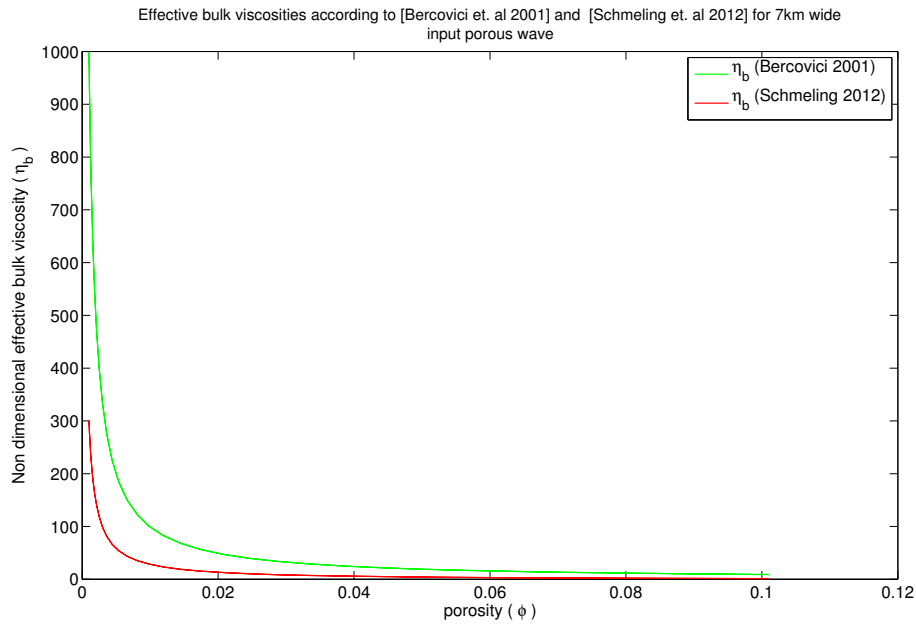
(a)
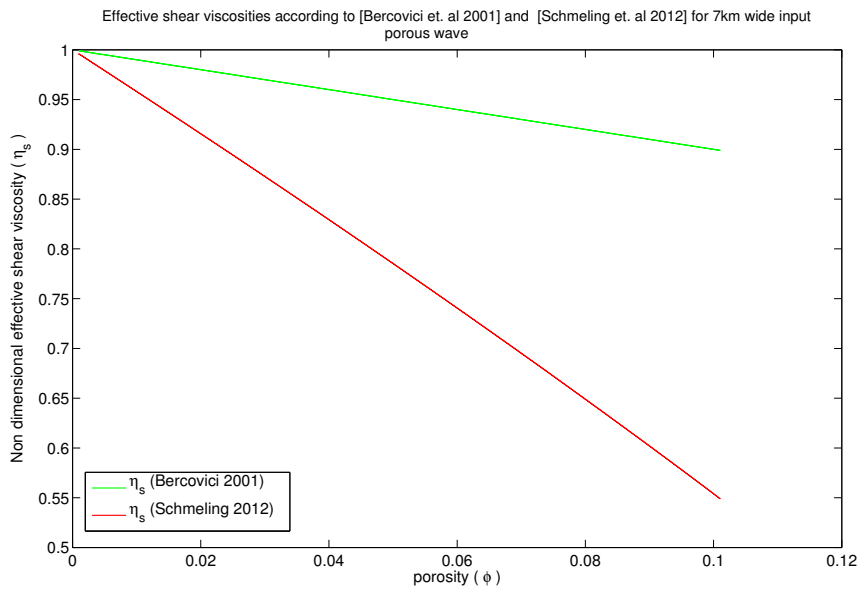
(b)

Fig. 6.5: Analytical formulation (1D) of (a) effective bulk viscosities and (b) shear viscosities proposed by [Bercovici et al., 2001] and [Schmeling et al., 2012]

(a)

(b)

(c)

(d)
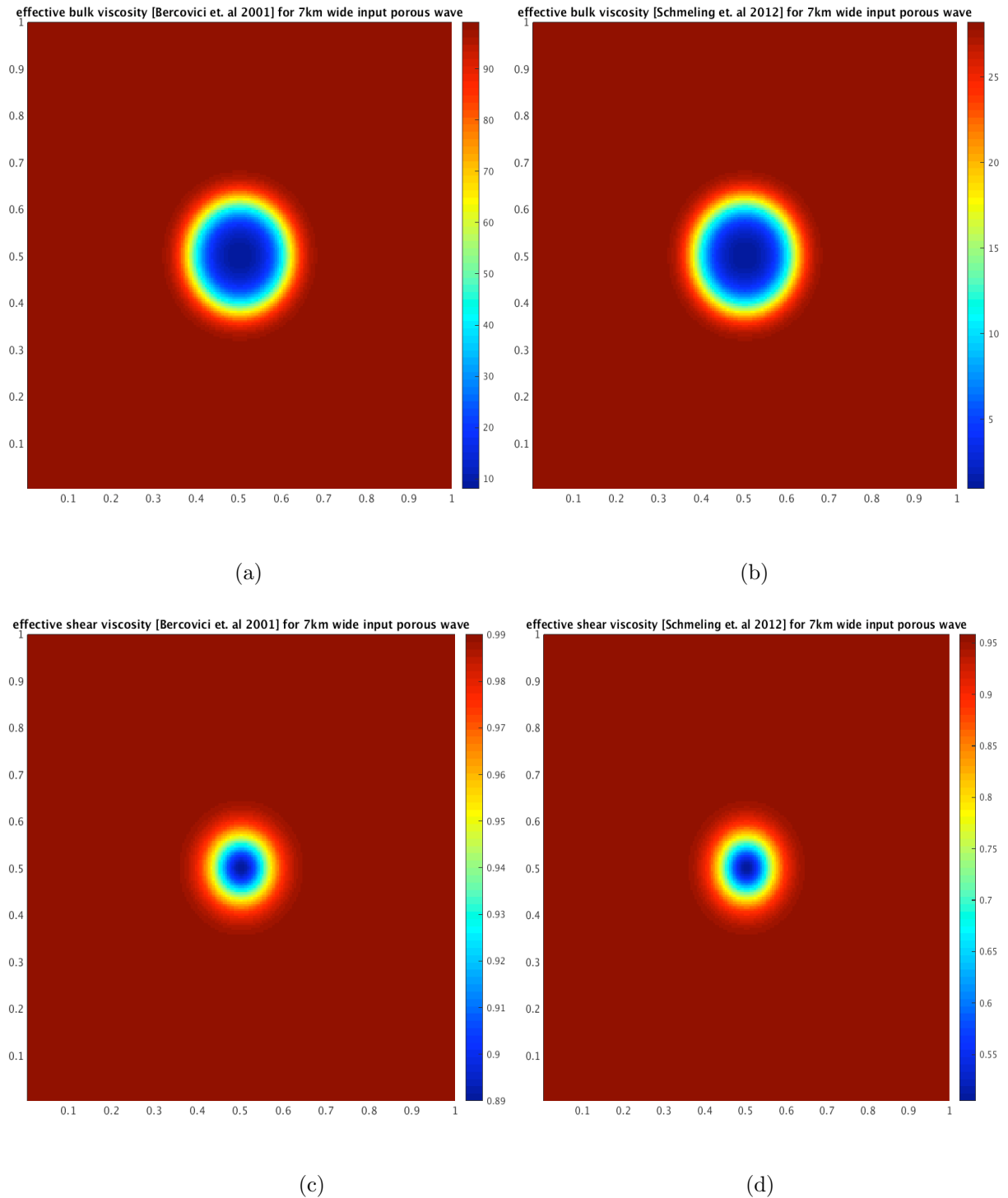
FIG. 6.6: With the input of porous wave having amplitude 0.1, background porosity as 0.01 and diameter as 7 km, the porosity dependent bulk and shear viscosities are: (a) effective bulk viscosity according to [Bercovici et al., 2001] (b) effective bulk viscosity according to [Schmeling et al., 2012] (c) effective shear viscosity according to [Bercovici et al., 2001] and (d) effective shear viscosity according to [Schmeling et al., 2012] formulation .
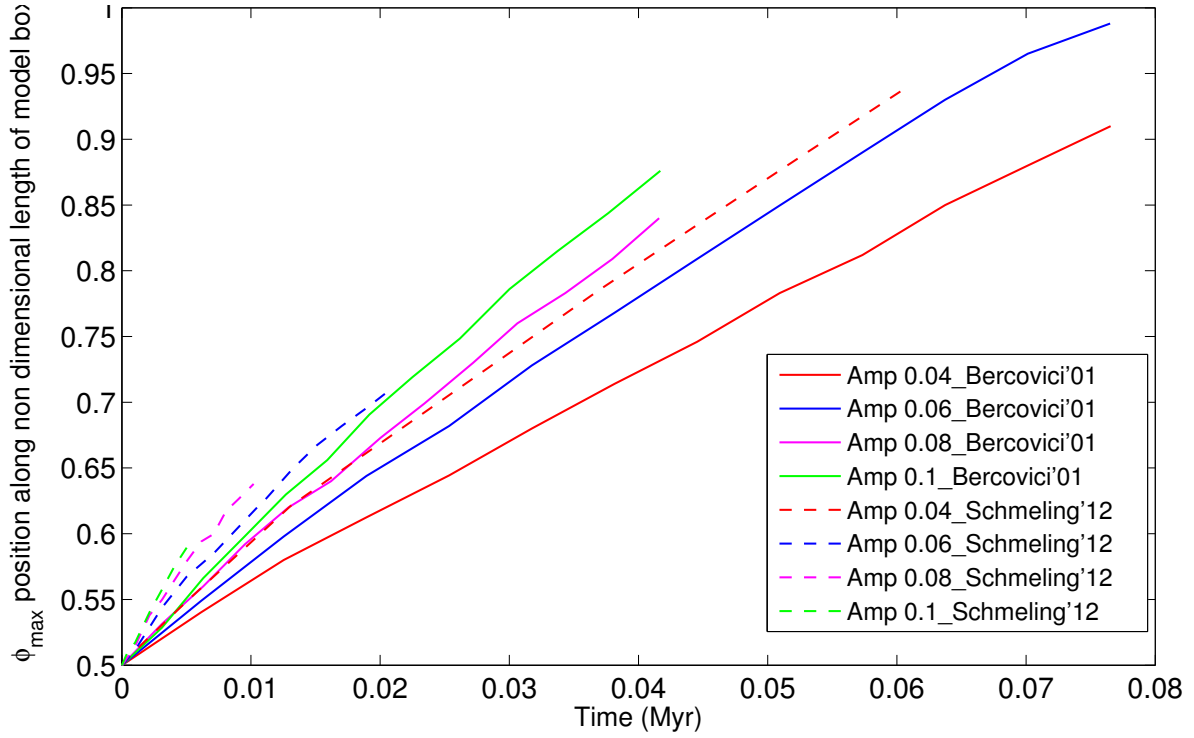
(a)
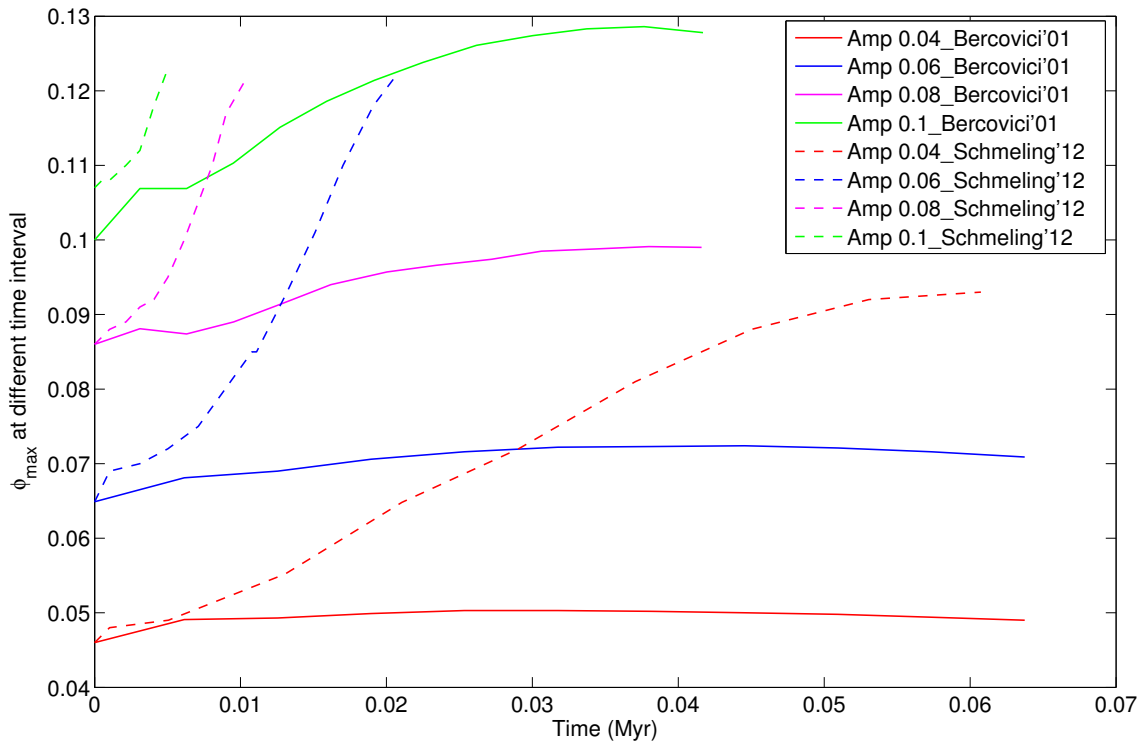
(b)

FIG. 6.7: (a) Position of ϕ_{max} at different time step and (b) Increment of maximum value of porosity (ϕ_{max}) in course of time for different non dimensional amplitudes (0.04, 0.06, 0.08 and 0.1 respectively) of two dimensional porous wave having 7 km maximum cross sectional diameter

An experiment is conducted for different amplitude of input porous waves having 7 km maximum cross sectional diameter to see their velocity and maximum amplitude variations with respect to time according to the viscosity formulations of [Bercovici et al., 2001] and [Schmeling et al., 2012]. The result of this experiment is presented in fig.6.7.

The vertical displacement rate of porous waves according to both the formulations are almost linear. From fig.6.7(a), it can be concluded that, for each amplitude, velocity of a porous wave having a certain amplitude and obtained from viscosity formulations of [Schmeling et al., 2012], is always higher than the velocity of the porous wave having the same amplitude, obtained from viscosity formulations of [Bercovici et al., 2001].

Also, the rate of increment of maximum value of porosity (ϕ_{max}) is higher according to [Schmeling et al., 2012] formulation compare to [Bercovici et al., 2001] formulation (cf. fig. 6.7(b)). The rate of increment of ϕ_{max} slows down for both the formulations as soon as the wave approaches towards the vertical upper boundary of the non dimensional model box since our model has a fixed boundary condition.

6.3.2   2D results from FDCON using the new viscosity formulation

Using the viscosity model as described in 6.3.1 following sets of results containing the propagation of porosity wave profile, horizontal and vertical segregation velocity profiles, effective bulk and shear viscosity profiles and stream function profiles, are presented. From fig. 6.11 and fig. 6.12 it can be observed that the amplitude of porous wave, stream function, horizontal and vertical segregation velocity increase much faster than the case where the viscosity formulations proposed by [Bercovici et al., 2001] have been used (cf. fig. 6.11, fig. 6.12 and left column of fig. 6.1 , fig. 6.2, fig. 6.3and fig. 6.4).

The core part of the vertical segregation profile is divided into two with the viscosity formulation proposed by [Schmeling et al., 2012] when it reaches near the upper boundary of the model box (cf. right column of fig. 6.12).

Also, the phase velocity of porous wave is much larger (42%) in fig. 6.11 when compared to fig.6.1 and its because of having lesser bulk viscosity in former case (cf. fig. 6.6).

From fig. 6.8 to fig. 6.19 it can be observed that, as soon as the amplitude of input porous wave increases from 0.04 to 0.1, speed of porous wave increases with course of time (cf. fig. 6.7) and the 8 petals pattern horizontal segregation velocity profile is first observed when the input porous wave's amplitude is 0.08. The reason behind this kind of pattern which starts to show up from this certain amplitude is probably because of the emergence of low viscous region surrounding the melt anomaly w.r.t increase of porosity (cf. fig. 6.5). Due to having low viscous region, the vertical segregation velocity will create some extra components in order to fill up the low viscous region. According to that mechanism, we get the 8 petals pattern of horizontal segregation velocity of which the inner 4 petals correspond to the flow in the low viscous regime and the outer 4 petals correspond to the flow through compacting to decompacting medium. Also, it can be observed that effective bulk viscosity influences the vertical segregation velocity profile and therefore the porosity profile as well. After the porous wave achieves a certain amplitude (approximately 0.15), FDCON fails to compute the porosity and other velocity profiles for further time steps due to the instability arose in the porous wave profile which causes the desegregation of melt.

(a)

(b)

(c)

(d)

(e)

(f)
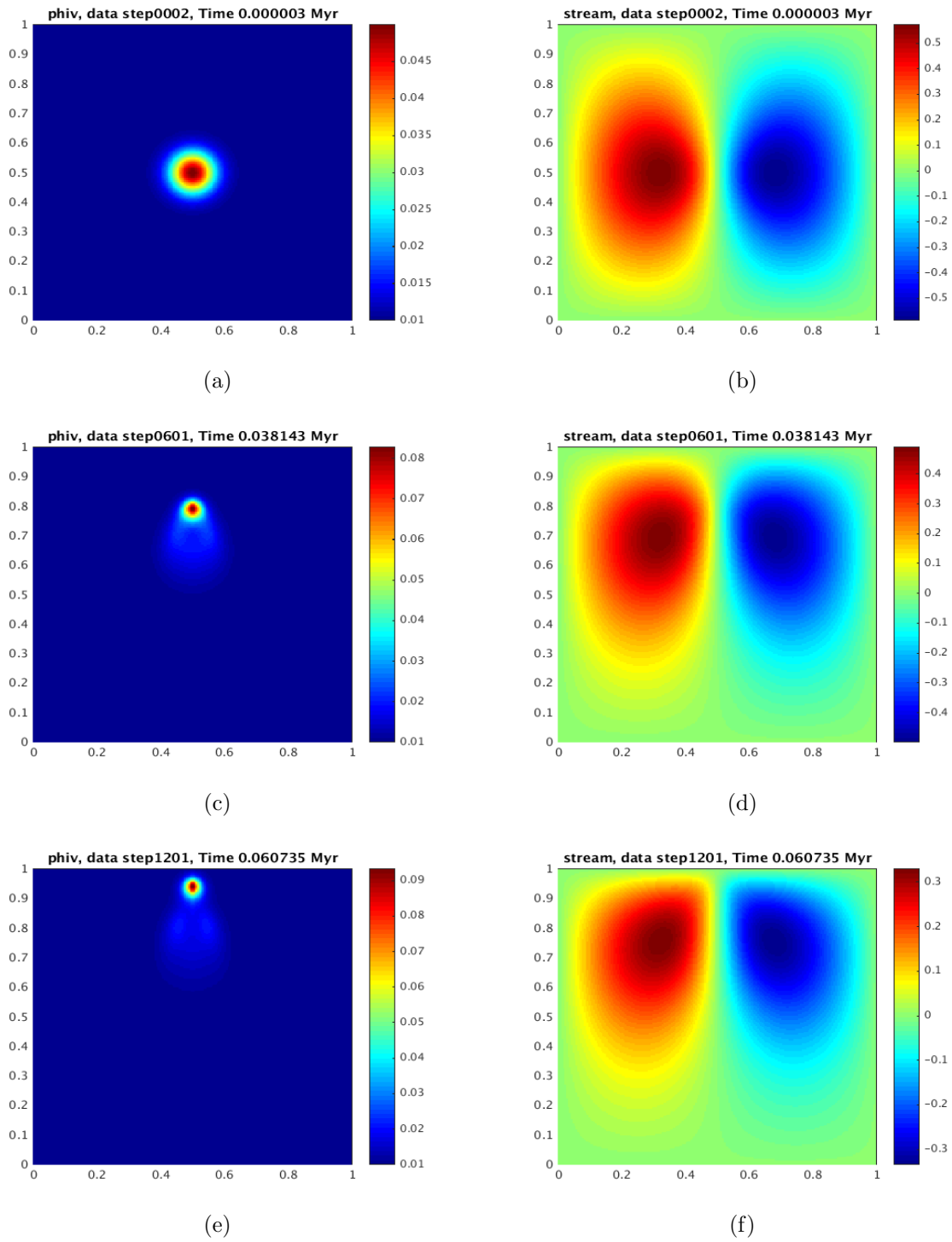
FIG. 6.8: The left column represents the time propagation profile of 7 km wide porous wave having amplitude 0.04, background porosity as 0.01 and the right column represents the time propagation of stream function profile using the new viscosity formulation [Schmeling et al., 2012].

(a)

(b)

(c)

(d)

(e)

(f)

FIG. 6.9: The left column represents the time propagation profile of horizontal segregation velocity and the right column represents the time propagation of vertical segregation velocity profile using the new viscosity formulation [Schmeling et al., 2012] when the input porous wave is 7km wide having amplitude 0.04 and background porosity as 0.01.

(a)

(b)

(c)

(d)

(e)

(f)

FIG. 6.10: The left column represents the time propagation profile of effective bulk viscosity and the right column represents the time propagation of effective shear viscosity profile using the new viscosity formulation [Schmeling et al., 2012] when the input porous wave is 7km wide having amplitude 0.04 and background porosity as 0.01.

(a)

(b)

(c)

(d)

(e)

(f)
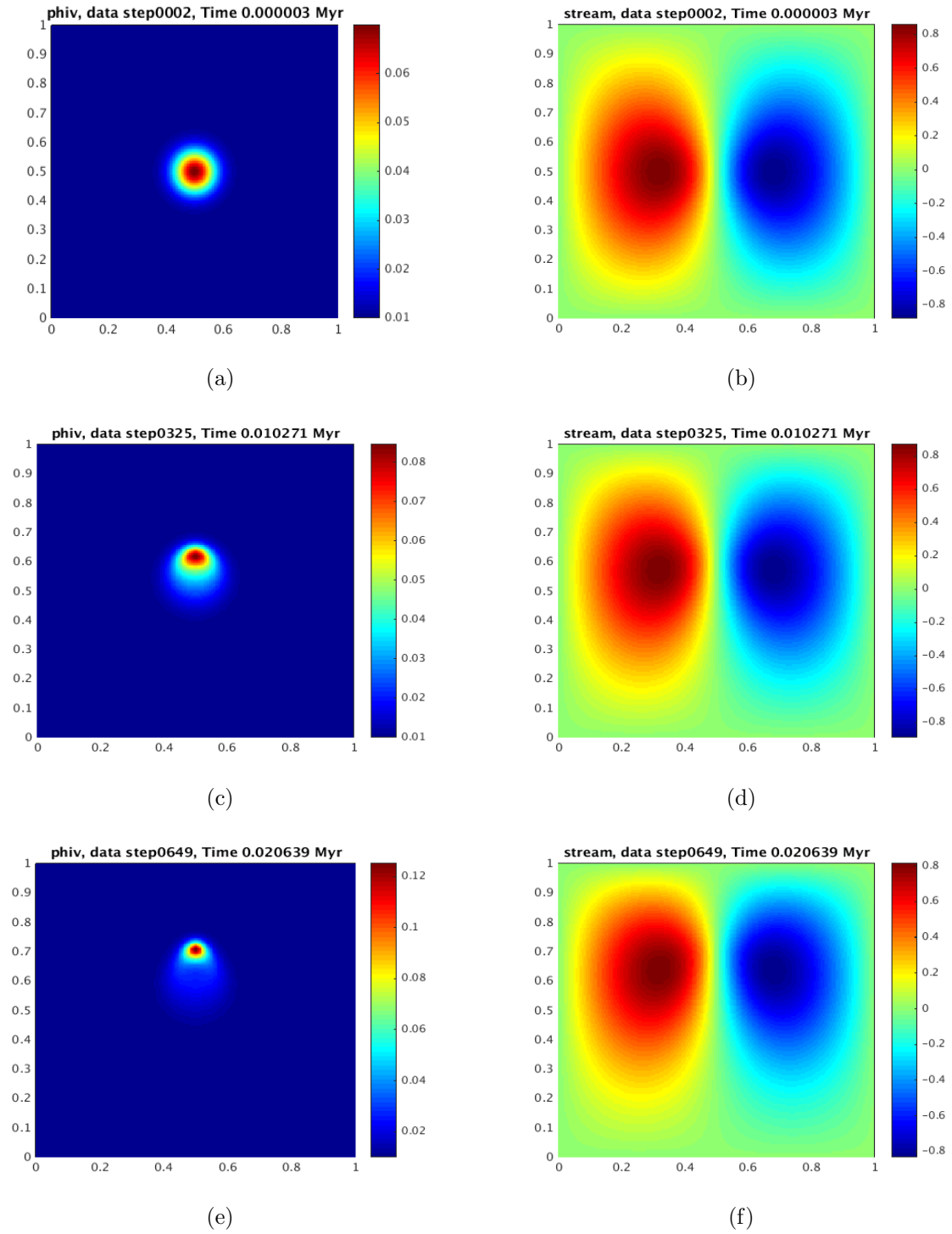
Fig. 6.11: The left column represents the time propagation profile of 7 km wide porous wave having amplitude 0.06, background porosity as 0.01 and the right column represents the time propagation of stream function profile using the new viscosity formulation [Schmeling et al., 2012].

(a)

(b)

(c)

(d)

(e)

(f)
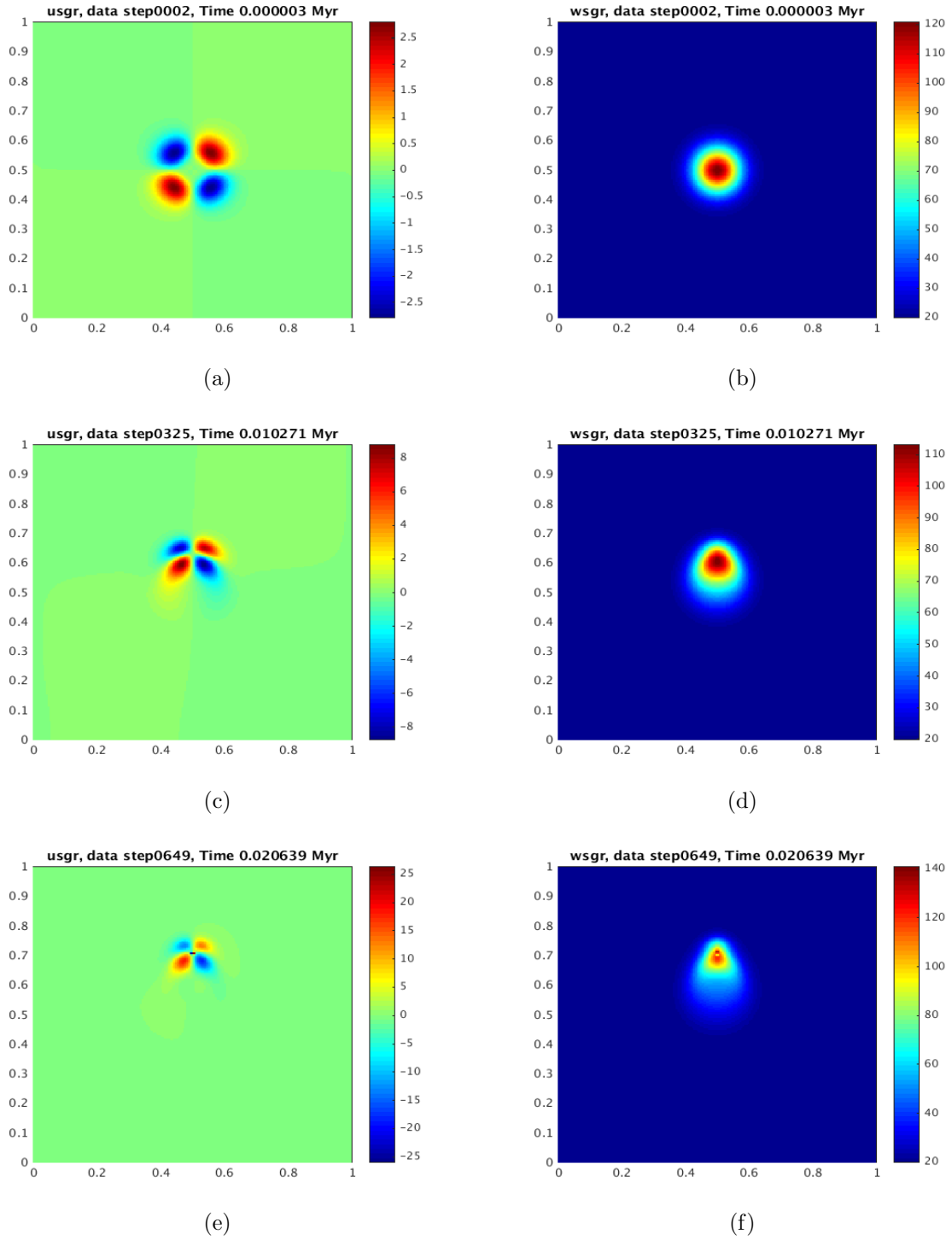
FIG. 6.12: The left column represents the time propagation profile of horizontal segregation velocity and the right column represents the time propagation of vertical segregation velocity profile using the new viscosity formulation [Schmeling et al., 2012] when the input porous wave is 7 km wide having amplitude 0.06 and background porosity as 0.01.

(a)

(b)

(c)

(d)

(e)

(f)
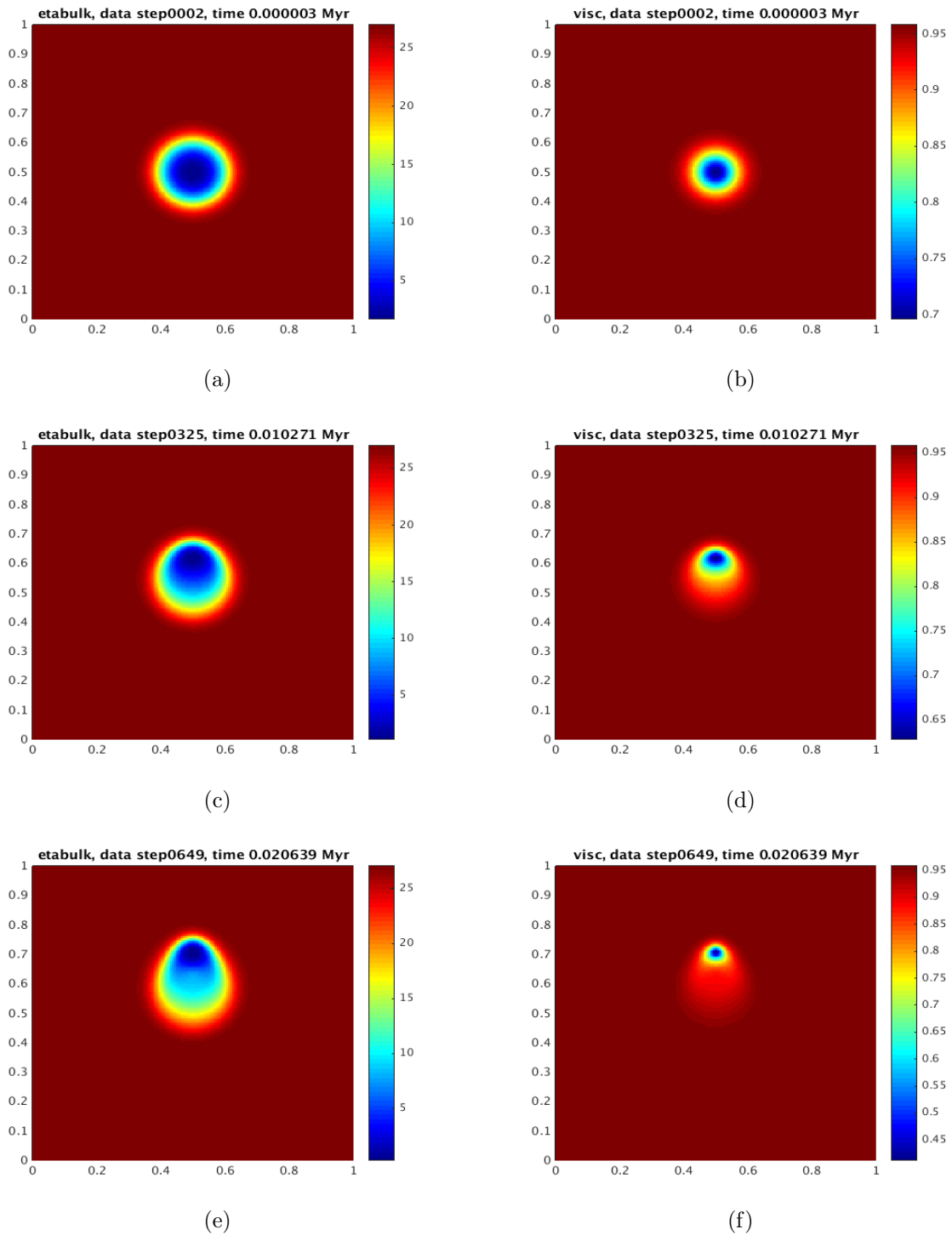
Fig. 6.13: The left column represents the time propagation profile of effective bulk viscosity and the right column represents the time propagation of effective shear viscosity profile using the new viscosity formulation [Schmeling et al., 2012] when the input porous wave is 7 km wide having amplitude 0.06 and background porosity as 0.01.

(a)   (b)

(c)   (d)

(e)   (f)
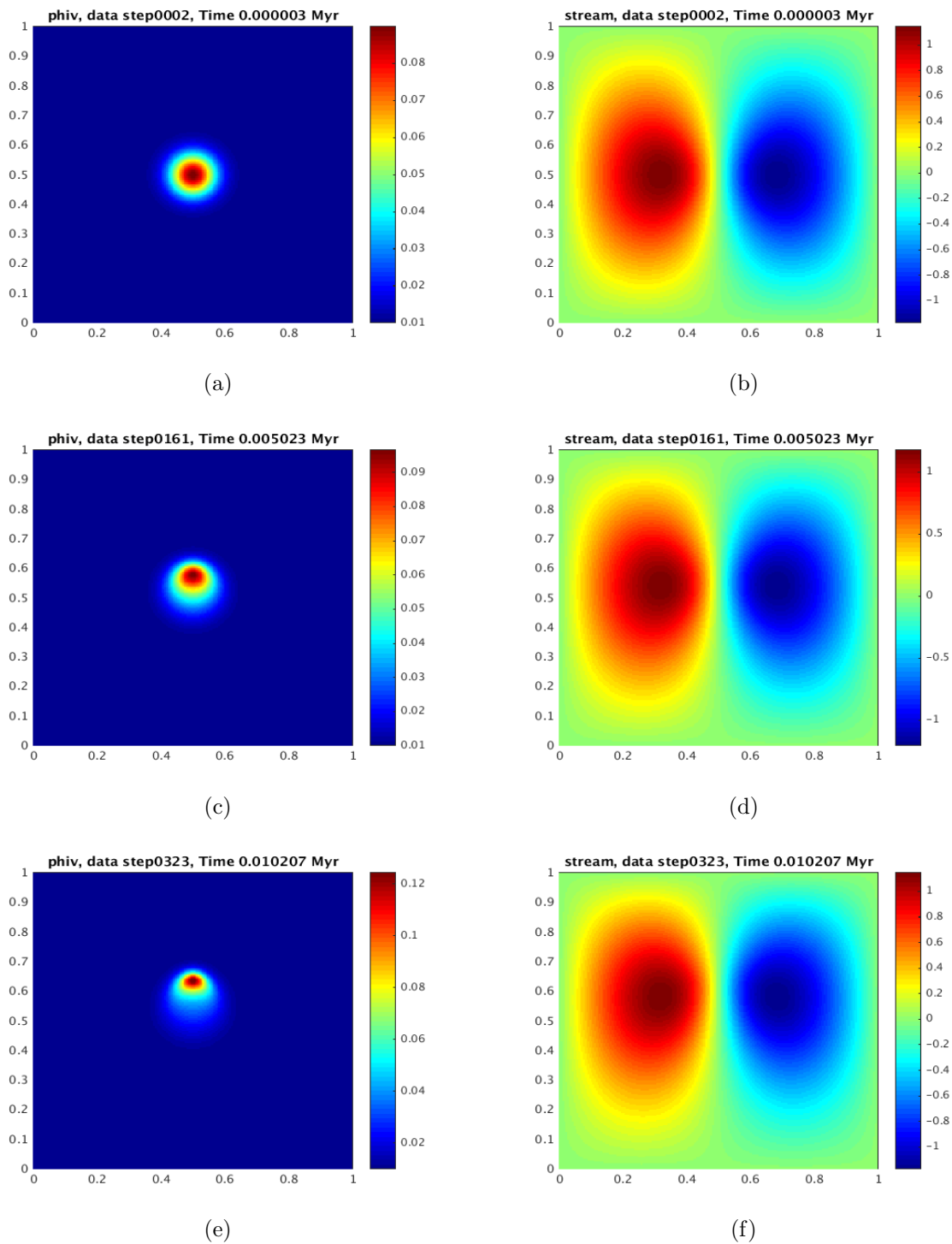
FIG. 6.14: The left column represents the time propagation profile of 7 km wide porous wave having amplitude 0.08, background porosity as 0.01 and the right column represents the time propagation of stream function profile using the new viscosity formulation [Schmeling et al., 2012] when the input porous wave is 7 km wide having amplitude 0.08 and background porosity as 0.01.
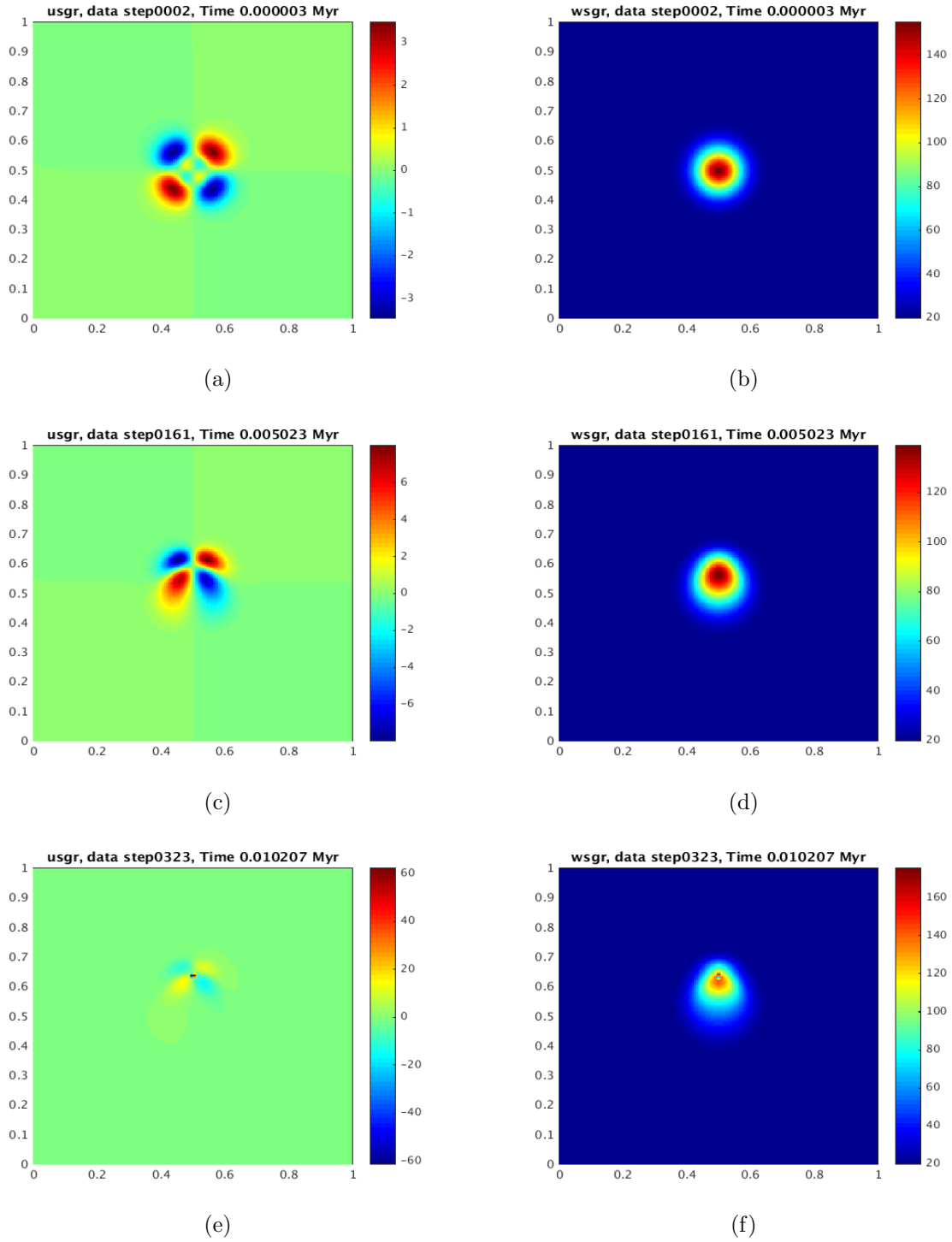
FIG. 6.15: The left column represents the time propagation profile of horizontal segregation velocity and the right column represents the time propagation of vertical segregation velocity profile using the new viscosity formulation [Schmeling et al., 2012].
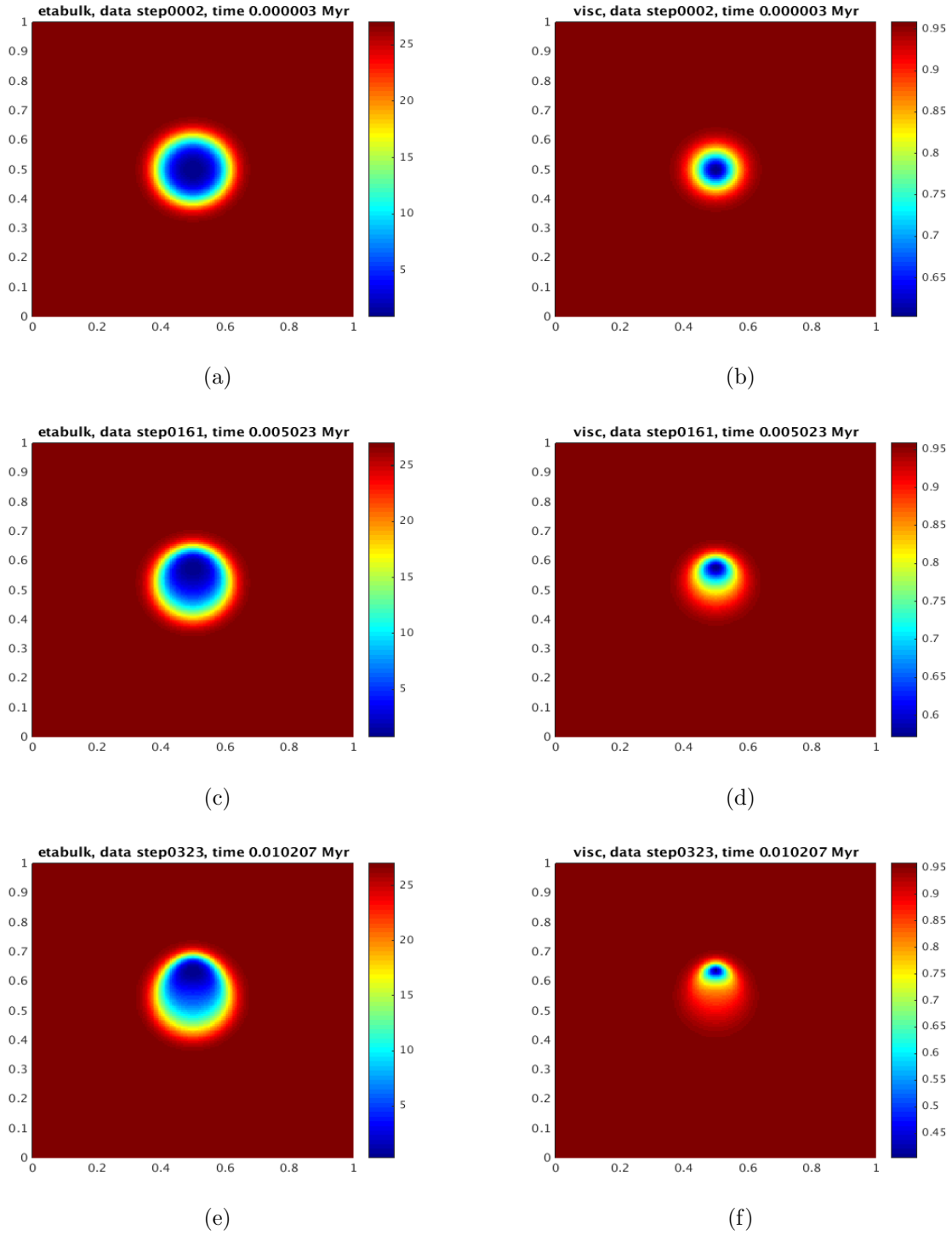
FIG. 6.16: The left column represents the time propagation profile of effective bulk viscosity and the right column represents the time propagation of effective shear viscosity profile using the new viscosity formulation [Schmeling et al., 2012] when the input porous wave is 7 km wide having amplitude 0.08 and background porosity as 0.01.

(a)   (b)

(c)   (d)

(e)   (f)
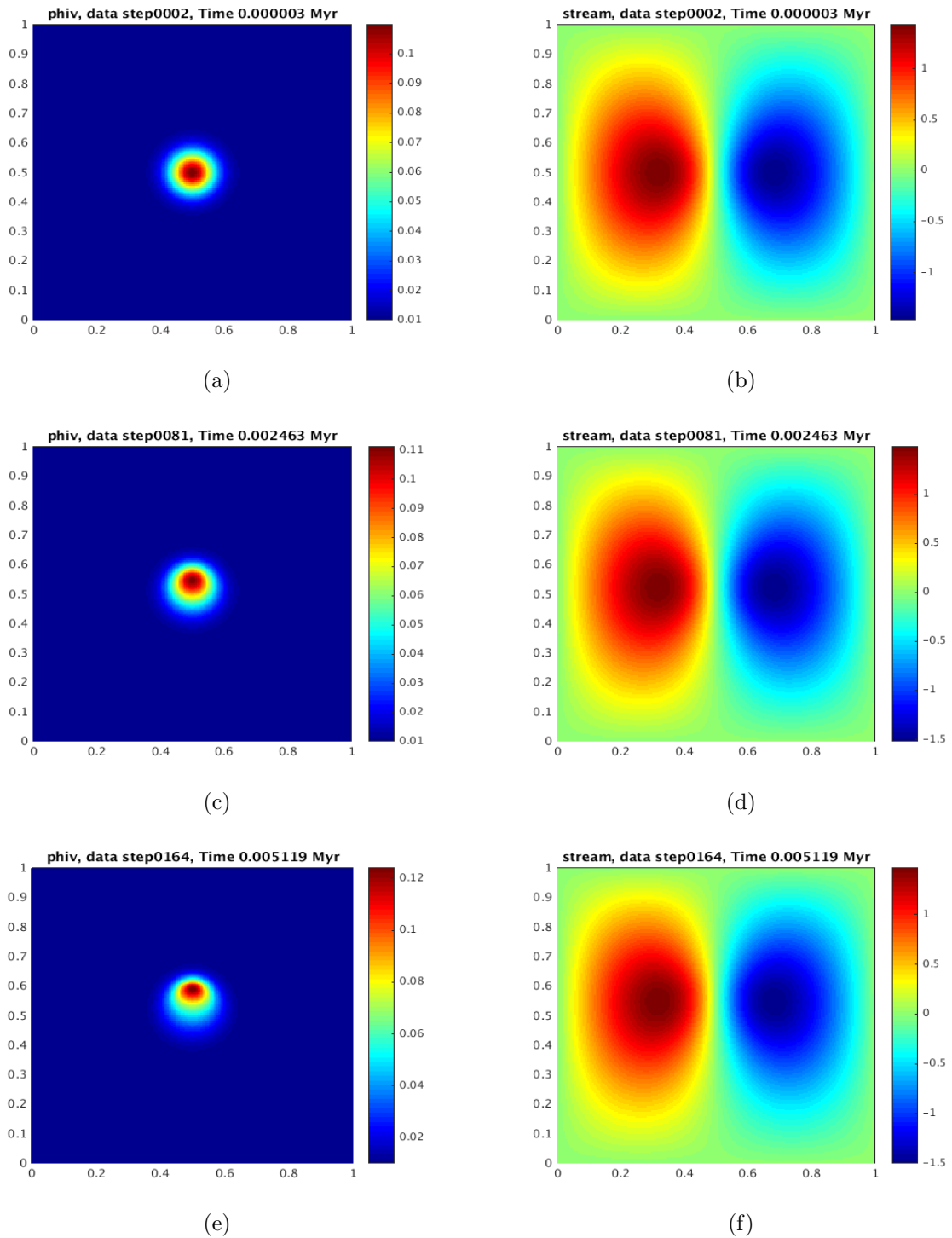
Fig. 6.17: The left column represents the time propagation profile of 7 km wide porous wave having amplitude 0.1, background porosity as 0.01 and the right column represents the time propagation of stream function profile using the new viscosity formulation [Schmeling et al., 2012].

(a)

(b)

(c)

(d)

(e)

(f)
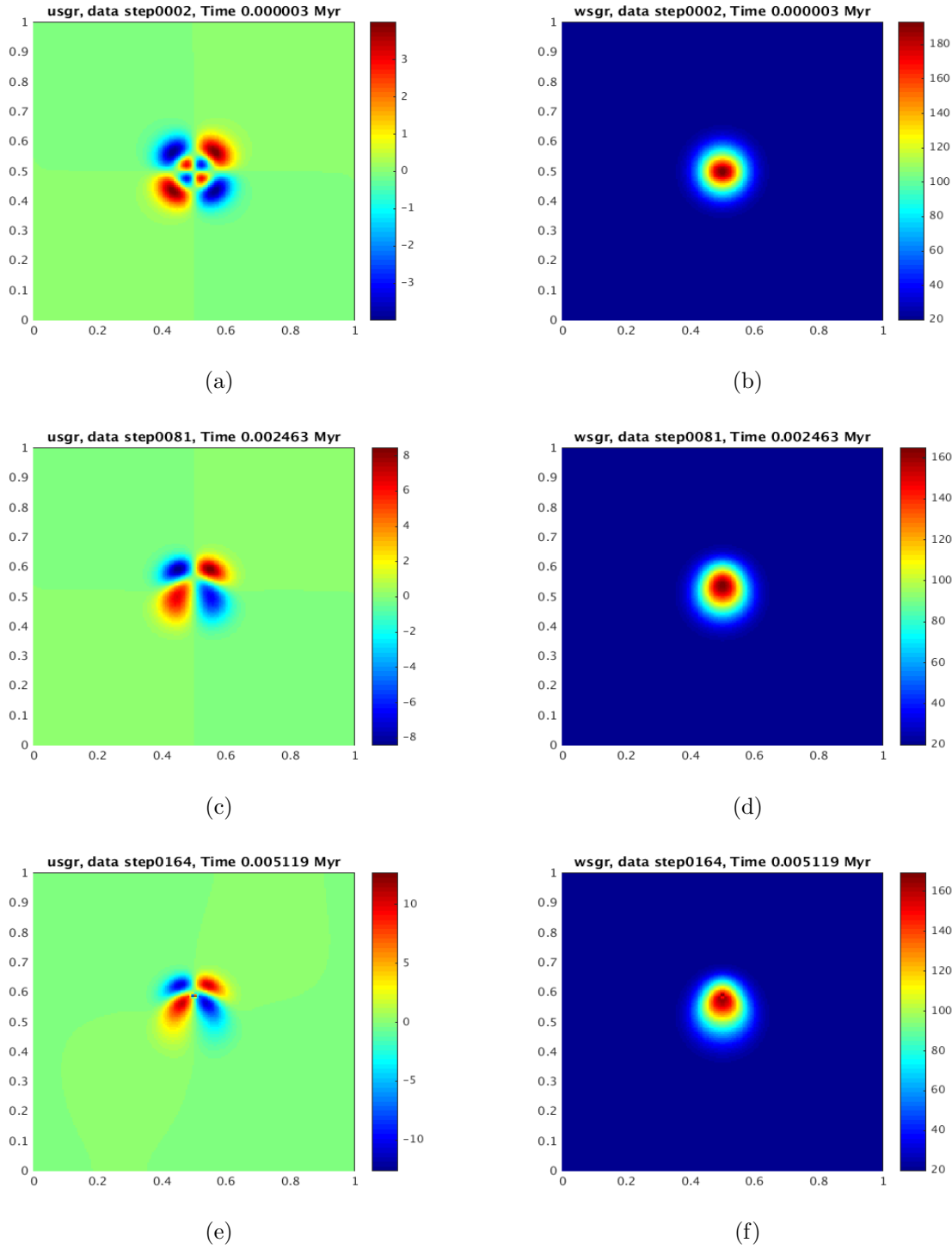
FIG. 6.18: The left column represents the time propagation profile of horizontal segregation velocity and the right column represents the time propagation of vertical segregation velocity profile using the new viscosity formulation [Schmeling et al., 2012] when the input porous wave is 7 km wide having amplitude 0.1 and background porosity as 0.01.
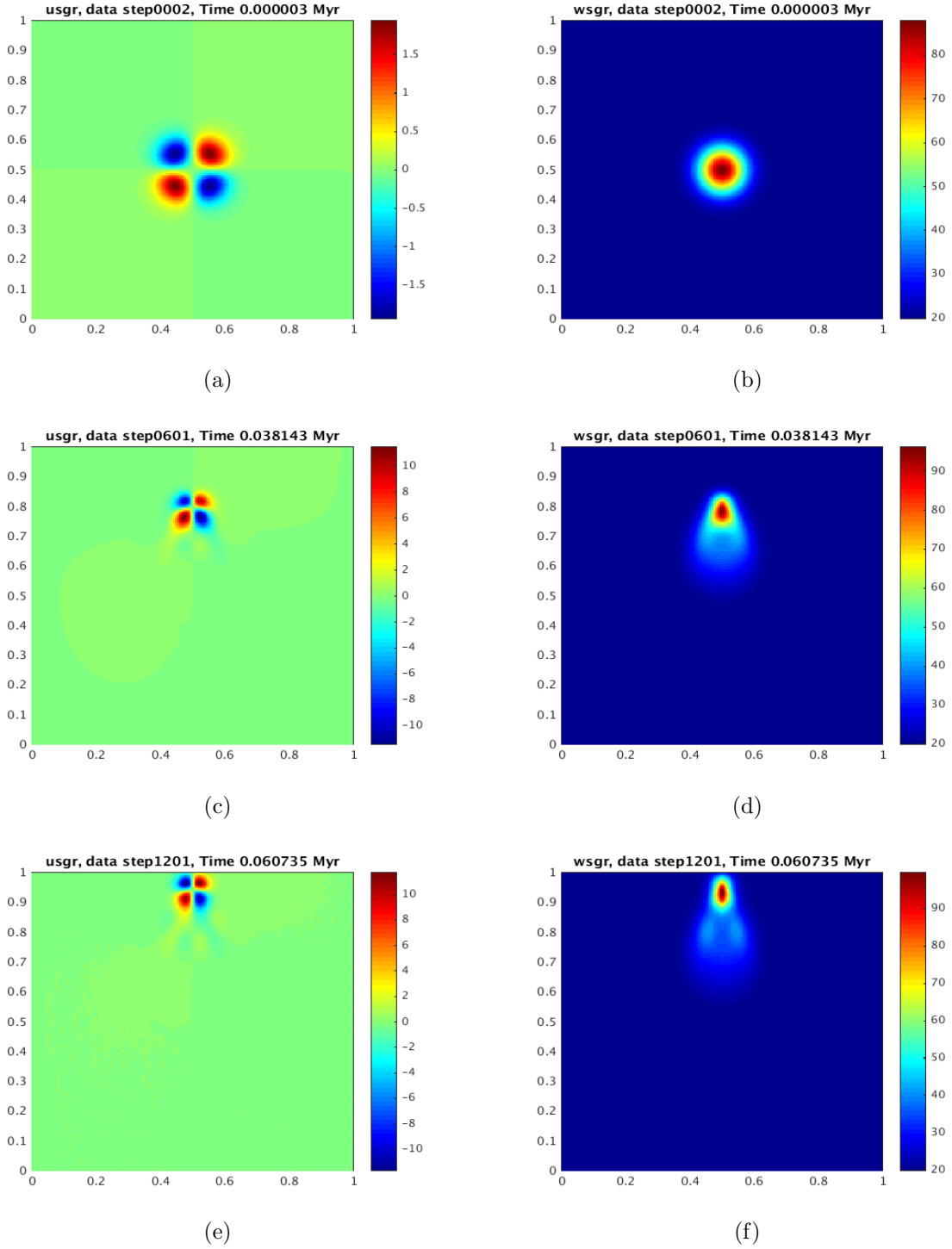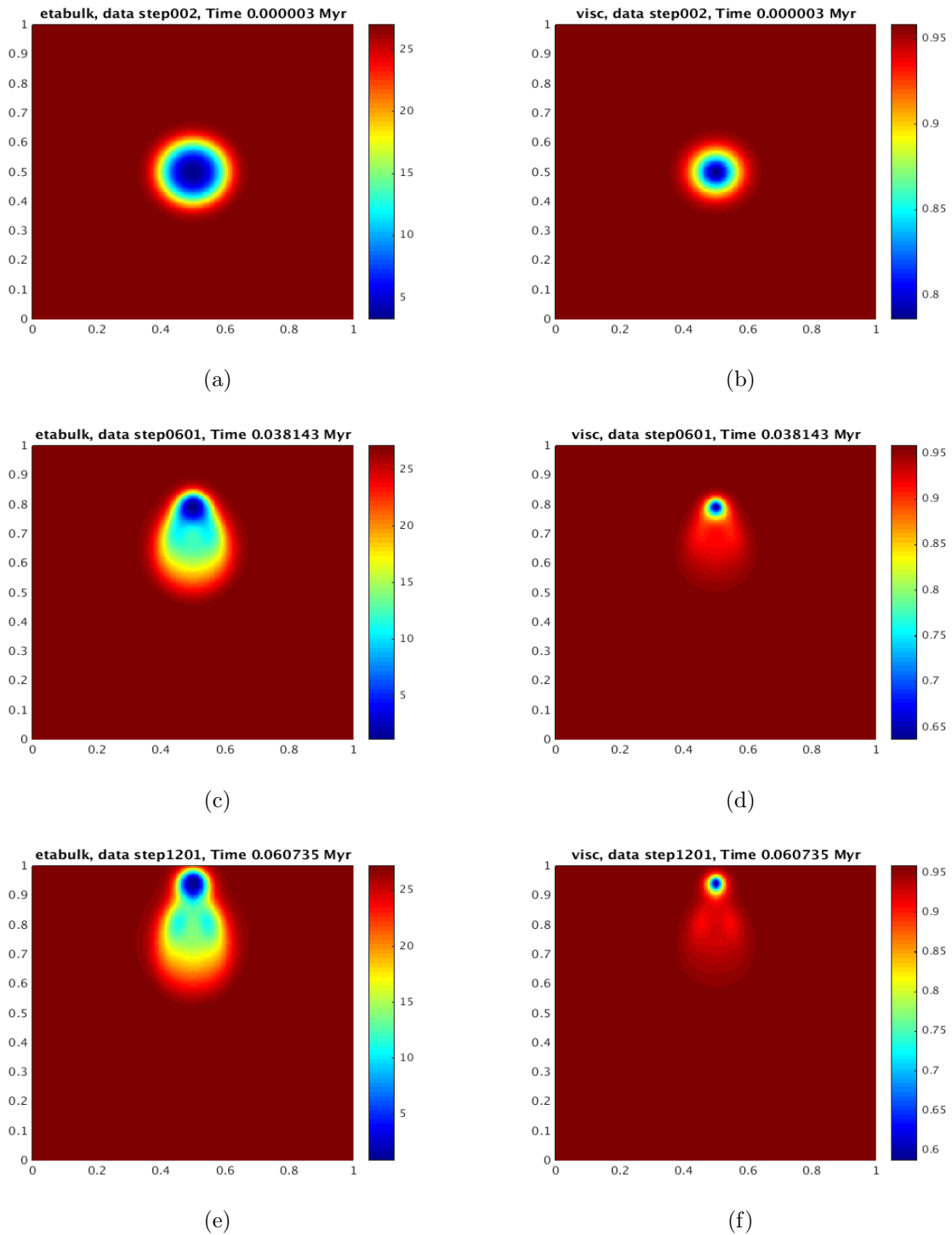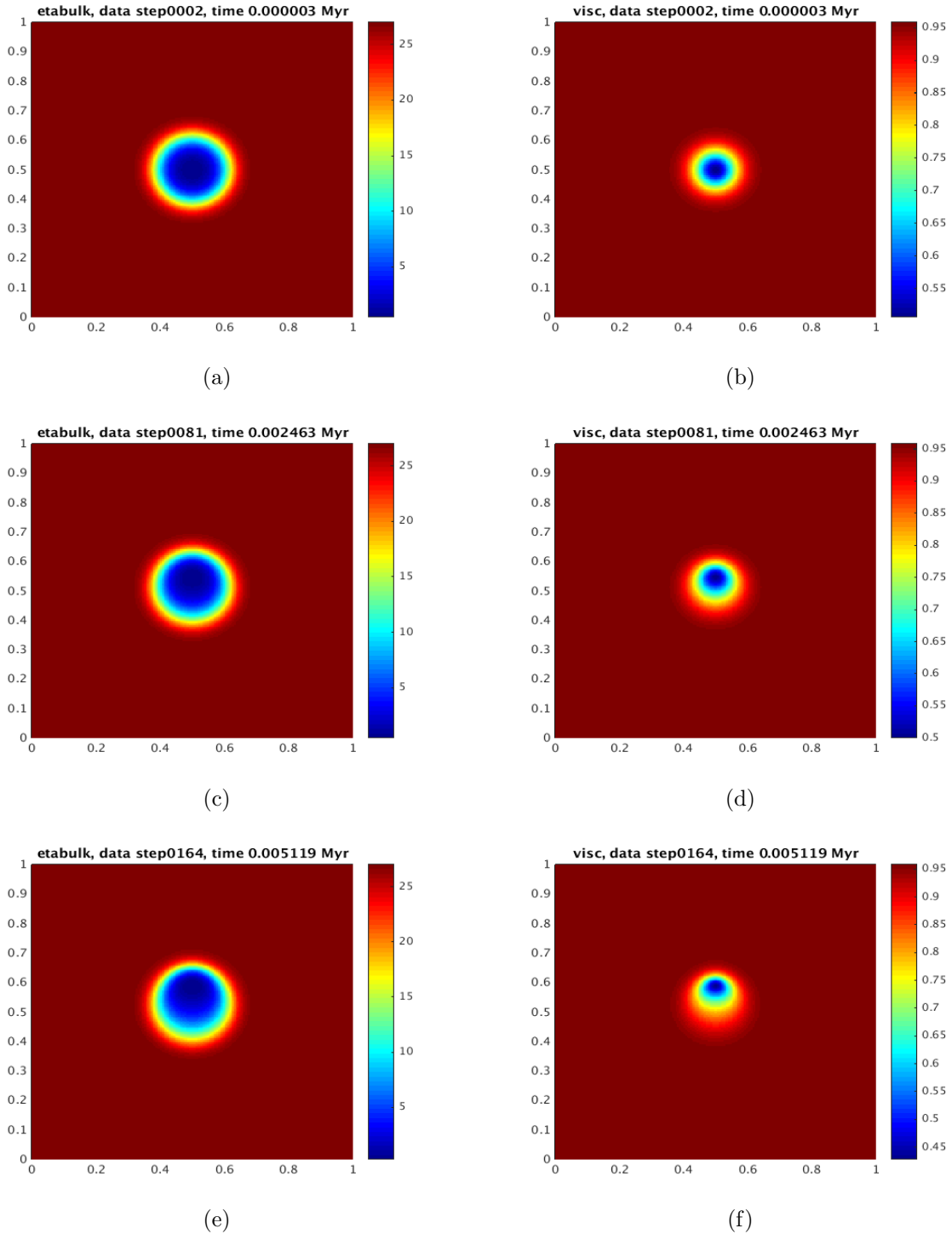
FIG. 6.19: The left column represents the time propagation profile of effective bulk viscosity and the right column represents the time propagation of effective shear viscosity profile using the new viscosity formulation [Schmeling et al., 2012] when the input porous wave is 7 km wide having amplitude 0.1 and background porosity as 0.01.

If fig. 6.1 - fig. 6.4 and fig. 6.11 - fig. 6.13 are compared it can be seen that the time propagation of porosity and the vertical segregation velocity distributions as obtained in fig. 6.11 - fig. 6.13 are narrower compare to fig. 6.1 - fig. 6.4. The possible explanation of this characteristics of these profiles is that, the local compaction length (computed according to [McKenzie, 1984] formulation i.e. $\delta = \sqrt{\frac{\zeta + \frac{4\eta}{3}}{\eta_f} k(\phi)}$, where ζ is the effective bulk viscosity, η is the effective shear viscosity, $k(\phi)$ is the permeability function and η_f is the viscosity of fluid.) incorporating both effective bulk and shear viscosity has a higher value when viscosity formulation of [Bercovici et al., 2001] is used compare to the local compaction length when viscosity formulation of [Schmeling et al., 2012] is used. Since the solitary wave solution to which the system of equations 6.2.1 - 6.2.7 tend to converge, is usually 22-25 local compaction length wide, is wider when viscosity formulation of [Bercovici et al., 2001] is used compare to the solitary wave solution when viscosity formulation of [Schmeling et al., 2012] is used. Therefore, the porosity and vertical segregation velocity profiles of fig. 6.11 - fig. 6.13 tend to converge to a narrower solitary wave solution compare to the fig. 6.1 - fig. 6.4. In order to compare this convergence process, we make a plot (cf. fig. 6.20) of speed of each input wave (i.e. of amplitudes 0.04, 0.06, 0.08 and 0.1 respectively) with varying time according to the formulations of [Bercovici et al., 2001] and of [Schmeling et al., 2012]. Combining the observations from fig. 6.7(b) and fig. 6.20, it can be observed that according to [Bercovici et al., 2001] formulations, the input porous waves having amplitudes 0.04 and 0.06 approach to their equivalent solitary waves (when compared to the dispersion relationship between speed and solitary wave amplitude as observed in fig. 2b of [Simpson and Spiegelman, 2011]) much faster than the porosity waves having similar amplitudes and obtained using the viscosity formulations from [Schmeling et al., 2012]. The higher amplitude waves (i.e 0.08 and 0.1) takes longer time to converge towards the solitary wave for both the formulations but the convergence process is always faster according to [Bercovici et al., 2001] compare to [Schmeling et al., 2012] formulation. The reason for unusual longer amplitude of non dimensional velocity for the wave having amplitude 0.1 and obtained using the [Schmeling et al., 2012] formulations, is probably the numerical instability arises in FDCON as soon as maximum value of porosity exceeds the value 15%.
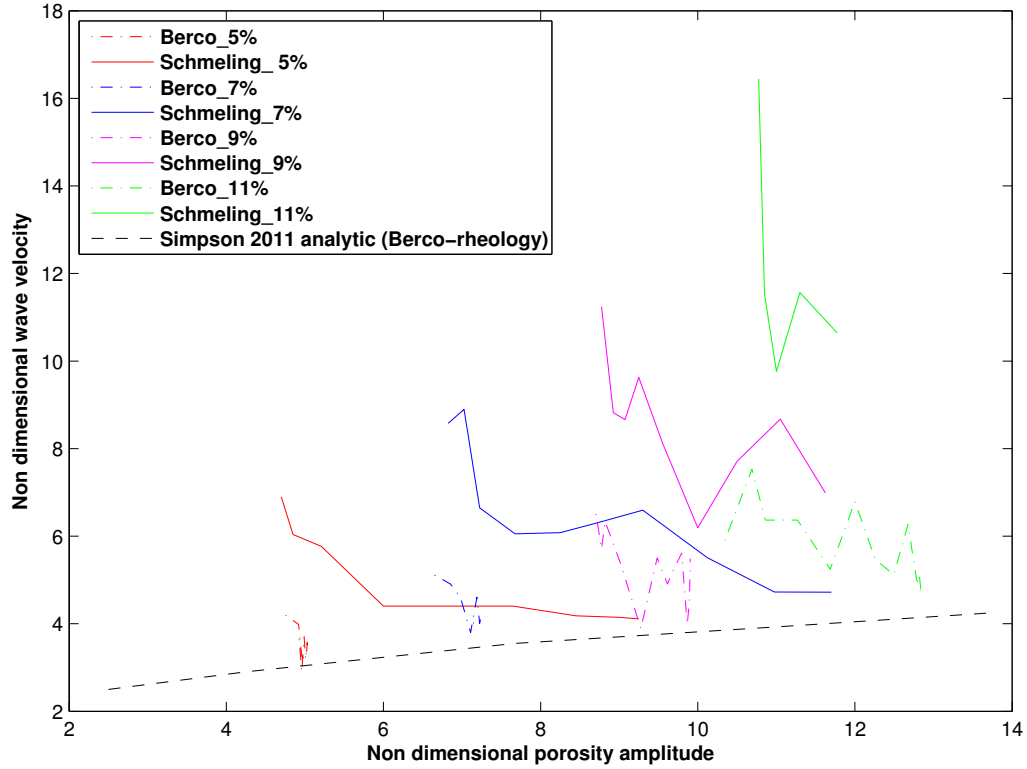
Fig. 6.20: Comparison of speed of the porous waves obtained from [Bercovici et al., 2001] and [Schmeling et al., 2012] respectively with the solitary wave speed profile as obtained from [Simpson and Spiegelman, 2011] with respect to the increment of ϕ_{max} at different time steps for the input of two dimensional porous wave having 7 km maximum cross sectional diameter and different non dimensional amplitudes (0.04, 0.06, 0.08 and 0.1 respectively)

Therefore, it can be concluded that, the strong porosity dependence of bulk and shear viscosity according to [Schmeling et al., 2012] formulation leads to significantly narrower porosity waves compared to the time evolution of porous waves obtained using the [Bercovici et al., 2001] formulation. Also, for a certain amplitude, weaker viscosity ([Schmeling et al., 2012]) makes propagation of porous wave faster almost by a multiple of 2 than the one which uses the stronger viscosity formulations of [Bercovici et al., 2001]. As the amplitude of input porous wave distribution increases from 0.04 to 0.1, the velocity of the wave also increases (cf. fig. 6.20) which we

have observe in 1D case as well (cf. fig. 4.12). But the speed decreases in fig. 6.20 with the increment of stationary maximum value of porous wave (i.e. ϕ_{max}).

In the next chapter summary and conclusions extracted from chapter 1 - 6 will be discussed.

Chapter 7

Summary of Results and Conclusion

Melt segregation is known as a combined process containing two stage of individual processes. The first one is generation of magma by partial melting at depth and the second one is melt migration towards the surface of the earth. Melt migration occurs through various methods like melt transport via channels, melt transport through dykes and melt transport through porous medium when the matrix is compacting. These various methods of melt transport take place at different regions inside the earth which is shown schematically at fig. 4.1.

This thesis focuses on the melt transport through porous medium considering the matrix compaction which takes place at greater depth of earth compare to rest of the melt transport processes. In this thesis it is shown that how a code is set up describing the two phase flow process through porous medium and thereafter how is it benchmarked in 1D and partially in 2D with the help of solitary wave solution and another two phase flow code FDCON respectively.

Partial melting depends on temperature, pressure, and chemical composition of the lithosphere and asthenosphere. Melt migration is governed by the principles of conservation of mass and momentum. The model of porous flow was first proposed by [Frank, 1968], in which a partially molten region is regarded as a saturated porous medium. This model is supported by experimental evidence. [Waff and Bulau, 1979] shows that liquid formed by small degrees of partial melting will be distributed in an interconnected network along the grain edges of the residual crystals if the angle between two crystal faces in equilibrium with liquid (dihedral angle) is less than 60°. The average dihedral angle is observed to be about 45° in experiments on partially molten basalts [Waff and Bulau, 1982, 1979; Watson, 1982]. The reconstructed 3-D melt distribution is shown in Fig.2.1 [Garapić et al., 2013], when the grain size is 33 μm and melt fraction is 3.6%

Crystalline material containing a small amount of melt can be regarded as a porous medium or matrix which is saturated with fluid (melt). Migration of melt through the matrix is driven by pressure gradients produced by the buoyancy of the melt or the deformation of the matrix by matrix compaction process.

Effective bulk and shear viscosity of matrix play an important role to drive the melt percolation in two phase flow setting and also for the mechanism of matrix compaction process. Theoretical framework regarding viscosity of the matrix considering the melt network geometry [Schmeling et al., 2012] has been applied to FDCON and the two phase flow characteristics due to implication of this new viscosity formulations also have been observed in this thesis

This thesis consists of six chapters.

The first chapter gives an overview of the theoretical background and motivations behind the study of numerical modeling of two phase flow through porous medium

under the matrix compaction considering the melt as a fluid phase and the matrix as a solid phase.

The second chapter describes the governing equations and the mathematical framework required to set up the code. A step by step algorithm which is used to set up the code is also provided in this chapter cf. fig.2.2.

Chapter 3 gives detail insight of the numerical solvers used in the code and a comparison between iterative solver and direct solver also has been discussed which concludes that use of direct solver is more effective than the use of iterative method for the particular numerical settings used to set up the code PERCOL2D.

Fourth chapter describes some numerical experiments which are executed to differentiate the effect of periodic and fixed boundary conditions. It is also shown that how the width of the input porous wave which is comparable to a certain number of compaction lengths behave differently when the compaction length is changed due to variation of either the matrix viscosity or the background porosity or the permeability constant. How the phase velocity of porous wave is changed under different conditions like different width and amplitude of the porous wave or due to use of different compaction lengths in the model are also discussed in this chapter. The numerical experiments under periodic boundary condition show almost solitary wave like characteristics when time propagation of porous wave, fluid velocity and matrix velocity are observed. This indicates that the governing equations have a solution which is a solitary wave [Barcilon and Lovera, 1989; Barcilon and Richter, 1986; Scott and Stevenson, 1984; Spiegelman, 1993a,b]

Chapter 5 gives the solution of this solitary wave (1D) when the two phase mixture effective bulk and shear viscosity are functions of porosity. The mathematical derivations and a schematic algorithm to get the 1D solitary wave solution from the governing equations (eq.2.1.1-eq.2.1.5) are provided and thereafter how both

the code PERCOL2D and FDCON have been benchmarked in 1D using the solitary wave solution, are also discussed in this chapter. A comparison of solitary wave's velocity obtained from the analytical solution given by the code SWG and the phase velocity obtained from time propagation profiles of porosity in the code PERCOL2D and FDCON are also presented in cf. fig. 5.5 to make this benchmarking more precise and clear.

Chapter 6 mainly gives an overview of a partial agreement of the time propagation of various profiles like porosity, fluid velocity, matrix velocity, stream function and the segregation velocity obtained from two different code PERCOL2D and FDCON. The agreement is partial because of the oversimplification of the terms θ and ξ whose gradient denotes the differential flux between the matrix and the fluid and flux due to matrix compaction respectively. In future the benchmarking needs to be completed upon removing the over simplification.

Another main aspect of this chapter is, implication of a different viscosity formulations proposed by [Schmeling et al., 2012] in FDCON and observing the two phase flow characteristics due to this implications.

To highlight, this thesis introduces the following facts:

1) 1D solitary wave solution obtained from the governing equations proposed by [Bercovici et al., 2001] to describe the two phase flow system considering the matrix compaction and assuming effective bulk and shear viscosity of matrix as a function of porosity.

2) Implication of the solitary wave solution to benchmark the code PERCOL2D and FDCON in 1D.

3) Implication of the bulk and shear viscosity of matrix considering the melt geometry [Schmeling et al., 2012] in FDCON and observation of the two phase flow characteristics from the time propagation profiles of porosity, melt and fluid ve-

locity, segregation velocity and the stream function. Here we found that, stronger porosity dependence of bulk and shear viscosity as formulated in [Schmeling et al., 2012] leads to the propagation of significantly narrower porosity waves compared to the time evolution of porous waves at corresponding time intervals which are obtained using the viscosity formulation of [Bercovici et al., 2001] and which has a weaker dependence on variation of porosity or melt fraction.

The work carried out in this thesis can be applied to model the subduction zone in future where at certain depths amphibole becomes unstable due to prescribed pressure and temperature condition and releases water [Iwamori, 1998; Maruyama and Okamoto, 2007]. By application of this code in subduction zone (parallel to trench) setting, how the water released by amphibole travels through the mantle wedge due to the compaction of matrix and thus triggers partial melting and forms magma chamber, can be explained. In reality, these magma chambers are the roots of the volcanoes observed at the surface. Therefore, this code will give a scope to investigate the relation between volcano spacing and fluid percolation in the mantle wedge in future by its successful implementation in the subduction zone settings. Also, application of this code in subduction zone (perpendicular to trench) setting, will be able to solve for the full two phase flow equation system in the mantle wedge with prescribed no-slip boundary conditions for the flow. This application will be unique in the sense that the formulation proposed by [Bercovici et al., 2001] allows for computing the pressure difference between the two-phases which enables to investigate the temporal evolution of the effective pressure produced by fluid generation due to phase change and by the background shear stress caused by the large scale subducting flow. The numerical modeling carried out in this thesis, can also be applied to highly porous region of mid ocean ridges. Because, strong porosity dependance of shear and bulk viscosity leads to (since the ratio of effective

bulk and shear viscosity is < 10 for porosity having amplitude 0.06 or larger) melt focussing even stronger in such highly porous region according to the study of [Katz, 2008] without assigning any arbitrary value to the constant which represents the ratio of effective bulk and shear viscosity of the matrix.

Bibliography

Aharonov, E., Spiegelman, M., and Kelemen, P. (1997). Threedimensional flow and reaction in porous media: Implications for the earth's mantle and sedimentary basins. Journal of Geophysical Research: Solid Earth (1978–2012), 102(B7):14821–14833.

Aharonov, E., Whitehead, J., Kelemen, P., and Spiegelman, M. (1995). Channeling instability of upwelling melt in the mantle. Journal of Geophysical Research: Solid Earth (1978–2012), 100(B10):20433–20450.

Ahern, J. and Turcotte, D. (1979). Magma migration beneath an ocean ridge. Earth and Planetary Science Letters, 45(1):115–122.

Asimow, P. D., Hirschmann, M., Ghiorso, M., O'Hara, M., and Stolper, E. (1995). The effect of pressure-induced solid-solid phase transitions on decompression melting of the mantle. Geochimica et Cosmochimica Acta, 59(21):4489–4506.

Barcilon, V. and Lovera, O. M. (1989). Solitary waves in magma dynamics. Journal of Fluid Mechanics, 204:121–133.

Barcilon, V. and Richter, F. M. (1986). Nonlinear waves in compacting media. Journal of Fluid Mechanics, 164:429–448.

Bear, J. (2013). Dynamics of fluids in porous media. Courier Dover Publications.

Bercovici, D. and Ricard, Y. (2003). Energetics of a two-phase model of lithospheric damage, shear localization and plate-boundary formation. Geophysical Journal International, 152(3):581–596.

150

Bercovici, D., Ricard, Y., and Schubert, G. (2001). A two-phase model of compaction and damage, 1. general theory. J. Geophys. Res., 106(B5):8887–8906.

Bercovici, D., Schubert, G., and Glatzmaier, G. A. (1989). Three-dimensional spherical models of convection in the earth's mantle. Science, 244(4907):950–955.

Berkowitz, B. and Ewing, R. P. (1998). Percolation theory and network modeling applications in soil physics. Surveys in Geophysics, 19(1):23–72.

Birchwood, R. and Turcotte, D. (1994). A unified approach to geopressuring, lowpermeability zone formation, and secondary porosity generation in sedimentary basins. Journal of Geophysical Research: Solid Earth (1978–2012), 99(B10):20051–20058.

Braun, M. G. and Kelemen, P. B. (2002). Dunite distribution in the oman ophiolite: implications for melt flux through porous dunite conduits. Geochemistry, Geophysics, Geosystems, 3(11):1–21.

Chadam, J., HOFF, D., MERINO, E., ORTOLEVA, P., and SEN, A. (1986). Reactive infiltration instabilities. IMA Journal of Applied Mathematics, 36(3):207–221.

Chapman, D. S. and Pollack, H. N. (1977). Regional geotherms and lithospheric thickness. Geology, 5(5):265–268.

Courant, R., Friedrichs, K., and Lewy, H. (1928). Über die partiellen differenzengleichungen der mathematischen physik. 100(1):32–74.

Daccord, G. (1987). Chemical dissolution of a porous medium by a reactive fluid. Physical review letters, 58(5):479.

Daines, M. and Kohlstedt, D. (1994). The transition from porous to channelized flow due to melt/rock reaction during melt migration. Geophysical Research Letters, 21(2):145–148.

Dake, L. P. (1983). Fundamentals of reservoir engineering. Elsevier.

Drew, D. (1983). Mathematical modeling of two-phase flow. Annual review of fluid mechanics, 15(1):261–291.

Drew, D. A. and Passman, S. L. (1999). Theory of multicomponent fluids. Springer.

Dullien, F. A. (1991). Porous media: fluid transport and pore structure. Academic press.

Ehrlich, L. (1972). Coupled harmonic equations, sor, and chebyshev acceleration. mathematics of computation, 26(118):335–343.

Ehrlich, L. W. (1971). Solving the biharmonic equation as coupled finite difference equations. SIAM Journal on Numerical Analysis, 8(2):278–287.

Emerman, S. H., Turcotte, D., and Spence, D. (1986). Transport of magma and hydrothermal solutions by laminar and turbulent fluid fracture. Physics of the earth and planetary interiors, 41(4):249–259.

Faul, U. H. and Jackson, I. (2007). Diffusion creep of dry, meltfree olivine. Journal of Geophysical Research: Solid Earth (1978–2012), 112(B4).

Fowler, A. (1990a). A compaction model for melt transport in the earth's asthenosphere, part i, applications. Magma transport and storage.

Fowler, A. (1990b). A compaction model for melt transport in the earth's asthenosphere, part ii, applications. Magma transport and storage, pages 15–32.

Fowler Jr, T. K. and Paterson, S. R. (1997). Timing and nature of magmatic fabrics from structural relations around stoped blocks. Journal of Structural Geology, 19(2):209–224.

Frank, F. C. (1968). Two-component flow model for convection in the earth's upper mantle. Nature, 220(5165):350–352.

Garapić, G., Faul, U. H., and Brisson, E. (2013). High-resolution imaging of the melt distribution in partially molten upper mantle rocks: evidence for wetted two-grain boundaries. Geochemistry, Geophysics, Geosystems, 14(3):556–566.

Goldschmidt, V. M. (1954). Geochemistry. Soil Science, 78(2):156.

Gregg, P., Hebert, L., Montési, L., and Katz, R. (2012). Geodynamic models of melt generation and extraction at mid-ocean ridges. Oceanography, 25:78–88.

Hart, S. R. (1993). Equilibration during mantle melting: A fractal tree model. Proceedings of the National Academy of Sciences, 90(24):11914–11918.

Hashin, Z. and Shtrikman, S. (1963). A variational approach to the theory of the elastic behaviour of multiphase materials. Journal of the Mechanics and Physics of Solids, 11(2):127–140.

Havlin, C. and Parmentier, E. (2014). Implications for melt transport and source heterogeneity in upwelling mantle from the magnitude of sp converted phases generated at the onset of melting. Geophysical Research Letters, 41(15):5444–5450.

Hesse, M., Schiemenz, A., Liang, Y., and Parmentier, E. (2011). Compaction-dissolution waves in an upwelling mantle column. Geophysical Journal International, 187(3):1057–1075.

Hewitt, I. (2009). Mathematical modelling of geophysical melt drainage. PhD thesis, Trinity College.

Hirschmann, M., Asimow, P. D., Ghiorso, M., and Stolper, E. (1999). Calculation of peridotite partial melting from thermodynamic models of minerals and melts. iii. controls on isobaric melt production and the effect of water on melt production. Journal of Petrology, 40(5):831–851.

Hirschmann, M. M. (2000). Mantle solidus: experimental constraints and the effects of peridotite composition. Geochemistry, Geophysics, Geosystems, 1(10).

Hirth, G. and Kohlstedt, D. L. (1995a). Experimental constraints on the dynamics of the partially molten upper mantle: Deformation in the diffusion creep regime. Journal of Geophysical Research: Solid Earth (1978–2012), 100(B2):1981–2001.

Hirth, G. and Kohlstedt, D. L. (1995b). Experimental constraints on the dynamics of the partially molten upper mantle: Deformation in the diffusion creep regime. Journal of Geophysical Research: Solid Earth, 100(B2):1981–2001.

Hoefner, M. L. and Fogler, H. S. (1988). Pore evolution and channel formation during flow and reaction in porous media. AIChE Journal, 34(1):45–54.

Holtzman, B. K., Groebner, N. J., Zimmerman, M. E., Ginsberg, S. B., and Kohlstedt, D. L. (2003). Stress-driven melt segregation in partially molten rocks. Geochemistry, Geophysics, Geosystems, 4(5):8607.

Holtzman, B. K. and Kohlstedt, D. L. (2007). Stress-driven melt segregation and strain partitioning in partially molten rocks: Effects of stress and strain. Journal of Petrology, 48(12):2379–2406.

Hubbert, M. K. (1940). The theory of ground-water motion. The Journal of Geology, pages 785–944.

Iwamori, H. (1998). Transportation of h2o and melting in subduction zones. Earth and Planetary Science Letters, 160(1-2):65 – 80.

Joseph, D. D. (2006). Helmholtz decomposition coupling rotational to irrotational flow of a viscous fluid. Proceedings of the National Academy of Sciences, 103(39):14272–14277.

Katz, R. F. (2008). Magma dynamics with the enthalpy method: Benchmark solutions and magmatic focusing at mid-ocean ridges. Journal of Petrology, 49(12):2099–2121.

Katz, R. F., Spiegelman, M., and Holtzman, B. (2006). The dynamics of melt and shear localization in partially molten aggregates. Nature, 442(7103):676–679.

Kelemen, P., Hirth, G., Shimizu, N., Spiegelman, M., and Dick, H. (1997). A review of melt migration processes in the adiabatically upwelling mantle beneath oceanic spreading ridges. Philosophical Transactions of the Royal Society of London. Series A: Mathematical, Physical and Engineering Sciences, 355(1723):283–318.

Kelemen, P. B., Johnson, K. T. M., Kinzler, R. J., and Irving, A. J. (1990). High-field-strength element depletions in arc basalts due to mantlemagma interaction. Nature, 345(6275):521–524.

Kelemen, P. B., Shlmlzu, N., and Saltersi, V. J. (1995a). Extraction of mid-ocean-ridge basalt from the upwelling mantle by focused flow of. Nature, 375:29.

Kelemen, P. B., Whitehead, J., Aharonov, E., and Jordahl, K. A. (1995b). Experiments on flow focusing in soluble porous media, with applications to melt extraction from the mantle. Journal of Geophysical Research: Solid Earth (1978–2012), 100(B1):475–496.

Keller, T., May, D. A., and Kaus, B. J. (2013). Numerical modelling of magma dynamics coupled to tectonic deformation of lithosphere and crust. Geophysical Journal International, 195(3):1406–1442.

Khodakovskii, G., Rabinowicz, M., Genthon, P., and Ceuleneer, G. (1998). 2d modeling of melt percolation in the mantle: the role of a melt dependent mush viscosity. Geophysical research letters, 25(5):683–686.

Kohlstedt, D. L. and Holtzman, B. K. (2009). Shearing melt out of the earth: An experimentalist's perspective on the influence of deformation on melt extraction. Annual Review of Earth and Planetary Sciences, 37:561–593.

Korenaga, J. and Kelemen, P. B. (2000). Major element heterogeneity in the mantle source of the north atlantic igneous province. Earth and Planetary Science Letters, 184(1):251–268.

Kühn, D. and Dahm, T. (2004). Simulation of magma ascent by dykes in the mantle beneath mid-ocean ridges. Journal of Geodynamics, 38(2):147–159.

Kumarapeli, S., St Seymour, K., Fowler, A., and Pintson, H. (1990). The problem of the magma source of a giant radiating mafic dyke swarm in a failed arm setting. Mafic dykes and emplacement mechanisms. Edited by AJ Parker, PC Rickwood, and DH Tucker. Balkema, Rotterdam, The Netherlands, pages 163–171.

Lensky, N., Sparks, R., Navon, O., and Lyakhovsky, V. (2008). Cyclic activity at soufrière hills volcano, montserrat: degassing-induced pressurization and stick-slip extrusion. Geological Society, London, Special Publications, 307(1):169–188.

Liang, Y., Schiemenz, A., Hesse, M. A., Parmentier, E. M., and Hesthaven, J. S. (2010). Highporosity channels for melt migration in the mantle: Top is the dunite and bottom is the harzburgite and lherzolite. Geophysical Research Letters, 37(15).

Maaløe, S. (1985). PRINCIPLES OF IGNEOUS PETROLOGY. XIV. Springer.

Maaløe, S. and Scheie, Å. (1982). The permeability controlled accumulation of primary magma, volume 81. Springer-Verlag.

Maruyama, S. and Okamoto, K. (2007). Water transportation from the subducting slab into the mantle transition zone. Gondwana Research, 11(1-2):148–165.

McKenzie, D. (1984). The generation and compaction of partially molten rock. J. Petrology, 25:713–765.

McKenzie, D. (1985). The extraction of magma from the crust and mantle. Earth and Planetary Science Letters, 74(1):81–91.

Michaut, C., Bercovici, D., and Sparks, R. S. J. (2009). Ascent and compaction of gas rich magma and the effects of hysteretic permeability. Earth and Planetary Science Letters, 282(1):258–267.

Michaut, C., Ricard, Y., Bercovici, D., and Sparks, R. S. J. (2013). Eruption cyclicity at silicic volcanoes potentially caused by magmatic gas waves. Nature Geoscience, 6(10):856–860.

Morgan, Z. and Liang, Y. (2003). An experimental and numerical study of the kinetics of harzburgite reactive dissolution with applications to dunite dike formation. Earth and Planetary Science Letters, 214(1–2):59–74.

Morgan, Z. and Liang, Y. (2005). An experimental study of the kinetics of lherzolite reactive dissolution with applications to melt channel formation. Contributions to Mineralogy and Petrology, 150(4):369–385.

Nakayama, M. and Mason, D. (1992). Rarefactive solitary waves in two-phase fluid flow of compacting media. Wave Motion, 15(4):357–392.

Nakayama, M. and Mason, D. (1999). Perturbation solution for small amplitude solitary waves in two-phase fluid flow of compacting media. Journal of Physics A: Mathematical and General, 32(35):6309.

Nicolas, A. (1986). A melt extraction model based on structural studies in mantle peridotites. Journal of Petrology, 27(4):999–1022.

Nicolas, A. and Jackson, M. (1982). High temperature dikes in peridotites: origin by hydraulic fracturing. Journal of Petrology, 23(4):568–582.

Olson, P. and Christensen, U. (1986). Solitary wave propagation in a fluid conduit within a viscous matrix. Journal of Geophysical Research: Solid Earth (1978–2012), 91(B6):6367–6374.

Ortoleva, P., Merino, E., Moore, C., and Chadam, J. (1987). Geochemical self-organization i; reaction-transport feedbacks and modeling approach. American Journal of Science, 287(10):979–1007.

Press, W. H., Teukolsky, S. A., Vetterling, W. T., and Flannery, B. P. (1992). Numerical recipes in fortran 77: the art of scientific computing. Cambridge University Press, Cambridge.

Quick, J. E. (1981). Petrology and petrogenesis of the trinity peridotite, an upper mantle diapir in the eastern klamath mountains, northern california. Journal of Geophysical Research: Solid Earth (1978–2012), 86(B12):11837–11863.

Rabinowicz, M., Ricard, Y., and Grégoire, M. (2002). Compaction in a mantle with a very small melt concentration: Implications for the generation of carbonatitic and carbonate-bearing high alkaline mafic melt impregnations. Earth and Planetary Science Letters, 203(1):205–220.

Rabinowicz, M. and Vigneresse, J.-L. (2004). Melt segregation under compaction and shear channeling: Application to granitic magma segregation in a continental crust. Journal of Geophysical Research: Solid Earth, 109(B4):B04407.

Raddick, M. J., Parmentier, E., and Scheirer, D. S. (2002). Buoyant decompression melting: A possible mechanism for intraplate volcanism. Journal of Geophysical Research: Solid Earth (1978–2012), 107(B10):ECV–7.

Ribe, N. M. (1987). Theory of melt segregation—a review. Journal of volcanology and geothermal research, 33(4):241–253.

Richard, G. C., Kanjilal, S., and Schmeling, H. (2012). Solitary-waves in geophysical two-phase viscous media: a semi-analytical solution. Physics of the Earth and Planetary Interiors, 198:61–66.

Richardson, C. N. (1998). Melt flow in a variable viscosity matrix. Geophysical Research Letters, 25(7):1099–1102.

Richter, F. M. and Daly, S. F. (1989). Dynamical and chemical effects of melting a heterogeneous source. Journal of Geophysical Research: Solid Earth (1978–2012), 94(B9):12499–12510.

Richter, F. M. and McKenzie, D. (1984). Dynamical models for melt segregation from a deformable matrix. The Journal of Geology, pages 729–740.

Rubin, A. M. (1993). Tensile fracture of rock at high confining pressure: implications for dike propagation. Journal of Geophysical Research: Solid Earth (1978–2012), 98(B9):15919–15935.

Rubin, A. M. (1998). Dike ascent in partially molten rock. Journal of Geophysical Research: Solid Earth (1978–2012), 103(B9):20901–20919.

Schmeling (2000). Partial melting and melt segregation in a convecting mantle. Physics and Chemistry of Partially Molten Rocks. Kluwer Academic Publisher, West Brookfield, ma, U.S.A.

Schmeling, H. (1985). Numerical models on the influence of partial melt on elastic, anelastic and electric properties of rocks. part i: elasticity and anelasticity. Physics of the Earth and Planetary Interiors, 41(1):34–57.

Schmeling, H., Kruse, J. P., and Richard, G. (2012). Effective shear and bulk viscosity of partially molten rock based on elastic moduli theory of a fluid filled poroelastic medium. Geophysical Journal International, 190(3):1571–1578.

Scott, D. R. and Stevenson, D. J. (1984). Magma solitons. Geophysical Research Letters, 11(11):1161–1164.

Scott, D. R. and Stevenson, D. J. (1986a). Magma ascent by porous flow. Journal of Geophysical Research: Solid Earth (1978–2012), 91(B9):9283–9296.

Scott, D. R. and Stevenson, D. J. (1986b). Magma ascent by porous flow. Journal of Geophysical Research-Solid Earth and Planets, 91(B9):9283–9296. Article.

Scott, D. R. and Stevenson, D. J. (1989). A selfconsistent model of melting, magma migration and buoyancydriven circulation beneath midocean ridges. Journal of Geophysical Research: Solid Earth (1978–2012), 94(B3):2973–2988.

Simpson, G. and Spiegelman, M. (2011). Solitary wave benchmarks in magma dynamics. Journal of Scientific Computing, 49(3):268–290.

Simpson, G., Spiegelman, M., and Weinstein, M. I. (2010a). A multiscale model of partial melts: 1. effective equations. Journal of Geophysical Research: Solid Earth (1978–2012), 115(B4).

Simpson, G., Spiegelman, M., and Weinstein, M. I. (2010b). A multiscale model of partial melts: 2. numerical results. Journal of Geophysical Research: Solid Earth (1978–2012), 115(B4).

Sleep, N. H. (1975). Formation of oceanic crust: Some thermal constraints. Journal of Geophysical Research, 80(29):4037–4042.

Sleep, N. H. (1988). Tapping of melt by veins and dikes. Journal of Geophysical Research: Solid Earth (1978–2012), 93(B9):10255–10272.

Sparks, D. W. and Parmentier, E. (1991). Melt extraction from the mantle beneath spreading centers. Earth and Planetary Science Letters, 105(4):368–377.

Spence, D., Sharp, P., and Turcotte, D. (1987). Buoyancy-driven crack propagation: a mechanism for magma migration. Journal of Fluid Mechanics, 174:135–153.

Spence, D. and Turcotte, D. (1985). Magmadriven propagation of cracks. Journal of Geophysical Research: Solid Earth (1978–2012), 90(B1):575–580.

Spiegelman, M. (1993a). Flow in deformable porous media. part 1 simple analysis. Journal of Fluid Mechanics, 247:17–38.

Spiegelman, M. (1993b). Flow in deformable porous media. part 2 numerical analysis–the relationship between shock waves and solitary waves. Journal of Fluid Mechanics, 247:39–63.

Spiegelman, M. (1993c). Physics of melt extraction: Theory, implications and applications. Philosophical Transactions of the Royal Society of London. Series A: Physical and Engineering Sciences, 342(1663):23–41.

Spiegelman, M. (2003). Linear analysis of melt band formation by simple shear. Geochemistry, Geophysics, Geosystems, 4(9):8615.

Spiegelman, M., Kelemen, P. B., and Aharonov, E. (2001). Causes and consequences of flow organization during melt transport: The reaction infiltration instability in compactible media. Journal of Geophysical Research: Solid Earth, 106(B2):2061–2077.

Spiegelman, M. and Kenyon, P. (1992). The requirements for chemical disequilibrium during magma migration. Earth and Planetary Science Letters, 109(3):611–620.

Šrámek, O. (2007). Modele d'écoulement biphaséen sciences de la terre: fusion partielle, compaction et différenciation. PhD thesis, ENS Lyon, Charles University in Prague Faculty of Mathematics and Physics.

Stevenson, D. J. (1989). Spontaneous small-scale melt segregation in partial melts undergoing deformation. Geophysical Research Letters, 16(9):1067–1070.

Takahashi, D., R. Sachs, J., and Satsuma, J. (1990). Properties of the magma and modified magma equations. Journal of the Physical Society of Japan, 59(6):1941–1953.

Takahashi, D. and Satsuma, J. (1988). Explicit solutions of magma equation. Journal of the Physical Society of Japan, 57(2):417–421.

Takei, Y. (1998). Constitutive mechanical relations of solidliquid composites in terms of grainboundary contiguity. Journal of Geophysical Research: Solid Earth (1978–2012), 103(B8):18183–18203.

Takei, Y. and Holtzman, B. K. (2009a). Viscous constitutive relations of solidliquid composites in terms of grain boundary contiguity: 1. grain boundary diffusion control model. Journal of Geophysical Research: Solid Earth (1978–2012), 114(B6).

Takei, Y. and Holtzman, B. K. (2009b). Viscous constitutive relations of solidliquid composites in terms of grain boundary contiguity: 2. compositional model for small melt fractions. Journal of Geophysical Research: Solid Earth (1978–2012), 114(B6).

Turcotte, D. and Ahern, J. (1978). A porous flow model for magma migration in the asthenosphere. Journal of Geophysical Research: Solid Earth (1978–2012), 83(B2):767–772.

Ulmer, P. (2001). Partial melting in the mantle wedge—the role of h 2 o in the genesis of mantle-derived 'arc-related'magmas. Physics of the Earth and Planetary Interiors, 127(1):215–232.

Šrámek, O., Ricard, Y., and Bercovici, D. (2007). Simultaneous melting and compaction in deformable two-phase media. Geophysical Journal International, 168:964–982.

Waff, H. and Bulau, J. (1982). Experimental determination of near-equilibrium textures in partially molten silicates at high pressures. Adv. Earth Planet. Sci, 12:229–236.

Waff, H. S. and Bulau, J. R. (1979). Equilibrium fluid distribution in an ultramafic partial melt under hydrostatic stress conditions. Journal of Geophysical Research: Solid Earth, 84(B11):6109–6114.

Wang, C.-Y. and Beckermann, C. (1993). A two-phase mixture model of liquid-gas flow and heat transfer in capillary porous media-i. formulation. International journal of heat and mass transfer, 36:2747–2747.

Watson, E. B. (1982). Melt infiltration and magma evolution. Geology, 10(5):236–240.

Weatherley, S. (2012). Melting and melt migration in heterogeneous mantle beneath mid-ocean ridges. PhD thesis, University College.

Weinberg, R. F. (1997). Diapir-driven crustal convection: decompression melting, renewal of the magma source and the origin of nested plutons. Tectonophysics, 271(3):217–229.

Whitehead, J. and Helfrich, K. R. (1991). Instability of flow with temperaturedependent viscosity: a model of magma dynamics. Journal of Geophysical Research: Solid Earth (1978–2012), 96(B3):4145–4155.

Whitehead, J. A. and Luther, D. S. (1975). Dynamics of laboratory diapir and plume models. Journal of Geophysical Research, 80(5):705–717.

Wiggins, C. and Spiegelman, M. (1995). Magma migration and magmatic solitary waves in 3d. Geophysical Research Letters, 22(10):1289–1292.

Wyllie, P. (1981). Plate tectonics and magma genesis. Geologische Rundschau, 70(1):128–153.

Wyllie, P. J. and Ryabchikov, I. D. (2000). Volatile components, magmas, and critical fluids in upwelling mantle. Journal of Petrology, 41(7):1195–1206.

Zhu, W., Gaetani, G. A., Fusseis, F., Montési, L. G., and De Carlo, F. (2011). Microtomography of partially molten rocks: three-dimensional melt distribution in mantle peridotite. Science, 332(6025):88–91.

Curriculum Vitae

Contact detail

Name:	Suranita Kanjilal
Current Address:	J.-W. Goethe Universität Frankfurt
	Institut für geowissenschaften
	Altehöferallee 1
	60438 Frankfurt a. Main, Germany
Contact:	kanjilal@geophysik.uni-frankfurt.de
	Tel.: +49(0)69-79840116
	Fax.: +49(0)69-79840116

Current position

10/2008 - present:	PhD student in Geophysics (Geodynamics group), J.W. Goethe University, Frankfurt am Main, Germany.
	Supervisor: Prof. H. Schmeling.
	Thesis title: *Theory and numerical modeling of two phase flow: melt percolation process through porosity dependent viscous matrix inside the Earth*

Education

2005 - 2007	MSc(Masters) in Mathematics, Indian Institute of Technology, Madras, India
2001 - 2004	BSc(Bachelors) in Mathematics, Vidyasagar University, India

Earlier Research and Work Experience

---

03 - 07/2008	Research associate (ISRO sponsored), Indian Institute of Technology, Kanpur, India; Supervisor: Dr. S. N. Tripathi *Modeling and parameterization of microphysical and optical properties of mixed-phase clouds*
07/2007 - 02/2008	Worked as a team member of Heymath Solution Group, Chennai, India
2005 - 2007	Masters research in Mathematics, Indian Institute of Technology Madras, India; Supervisor: Prof. K. C. Sivakumar
06 - 07/2006	Summer research student, Indian Statistical Institute, Kolkata, India; Supervisor: Prof. Dr. A. B. Raha

Publication

2012	G. C. Richard, **S. Kanjilal**, H. Schmeling: Solitary-waves in geophysical two-phase viscous media: A semi-analytical solution, Physics of the Earth and Planetary Interiors, 198-199 (2012) 61-66

Oral/Poster Presentations

2007	Oral presentation at IIT Madras, India during MSc thesis defense
2009	Poster presentation at SSP International Symposium on 'Deep slab and mantle dynamics' at Kyoto
2009	Poster presentation at International Workshop on Modeling of Mantle Convection and Lithospheric Dynamics, Braunwald, Switzerland
2009	Oral presentation at Physical research Laboratory, Ahmedabad, Gujrat, India
2011	Poster presentation at EGU, Vienna
2011	Poster presentation at International Workshop on Modeling of Mantle Convection and Lithospheric Dynamics, Potsdam
2012	Oral presentation at Institute of Physics, Bhubaneswar, India

Software and Programing Skill

FORTRAN (v.77, v.90, v.95), C, MATLAB

Prizes, Awards, Scholarships

2008-2012	DFG grant for executing PhD
2005	Scholarship obtained from IIT-Madras, Chennai, India during Masters study

Interests, Hobbies

Reading, writing, painting, traveling, photography

Personal detail

Citizenship:	Indian
Sex:	Female
Date of Birth:	28th January, 1983